Experimental and Theoretical Study of the Characteristics of Submerged Horizontal Gas Jets and Vertical Plunging Water Jets in Water Ambient

Doctoral Thesis

at the

Polytechnic University of Valencia

Institute for Energy Engineering

Department of Chemical and Nuclear Engineering

by

ENG.: Khaled Harbi Mohamed Abd-Alaal

Supervisor: Dr.: José Luis Muñoz-Cobo González

Dr.: Sergio Chiva Vicent

Valencia, Spain

November, 2012

Experimental and Theoretical Study of the Characteristics of Submerged Horizontal Gas Jets and Vertical Plunging Water Jets in Water Ambient

This thesis is submitted in partial fulfillment of the requirements

for the degree of

Doctoral of Philosophy

at the

Polytechnic University of Valencia

Institute for Energy Engineering

Department of Chemical and Nuclear Engineering

(Doctoral Program in Energy Technology)

by

Eng.: Khaled Harbi Mohamed Abd-Alaal

Thesis Supervisor:

Dr.: José Luis Muñoz-Cobo González

Department of Chemical and Nuclear Engineering

Dr.: Sergio Chiva Vicent

Department of Technology and Fluid Mechanics Area

Valencia, Spain

November, 2012

Experimental and Theoretical Study of the Characteristics of Submerged Horizontal Gas Jets and Vertical Plunging Water Jets in Water Ambient

Ph.D Thesis

by

Eng.: Khaled Harbi Mohamed Abd- Alaal

Thesis Supervisor

Dr. José Luis Muñoz-Cobo González

Polytechnical University of Valencia

Dr. Sergio Chiva Vicen

Jaume I University, Castellón

Examining Committee:

Chairman**:**   **Dr. José Miguel Corberán Salvador**

Polytechnic University of Valencia

Secretary: **Dr. Facundo Alberto Escriva Castells**

Polytechnic University of Valencia

Members: **Dr. Luis Enrique Herranz Puebla**

Center for Energy, Environmental and Technology (CIEMAT), Madrid

Dr. Joaquín Navarro Esbrí

Jaume I University, Castellón

Dr. José Enrique Juliá Bolívar

Jaume I University, Castellón

Estudio Experimental y Teórico de las Características de Chorros de Gas Sumergidos Horizontales y de Chorros de Agua Verticales Sumniendo en Ambiente de Agua

Tesis Doctoral

Universidad Politécnica de Valencia

Instituto de Ingeniería Energética

Departamento de Ingeniería Química y Nuclear

(Programa Doctoral en Tecnología Energética)

Presentada por: Khaled Harbi Mohamed Abd- Alaal

Dirigida por: Dr. José Luis Muñoz-Cobo González

Dr. Sergio Chiva Vicent

Valencia, 2012

Certainties....

Something unknown is doing we don't know what
Sir Arthur Eddington (1882 - 1944)

I would never die for my beliefs because I might be wrong
Bertrand Russell (1872 - 1970)

I dedicate this work to

Allah,

my family,

and to everyone

who awakened in me

the curiosity to learn

Acknowledgements

This work could not have reached its fruition to a successful climax without the help of certain individuals. For those persons who went beyond the call of duty in helping me to produce this work I wish to acknowledge first.

My sincerest thanks go to my supervisor Dr. **José Luis Muñoz-Cobo** head of thermal hydraulic and reactor safety group for his confidence in me in handling all aspects of this project and for their contribution to this work through useful scientific discussions. I especially appreciate his honest insights into the wider research community, giving me a right perspective from which to grow as a researcher.

My thanks are also extended to my supervisor Dr. **Sergio Chiva Vicent** for help and advice with the development and construction of the experimental facilities and technical advice and for his enthusiasm developed my interest in fluid mechanics as an under-graduate student. His comments as an expert in fluid dynamics slightly outside the current area of study were especially helpful in increasing the standard of the project. I convey my sincerest thanks to José Luis and Sergio Chiva for the help they provided, support and tolerance that enabled this research to be carried out.

I thank the doctoral students and professors of the Chemical and Nuclear Engineering Department and Thermal Hydraulic and Nuclear Engineering Laboratory for their comments and technical discussions. I also wish to express my gratitude to all of the professors of the Energy Technology for Sustainable Development Master. Deep thanks also to Doménec Vidal and Juan Suelves, for their support and advice throughout my time in Valencia, and the experiences have given me

I am indebted also to the group of Thermal Systems Research and Design of the Institute for Energy Engineering, Dr. Isra, Javi and all the thermal workshop staff, for help and advice with the development of the experimental facilities, also Rafa for technical information and computer guide. I would also like to thank all my Arabic and Egyptian friends here in Valencia for all the moments that we have spent together and for all the encouragement that they have given to me.

Finally, I would like to say that my words would not suffice to convey what I am feeling inside. My parents, without you and your praying for me, I would not have reached this level. My parents thank you for all your encouragement and support during all this time. I would also like to express my gratefulness to my wife "Dr. Safaa" for her tolerance and support through this research. She has always support me to reach this goal and to our beautiful son "Amr". Also many thanks for all who have crossed paths with me during my lifetime, given me spiritual or intellectual guidance, appealed to my senses, or my energy or my desire for adventures, or has otherwise challenged me to think in new ways. However, they also helped me remember what is really important in life.

Khaled H.

Abstract

Turbulent jet motions are prevalent in the natural environment and are essential in industrial applications, they can lead to complex multiphase flow. The flow structure and processes are essentially unsteady and turbulents. In this study, two different test-rigs were constructed to investigate first the horizontal buoyant gas jets and second the vertical plunging water jets, also an Integral Numerical Model was developed to predict the jet trajectories and the parameters and it was validated with the experimental results previously obtained.

A flow visualization technique using a CCD camera, which allowed simultaneous measurements was used to investigate such flows. This enabled to record the behaviour of the two-dimensional trajectories with relative ease. However, this technique provides a direct measurement of the interfacial behavior between the gas jet or bubbles and the liquid ambient. Two different methods were used in this study to obtain and analyze the shadowgraph images denoted as the summation and the statistical and we have found that both methods yield almost identical results.

In the first part of this work, experiments were carried out to investigate the behavior of horizontal buoyant gas jets in water ambient. The following magnitudes were obtained from recorded time-averaged images: gas jet pinch-off, oscillation, unsteadiness of the jet interface, jet penetration length, jet half width, and the expansion angle. Few experimental data and calculations on horizontal buoyant jet with large density variations can be found in the open literature.

Experimental results indicated that the penetration length of the gas jets is strongly influenced by the nozzle diameter and the Froude number as well as with the injection mass flow and jet momentum flow rate. Increasing the Froude number and the injector diameter leads to increase the jet unsteadiness. In addition, the maximum location before the jet pinch-off is shown to have a logarithmic relation with the Froude number for all the jet diameters. Empirical correlations are also developed to predict these parameters.

An integral model is developed to assist in the design and to monitor the performance of the experimental investigation. Unlike the other models, the trajectory of the buoyant-jet is divided into two regions named, momentum and buoyant-dominated due to the effect of momentum and buoyancy force respectively. Each region was studied individually under certain assumptions and governing relations. In addition, the local rate of entrainment is considered variable along the jet trajectory and consisted of two components; one is due to the jet momentum force while the other is due to the jet buoyancy force. In addition, an interfacial shear stress acting at the interface between the jet flow and the ambient in the opposed direction to the main jet momentum flux is considered. Also, an approximately assumption of the momentum of the entrained water droplets into the jet flow is considered. The jet trajectory, penetration lengths, half-width, and velocity along the jet axis defining the jet trajectory are predicted and solved as variables along the jet path. Predictions from the Integral Model are compared with data from the current experimental data and good agreement predictions were found.

In the second part of this work, a series of experiments were performed on the plunging water jets injected vertically downward through short circular nozzles onto a water surface. The effect of the operation conditions including initial jet diameters (d_N), initial jet velocity, and jet length (x_1) on the flow characteristics such as the inception velocity of the gas entrainment, the bubble penetration depth (H_p), the gas entrainment rate (Q_a), the centerline jet velocity (V_c) and the axial jet velocity distribution (V_x) below the free water surface were evaluated.

The results obtained showed that the bubble penetration depth (H_p/d_N) decreases with the dimensionless jet length (x_1/d_N) up to 25, after this point was almost constant. Also, the bubble penetration depth was found to increase with the jet velocity and nozzle diameters. The entrainment rate tended to increase with increasing the jet velocity and their curves were divided into three regions depending on the jet velocity range. The value of Q_a was found also to increases as x_1 and d_N increased for the same jet flow rate. The jet centerline velocity decay (V_c) was measured and found to be a function of the jet impact velocity (V_1) with the plunge water surface, jet diameter (d_1) and the plunge depth (x). The axial velocity distributions (V_x/V_c) were found to be approximately Gaussian distributions for all the cases when plotted against (r/b_u). Empirical relationships were proposed to predict the jet parameters were compared with other available experimental data and correlations. A good agreement was found between predicted and experimental results.

Resumen

Los chorros turbulentos son abundantes en el medio natural y son esenciales en las aplicaciones industriales. Estos suelen conducir a complejos flujos multifase. La estructura y los procesos que allí ocurren son esencialmente inestables y turbulentos. En este estudio se han construido dos diferentes instalaciones para investigar primero los chorros de gas horizontales y en segundo lugar los chorros verticales de agua que impactan sobre superficies libres de fluido, también se ha desarrollado un modelo numérico integral para predecir las trayectorias de estos jets y sus parámetros más importantes, validándose con los resultados experimentales obtenidos.

Se han utilizado técnicas de visualización de flujo mediante cámara CCD, que permiten mediciones simultáneas de diferentes parámetros. Esto permitió registrar el comportamiento de las trayectorias bidimensionales con relativa facilidad. Además, esta técnica proporciona una medición directa del comportamiento interfacial entre el chorro de gas o las burbujas y el ambiente líquido. Se utilizaron dos diferentes métodos en este estudio para obtener y analizar los resultados experimentales.

En la primera parte de este trabajo, se han realizado experimentos para investigar el comportamiento de chorros de gas horizontales penetrando en agua. En ellos se obtuvieron magnitudes de las imágenes grabadas como el pinch-off, la oscilación, inestabilidad de la interfaz de jet, longitud de penetración de jet, anchura media de jet o ángulo de expansión.

Los resultados experimentales indicaron que la longitud de penetración de los chorros de gas está fuertemente influenciada por el diámetro de la boquilla y el número de Froude, así como con el flujo de masa de de entrada y su momento. Aumentar el número de Froude y el diámetro del inyector lleva a aumentar la inestabilidad de jet. Además, la máxima ubicación antes de jet pinch-off se muestra que mantiene una relación logarítmica con el número de Froude para todos los diámetros de jet. Se han desarrollado correlaciones empíricas para predecir estos parámetros.

Se ha desarrollado un modelo basado en la integración de las ecuaciones de conservación para que resulte útil en el diseño de aplicaciones en las que

participen chorros horizontales así como para asistir a la investigación experimental. A diferencia de los otros modelos, la trayectoria de jet es dividida en dos regiones la dominada por el momento inicial del jet y la dominada por las fuerzas de flotabilidad. Cada región ha sido estudiada individualmente. Se considera el entraiment de gotas en la fase gas, y considerándose este como variable a lo largo de la trayectoria del chorro y consistente en dos componentes; uno debido a la fuerza de impulso de jet y otra es debido a la fuerza de flotabilidad de jet. Además, se ha considerado un esfuerzo cortante interfacial. También se considera el aumento del momento producido por la inclusión de las gotas que penetran el chorro. Parámetros como la trayectoria del jet, longitudes de penetración, el ancho del jet y velocidad a lo largo del eje de chorro se han resuelto como variables a lo largo de la trayectoria de jet. Las predicciones del modelo integral se comparan con los datos de los datos experimentales obtenidos con muy buenos resultados.

En la segunda parte de este trabajo, se realizaron una serie de experimentos con de chorros de agua, inyectados verticalmente hacia abajo, a través de toberas circulares que impactan sobre una superficie de agua. Se ha estudiado el efecto de parámetros como el diámetros de chorro inicial, la velocidad de reacción inicial o longitud de chorro en las características del flujo resultante como la velocidad de inicio del arrastre de gas, profundidad de penetración de la burbuja, la velocidad de arrastre de gas, la velocidad del chorro de la línea central y la distribución de velocidad de chorro axial debajo de la superficie de agua libre.

Los resultados obtenidos mostraron que la profundidad de penetración de la burbuja disminuye con la longitud del chorro, pero que después de ciertas condiciones se mantiene casi constante. Además ésta aumenta con los diámetros de la boquilla y la velocidad del chorro. La velocidad de arrastre tiende a aumentar con el aumento de la velocidad de reacción. El valor del caudal de aire atrapado por el jet aumenta para un caudal dado si el diámetro de la boquilla o la distancia entre la salida del jet y la superficie libre aumentan. El decaimiento de velocidad de la línea central de jet fue medido y se encontró que es función de la velocidad de impacto de chorro con la superficie del agua el diámetro y la profundidad de penetración. Las distribuciones de velocidad axial en planos transversales son aproximadamente gausianas. Se han propuesto en la tesis correlaciones empíricas para predecir todos estos parámetros de jet estudiados experimentalmente.

Resum

L'estructura i moviment produït pels jets turbulents són abundants en el medi natural i són essencials en aplicacions industrials. Aquests solen conduir a complexos fluxos multifase. L'estructura i els processos que hi tenen lloc són essencialment inestables i turbulents. En aquest estudi s'han construït dos diferents instal.lacions per investigar primer els dolls de gas horitzontals i en segon lloc els dolls verticals d'aigua que impacten sobre superfícies lliures de fluid, també s'ha desenvolupat un model numèric integral per predir les trajectòries d'aquests jets i seus paràmetres més importants, validant amb els resultats experimentals obtinguts.

S'han utilitzat tècniques de visualització de flux mitjançant càmera CCD, que permeten mesuraments simultanis de diferents paràmetres. Això va permetre registrar el comportament de les trajectòries bidimensionals amb relativa facilitat. A més, aquesta tècnica proporciona una mesura directa del comportament interfacial entre el jet de gas o les bombolles i l'ambient líquid. Es van utilitzar dos diferents mètodes en aquest estudi per obtenir i analitzar els resultats experimentals.

A la primera part d'aquest treball, s'han realitzat experiments per investigar el comportament de dolls de gas horitzontals penetrant en aigua. S'hi van obtenir magnituds de les imatges gravades com el pinch-off, l'oscil lació, inestabilitat de la interfície de jet, longitud de penetració de jet, amplada mitjana de jet o angle d'expansió.

Els resultats experimentals van indicar que la longitud de penetració dels jetss de gas està fortament influenciada pel diàmetre del broquet i el nombre de Froude, així com amb el flux de massa de d'entrada i el seu moment. Augmentar el nombre de Froude i el diàmetre de l'injector porta a augmentar la inestabilitat de jet. A més, la màxima ubicació abans de jet pinch-off es mostra que manté una relació logarítmica amb el nombre de Froude per a tots els diàmetres de jet. S'han desenvolupat correlacions empíriques per predir aquests paràmetres.

S'ha desenvolupat un model basat en la integració de les equacions de conservació perquè resulti útil en el disseny d'aplicacions en les quals participin dolls horitzontals així com per assistir a la investigació experimental. A

diferència dels altres models, la trajectòria de jet és dividida en dues regions la dominada per el moment inicial del jet i la dominada per les forces de flotabilitat. Cada regió ha estat estudiada individualment. Es considera el entraiment de gotes en la fase gas, i considerant aquest com a variable al llarg de la trajectòria del raig i consistent en dos components: un a causa de la força d'impuls de jet i una altra és causa de la força de flotabilitat de jet . A més, s'ha considerat un esforç tallant interfacial. També es considera l'augment del moment produït per la inclusió de les gotes que penetren el jet. Paràmetres com la trajectòria del jet, longituds de penetració, l'ample del jet i velocitat al llarg de l'eix de raig s'han resolt com variables al llarg de la trajectòria de jet. Les prediccions del model integral es comparen amb les dades de les dades experimentals obtingudes amb molt bons resultats.

A la segona part d'aquest treball, es van realitzar una sèrie d'experiments amb dolls d'aigua, injectats verticalment cap avall, a través de toveres circulars que impacten sobre una superfície d'aigua. S'ha estudiat l'efecte de paràmetres com el diàmetres de jet inicial, la velocitat de reacció inicial o longitud de jet a les característiques del flux resultant com la velocitat d'inici de l'arrossegament de gas, profunditat de penetració de la bombolla, la velocitat d'arrossegament de gas, la velocitat del raig de la línia central i la distribució de velocitat de raig axial sota la superfície d'aigua lliure.

Els resultats obtinguts van mostrar que la profunditat de penetració de la bombolla disminueix amb la longitud del jet, però que després de certes condicions es manté gairebé constant. A més aquesta augmenta amb els diàmetres del broquet i la velocitat del raig. La velocitat d'arrossegament tendeix a augmentar amb l'augment de la velocitat de reacció. El valor del cabal d'aire atrapat pel jet augmenta per a un cabal donat si el diàmetre del broquet o la distància entre la sortida del jet i la superfície lliure augmenten. El decaïment de velocitat de la línia central de jet va ser mesurat i es va trobar que és funció de la velocitat d'impacte de jet amb la superfície de l'aigua el diàmetre i la profunditat de penetració. Les distribucions de velocitat axial en plans transversals són aproximadament gausianes. S'han proposat a la tesi correlacions empíriques per predir tots aquests paràmetres de jet estudiats experimentalment.

Keywords

Table of Principal Sections and Chapters

Table of Contents

List of Figures

List of Tables

List of Notations

Nomenclature

b	Jet half width (m)
B_0	Initial buoyancy flux (N)
d_1	Jet diameter at the impact with the water surface (m)
d_N	Nozzle diameter (m)
E	Local rate of entrainment (kg/s)
E_{buoy}	Entrainment rate due to buoyancy (kg/s)
E_{mom}	Entrainment rate due to momentum (kg/s)
Fr_0	Initial Froude number at nozzle exit (-)
Fr_1	Froude number at the impact with the water surface (-)
Fr_s	Local Froude number (-)
g_0'	Reduced gravity (kg/m^3)
H_p	Maximum penetration depth of air bubbles (m)
L_b	Buoyant jet penetration length (m)
L_m	Momentum jet penetration length (m)
l_N	Nozzle length (m)
L_Q	Geometric length, $\sqrt{A_N}$ (m)
L_s	Characteristic length scales (-)
$\dot{m}_d$	Water droplets flow rate (kg/s)
M_0	Initial momentum flux at the injector exit (N)
M_x	Jet momentum flux in x-direction (N/m)
M_y	Jet momentum flux in y-direction (N/m)
Q_0	Initial volume flux (m^2/s)
Q_a	Air entrainment volumetric flow rate (m^3/s)

$Q_{corrected}$	Corrected volumetric flow rate (m^3/s)
O_h	Ohnesorge number (-)
$Q_{reading}$	Volumetric flow rate measured by the flow meter (m^3/s)
Q_w	Jet volumetric flow rate (m^3/s)
R_e	Reynolds number (-)
R_i	Richardson number (-)
s	Plume path, s- axis (m)
u_0	Initial jet velocity at the nozzle exit (m/s)
u_d	Water droplets velocity (m/s)
u_e	Entrainment liquid velocity (m/s)
$\overline{u}_g$	Mean gas velocity at the jet interface (m/s)
u_s	Local jet centerline velocity (m/s)
V_1	Jet velocity at the impact with the water surface (m/s)
$V_c(x)$	Centerline jet velocity (m/s)
V_e	Inception or onset velocity (m/s)
V_N	Jet velocity at the nozzle exit (m/s)
$V_x(x,r)$	Axial velocity distribution (m/s)
W_{ea}	Weber number (-)
x	Axial distance along the jet centerline (m)
x_1	Jet length (m)
x_p	Maximum axial distance before pinch-off (m)

Greek Symbols

ρ	Jet fluid density (kg/m^3)
ρ_a	Air density at impact with the water surface (kg/m^3)
ρ_g	Air jet density (kg/m^3)
ρ_w	Density of water (kg/m^3)

α	Local coefficient of entrainment (-)
α_j	Pure jet entrainment coefficient (-)
α_p	Pure plume entrainment coefficient (-)
μ_g	Jet dynamic viscosity (kg/m.s)
τ_i	Interfacial shear stress (N/m)
Ө	Local angle of inclination of the jet (degree)
β	Buoyancy force per unit length (N/m)
σ	Standard deviation

Subscripts

0	Initial
a	Air
g	Gas
L	Liquid
N	Nozzle exit
r	Radial
w	Water
x	Axial

Abbreviations

CCD	Charge-Coupled Device
ECC	Emergency Core Cooling
LOCA	Loss of Coolant Accidents
ODE	Ordinary Differential Equation
ZEF	Zone of Established Flow
ZFE	Zone of Flow Establishment

Chapter 1

Introduction

1.1 General Introduction

Turbulent jets form a complex multiphase system, which have a great interest in environment and many industrial applications. The methodology entails setting up and executing two different experiments and image processing the data. The structure of this thesis is divided into the following three main parts;

(i) Experimental study of the buoyant gas jets injected horizontally in stagnant water ambient and investigation of the different parameters that affect on the jet characteristics.

(ii) Developing an Integral Model to predict the jet trajectories and other jet parameters of the buoyant gas jets and validate the model by the experimental results.

(iii) Experimental study of the vertical plunging water jets on a free water surface, and investigation of the different parameters associated and affect on the rate of air entrainment.

Both types of these jets considered form multiphase flow configurations, which are of great interest in many industrial applications especially in the nuclear power plant accidents and represent challenging cases for multiphase experiments and model validation.

1.2 Buoyant Gas Jets

A buoyant gas jet is formed when a continuous stream of gas flows from a nozzle into a surrounding liquid medium. Because of its inherent instability, the jet breaks up into a train of bubbles, either immediately at the nozzle exit or at some distance downstream depending on its initial momentum and the density difference between the two fluids. As the jet penetrates into the liquid ambient, it gradually evolves along a trajectory within it.

Besides a problem of basic interest in fluid mechanics, the study of jets and plumes has applications in many practical problems. Gas injection into liquid is prevalent in the natural environment and in a wide range of industrial applications. It can lead to complex multiphase flow scenarios such as those often observed in volcano eruption in deep sea, direct contact condensers,

metallurgical processes, underwater cutting/propulsion, nuclear reactor pressure-suppression systems, and injection devices in chemical reactors. The metallurgical industry uses submerged gas jets for liquid metal stirring and gas-metal reactions, but it has been shown that if the gas jet enters the bubbling regime close to the gas injection nozzle significant pressure fluctuations on the nozzle tip ensue which tends to cause nozzle erosion. For example, nozzle erosion decreases productivity and efficiency (Sahai and Guthrie, 1982). Thus understanding the conditions that control the stability of the gas jet is important to prolonging the life of the gas injection tip and determining the hydrodynamics and efficiency of the mixing process.

These multiphase phenomena are of interest to the nuclear industry for fast breeder reactor technology as the postulated core disruptive accident involves the penetration of nuclear fuel vapor into cold liquid sodium. This interaction has potentially disastrous results for the reactor and thus understanding the dynamics and penetration of the gas jet into the ambient fluid is of utmost importance (Epstein et al. 2001).

Three general groups of factors govern the turbulent buoyant-jet behavior discharged into a fluid: (i) jet parameters, (ii) environmental parameters, and (iii) geometrical factors. The first group includes the initial jet velocity distribution and turbulence level, the jet mass, momentum, and density deficit between the jet and the ambient fluid. The second group of variables includes the ambient fluid parameters, such as turbulence level, currents, and density stratification. These factors usually begin to influence jet behavior at some distance from the orifice. The geometrical factors of importance include the depth of submergence of the jet, the jet shape, its orientation and proximity to solid boundaries or to the free surface.

Numerous past studies have confirmed the presence of two main gas flow regimes depending on the initial jet velocity. At low jet velocities (low flow rate), discrete bubbles are formed from the nozzle, marking the single bubbling regime, characterized by the production of bubbles that break near the orifice and rise independently in the direction dictated by gravitational or density effects. At high gas velocities (high flow rate), where the inertia force of the injected gas plays an important role, a coherent gas jet forms which splits into small bubbles at the end of the jet, marking the jetting regime.

A buoyant-jet flow can be divided into distinct main flow regimes, which characterize the development of the jet flow after leaving the nozzle. These flow regimes are the jet like region, plume like region, and the transition region. In each one of these regimes the flow is dominated by a group of independent flow parameters, and the overall flow behavior can therefore be described by a sequence of these distinct flow regions. An example of horizontal buoyant gas jet injected into a liquid ambient is illustrated in Figure (1.1).
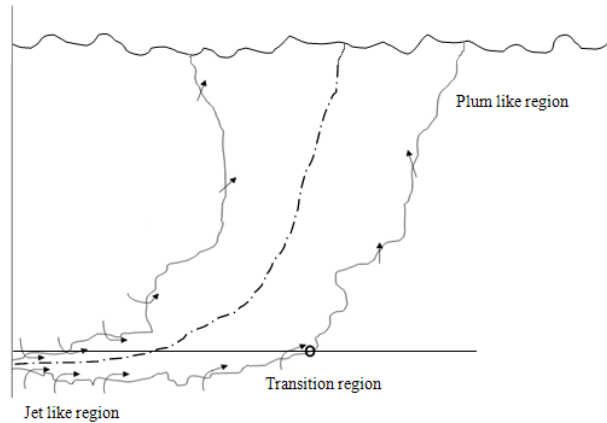
Figure (1.1): Buoyant gas jet into a liquid ambient

Few experimental data and calculations on the horizontal buoyant gas jets with large density variation can be found in the open literatures. Most of the experiments were carried out for small density variation when the Boussinesq approximation is valid and the jet is discharged vertically. However, there is still very little experimental data to understand well these flows and to predict and verify the numerical models.

1.3 Integral Model for Buoyant Gas Jets

One of the objectives of the present study is to develop a theoretical model for horizontal buoyant gas jets. To support the development experiments were conducted to investigate the jet trajectories and the jet parameters of the buoyant jet covering the full range from jet-like to plume-like.

Typical jets are injected into an ambient fluid and their behavior can be modeled in a simplified way as two-dimensional. The jet begins to spread as it is injected into the ambient while also entraining the ambient fluid into the jet. A number of theoretical models to describe the jet development have been

proposed. They range from simple "top-hat" models to complex models of the two-phase flow field in the vessel involving computational of turbulent flow fields. A comparatively simple treatment is that with "entrainment" or "integral" models. These models have been developed in analogy to models for single phase buoyant jets. They are based on assumptions for the radial profiles which usually are taken to be Gaussian, and involve equations for conservation of mass and momentum in integrated forms. The numerical solution of the system of equations is inexpensive.

Integral models developed in order to predict the behaviour of turbulent jet dispersion in the ambient have been the subject of numerous previous studies. These models present differences concerning the assumptions used for the self similar profiles on the one hand and for the turbulent closure of the set of conversation equations on the other hand. Integral models, which are based on the conservation equations of mass, momentum, buoyancy and (where appropriate) species concentration fluxes, are widely used in engineering practice for the prediction of initial dilution for these buoyant jet discharges. One can call the earlier work of Morton et al. (1956) on the integral models for buoyant plume who applied a formulation of the entrainment of the surrounding flow with a mean velocity proportional to the centerline velocity. This approach has been extended later on for buoyant jets.

Buoyant jets are classed as non-Boussinesq at their source if the difference in density between the fluid rising from the source and the surrounding environment is significant compared with a typical reference density ρ_0, for example, the density of the local surroundings. Air injected in water ambient is an example of injecting a low-density gas jet into high-density ambient. This kind of buoyant jets 'plume' is classified as non-Boussinesq; since the initial fractional density difference is high, which is defined as, $\Delta\rho_0/\rho_a = (\rho_a-\rho_g)/\rho_g$, where ρ_g is the initial centerline density and ρ_a is the ambient density.

1.4 Vertical Plunging Water Jets

A vertical liquid jet that plunges into a liquid surface after passing through a surrounding gas phase and it entrains a large amount of gas bubbles into the receiving pool, and forms a large submerged two-phase region with a considerable interfacial area is studied. At the intersection of the plunging jet and the liquid surface, free-surface instabilities develop, and gas entrainment

may be observed. Depending on the situation under consideration, the entrainment is considered as welcome or unwelcome.

Many industrial and environmental processes involve the aeration of a liquid by the entrainment of air bubbles produced when another liquid of the same or different properties impacts on its surface, which is of particular interest within the geophysical, marine, chemical and energy sciences. Aeration by air entrainment is a welcome effect since it reduces damages due to cavitations or it enhances mass transfers producing larger interfacial area densities (Chanson, 1992).

Impinging jets may occur in different situations related to reactor safety analysis. One example is the emergency core cooling (ECC) injection into a partially filled cold leg, which occurs in some scenarios of loss of coolant accidents (LOCA). In this case, the injected cold water impinges as a jet on the surface of the hot water. Depending on the velocity of the jet, stream bubbles may be entrained below the surface by the impinging jet. These bubbles contribute to heat exchange and mixing of the fluids. Heat transfer between cold and hot water and mixing in the cold leg play an important role since the mixed water enters the reactor pressure vessel and may cause high temperature gradients at the wall of the vessel (pressurized thermal shock). An impinging jet may also occur, when an emergency coolant tank is filled up with water and the initial water level is below the inlet. Here, the mixing of the injected water and the water in the tank is a point of interest if the temperatures or the boron concentrations are different. Another scenario for the occurrence of plunging jet phenomenon can be found in the case of a pipe break. The water released from the break can fall as a jet into the reactor sump and transport insulation material toward the sump strainers.

The gas entrainment may however be undesirable in other circumstances, when it occurs during pouring and filling containers with liquids. For liquids such as molten gases, molten metal's, plastics, cosmetics, paints or food products, it is highly undesirable because of the presence of gas bubbles entrained in the liquid phase during these operations, so prevention of gas entrainment in this case is of interest. In many chemical reactors, a plunging jet impinging in a pool or the buffeting of the bulk fluid give rise to bubbly plums, which are responsible for foaming. This foaming is often considered as an inopportune and unwelcome effect.

In order for the gas entrainment to take place, the jet impact velocity has to exceed a characteristic velocity (the onset or threshold velocity) that is a function of the plunging flow conditions. Other factors controlling the mechanisms of air entrainment include the physical properties of the liquid, the design of the jet nozzle (e.g. the nozzle diameter and nozzle length), the distance from the jet outlet to the liquid surface, the jet angle, and the turbulence of the jet. Figure (1.2) shows a definition sketch for air entrainment at a vertical circular plunging jet.
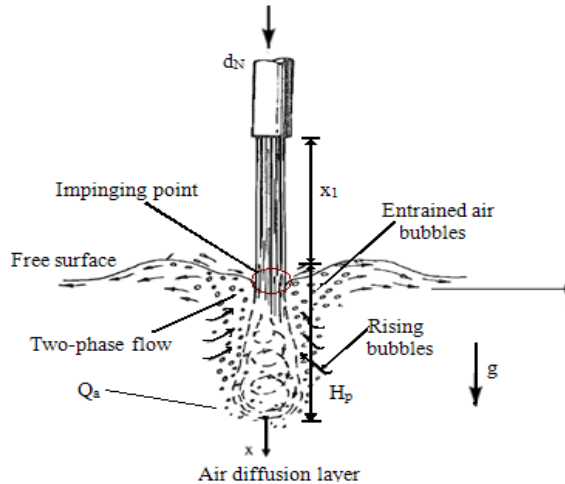
Figure (1.2): Sketch of the plunging jet apparatus

For small jet velocities that are larger than the threshold velocity, air is entrained in the form of individual air bubbles, while large packets of air are entrained and broken up subsequently in the shear flow at higher jet velocities. When the distance from the nozzle outlet to the liquid surface is short, the surface of the liquid jet is not disturbed by the shear forces induced by the surrounding air, and, thus, many small bubbles are generated and dispersed in the whole liquid body. If the jet length is long, the surface of the liquid jet becomes highly disturbed, and relatively large bubbles are generated and dispersed in a localized region in the liquid beneath the nozzle exit. These two patterns occur simultaneously for an intermediate distance (Mahad, 2012).

Reviewing the existing studies on vertical plunging water jets, most of these works were carried out in long nozzles, which had a value of l_N/d_N exceeding 50. In such systems, useful information is available on the gas entrainment characteristics. In contrast, there are few studies on the vertical short nozzles of small length-to-diameter ratios below 5 can be found in the literatures.

Considering practical application of the jet aeration system, it is assumed that there are cases where a long nozzle with a large l_N/d_N ratio cannot be used due to the structural limitation of the reactors or difficulties in the piping and the liquid feeding, etc. For example, consider the case of using a nozzle of 2 mm diameter; the nozzle must be longer than 1 m to satisfy the condition of l_N/d_N greater than 50. Long nozzles of a large l_N/d_N seem to be of no practical use.

However, entrainment of non-condensable gases by plunging liquid jets impacting liquid pool is related to some important practical problems and is a particularly challenging case for multiphase models. Further experimental and theoretical study on the air entrainment by vertical plunging water jets is needed to provide a better understanding.

1.5 **Thesis Objectives**

While much more work is necessary to completely understand the buoyant gas-liquid jets and the vertical plunging water jets concept, these experiments and numerical model have provided a framework for its study and will allow to improve our understanding of these basic phenomena. By utilizing an optical global measurement technique, as opposed to the point measurement techniques used by past researchers, new information on the two-phase flow pattern has been gathered, providing an understanding of the basic characteristics of the gas-liquid interface.

- The primary objective of this work are to develop empirical correlations to describe the different jet parameters and to develop an integral model to predict the jet trajectories and the different parameters of the buoyant gas jets and the validation of this model with the experimental data.

- The second objective is to study the entrained air by vertical plunging water jets on a free water surface and to investigate the different parameters associated and which affect the rate of air entrainment, and to study the jet velocity distribution in the water pool. Further, they can be useful in deciding the depth of the aeration tank, determining the optimum geometry/configuration and comparing the performance of different geometries and configurations of plunging jets under similar flow conditions.

- Another goal is trying to arrive to the best design and form of the jet injection methods includes the injector size and the effect of the operating parameters. Also, to obtain more data and to get a set of database about these jets and its injection process to improve and make a validation of the existing system codes such as; ReLap, etc. and CFD codes such as; CFX, Fluent, etc. also to provide good support for the future work.

- The last objective is to develop a complete data bank of flow visualization images able to provide good support for future velocity measurements and CFD simulations. Moreover, flow visualization is used to provide a general idea of the complicated, unstable and unsteady flow field.

1.6 Outline and Work Organization

The thesis is mainly divided into five chapters. The outline of this thesis and a brief summary of the work comprising each chapter can be defined as follows:

The first chapter presents a general introduction, motivation and objective of this thesis. Chapter (2) provides the experimental and theoretical historical review of the horizontal buoyant jets and the vertical plunging water jets. The third chapter describes the set-up constructed to perform the experiments of the horizontal buoyant gas jets and the instrumentation used. Chapter (4) describes the visualization technique, photographic measurement and the analysis methods used to extract quantitative information from the digital images in order to predict the different jet parameters. Chapter (5) contains the experimental results obtained by the buoyant gas jets with a comprehensive assessment of the data quality of this experimental work. Chapter (6) develops the governing equations for the Integral Model to predict the gas jet trajectory and the jet parameters. Chapter (7) predicts and validates the Integral Model developed with the experimental results obtained by predict the jet trajectory and other parameters. Chapter (8) gives a complete description of the test-rig of the second part of this thesis and provides details of the test strategy, instrument implementation, and test matrix. Chapter (9) presents the experimental results obtained by the vertical plunging water jets, and discusses and compares the results with the available experiments and empirical corrections found in the literature. Some conclusions and recommendations for further study are given in the final part, Chapter (10).

Chapter 2

Overview and Literature Survey

2.1 Introduction

A basic understanding of two areas (horizontal buoyant gas jets and vertical plunging water jets) of research must be gained to put the current work in its proper context. In this chapter, an overview is given and is divided into two major parts:

First part*:* Summarizes the established theories of buoyant gas jets and review the previous experimental studies that are found in the open literature together with the integral model used to predict the jet parameters with correlations of their properties.

Second part*:* Summarizes the reviews of the literature of the available experimental and theoretical studies on the gas entrainment by plunging water jets. Wherever, possible empirical correlations enabling estimation of the quantities characterizing the entrainment phenomena are given and discussed.

2.2 Submerged Gas Jets

This part of review is divided into two different parts. In the first part the flow configuration and the basic parameters which describe the different jets are presented. The second part covers the history and previous experimental work done by many researchers on the behavior of horizontal buoyant gas jets, previous numerical studies and a look on the problem formulation of the buoyant jet will be introduced to make the point more clear.

2.2.1 Flow Configurations

In this section, different flow configurations (vertical gas jets and horizontal gas jets include; pure jets, pure plumes, and buoyant jets) and relationships are discussed and sources of experimental data listed.

2.2.1.1 Vertical Gas Jets

A vertical jet is a jet that is discharged in the same or opposite direction as the gravitational field. An example of submerged gas injected vertically into a liquid environment is described in Figure (2.1).
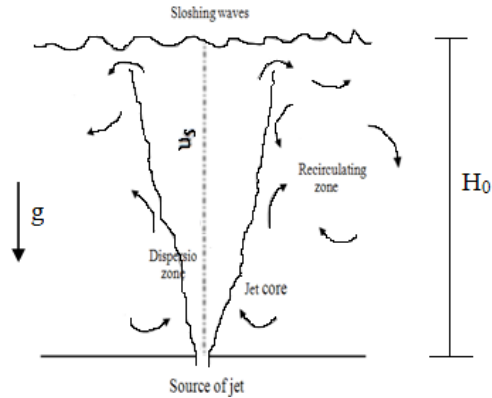
Figure (2.1): Vertical gas jet discharging into deep stagnant ambient water

The gas originates from a point source at water depth H_0: The flow close to the source is dominated by the following: the initial momentum of the gas, the gas expansion and the breakup of the gas into bubbles. The pure plume is driven by buoyancy only and consists of an inner core where most of the bubbles are found and a wider region with substantial upward velocity. The rising water is deflected outwards in a radial surface flow. This turning process causes an elevation of the water surface, which is referred to as the fountain. The vertical gas jets can be found in environment and many engineering applications such as volcanoes, underwater releases of natural gas, resulting from accidents in offshore drilling (blowouts) or broken gas pipelines, metal processing, and nuclear reactor pressure suppression systems.

2.2.1.2 Horizontal Gas Jets

A horizontal gas jet is a jet that discharged perpendicular to the gravitational field. The behavior from a horizontal gas jet is not as well documented as the behavior of a vertical gas jet. The amount of literature available for the studying of a vertical gas jet exceeds the available literature for the studying of a horizontal gas jet. Furthermore, the measurement techniques used to track jet trajectory are typically either intrusive, point wise-based, or both.

2.2.1.2.1 Pure Jets (Non-Buoyant Jets)

A simple jet flow has no buoyancy flux, as the density of the fluid in the jet (ρ) and the density of the ambient fluid (ρ_a) are the same, and the ambient

environment is stagnant. The behavior of the flow is therefore dominated by the initial momentum flux.

$$M_0 = \frac{Momentum}{time} = \frac{mass}{time} \times velocity = \rho Q_0 u_0 \qquad (2.1)$$

where, u_0 is the initial velocity of the flow at the nozzle exit, and Q_0 is the flow rate of the discharge. Figure (2.2) shows a schematic presentation of a simple round jet, including a mean cross-section velocity profile at some distance away from the source.
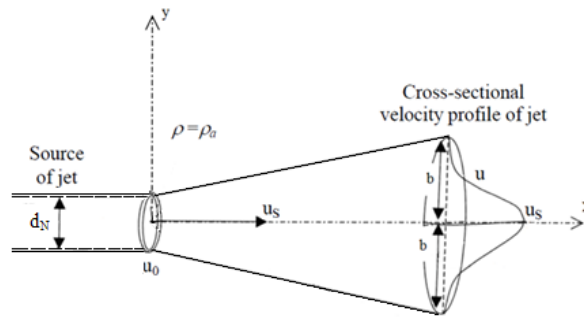
Figure (2.2): Initial conditions and cross-sectional velocity profile for a pure jet

where, x is the Cartesian coordinate in the same direction as the direction of the horizontal component of the initial jet velocity, y is the Cartesian coordinate in the same direction as the vertical component of the initial jet velocity and is perpendicular to the x-coordinate in the horizontal plane, and s is the distance from the source along the trajectory of the flow.

Upon entering the ambient fluid, a shear layer will form between the jet and the ambient fluid. The behavior of the jet may be broken into two distinct zones, the Zone of Flow Establishment (ZFE), and Zone of Established Flow (ZEF). Within the first zone (ZFE), the shear forces generated by the interaction of the jet and the ambient fluid have not penetrated into the center of the jet, and there exists a jet core in which the velocity remains equal to the jet exit velocity. After a short distance from the jet exit, approximately 6.2 nozzle diameters, the Zone of Established Flow (ZEF) begins. Within this zone the velocity and concentration profiles become Gaussian. As a result, the time-averaged profiles

of velocity can be expressed as a maximum value at the jet centerline, and the distance from the jet centerline.

The study of high-speed fluid flowing from an orifice into quiescent fluid, defined as a jet, is a classic subject in fluid mechanics. Helmholtz (1868), Kelvin (1871), and Rayleigh (1879) were among the first who studied this problem. Although the literature contains a large body of works on single phase jets (Dimotakis et al. 1983 and Wang and Law 2002) such as water jet in a water environment.

2.2.1.2.2 Pure Plumes

Like the simple jet, the pure plume flows into a still ambient. But, unlike the simple jet, there is a buoyancy flux due to the difference in the density between the ambient fluid (ρ_a) and the plume fluid (ρ), and the initial velocity of the flow is almost negligible. A schematic diagram is shown in Figure (2.3). Due to the low initial velocity of the flow, the source direction does not influence the behavior of the flow. In the environment, the ambient fluid is generally denser than the pure plume fluid and therefore the buoyancy flux acts vertically upwards. Examples are heated air released from a vertical smokestack or wastewater released into an ocean.
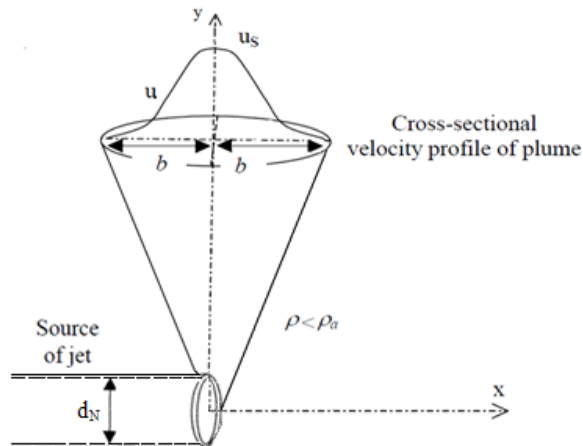
Figure (2.3): Initial conditions and cross-sectional velocity profile for pure plume

The flux of the buoyancy in the plume is calculated by considering an element of the buoyant fluid of volume δV and density ρ in an environment of density ρ_a. The weight of the fluid in the element is w $= \rho g \delta V$ which a downward

force. The pressure force on the surface of the fluid element is equal to the weight of ambient fluid displaced by this element is $P = \rho_a g \delta V$, which is an upward force. The net force is the difference between the upward pressure force P and the downward force of the weight w, and that is the buoyancy force $(\rho_a - \rho)g\delta V$.

If the buoyancy in the plume is produced by discharging fluid of density ρ at a rate Q_0 (volume flux) into an ambient fluid of density ρ_a, the buoyancy flux associated with the discharge would be

$$B_0 = \frac{buoyancyforce}{time} = \frac{buoyancyforce}{mass} \times \frac{mass}{time} = g'_0 \rho Q_0 \qquad (2.2)$$

where, g'_0 is the reduced gravity, given by:

$$\text{Reduced gravity } (g'_0) = \frac{(\rho_a - \rho)g}{\rho_a} \qquad (2.3)$$

The reduced gravity is a term introduced to describe the distribution of the force per unit mass of the fluid while the velocity is to specify the distribution of the momentum per unit mass of the fluid.

2.2.1.2.3 Buoyant Jets

A buoyant jet can be defined as the fluid motion caused by the sustained injection of a low-density fluid with large momentum through an orifice into a fluid ambient of bigger density. As the jet penetrates into the fluid ambient, it gradually evolves along a trajectory within it.

Most of plume experiments have a significant initial momentum flux, and these experiments are better described as buoyant jet flows. The flow travels firstly through a region where the initial momentum flux dominates and the behavior of the flow is jet-like. In the region where the flow is driven by the buoyancy force, the buoyancy-generated momentum flux dominates and the behavior is plume-like. In this region, the flow starts to rise more dramatically depending on the relative densities of the two fluids (see Figure 2.4). However, buoyant

jets are characterized by their inertial and buoyancy forces in the form of non-dimensional numbers. The inertial forces are described by the Reynolds number while the buoyancy forces are described in the referenced literature by alternatively, the Froude or Richardson number depending on the author.
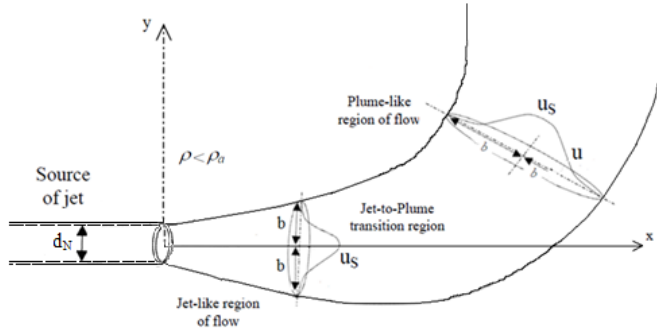
Figure (2.4): Flow regions of a buoyant jet

The buoyant jet is characterized in the near field by the source Froude number:

$$Fr_0 = \frac{u_0}{\sqrt{g_0' d_N}} \tag{2.4}$$

Making use of the definitions in Fischer et al., (1979), there are three expressions that are useful in describing the conditions in a buoyant jet:

$$\text{Volume flux,} \qquad \mu = \int_A u dA \tag{2.5}$$

$$\text{Momentum flux,} \qquad m = \int_A u^2 dA \tag{2.6}$$

$$\text{Buoyancy flux,} \qquad \beta = \int_A g' u dA \tag{2.7}$$

These quantities will vary with location in the jet as fluid is entrained and velocities decrease. For purposes of determining how the jet will behave it is

often more convenient to state these quantities in terms of the initial jet magnitudes.

2.2.2 Research History

Buoyant jets have been observed and commented on since the beginning of modern science, for example, they were observed coming out of smokestacks and volcanoes. Jirka (2004) gives an extended overview of the history of research on the buoyant jet.

An investigation was lead by L. Prandtl in the 1920's; he applied boundary layer theory to the jet flow. Soon it was followed by measurements on the round non-buoyant jet (Zimm, 1921) and the plane non-buoyant jet (Förthmann, 1934). These measurements were the basis for the development of the similarity solutions for the spread and the velocity decay of the jet (Görtler, 1942, Reichardt 1942, and Tollmien 1926). Prandtl's turbulent mixing length hypothesis was used to relate the shear stresses to the mean flow of the jet and this method was taken a step further to include a pure vertically rising plume by Schmidt (1941). Reichardt (1943) was the first to determine that the cross-sectional properties of the jet could be approximated by Gaussian profiles, forming the foundation of the jet-integral method. The method was further developed into a jet integral model with the results of more detailed experiments carried out on the simple jet (Albertson et al. 1949) and the pure plume (Rouse et al. 1952).

Morton et al. (1956) introduced the idea that fluid momentum, vorticity and scalars in a jet are spread by turbulent entrainment rather than turbulent diffusion. They hypothesized that non-turbulent, irrotational fluid from outside the jet was entrained into the turbulent jet. This viewpoint was quickly incorporated into the already existing jet-integral methods. Aoki et al. (1982) tested straight type of nozzles by which the maximum jet velocity was sonic. Loth et al. (1989) reported the structure and mixing properties of underexpanded round turbulent air jets submerged in quiescent water at relatively low pressures. They measured the static pressure distributions along the jet axis, void fraction distributions and entrainment rates.

2.2.3 Problem Formulation of the Buoyant Jets

The high water-to-gas density ratio can result in complicated flow structures; hence, it remains a challenging issue to calculate the flow structures numerically and to measure experimentally. A series of experimental investigations are needed in order to understand relevant phenomena and characteristics.

The high velocity gradients at the interface between the jet and the ambient fluid make it highly unstable, and cause the jet fluid to rotate. These turbulent vortices entrain the ambient fluid into the jet, causing the mixing processes and the dissipation of the energy from the discharge (Jirka and Harleman, 1979).

There is relatively little work on the behavior of submerged gas jets in water. Here the term "behavior" is used broadly encompassing gas jet characteristics such as the unsteady motion of the gas-liquid interface and how far the gas jet penetrates into the liquid bath and how it expands. The present study is devoted to the subsonic regime, namely experimental study of the characteristics of submerged horizontal round gas jets in a liquid pool. Only a small number of previous investigations can be found in the literature on this subject.

2.2.4 Previous Experimental Study

Outside the laboratory, it is not possible to measure all the major factors influencing the flow behavior and therefore the data are difficult to interpret. Because of the less-controlled environment outside the laboratory, the results were less accurate. Inside the laboratory, it is possible to separate the important independent parameters, the initial momentum flux and the buoyancy-generated momentum flux, from outside influences and from each other. This enables the researcher to carefully determine the influence of each of the factors on the flow. The laboratory studies differed in the use of measurement techniques, aims and types of flow. Because of the increase in the technology available to researchers over time, the studies have become more detailed; the flow measurement techniques more accurate and more complex flow configurations have been monitored. Data from experimental investigations has been used for verification of models as well as for the determination of the empirical parameters in the integral models.

The whole gas injection consists of several regions, a jet region, a transition region, a plume region, a two-phase turbulent zone of gas dispersed in liquid, a liquid recirculating zone, and sloshing waves formed on the surface of the bath when the gas flow rate is high enough. An example of horizontal buoyant jet injected into a liquid ambient is illustrated in Figure (2.5).
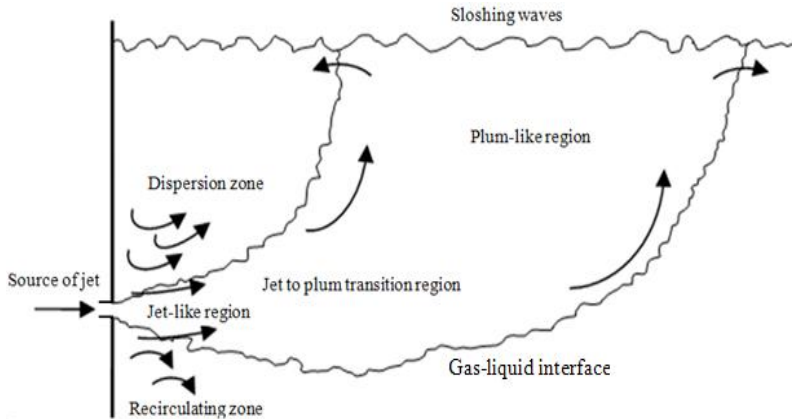
Figure (2.5): Submerged gas jet into a liquid ambient

Previous past experimental studies suggested that a buoyant jet flow can be divided into distinct main flow regions, which characterize the development of the gas flow after leaving the nozzle (for example Davidson, 1998 and Jirka, 2004). These flow regions are the jet like region, plume like region, and the transition region (see figure 2.4). In each of these regions the flow is dominated by a group of independent flow parameters, and the overall flow behavior can therefore be described by a sequence of these distinct flow regions.

In the jet regime, the discharged flow is mainly governed by the jet momentum force and the self-generated turbulence plays a dominated role in the path of the jet; the gas jet does not disintegrate until it reaches some distance from the nozzle, where the jet breaks up into a column of rising bubbles. In the plume regime, the flow is chiefly controlled by the buoyancy force and characterized by the production of bubbles that break and rise independently in the direction dictated by gravitational or buoyancy effects. Between the jet and plume regimes, there exists an intermediate regime called transition stage (Miyahara et al. 1983). In the transition stage, the effluent flow is governed by both momentum and buoyancy force and will cause the jet to move horizontally with radial velocities as soon as the jet reaches the water free surface.

Some studies performed on the transition regime, for example, Mersmann (1980) found that the transition from bubbling to jetting regimes in the air/water system occurs at a critical Weber number of 2, irrespective of the orifice diameter. Through studying bubble formation at high gas flow rates with a high-speed camera, Miyahara et al. (1983) proposed an empirical correlation to predict the transition point in the liquid using dimensionless Weber and Bond numbers ($B_o = \rho g L^2/\gamma$). Mori et al., (1982) were among the first to define a useful quantitative metric to describe the bubbling/jetting transition point. They showed experimentally that the sonic flow region defines the transition point between bubbling and jetting behavior. The system pressure or gas density has a significant effect on the bubbling-jetting transition. Ozawa and Mori (1986) studied the effects of the physical properties of gas and liquid on the bubbling-jetting transition in liquids, they found that the bubbling-jetting transition occurs at lower gas velocities when they increased the ratio of gas to liquid densities.

Kitscha et al. (1989) and Zhao et al. (1990) were among the first to identify the importance of such instability mechanisms in dictating the bubbling to jetting transition point and explained that jetting occurs when perturbations travel on the phase boundary faster than they can accumulate. Chen and Richter (1997) conducted perturbation analysis of a compressible gas jet injected into an unbounded inviscid liquid environment. They computed the transonic regime as the bubbling/jetting transition point, and argue that the physical mechanism for this behavior is the accumulation of vorticity that is generated by compressibility effects.

Few experimental data and calculations on horizontal buoyant jets with large density variations can be found in the open literatures. Most of the experiments were carried out for small density variation when the Boussinesq approximation is valid and the jet is discharged vertically.

2.2.4.1 Jet Pinch-Off

The injection of gas into liquid introduces an additional level of complexity in the jet character, which is marked by the unsteadiness and pulsating behaviour of the phase interface. The submerged gas jet can even rupture into multiple independent bubbles which rise independently, and the jet is no longer continuous from the nozzle to the free surface, this phenomenon known as pinch-off.

When the gas jet enters the water initially, the pressure of the gas is not high enough to overcome the inertia effect of the water due to the large density ratio between the jet and the ambient water. Therefore a "gas bag" enclosed by the surrounding water will form behind the nozzle exit, so-called bulge phenomenon. The pressure inside the "gas bag" will accumulate and keep increasing, and once it is high enough to overcome the suppression of the water, the gas can expand freely to complete the expansion process. Bulging of the jet occurs many times before the more violent jet expansion feedback occurs. During the feedback process, the jet diameter can become several times that of the original one depending on the jet Mach number. As a result, the "gas bag" will be compressed in the direction perpendicular to the centerline. The "gas bag" will collapse and separate the gas jet into two parts, which is the so-called pinch-off (necking/breaking). This breaking will narrow the jet diameter and hence the gas jet newly supplied from the nozzle will encounter difficulties passing through this area. As a result, the pressure between the breaking point and the nozzle exit will become much higher. Meanwhile, a shockwave will move into the nozzle, and the velocity at the nozzle exit will decrease. This breaking phenomenon plays a very important role in causing the jet process to become more unsteady and turbulent. However, this mechanism cannot be observed in gas-gas jets due to their comparable density ratio (Shi, 2010).

Christopher (2009) studied experimentally the phenomenon of the gas jets pinch-off produced by rectangular submerged nozzles in a water ambient using a photographic technique and he showed that the number of pinch-off events decreases in a logarithmic function when increasing the Mach number and when appropriately scaled by the total viewing length, and a geometric length scale (L_Q) that is relatively constant across all aspect ratio nozzles. The location of pinch-off is also a function of the aspect ratio.

2.2.4.2 Unsteady Jet Interface Characteristics

One important difference between injection of a gas jet into a liquid and the baseline case of a gas jet into a gas is the characteristic unsteadiness associated with gas injection into liquids. Gas jets submerged into liquids are complicated by effects of unsteadiness at low flow rates, similar to the pulsatile behavior of highly buoyant single-phase flows. This involves oscillatory release of gas which can cause liquid to slug into the jet passage. The unsteadiness is accompanied by appreciable fluctuations of static pressure in the flow nozzle and beyond the jet boundaries, often resulting in excessive noise and vibration

as well as blockage of the passage in cases where the gas reacts with the liquid (for round jets see Kerney et al. 1972, Chan 1974, Avery and Faeth 1974). While the structure and stability of single-phase jets have been studied for quite some time, multiphase systems formed by a gas jet submerged into liquid are infrequently studied.

Lin (1986) showed that increasing the fluid density ratios (ρ/ρ_a) yielded a less stable discharge. Another feature of multiphase jets involves the highly nonlinear variation of the two-phase acoustic velocity (noted by Semanov and Kosterin, 1964 and Wallis, 1969) which probably affects the gas dynamic processes for air injection into water. However, the unsteadiness and turbulence together with the large density ratio across the interfaces lead to difficulties in the experimental measurements and numerical approaches, and hence it remains challenging to measure and investigate the flow structures with numerical methods.

Dai et al. (2006) have performed experiments to display the flow pattern and hydrodynamic effect of underwater gaseous jets from supersonic and sonic nozzles experimentally. Their results show that high-speed gaseous jets in stagnant water can induce large pressure pulsations in the upstream of the nozzle exit. Shi et al. (2005 and 2010) have indicated that the process of supersonic air jets into water causes large flow oscillation, which can be related to shock waves reflecting in the gas phase.

2.2.4.3 Jet Penetration Distance

The jet penetration distance is defined as the maximum length along the jet centerline in the ambient, and it is governed by several parameters, such as the diameter of the nozzle, the water depth, and the jet mass flow rate. The jet penetration length in the water ambient is pulsated and is varies in time along the jet axis. Several previous works have measured the penetration distance of submerged round gas jets using electro resistive or optical probes lowered into the water and traversed through space (eg. Castillejos, 1987 and Ito, 1991).

Ozawa et al. (1986) for example used this method to measure how far gas penetrates into the surrounding water. If water was present at the measurement point an electrical circuit was completed and registered a value of 1 and if gas was present a value of 0 was recorded. By summing up all of these values in time for a given points the time fraction of gas penetration at that point was

calculated. Other researchers measured the jet penetration distance by means of a simple rule fixed on the tank wall.

The most widely used technique to calculate the jet penetration length is the direct visualization technique. Their use involves the utilization of a camera which resort to Charge-Coupled Device (CCD) and lighting systems based on solid-state and stroboscopic light sources that enable to measure the interface position of the gas jet spatially at each instant of time. By sum the values of each pixel over time by the total number of frames is possible to arrive at a time fraction of gas presence for all pixel locations. One advantage of this approach is that it enables distinguishing between bubbles that have fractured from the gas jet column and an injector continuous jet, which is not possible using the electroresistive probe.

Kerney et al. (1972) and Weimer et al. (1972) studied the penetration length of sonic steam jet submerged horizontally in quiescent subcooled water experimentally and theoretically, they obtained correlations to calculate the dimensionless penetration length. Hoefele and Brimacombe (1979) have investigated the dynamics of a gas jet discharging horizontally into liquids over a wide range of the gas flow rates. They have found that flow regimes and penetration distance depend both on the Froude number and density ratio ρ_g/ρ_a. Engh and Nilmani (1988) have examined the effects of high gaseous flow rates and high viscosities in submerged gas injection, and indicated that viscosity can retard the gas flow velocity.

Christopher (2009) investigated submerged high speed gas jets ranging from subsonic to supersonic Mach numbers using the photographic technique by using a CCD camera, which allowed simultaneous measurements of the entire interface between the gas jet ant water ambient. The experimental results showed that the jet penetration length increased when increasing the jet mass flow rate in a power law relationship, and increased linearly with the Mach number when he used rectangular gas jets with aspect ratio of 2, 10 and 20.

Satoshi et al. (2011) investigated the underexpanded gas jet injected into water ambient by using the photographic technique (CCD camera). The gas jet penetration distance and jet expansion angle were obtained from time-averaged images captured using a high-speed camera. It was found that the gas jet length and expansion angle increased approximately linearly when increasing the jet stagnation pressure.

2.2.4.4 Jet Spreading Rate

The entrainment process and the spreading rate of a turbulent jet are determined by the large and dominant eddies extending across the full width of the jet. The ultimate mixing of the entrained fluid with the source fluid is carried out by the small eddies that circulate around the dominant eddies. Due to its momentum, the jet entrains ambient fluid from outside of the jet boundary into the main turbulent stream thus increasing the volume flux of the jet. The mixing results in a change in both the jet velocity and width. The radius of the jet (b) is expected to depend on the initial momentum flow rate of the jet, the fluid density and the distance from the source (x):

$$b = fn(M_0, \rho, x)$$

(2.8)

The only dimensionless parameter in this functional relation is b/x, which must be a constant. According to this dimensional consideration, the width of the jet increases linearly with the distance from the source.

Christopher (2009) studied experimentally gas jets submerged in water using rectangular gas jets with aspect ratio of 2, 10 and 20 and a photographic technique. The experimental results showed that the jet-spreading rate is a function of both: the Mach number and the injector size. Increasing injector aspect ratio and Mach number increases the spreading rate in a nonlinear form.

A series of experimental investigations are needed in order to understand some relevant phenomena. Therefore, in the present study, as a preliminary step towards clarifying the flow of a gas jet injected into water horizontally, flow visualization was performed using a high-speed camera, and the behavior of the gas jet was investigated at different Froude number and nozzle diameter conditions.

2.2.4.5 Flow Visualization Techniques

In their efforts to understand the characteristics of submerged gas jets, past researchers have relied on point measurements such as electroresistivity probes to separate the liquid and gas phases for study (Mori et al., 1982 and Ito et al., 1991). In these techniques, the probe lingers at the measurement spot for some

time and it is traversed in space. The sensing element can be a singular measurement point or be composed of several measuring points capable of simultaneous measurement at multiple spatial locations. In either case the probe itself is intrusive and only permits time-averaged whole-field measurements since the probe can only exist at one (or several) points in space at any given time. In such an unsteady and highly irregular flow field a global measurement is preferred since instantaneous information can be obtained. An example of a global measurement is high-speed photography, which has been used in the past (McNallan and King, 1982 and Loth and Faeth, 1989) to observe the interface.

Flow visualization techniques are an important tool in the fluid dynamics research; it is used extensively in engineering, physics, medical science, meteorology, oceanography and aerodynamics etc. Specially, these techniques are widely used in the study of different phenomena associated with two-phase flow. In particular, is possible to study the processes of rupture and coalescence of bubbles present in the fluid by visualizing them. It is possible to classify these techniques into two main sections: direct visualization techniques, and advanced visualization techniques.

Direct visualization techniques are the most widely used and they normally used cameras with Charge Coupled Devices (CCD) and illumination systems based on solid-state light sources and stroboscopic. The technical characteristics of the CCD cameras must be such that will be possible to attain a high possible resolution, short shutter speeds (in the order of microseconds, due to the necessity of capture images of fast-moving objects). Finally having the capacity to acquire a high amount of images per second due to the fact that in many applications it is necessary to obtain information about the path followed by the bubbles. Some applications involve a set of studies on the bubble formation process (Manase, 1998), bubble diameter measurements (Otake 1977, Snabre 1998, and Tsao 1997), and the study of the processes leading to their coalescence (Tse, 1998).

Furthermore, direct visualization techniques are typically used as a complement to other experimental techniques such as hot filament anemometry, conductivity probes, etc. As to the limitations posed by these types of techniques, the main one stems from the fact that it is not possible to apply them in two-phase flow with thick bubble clouds, given that in this case the bubbles which happen to be closer to the CCD overlap with the farthest ones,

thereby rendering their visualization impossible. Besides it is necessary to perform digital processing of the obtained images aiming at obtaining quantitative results and the precision of these results will be determined both by the quality of the images and by the type of digital processing performed upon them. The next diagram displayed in Figure (2.6) shows the simplified scheme of a two-phase flow visualization system.
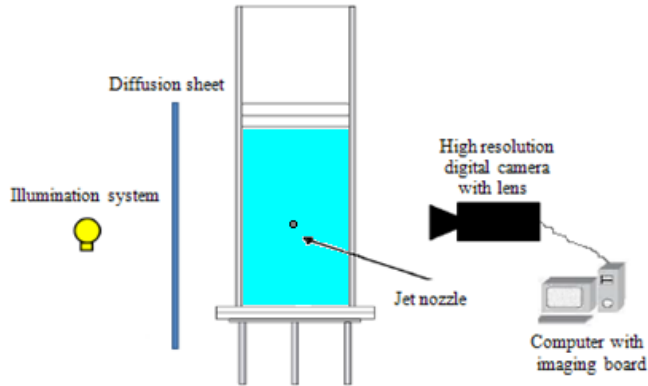
Figure (2.6): Basic scheme of a visualization system

Advanced visualization techniques are more complex, these are experimental techniques that use a laser system (sheet) as an illumination source. With this way, it is possible to carry out tomography studies of bubble clouds and to solve, at least partly, the problems associated to two-phase flow measures with a high bubble density. Within this block, the most extended techniques are the Particle Image Velocimetry (PIV), which are still very expensive experimental techniques but which yield extensive flow speed fields (Lindken, 2002 and Funfschilling, 2001). Furthermore, there are simpler techniques, based in interferometry principles which allow measuring the diameters of bubbles with high precision (Kawaguchi, 2001). The kind of visualization system equipment and its resolution is very important to get a good quality of information in the pictures of the phenomena.

Since a major goal of this work was to study the interface motion itself, the technological limitations imposed by traditional measurement techniques (electroresistivity probes) were unacceptable. As indicated in the previous sections, buoyant jet flows can be classified based on their trajectory (including jets and plumes). For those flows with two-dimensional trajectories, it is possible to detect the boundary between the gas jet region and the water ambient by measuring with a video (CCD) camera located such that it is perpendicular to the flow path.
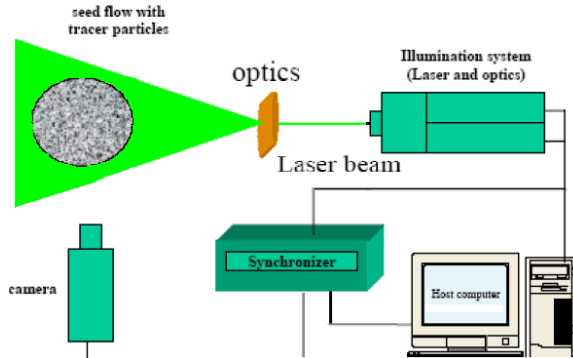
Figure (2.7): Basic principle of PIV

Direct flow visualization using a high velocity camera and illumination system is used in the present study to record the position and motions of the entire gas jet to achieve measurement goals of different jets parameters and the digital images are analyzed to extract the interface position.

2.2.5 Previous Numerical Studies

The considerable research activity in the area of buoyant jets over the past 50 years has resulted in a number of different models that mathematically describe the trajectory of buoyant discharges. Over time, these models have expanded to incorporate more complex flow configurations. The different models can generally be split into three different categories, integral models, length-scale models, and models that use a combination of both length-scales and integral techniques.

Many of these models have been developed using dimensional analysis in combination with experimental results to quantify coefficients or parameters. Some models have been theoretically derived using an integral analysis for a particular discharge or environmental conditions. Whether developed in Eulerian or Lagrangian framework, the governing equations are under-specified and it is the type of closure scheme adopted that separates most models. The historical development of buoyant fluid models can be traced through the assumptions made for the closure schemes, which are achieved by specifying the way in which the ambient fluid is entrained into the buoyant fluid. This usually takes the form of an entrainment assumption. An underlying assumption of most buoyant jet models, including the model presented in this

thesis, is that of similarity. That is, the profiles of mean velocity and buoyancy are assumed to remain the same at all distance from the source.

The integral models, which are based on the conservation equations of mass, momentum, and buoyancy fluxes, are widely used in engineering practice for the prediction of characteristics for these buoyant jet discharges. Standard references can be found in, for example Fischer et al. (1979). For a round turbulent buoyant jet, numerous experimental investigations have been conducted in the past few decades and the results provided support for the integral modeling approach. Most existing integral models consider only the mean mass and momentum fluxes in the set of conservation equations. Hence, they can be referred to as first-order integral models.

Crapper and Baines (1977) suggested that the upper bound of applicability of the Boussinesq approximation is that the initial fractional density difference $\Delta\rho_0/\rho_a$ is 0.05. In general, one can say that the Boussinesq approximation is valid for small initial fractional density difference, $\Delta\rho_0/\rho_a \ll 1$. However, in these cases of invalid Boussinesq approximation a density equation must be used. Moreover, a discussion of this classification is given by Spiegel and Veronis (1960) and the non-Boussinesq plume was studied, for example by Woods (1997) and Carlotti and Hunt (2005).

Xiao (2009) Studied and developed a non-Boussinesq integral model for horizontal buoyant round jets with a modified entrainment hypothesis. The system of conservation equations of the integral model are solved to obtain numerical solutions in the transition region from jet-like to plume-like. The model was validated by the pure jet and horizontal buoyant jets with small/large density variations and good agreements with the experimental data were obtained. For strongly buoyant jet the Boussinesq approximation is violated which will over-predict the mass entrainment and under-estimate the buoyancy effect (Xiao et al., 2008). It reveals that the Boussinesq approximation is valid when the density variation is less than 10%. The entrainment assumption taking into account the Richardson number and the angle was used in the integral model, and satisfactory predictions for the modeling of horizontal buoyant jets were provided.

Other authors predicted the behaviour of the buoyant jet by using integral equations, formulated under the assumption of axial symmetry and self-similar transverse profiles (Fisher et al. 1979, Wood et al. 1993 and, Pantokratoras

1998). These models are very useful for engineering purposes such as environmental assessment, but do not help to clarify the transverse structure of the buoyant jet.

2.2.5.1 Local Rate of Entrainment

The entrainment rate of the turbulent buoyant jet is defined as: the ambient fluid that is mixed across the jet edge and becomes incorporated into the body of the jet. This process has the effect of increasing the total jet mass flux. The entrainment assumption is a key requirement for the integral model. The turbulent entrainment is usually parameterized by relating the inflow velocity (u_e) to the mean flow in the jet body; instead of using details that depend on transfers of mass and momentum at small scales which are very difficult to compute (Agrawal et. al. 2004 and Agrawaland Prasad 2004).

The agents of entrainment are turbulent eddies forming a mixing layer between the jet and its surroundings. The entrainment hypothesis was first introduced by Morton et. al., (1956). The first to incorporate the entrainment approach into a general jet model was Fan (1967) which used an Eulerian integral method, in which the flow passes through a fixed control volume, and integrated the equations of motion over that control volume. Others who have used this approach are Fan and Brooks (1969), Muellenhoff et al. (1985), Wood (1993), Chu and Lee (1996) and, Jirka (2004). Morton et al. (1956) used the boundary layer assumption to show that the average profiles are self-similar and that there was an average entrainment into the jet-like flow that was proportional the mean centre-line velocity. They introduced the continuity equation and proceeded, using an integral method, to the solution.

List (1989) showed that the entrainment mechanism is the same in both jets and plumes and is dominated by almost periodic large scale motions which engulf the ambient fluid. The unmixed fluid is transported well into the turbulent fluid and mixed by the action of small eddies. However, plume-like flows oscillate more than jets and measurements of intermittency, the percentage of time a probe is in the turbulent flow, show that during entrainment the penetration of tongues of ambient fluid from outside to the centerline is much greater in plumes than jets. This allows the flux of volume to increase more rapidly in the plume case and shows that standard deviation of any tracer is very much greater in the plume flow. It also leads to the average entrainment constant for the jet like flow being less than in a plume-like flow. Abraham (1963) noted that the

rate of expansion of a buoyant flow was independent of the type of flow (jet-like or plume-like) and with this alternative assumption proceeded to the solution. List and Imberger (1973) and Jirka and Harleman (1979) were able to relate the two assumptions and derive the entrainment constants for the jet and the plume. The solutions discussed above are for average velocities and concentrations inside the narrow buoyant jet region. Outside this region the flow is irrotational and its form depends upon the boundary conditions and whether the flow is dominated by the initial momentum or the buoyancy generated momentum (Taylor, 1958 and Kotsovinos, 1975).

The entrainment assumption was initially regarded as a constant ratio between the velocity with which the ambient fluid was entrained into the buoyant fluid and the mean velocity of the buoyant fluid. Initially, this was developed for discharges from round sources into stagnant ambient fluids, based on the work of Morten (1956). Their integral approach in an Eulerian framework is a benchmark paper in which the conservation equations for volume (mass), momentum and density solutions for a continuous discharge from a round source into a stagnant environment that may be stratified or unstratified. Closure of the system of governing equations was achieved by assuming that "the rate of entrainment at the plume surface is proportionality, the entrainment constant, and its value was obtained using the experimental results and found to be about 0.08. In summary, buoyant fluid models were initially developed using constant entrainment coefficient for discharges into stagnant ambient fluids. The next generation of buoyant fluid models included entrainment functions that depended on the Froude number.

Numerous experimental and numerical studies provided values of the entrainment rate (E) for example Houf and Schefer (2008), El-Amin et. al., (2010), and El-Amin and Kanayama (2009) when they studied the problem of low-density gas jet injected into high-density ambient and they assumed that the local rate of entrainment consisted of two components; one was the component of entrainment due to jet momentum while the other was the component of entrainment due to buoyancy. Also, they reported that the local rate of entrainment increases as the jet leaves the momentum-dominated region and enters a region where the effects of buoyancy become more pronounced. To incorporate this experimentally they observed an increase in the local rate of entrainment due to buoyancy, thus the volumetric entrainment rate correlation was given in the form:

$$E = E_{mom} + E_{buoy} \tag{2.9}$$

Therefore, the turbulent entrainment rate is considered to be composed of a component of entrainment due to momentum (E_{mom}) as calculated by Houf and Schefer (2008) and Ricou and Spalding (1961) and a component of entrainment due to buoyancy (E_{buoy}) as calculated by Hirst (1971):

$$E_{mom} = 0.282(\frac{\pi d_N^2}{4} \frac{\rho_0 u_0^2}{\rho_a})^{\frac{1}{2}} \rho_a \tag{2.10}$$

$$E_{buoy} = \frac{2\pi u_s b a_2}{Fr_s} \rho_a \tag{2.11}$$

where, Fr_s is the local Froude number, which presents the ratio of momentum to buoyant forces and is given by the following expression:

$$Fr_s = \frac{u_s}{\sqrt{gd_N(\rho_a - \rho_s)/\rho_a}} \tag{2.12}$$

Being d_N the nozzle diameter, u_s the local centerline jet velocity, b the jet radius. In the initial development of the jet, momentum dominates and the local Froude number (Fr_s) is high and hence the $1/Fr_s$ dependence of Equation (2.11) causes E_{buoy} to be negligibly small compared to E_{mom} in the total entrainment expression Equation (2.9). As the jet progresses, buoyancy forces become more important, the local Froude number decreases, and the E_{buoy} term begins to contribute, producing the increase in the local jet entrainment observed in the buoyant jet experiments. Determination of the constant a_2 of Equation (2.11) was developed by Houf and Schefer (2008) based on the experiments of the vertical hydrogen jet, and it was dependent on the Froude number Fr_0.

$$a_2 = 17.313 - 0.11665 Fr_0 + 2.0771 \times 10^{-4} Fr_0, Fr_0 \langle 268$$
$$a_2 = 0.97, Fr_0 \geq 268 \tag{2.13}$$

where, Fr_0 is the initial Froude number which is defined as:

$$Fr_0 = \frac{u_0}{\sqrt{gd_N(\rho_a - \rho_g)/\rho_a}}$$

(2.14)

Another equation used to calculate the entrainment rate (E) can also be expressed in terms of the local jet centerline velocity, u_s, and jet radius, b, in an expression of the form:

$$E = 2\Pi b \rho_a u_e = 2\Pi b \rho_a \alpha u_s$$

(2.15)

where α is the local mass entrainment coefficient where value increase as the jet progresses from the momentum dominated near-field to the more buoyantly dominated far field, being u_e is the local entrainment velocity.

Previous experiments have shown that the entrainment coefficients (α) for jets and plumes differ. The entrainment coefficient (α) varies from α_j to α_p during the transition from jet-like to plume-like. To model this variation, two types of formulation are commonly used in the existing integral models. This formulation allows predicting successfully the change of entrainment when there is either a jet or a plume. One was derived based on the conservation of energy given by Priestley and Ball (1955) as:

$$\alpha = \alpha_j - (\alpha_j - \alpha_p)\left(\frac{R_i}{R_p}\right)^2 \sin\theta$$

(2.16)

The other is an empirical function proposed by List (1982):

$$\alpha = \alpha_j \exp\left[\ln\left(\frac{\alpha_p}{\alpha_j}\right)\left(\frac{R_i}{R_p}\right)^2\right]\sin\theta$$

(2.17)

List (1982) summarized much of the work on the entrainment hypothesis and proposed values for the pure jets of $\alpha_j = 0.052 \pm 0.003$ and for the pure plumes as $\alpha_p = 0.0833 \pm 0.0042$.

In the above two equations, R_i is the local Richardson number, it represents the ratio of buoyancy to inertial force which is defined as:

$$R_i = \frac{Q_0 \beta^{1/2}}{m_0^{5/4}}$$

(2.18)

where, Q_0 is the volumetric flux, m_0 is the momentum flux, and β is the local buoyancy flux. The Richardson number in the pure plume region (R_p) is constant and is varies from 0 in jets to a constant value in plumes. Both (2.16) and (2.17) are essentially different types of interpolation between the entrainment coefficients for jets and plumes that satisfy the two asymptotic cases.

In Jirka's paper (2004), the local rate of entrainment coefficients for a horizontal buoyant jet depending on the Froude number is specified as:

$$\alpha = \alpha_j + \alpha_p \frac{Fr_p^2}{Fr_s^2} \sin\theta$$

(2.19)

The larger entrainment in plumes than in jets is usually interpreted as an effect of the buoyancy-induced turbulence. Other parameterizations have been proposed depending on the Froude number to characterize the jet flow when initially is jet like and finally it approximates a plume. List in Fischer et al. (1979) proposed two correlations for the entrainment coefficient, the first for the vertical buoyant jet given by:

$$\alpha = \alpha_j + (\alpha_p - \alpha_j)\left(\frac{Fr_p}{Fr_s}\right)^2$$

(2.20)

where, Fr_p is the final constant Froude number that is between 3.4 and 3.7. For the case when the jet is ejected horizontally:

$$\alpha = \alpha_j + (\alpha_p - \alpha_j)\left(\frac{Fr_p \sin\theta}{Fr_s}\right)^2 \tag{2.21}$$

In the present study we have used this last equation (2.21) to describe the local entrainment coefficient for the horizontal buoyant jet with $\alpha_j = 0.055$ for the pure jets and $\alpha_p = 0.085$ for the pure plume.

2.2.5.2 Dimensional Arguments

Consider a jet of lower fluid density, issued horizontally from a 'point' source, into a stagnant ambient of higher density. We assume that the jet starts abruptly discharging constant mass flux of lighter fluid. The flow travels firstly through a region where the initial momentum flux dominates until it reaches a maximum horizontal length (L_m) from the nozzle, and then the flow starts to rise vertically (buoyancy) more dramatically depending on the relative densities of the two fluids.

The terminal steady state horizontal penetration length L_m of the jet, depends upon the parameters that characterize the jet boundary conditions and are; the volume flow rate (Q_0), the kinematic momentum flow rate (M_0), and the kinematic buoyancy flux (B_0) (Fisher, 1979). Ignoring viscosity (the jet is assumed turbulent), a general functional relationship for the dependent variable L_m is given by:

$$L_m = f(Q_0, M_0, B_0) \tag{2.22}$$

where, Q_0, M_0, and B_0 are the initial flow rate, the kinematic momentum flow rate, and the kinematic buoyancy flux, respectively, computed as:

$$Q_0 = \int_{a_0} u\,ds = \frac{\Pi d_N^2}{4} u_0 \tag{2.23}$$

$$M_0 = \int_{a_0} u^2\,ds = Q_0 u_0 \tag{2.24}$$

$$B_0 = \int_{a_0} g \frac{\Delta\rho}{\rho_g} u ds = \frac{\rho_a - \rho_g}{\rho_g} g Q_0 = g_0' Q_0 \qquad (2.25)$$

The point at which the buoyant jet flow changed its behaviour from that resembling a jet flow into that resembling a plume is called the jet-plume transition point. Using the length-scale method, Davidson (1998) and Fischer (1979) have defined two characteristic lengths named, length scale (L_s) and geometric length scale (L_Q) based upon the initial kinematic buoyant jet characteristics defined as:

$$L_s = \frac{M_0^{3/4}}{B_0^{1/2}} = \left(\frac{\pi}{4}\right)^{\frac{1}{4}} d_N Fr_0 \qquad (2.26)$$

$$L_Q = \frac{Q_0}{\sqrt{M_0}} = \sqrt{A_0} \qquad (2.27)$$

where, L_s and L_Q are the characteristic length scales of kinematic momentum and volume flux respectively. The buoyancy effect becomes comparable to that due to the initial momentum at distance $x=L_S$ from the source. Eventually at large distances from the source $x \gg L_S$, the buoyant jet behaves like a plume. In fact it describes only the exit geometry, so if the distance from the orifice x is of order L_Q, the initial conditions are meaningful, and for $x \gg L_Q$ they do not influence the flow anymore and the jet is fully developed.

The discharge contains both initial momentum and buoyancy fluxes. Depending on the relative importance of the inertial and buoyancy force, the flow can be classified as jet-dominated or plume-dominated. The ratio between the two length scales L_Q/L_s represents the relative importance of buoyancy and momentum and is called the initial buoyant jet Richardson number R_i:

$$R_i = \frac{L_Q}{L_s} = \frac{Q_0 \sqrt{B_0}}{\sqrt[4]{M_0^5}} = \left(\frac{\Pi}{4}\right)^{1/4} \sqrt{\frac{g_0' d_N}{u_0^2}} \qquad (2.28)$$

That is the first non-dimensional group controlling the flow. If the Richardson number is much less than unity ($R_i \ll 1$), buoyancy is unimportant in the flow (forced convection). If it is much greater than unity ($R_i \gg 1$), buoyancy is

dominant (in the sense that there is insufficient kinetic energy to homogenize the fluids) (free convection). If the Richardson number is of order unity (R_i=1), then the flow is likely to be mixed (transition).

Froude number is the ratio of inertial to buoyancy forces. This dimensionless number can be viewed as a "measure" of how buoyant a jet is. The strength of the jet is directly related to the value of its Froude number, Fr_0. Then, as greater the value of the Froude number is, and then the flow is determined strongly by the jet's initial momentum. The jet turns rapidly into a plume when Fr_0 is small. Froude number is the first non-dimensional group controlling the flow. Some authors prefer to describe the flow in terms of Froude number,

$$Fr_0 = (\frac{\Pi}{4})^{\frac{1}{4}} \frac{1}{R_i} = \frac{u_0}{\sqrt{g(\Delta\rho/\rho_g)d_N}}$$

(2.29)

The Richardson number is inversely proportional to the initial jet Froude number Fr_0. The Froude number is preferred in this study, since for the case of a buoyant jet, a real case, gives an infinite Richardson number, a limit case, whereas zero density difference between jet and ambient fluid (a limit case) gives R_i= 0. On the contrary Fr_0= ∞ for a zero density difference and zero when the density difference is infinite.

Based on the above dimensional analyses and assuming self-similarity, both the jet and the plume behavior can be described. Under the same assumptions a buoyant jet released horizontally can be described in terms of simple jet behavior at distances much lower than L_s and in terms of plume behavior when the distance, x, is much greater than L_s.

2.3 Vertical Plunging Water Jets

2.3.1 Introduction

When a plunging liquid jet passing through a surrounding gas it entrains a large amount of gas bubbles into a receiving pool and forms a large submerged two-phase contacting area. Entrainment of non-condensable gases by a plunging liquid jets impacting a liquid pool of the same or different liquid are related to some important practical problems and is a particularly challenging case for multiphase models.

The entrainment will take place when the liquid jet velocity exceeds a critical value. The quantities of interest for plunging jets are the jet conditions at the plunging point with the liquid surface (jet diameter, d_1 and jet impact velocity, V_1), the minimum entrainment velocity, V_e, and the resulting volumetric flow rate of air being entrained once the threshold is exceeded, Q_a, as well as the bubble penetration depth in the water pool, H_p. The following sections review the experimental studies and correlations concerning on the vertical plunging liquid jets.

2.3.2 Jet Characteristics at the Plunging Point

Between the nozzle exit and the water surface, the jet characteristics such as diameter and velocity changed depending on this distance. A main problem in the plunging jet calculations is the calculation of the diameter (d_1) and the velocity (V_1) of the jet at the plunging point with the water surface.

2.3.2.1 Jet Diameter at Plunging Point

For laminar jets, gravity forces affect the diameter and velocity of the jet. Theoretical treatment of free liquid jets is complicated by factors such as contraction (or expansion) of the jet at the nozzle outlet and the velocity profile relaxation after the point of efflux. An energy balance, neglecting the effects of the surrounding gas and small contribution of the surface energy, would lead to the following equation given by Bin (1993):

$$\frac{d_1}{d_r} = \left(\frac{\Pi^2 g x_1 d_r^4}{8 Q_w^2} + 1 \right)^{-1/4} \tag{2.30}$$

where, d_r is the jet diameter at the reference point and Q_w is the water jet volumetric flow rate. The jet diameter d_r cannot simply be taken as the nozzle diameter. Lin (1963) found that when d_r was taken at $x_1 = 0.03$ m, the further variation of d_1 with the jet length, x_1, obeyed equation (2.30). The jet velocity profile relaxation does not extend far beyond $x_1/d_N = 3$.

For high velocity jets the jet is subjected to violent gas friction. This leads to surface tension forces controlling the surface character, so the jet surface becomes ill defined. Long-time exposure photographs showed that the jet spreads in a dispersed, generally conical form. Van de Sande and Smith (1973) suggested the following function:

$$\frac{d_1}{d_N} = C_3(We_a\, Re_{length})^m \tag{2.31}$$

This function is valid for $We_a \times Re_{length} > 7 \times 10^5$ and for jets produced from long cylindrical nozzles $l_N/d_N \geq 50$ and C_3 and m are constants 0.125 and 1/6 respectively. Re_{length} defines the development of the accompanying air boundary layer; $Re_{length} = V_N x_1/\nu_w$ and Weber number $We_a = V_N^2 d_1 \rho_a/\sigma$.

This equation is applicable to other authors' data (Ahmed, 1974 Cumming, 1975 and Evans, 1990), although with possibly different values of C_3 and m. This is likely these two factors are dependent on the nozzle design or the developed turbulence level in the jet (Bin, 1993).

2.3.2.2 Jet Velocity at Plunging Point

Assuming free fall of the water jet after leaving the nozzle, the jet impact velocity (V_1) at the liquid surface ($x=x_1$) can be simply calculated by using Bernoulli equation between the nozzle exit and the plunging point as follow:

$$V_1 = (V_N^2 + 2gx_1)^{1/2} \tag{2.32}$$

Although strictly speaking V_1 estimated in this way may differ from the real values because of a loss of energy due to the developed jet turbulence.

2.3.3 Inception (Minimum) Velocity of the Entrained Bubbles

At the impact of the plunging jet with the receiving pool, air bubbles start to be entrained when the jet impact and velocity (V_1) exceeds a critical value (V_e) called inception, onset, threshold, or characteristic velocity. The inception velocity for air entrainment is defined as the mean jet velocity at impact. Inception of air bubble entrainment is not a precise condition. For example, entrainment of bubbles of less than 0.2 mm diameter is very difficult to detect visually. Further, a jet may entrain one or a few bubbles only every few minutes and the selection of the investigation period is critical (Cummings and Chanson 1999). However, several studies showed that the inception velocity V_e is function of the plunging flow conditions and the fluid properties such as, turbulence characteristics and angle of the jet with the free-surface (e.g. Bin 1993, McKeogh and Ervine 1981, McKeogh 1978, Chanson 1996, and Cummings and Chanson 1999).

Qu et. al (2011) studied experimentally the air entrainment by vertical plunging water jets (d_N=6 mm and l_N=0.55 m) using a video camera. In addition, he observed that the air entrainment by plunging jets takes place when the jet impact velocity exceeds a critical value, which depends among other things on jet instability and its interaction with turbulence. Also, it observed that the inception velocity V_e increased with increasing the jet length x_1 for a given experiment.

Chanson et. al (2002) studied experimentally the vertical plunging water jets by using different nozzle diameters. The inception velocity was defined for d_N= 25mm as the flow conditions for which one bubble was entrained during a 1 minute period, and for smaller jets d_N= 6.83 and 12.5 mm when less than three bubbles were entrained during a 3 minutes period, in the absence of bubbles in the plunge pool. Longer investigation period was selected for the smaller jets because of occasional entrapment of fine bubbles. Also he showed in general that the onset velocity was observed to reduce when increasing the turbulent intensity, approaching the value of V_e=0.8 m/s for large turbulence levels. In addition, it was observed consistently that the inception velocity V_e increased with increasing jet length x_1 for a given experiment.

Bin (1993) concluded that a simple correlation of all the available experimental data between the minimum entrainment velocity V_e and the ratio x_1/d_N, is not possible. Figure (2.7) illustrates the experimental results obtained by many researches.

It can be concluded from this figure that a large scatter of the experimental data points is evident for jets produced from long cylindrical nozzles. The length of the cylindrical section of the issuing nozzle is responsible for the level of turbulence produced in the jet. The values of V_e, obtained at different turbulence intensities, are indicated for comparison.
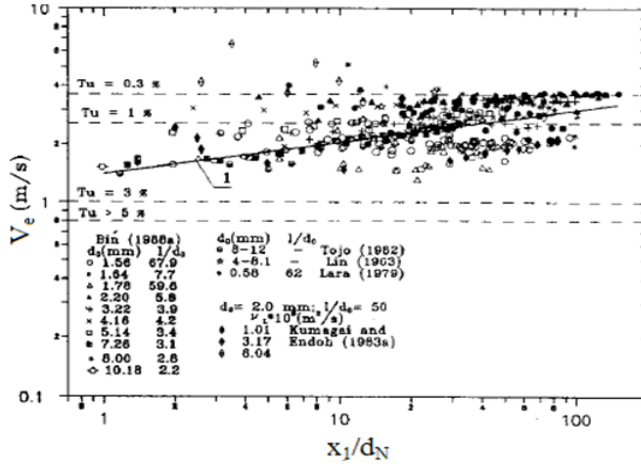
Figure (2.8): Dependence of the minimum entrainment velocity V_e, on the ratio x_1/d_N for the continuous jet region, (Bin, 1993)

For large nozzle jet diameters ≥ 7 mm an empirical correlation can be recommended given by:

$$V_e = 1.4 \left(\frac{x_1}{d_N} \right)^{0.164}$$

(2.33)

This equation is also applicable for short cylindrical nozzles ($l_N/d_N \leq 3$) and within $x_1/d_N = 1-100$.

Bin (1988) suggested a rough estimation of V_e in m/s obtained by using the following relationship:

$$V_e = 5 x_1^{0.534}$$

(2.34)

This equation is valid for x_1 ranging from 0.015 to 0.4 m and jets produced from nozzles with diameters ranging from 2 to 10.2 mm. The general accuracy of this equation is within $\pm 22\%$.

Sene (1988) and Chanson and Brattberg (1996) demonstrated that the onset velocity of the air entrainment for turbulent plunging water jet is close to 1 m/s. Other researchers (Ervine, 1980) have reported values for the onset velocity in the range of 0.8-3.0 m/s.

2.3.4 Mechanism of Gas Entrainment

Before 1970, there were only a few serious attempts to study the phenomenon of the gas entrainment by plunging liquid jets. Since then, the interest and the scope of the experimental data on plunging liquid jet systems have increased considerably. From studies and observations of many authors at different flow conditions, it is evident that the mechanisms of gas entrainment by plunging liquid jets are very complex process largely controlled by the jet velocity at impact. Also, depends on the physical properties of the fluid (mainly viscosity and surface tension), σ, the design of the jet nozzle (e.g. the nozzle diameter, d_N and nozzle length, l_N), the jet angle (α), the length of the free-falling jet, x_1, and the jet turbulence, T_u, (Bin 1993, Chanson et al. 2004, Cummings and Chanson 1997, Kusabiraki et al., 1990, Ohkawa et al. 1986).

In order for the gas entrainment to take place, the jet impact velocity has to exceed the inception velocity that is a function of the plunging flow. The near-flow field (next to and downstream of the impingement point) is characterized by a developing shear layer with some momentum transfer between the high-velocity jet core and the receiving water pool. When the gas entrainment occurs, a gas bubble diffusion layer takes place. The gas diffusion layer may not coincide with the momentum shear layer, and the interactions between the momentum shear layer and the air diffusion layer contribute to the complexity of the gas-liquid flow (Cummings and Chanson 1997 a,b). Further downstream the jet flow becomes fully developed.
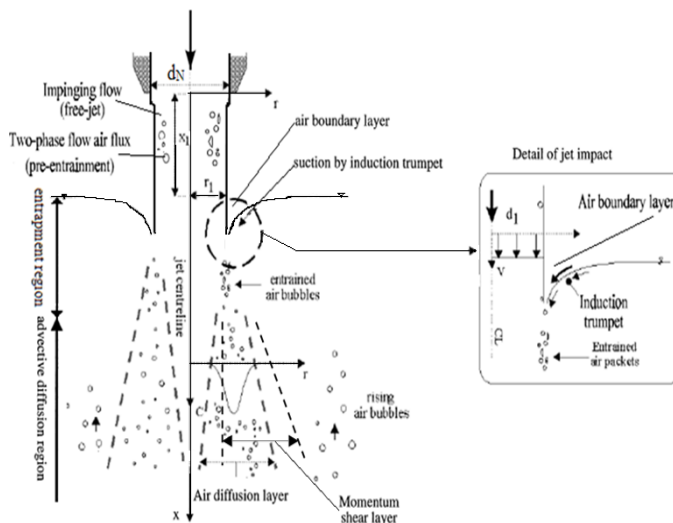
Figure (2.9): Definition sketch for air entrainment at a vertical circular plunging jet

For small jet velocities (at the nozzle outlet) that are larger than the inception velocity, air is entrained in the form of individual air bubbles, while large packets of air are entrained and broken up subsequently in the shear flow at higher jet velocities (Bin, 1993; Chanson et al., 2004). When the distance from the nozzle outlet to the water surface (x_1) is short, the surface of the water jet is not disturbed by the shear forces induced by the surrounding air, and, thus, many small bubbles are generated and dispersed in the whole water body. If x_1 is long, the surface of the water jet becomes highly disturbed, and relatively large bubbles are generated and dispersed in a localized region in the water beneath the pipe exit. These two patterns occur simultaneously for an intermediate distance. Furthermore, the nozzle length to diameter (l_N/d_N) ratio is an important factor in nozzle design (Bin, 1993; Burgess and Molloy, 1973; Ohkawa et al., 1986; Vandesande and Smith, 1976). For practical reasons, Ohkawa et al. (1986) recommended the use of a relatively small l_N/d_N ratio (much smaller than 50).

As has been outlined above, different mechanisms of gas entrainment by plunging liquid jets complicate quantitative the prediction of the performance of the plunging jet system, at least in terms of the effects of the primary variables (jet diameter, jet velocity and length, as well as physical properties of the fluids involved). Many secondary factors (nozzle design, angle of jet inclination, pressure of vibrations, etc.) can also exert profound influence on jet behavior.

2.3.5 Penetration Depth of the Entrained Bubbles

As a result of the air entrainment by plunging water jets, bubbles are penetrate and dispersed below the water pool surface. McKeoch and Ervine (1981) showed that the dispersed bubbles form two distinctly different regions:

(i) A biphasic conical region comprising fine bubbles with diameters less than 1 mm, this bubbles penetrates the water pool to some maximum depth due to the momentum of the submerged water jet. At the maximum depth of penetration, buoyancy forces counteract this momentum and the bubbles may grow by coalescence and escape sideways until they are free to rise to the water surface.

(ii) A region of bigger rising bubbles (secondary bubbles), which surrounds the former one. There is general agreement that for the air-water system, bubbles formed during entrainment by vertical or inclined jets in the rising bubbles

region (secondary bubbles) have (Sauter) diameters of about 3-4 mm, practically independent of the experimental conditions. In the biphasic cone, bubbles are much smaller than the bubbles in the rising bubble region (<1.4 mm). Bubble size were most frequently estimated from photographs by many researchers, and obviously only secondary bubbles could be measured in this way (Bín, 1993).

However, the structure of the biphasic cone and the surrounding bubble column is complex. In the cone, high turbulence intensities and shear stresses, created by the bubbles, break the captured gas into fine bubbles. Bubbles escape from the cone at its boundaries and at the bottom as the buoyancy forces overcome the jet momentum and the liquid local velocity decreases. Coalescence also takes place in these sections of the cone. The air bubbles entrained into the liquid give a buoyancy effect to the diffusion of jet and contribute to a velocity decrease in the diffusion region. These effects may result in giving a limit to the bubble penetration depth Hp.

The maximum penetration depth of the bubbles entrained to the water pool is not strictly defined since the lower limit of the bubble swarm fluctuates continuously, but a time average can be estimated. However, the maximum bubble penetration length (H_p) can be defined as the distance from the water surface of the water tank to a point at which the gas arrives with zero vertical velocity component as illustrated in Figure (2.9).
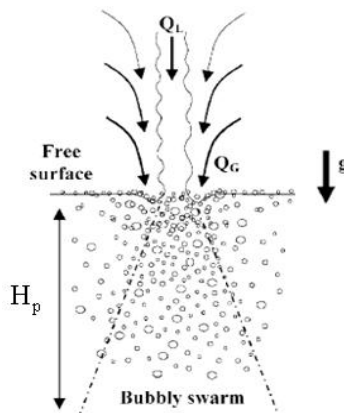
Figure (2.10): Plunging jet penetration length, Bín (1993)

Several authors studied and measured the maximum depth of bubble penetration in the vertical plunging jet systems. Ciborowski and Bín (1972b) and Smigelschi and Suciu (1976) suggested a simple theoretical consideration

based on the assumption that at the maximum depth of bubble penetration, the local liquid velocity in the submerged jet at that point is assumed to be equal to the bubble free rise velocity. This led to a direct linear relationship between the maximum penetration depth and the product of the jet diameter and jet velocity. However, buoyancy forces resulting from the entrained gas complicate such an analysis. A further attempt was made by Cumming (1975), who theoretically predicted that the maximum depth of bubble penetration should be related to the square of the jet velocity and the entrainment ratio.

Suciu and Smigelschi (1976) studied the air entrainment by vertical water jets and they suggested an experimental correlation between H_p and variable as $V_N d_N$, given by a linear relationship as the follow:

$$H_p = 10(V_N d_N)$$
(2.35)

Variable $V_N d_N$ is a typical term representing the momentum of the jet flow in the submerged biphasic diffusion region of vertical plunging water jet systems. Also, this variable have been used latter by many researchers and has been used successfully for the prediction of H_p in other vertical plunging water jet systems.

McKeoch and Ervine (1981) for example, suggested a similar empirical correlation given by:

$$H_p = 2.6(V_N d_N)^{0.7}$$
(2.36)

This correlation was obtained for a jet velocity between 0 and 10 m/s and nozzle diameters between 6 and 25 mm and jet height between 0 and 6 m. Other Authors (e. g. Bin 1983, Bonsignore et. al. 1985, McKeogh and Ervine 1981, and Van de Sande and Smith 1974) suggested purely empirical relationship for the maximum penetration depth for both small and large diameter jets and the simplest one of these is:

$$H_p = C_1 V_N^n d_N^p$$
(2.37)

when, $V_N d_N \geq 0.01$ m^2/s, n= p = 0.66 and C_1 = 2.4, whereas for $V_N d_N < 0.01$ m^2/s, n = p = 1.36 and C_1 = 2.4.

Van de Sande and Smith (1975) suggested another empirical relationship containing the volumetric entrainment rate (Q_a) given by:

$$H_p = 0.42 V_1^{4/3} d_1 Q_a^{-1/4}$$

(2.38)

This correlation was obtained from experimental data with nozzle diameter ranging from 3.9 to 12 mm and $x_1 < 0.5$ m.

Ohkawa et al. (1986) studied experimentally the vertical water jets using PVC short nozzles ($l_N/d_N = 5$) of diameters ranged between 7 and 13 mm, jet velocity between 2 and 14.3 m/s and nozzle height $x_1 = 0.025\text{-}0.75$m. He revealed that the depth of bubble penetration ratio (H_p/d_N) is dependent on the nozzle geometry (l_N/d_N) and the nozzle height ratio (x_1/d_N). Both these affects disappear for $l_N/d_N > 15$ and for $x_1/d_N > 20$. And he suggested empirical equations which may be used to predict the dimensionless bubble penetration depth over the range of conditions tested as the following;

Below x_1/d_N, H_p/d_N can be correlated as;

$$H_p / d_N = 10^{f(Fr_0)} (x_1 / d_N)^{-0.2}$$

(2.39)

where, $f(Fr_0) = 1.76 - 0.8 \log Fr_0 + 0.64(\log Fr_0)^2$ on the other hand above $x_1/d_N = 20$ values, H_p/d_N could be correlated by the following equation;

$$H_p / d_N = 10^{1.62 - 0.82 \log Fr_0 + 0.59(\log Fr_0)^2}$$

(2.40)

Mahad et al. (2012) studied two inclined plunging water jets and he suggested an empirical correlation for H_p for an inclined water jet:

$$H_p = C_1 (V_N d_N)^{c_2} (x_1 / d_N)^{c_3} (\sin \alpha)^{c_4}$$

(2.41)

where c_1, c_2, c_3, and c_4 are empirical constants that can be determined experimentally. The values of c_1, c_2, c_3, and c_4 were found to be 10.5, 0.54, -0.56, and 1.39, respectively, for two inclined plunging jets and 5.5, 0.73, -0.26, and 1.11 respectively for one inclined plunging jet by given Ohkawa et al. (1986).

Ohkawa et al., (1987) studied the vertical water jets and suggested for the dimensionless bubble penetration depth, H_p/d_N, the following expression:

$$H_p / d_N = \text{func.}(x_1 / d_N, l_N / d_N, Fr_0) \tag{2.42}$$

2.3.6 Volumetric Flow Rate of the Entrained Gas

2.3.6.1 Methods of Entrained Gas Measurements

Two main groups of measurement techniques for the entrained gas flow rate were developed in the literature, based respectively on:

i) Catching the entrained gas after it has been entrained into the liquid pool: This group mainly use a bubble traps. A bubble trap is a device what collects the amount of gas that withdrawn from the water tank, after been entrained by the jet and this bubble trap is connected to an appropriate flow rate device (mass flow meter, orifice, rotameter, anemometer or from volumetric and time readings) to measure the amount of the gas being collected (see Figure, 2.11). This technique has been developed mostly in the experiments on inclined jets (Lin and Donnelly, 1966; Van de Sande and Smith, 1973, 1976; Ervine et al., 1980; McKeogh and Ervine, 1981, and Kusabiraki et al., 1990) and in the experiments for which bubble traps are specifically developed (Henderson et al., 1970 and Cumming, 1975). The technique developed in the present study belongs to this group.
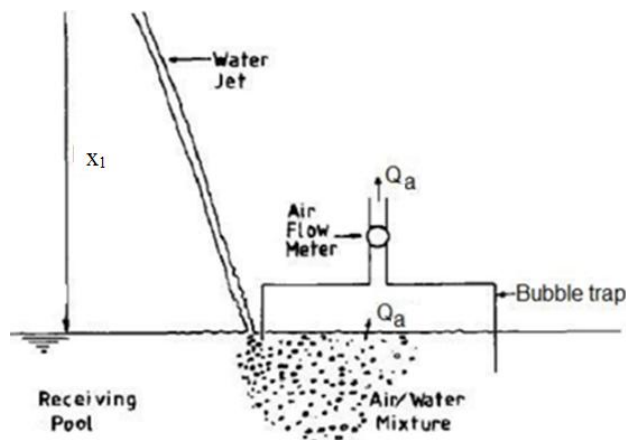
Figure (2.11): Schematic representation of a bubble trap apparatus (MacKeogh and Ervine, 1981)

ii) Measuring the removal of the gas from a gaseous space above the pool surface around the plunge point. This second group is the gas removal arrangements (see Figure, 2.12). The gas space above the pool in the vicinity of the plunging point is in this case separated from the ambient, and a supplementary known gas flow rate is introduced into this space through an appropriate flow rate device (rotameter, anemometer or from volumetric and time readings, etc).
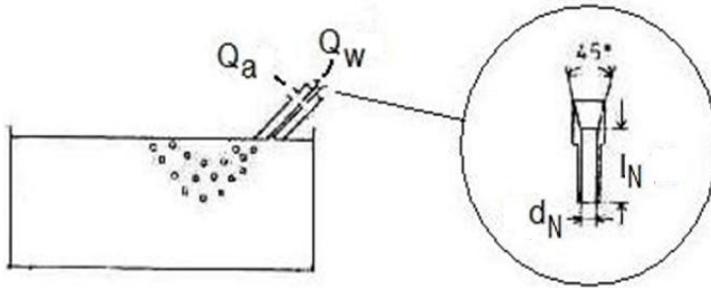
Figure (2.12): Gas removal measuring apparatus (Kusabiraki et al. 1990)

This second technique is involved in the devices used by Ciborowski and Bin (1972b), Ahmed (1974), Ohkawa et al. (1987), Evans (1990) and Kusabiraki et al. (1990a). However, each of the above-mentioned techniques has its own shortcomings. The first group for example, when it used to carry out experiments with different angles of jet inclination, an extrapolation of the data to vertical position is required. Such an extrapolation may result in a non-negligible deviation (Van de Sande and Smith 1976). The second technique based on air removal arrangements may interfere with the free-surface flows. However, since the air-entrainment phenomenon depends mainly on the flow in the direct neighborhood of the plunging point, an appropriate submergence and geometry of the trap should not greatly affect the amount of entrained air.

2.3.6.2 Entrainment Rate (Q_a)

In an attempt to clarify the effect of different parameters such as: nozzle geometry, jet length, and physical properties of the liquid phase on the entrainment rate, many studies are available in the open literature (e. g. Mahad 2012, Martim 2009, Tamer and Nusret 2003, Ohkawa et al. 1987, Iguchi, 1998, and Kusabiraki et al. 1990). Theses authors established three regions of the entrainment rate curve as shown in Figure (2.13), thus, a typical S-shaped

entrainment rate curve is observed for the whole region of the jet velocities, that it was divided into three regions as follows:

(i) Initial and/or low jet velocity region,
(ii) Transition region,
(iii) High jet velocity region.
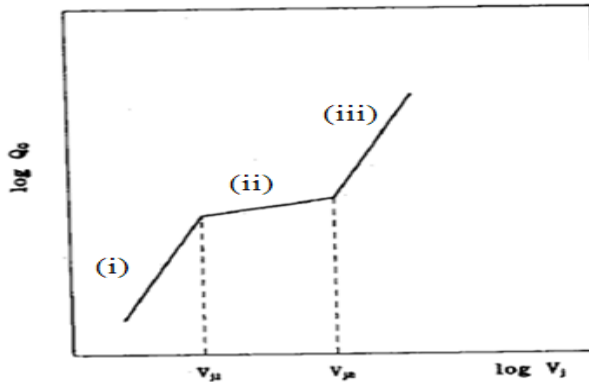
Figure (2.13): Typical mechanism-velocity curve (Bín, 1993)

The shape of entrainment rate curve vs the jet velocity showing a sharp increase with the jet velocity for the low velocity region, then decreasing slightly into a shallow minimum and again increasing with a further increase in V_1.

(i) Low Jet Velocity Region

Van de Sande and Smith (1974 and 1976) concluded that the low jet velocity region extends up to about 5 m/s, also concluded that the rate of gas entrainment by plunging jets is directly related to the kinetic energy (power) of the jet. For shorter jets, they suggested an air entrainment rate expression given by:

$$Q_a = 0.0015 X^{0.75} \tag{2.43}$$

where, $X = d_N^2 V_1^3 x_1^{0.5} (\sin \alpha_1)^{-1.5}$. This equation is valid for $X = 10^{-4} - 10^{-2}$. Their experiments were carried out with jets produced from nozzles with $d_N = 2.85 - 10$ mm, jet velocity within $V_1 = 2-5$ m/s, jet length, $x_1 < 0.5$ m and jet angle $\alpha_1 = 20-60°$. In addition, he concluded that the jets produced from nozzles with shorter cylindrical sections would entrain less air at the same X.

(ii) High Jet Velocity Region

The high jet velocity region was fixed by Van de Sande and Smith (1973) at the value of $We_a > 10$. The data of Kusabiraki et al (1990), showed that the transition to this region is dependent on the experimental conditions such as $(d_N, x_1, L_N/d_N, \alpha_1, v_w)$.

High velocity jets not only carry air captured within the mean containing envelope, but also entrain air in the boundary layer that develops outside that envelope into the pool. Thus, the total amount of entrained air is made up of two parts (Bin, 1993):

$$Q_a = Q_{a1} + Q_{a2} \tag{2.44}$$

The portion of air captured by the jet roughness is given by:

$$Q_{a1} = \frac{\pi V_N}{4} (d_1^2 - d_N^2) \tag{2.45}$$

Whereas, the boundary layer can be expressed by:

$$Q_{a2} = \int_{d_1/2}^{\infty} V_L \, 2\Pi r dr \tag{2.46}$$

where, V_L is the local velocity of the air boundary layer at a given radius measured from the jet axis.

(iii) Transitional Jet Region

The transition from low velocity region to high velocity region is continuous. Van de Sande and Smith (1974) suggested a simple procedure to predict the entrainment rate for this region, based on interpolation between the amount of entrained air at $V_1 = 5 m/s$ calculated from Equation (2.44) and that calculated from the jet velocity corresponding to $We_a = 10$ from equation (2.45) and (2.46). This procedure has been checked against the experimental data of other authors and the error involved is within $\pm 20\%$ (Bin, 1993).

2.3.6.3 Entrainment Ratio Q_a/Q_w

The entrainment ratio is defined as the ratio of the volumetric flow rates of the air entrained (Q_a) and the water jet (Q_w) and is a measure of the performance of the plunging jets. Burgess (1973) defined the ratio of air flow to water flow by an empirical correlation for high velocity water jets as:

$$\frac{Q_a}{Q_w} = \left[\frac{d_1}{d_N}\right] - 1$$

(2.47)

where, d_1 and d_N are the jet diameter at the plunge point and nozzle diameter respectively. This equation implies that only the air within the diameter that contains the surface roughness is brought below the water surface.

Bin (1993) proposed an empirical expression for all regions of entrainment vertical jets as:

$$\frac{Q_a}{Q_w} = 0.04 Fr_1^{0.28} (x_1/d_N)^{0.4}$$

(2.48)

This equation seems to give satisfactory agreement with experiments of other authors provided that $x_1/d_N \leq 100$, $(l_N/d_N \geq 10)$ and $Fr_1^{0.28}(x_1/d_N)^{0.4} \geq 10$, where $Fr_1 = V_1^2/gd_1$. Similar values of the power exponent on the x_1/d_N ratio, namely between 0.45 and 0.48 observed for the experimental data of Evans (1990). Ervine et al (1980) concluded that the numerical values of the constant in Equation (2.55) may be dependent on the turbulence level in the jet stream, when he studied jets with turbulence level greater than 4% and the data were approximated by Equation (2.55) with a higher value of the constant about, 0.069, and by the data of Ahmed (1974), for which the constant in this equation is 0.060±0.019. However, maximum deviation from this equation are between +28% and -50%.

Van de Donk (1981) actually neglected the small effect of the jet velocity on the entrainment ratio and approximated his data for vertical jets by a simpler correlation;

$$\frac{Q_a}{Q_w} = 0.09 (x_1/d_N)^{0.65}$$

(2.49)

With a standard deviation of about 8% for the range of the system parameters: V_N= 2-10m/s, x_1/d_N= 2.5-100, and d_N= 0.01-0.1m. In addition, he studied the effect of nozzle design on the entrainment ratio for different types of nozzle diameter.

Ohkawa et al. (1986) studied experimentally the vertical water jets produced from short nozzles with l_N/d_N= 5. He showed that smaller values of the air entrainment ratio Q_a/Q_W for shorter nozzles could be obtained as a comparison to the larger nozzles at the same values of the main parameters (V_1, x_1, d_N).

Kusabiraki et al., (1990) studied experimentally the vertical liquid jets using different nozzles diameter ranged between 7 and 17.8 mm, l_N/d_N= 5 to 70 with a contraction angle of 45°, nozzle height x_1= 0.025 - 0.75m and jet velocity between 2 and 13.5 m/s using various liquids. He revealed that the air entrainment ratio (Q_a/Q_w) is depending on the jet velocity, nozzle geometry (l_N/d_N), nozzle height ratio (x_1/d_N) and jet properties (Ohnesorge number O_h= $\mu/\rho\sigma d_N$). An empirical correlation was suggested to predict the entrainment ratio over the range of conditions tested as the following on:

$$Q_a / Q_w = a.Fr_0^{b(x_1/d_N)}(x_1 / d_N)^c (l_N / d_N)^d O_h^e \qquad (2.50)$$

where, a, b, c, d and e are empirical constants which depend on the ranges of l_N/d_N, V_N and liquid properties.

2.3.7 Water Jet Velocities

Many parameters affect the jet velocity decay in the jet diffusion region as it disperses into the plunge water pool, it can be seen in the following general expression:

$$V_x(x,r) = f(V_1, d_1, x_1, x, r, \rho_a, \rho_w, g) \qquad (2.51)$$

Some investigators studied the jet velocity distribution, for example McKeogh and Ervine (1981) studied experimentally smooth plunging water jets and they measured the velocity profiles in the submerged jet region (within the biphasic cone) for the conditions of d_N=0.009 m and V_1=2.5-3.9 m/s. The centerline velocity decay V_c was measured with a Pitot tube at values of x/d_1 ranging from about 3:20 in the presence of turbulence production in the wake of bubbles for

$x/d_1 > 3$. The expression suggested for the centerline velocity decay showed that V_c/V_1 decreased linearly with the increase of x/d_1 given by:

$$V_c / V_1 = 3.3(d_1 / x)^{1.1}$$
(2.52)

where, V_c is the jet centerline velocity at a distance x from the water surface. Also they concluded that the rate of velocity decay in the biphasic plume resulting by a vertical plunging jet is greater than in the single phase flow (without air entrainment at $x_1=0$ cm). Also, he studied the axial velocity profile distribution and suggested the following practical relation as:

$$V_x / V_c = \exp(-r^2 / 2\sigma^2)$$
(2.53)

where, V_x is the axial velocity at radius r, σ is the standard deviation and r is the radial distance from the jet centerline. V_x/V_c showed a Gaussian normal probability distribution when plotted against r/r_c for various values of (x/d_N), where r_c is the radius at which the axial velocity equals $V_x/2$. The velocity of the water jet decays laterally from the nozzle centerline to reach zero away from the jet centerline. However, the Gaussian velocity profile shape observed by many others researchers as McKeogh and Ervine (1981), Bonetto and Lahey (1993), Hammad (2010), and Ma et al. (2010). Also, it's found that the bubbles of approximately 2 mm diameter will rise within a column of water at a velocity of 0.26 m/s. It seems reasonable to suggest that if the water is moved downward at this velocity a bubble will remain stationary relative to any arbitrary datum. The value of 0.26 m/s can be taken as the critical downward water velocity below which bubbles will rise to the surface.

Kusabiraki (1990) studied the vertical liquid plunging jets using various liquids. The velocity profiles measured in the submerged jet region, for conditions of $d_N=0.007$ m, $V_N=3.9$ m/s, and liquid jet length $x_1=30$ cm. It's found that the rate of decrease of V_c/V_1 was not constant throughout the whole range of x/d_1, as shown in Figure (2.14). Thus, the rate of decrease as x/d_1 above about 15 tended to larger that below 15.

Also, he found from the comparison between the cases with and without gas entrainment (i.e., two phase flow and single phase flow) that the decrease of the center-line velocity in the single phase flow is smaller than that in the two-phase flow since there is less turbulence generated in the diffusion process.

McKeogh and Ervine (1981) and Ohakawa et al. (1990) observed a similar phenomenon.
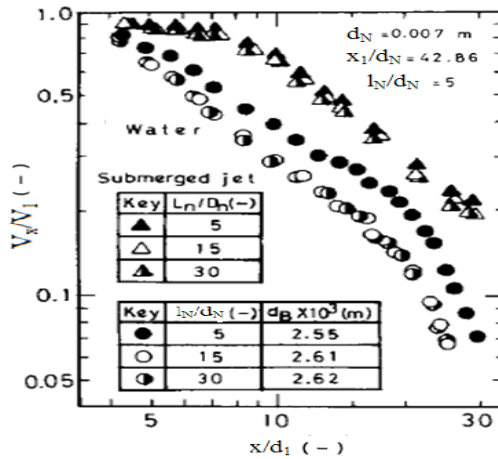
Figure (2.14): Centerline velocity decrease with the distance, Ohkawa (1990)

Ishigaki (1982) and Iguchi et al. (1989) suggested that the measured centerline velocity V_c values for a water jet velocity ranged between 3.5-13 m/s and can be approximated by the following empirical equation for single-phase free jets ($x_1=0$ cm):

$$\frac{V_c}{V_N} = 6.2 \frac{d_N}{x}$$

(2.54)

This equation is known to be valid for $x/d_N \geq 10$. Single-phase free jet means a jet issuing from a nozzle into an infinite space occupied by the same fluid as the jet in the absence of air entrainment.

Iguchi et al. (1998) studied vertical plunging jets injected from straight circular tube onto a water bath contained in a cylindrical vessel using the LDV technique to measure the velocity in the bubble dispersion region. The jet conditions were $d_N=5$ mm, $l_N=120$ cm, with two different jet flow rate, 50 cm^3/s and 66.7 cm^3/s. He found that the values of the measured axial mean velocity (V_x) obtained at $x_1=0.2$ cm for both water jet flow rates can be approximated satisfactorily by the empirical equation of Ishigaki (1982) and Iguchi et al. (1989) for single phase free jets (equation 2.54) when plotted against the axial distance x.

Chapter 3

Experimental Apparatus and Instrumentation of the Submerged Gas Jets

3.1 Introduction

This chapter aims at describing in detail the experimental construction and instrumentation techniques that were used during the experiments of the submerged gas jets. The set-up is made to investigate the submerged gas jet injected horizontally in water pool. The experimental techniques employed to obtain appropriate measurements required to predict the jet behavior such as, penetration length, spreading angle, curvature, etc., as well as the jet pinch-off and the jet interface unsteadiness or the system analysis are presented.

This chapter is divided into three parts; the first part describes the construction and dimensions of the experimental set-up and its main components. The second section shows the instrumentation that allows for flow measurement, pressure and temperature and far above the main phase flow parameters. The third part is devoted to describing the control software that enables all systems of the installation to operate both in obtaining measurements as well as in analysis.

3.2 Experimental Facility Description and Dimensioning

The experimental set-up of the buoyant gas jets in water ambient consists in five parts that are a water tank, air injectors (straight tubes) supported horizontally in the water tank side, air compressor, and an illumination system for flow visualization technique. Figure (3.1) illustrates a general layout of the experimental set-up arrangement for gas jet injected horizontally in stagnant water, and Figures (3.2) show photographs of the experimental arrangement. In all cases dried filtered air was used as the working fluid and treated tap water was used as the stagnant ambient fluid.

Proper instrumentation was located at the different sections of the system. The experiments were conducted in the Thermal-Hydraulic and Nuclear Engineering Research Laboratory of the Institute for Energy Engineering at Polytechnic University of Valencia.

3.2.1 Water Tank

The air jet was injected horizontally from the jets to the water ambient contained within a rectangular transparent tank. The water tank used in this experiment is made of an open rectangular stainless steel sheets (11 mm thick) with transparent (Perspex) sides has a dimensions (length x width x deep) 1000mm x 400mm x 750mm.

Air filtering, adjusting and controlling unit

A- Air compressor
B- Air filter
C- Gas tank
D- Pressure regulator valve
E- Air flow meter
F- Air injector (Tube)
G- Water tank
H- Illumination system
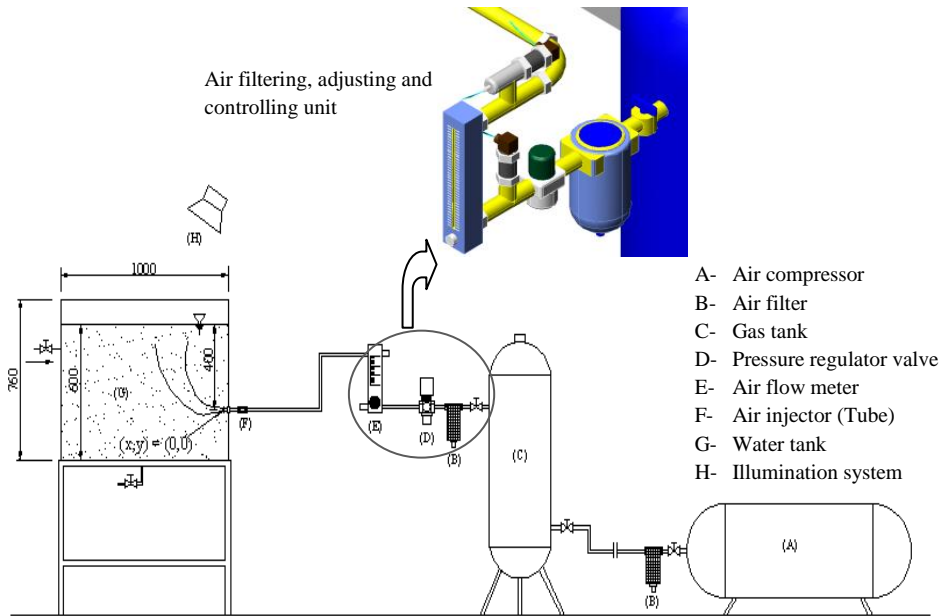
Figure (3.1): Schematic diagram of the experimental set-up for submerged gas jets in stagnant water

Figure (3.2): Photographs showing the experimental set-up

The sidewalls of the tank were made of transparent sheets to allow for flow visualization and optical measurements also, pictures of the jet can be taken at any angle through the tank walls. The lighting can also be set at different angles. The upper side of the tank was open to the ambient environment, where the air then is released to the atmosphere. The right side of the water tank was prepared with three holes at a different distance 200, 400 and 600 mm far from the tank bottom to give a flexibility of varying vertically the positions of the air injector (in the future work) and a hole in the bottom side for the water drain. A schematic diagram and dimensions of the water tank can be seen in Figure (3.3).
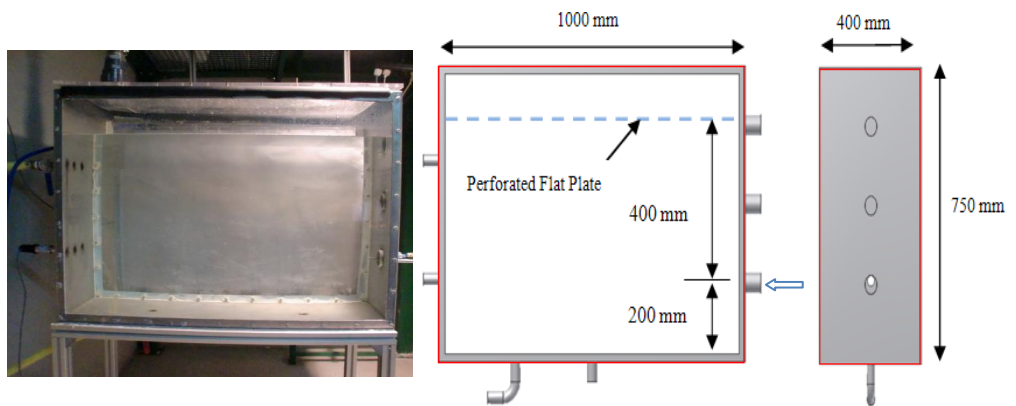
Figure (3.3): View with dimensions of the test section. Perforated sheets helped to control the surface disturbances were used.

The free water surface was covered with a perforated flat plate to limit surface waves (sloshing) and provide a constant hydrodynamic pressure (minimize the pressure oscillation phenomenon).

The tank was filled with treated tap water to a constant depth of 600 mm at room temperature (27.6 ^{o}C). The water used in the experiments was obtained after a decalcification process that reduced the hardness and avoids deposition on the test section and measurement instruments.

Before the decalcification process, the water has a hardness of approximately 350 ppm, the hardness decreases to about 150 ppm after this processing. The decalcification equipment is brand INSA, model series 255 Logix 760 with a capacity of 35 L.

3.2.2 Air Injectors (Straight Tubes)

The air injector is a mechanical device designed to control the direction or characteristics of a fluid flow as it exits (or enters) an enclosed chamber or pipe via an orifice. A set of four interchangeable straight tubes (calibrated tubes) made from stainless-steel of inner diameters 2, 3, 4 and 5 mm with all the tubes sharing a common length (l_N=18 cm) and the same material thickness. The value of the pressure drop over the injector length is calculated and found to be small.
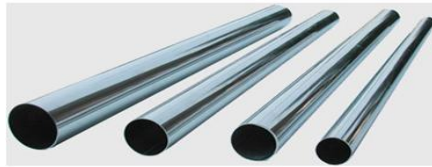
Figure (3.4): Stainless steel straight tubes tested 2, 3, 4 and 5 mm internal diameter

The tubes were fixed horizontally at the submergence depth of 400 mm and 200 mm above the water tank bottom. The 200 mm distance above the tank bottom designed to permit freely the entrainment of ambient water, ensuring that the tank boundaries had minimal effects on the flow. The environmental pressure at the nozzle exit was calculated.

(A) Air injector, (B) pressure transducer, (C) Non-return valve
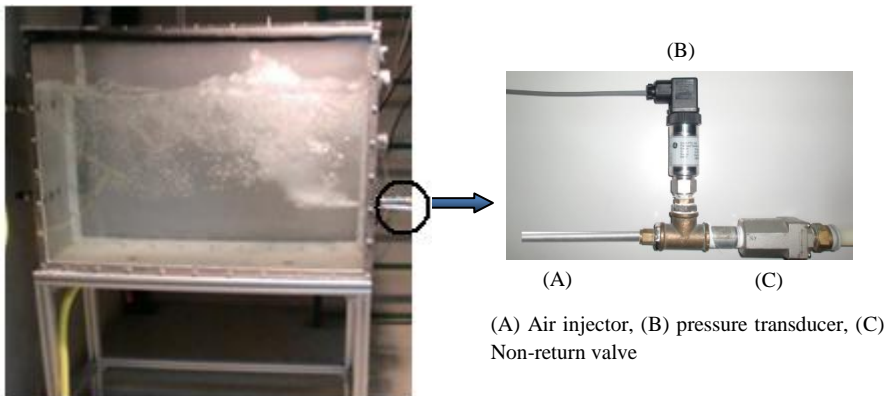
Figure (3.5): Air injector location in the water tank

A non-return (check) valve that does not allow to the water to enter in the air pipe was located before the air injector to prevent the ingress of water to the air tube as shown in the last figure (3.5).

3.2.3 Air Compressor

The compressor used in the present study, is ABAC reciprocating air compressor model ZENITH15, with 1.42 m^3/m free air delivery and 1 MPa working pressure. It consists of an air vessel of 500L capacity for equalizing the pressure variation from the start/stop and modulating sequence of the compressor and storage of air volume equalizing the variation in consumption and demand from the system. Air leaving the compressor passes through a stainless steel tube of 20 mm diameter to another vertical air reservoir 0.1 m^3 volumes (100 L) located near to the water tank this helps to eliminate pulsations in the discharge line and also act as storage capacity during intervals work, and it was located close the air supply point to the system.

3.2.4 Illumination System for Flow Visualization Technique

Observations of the gas jet parameters such as the length of penetration and the interface between the jet and water ambient were performed with direct visualization technique using a high speed camera (CCD) and system of illumination. The flow was backlit with a continuous source of light contained in a separate aluminum frame. During the experiments, several light sources were tested. The chosen light source was the one that give and provided the most constant and uniform light intensity and was independent of time. The combination of the camera with the halogen lamplights at 50 Hz had the least variation and was the most uniform. The illumination system was a white-light bank consisting of six 500 W halogen lamps, evenly distributed over the test section. Backlighting was used during the experiments in order to ensure a proper exposure at the required filming rate. Figure (3.6) shows a schematic diagram dimensioned and a picture of the used illumination system.
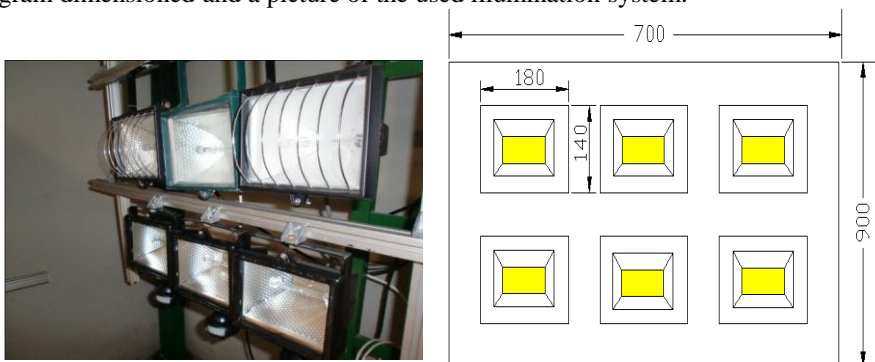
Figure (3.6): A schematic of solid light system

An opaque Perspex diffusion sheet covered with a sheet white paper has a thickness of approximately 10 mm (length and height were a 1000 mm X 750 mm respectively) was placed behind the water tank, and in front of the bank of lights. This Perspex sheet acted as a light diffuser creating uniform light sheet and reduces the intensity of the illuminating light of the jet before entering the camera. The distance between the frame supporting the light bulbs and the frame supporting the diffusion sheet was approximately 300 mm. Figure (3.7) shows a cross-sectional cut at the tank and a picture with the positions of the light source, Perspex sheet and the video camera relative to the main illustrated.
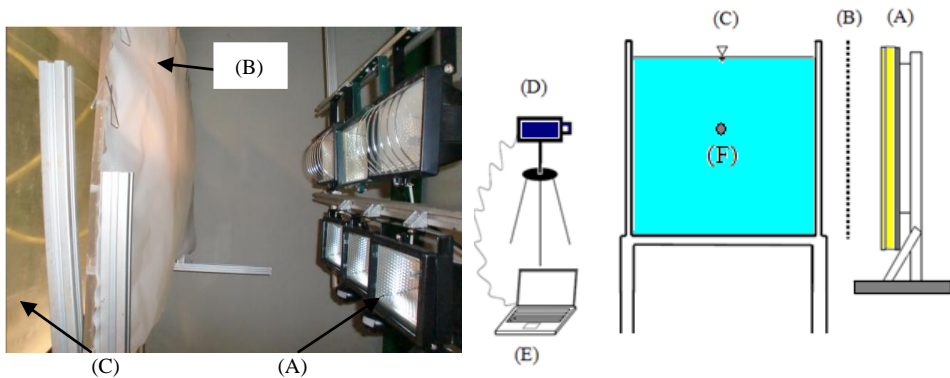
(A) Illumination system (B) Diffusion sheet (C) Water tank (D) Camera (E) Computer (F) Jet nozzle

Figure (3.7): Schematic and photograph showing the shadow photography system consists of a CCD camera, a distributed light source, and a light diffuser

During the experiments, the light bank was covered with black cloth to minimize the chance of light reaching the camera other than through the selected area.

3.3 Instrumentation and Measurements Details

A series of experiments and measurements were carried out to investigate the submerged gas jets injected horizontally in the water tank over a range of Reynolds number between 0.86 and 4.46. The system was designed to deliver a constant air mass flow rate to the injector.

In this section, the description of the measuring instruments and the methods of operation are presented. The measured magnitudes include photographic, air volumetric flow rate, pressure, and temperature measurements. A scheme diagrams illustrating the instrumentation and control system are shown in Figures (3.8) and (3.9).
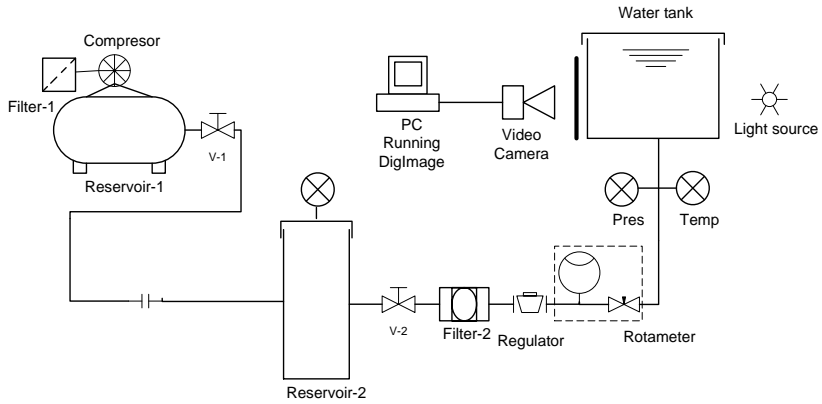
Figure (3.8): Scheme of the instrumentation and control system
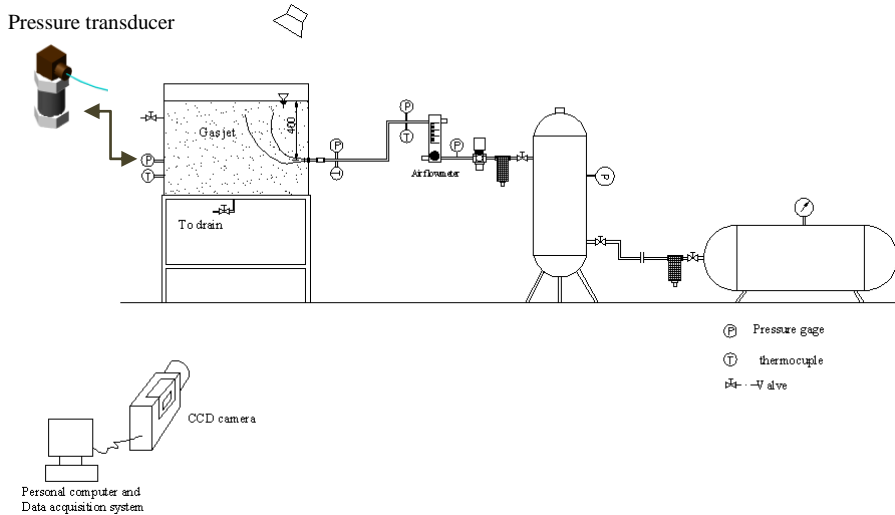
Figure (3.9): Schematic of the instrumentation and control system

3.3.1 Air Volumetric Flow Rate Measurements

Air was delivered from vertical air reservoir to the water tank through a set of filter elements that were installed as a part of air treatment that separates the moisture or solid particles from the compressed air then the air pass through a modular pressure regulator. A pressure regulator valve (AR40-F04 model) 0.5 to 8.5 bars with maximum working pressure 10 bar was used in conjunction with the vertical gas tank that was insensitive to backpressure changes in gas tank. The pressure downstream of the gas regulator was monitored to ensure a constant delivery pressure. Prior to each test the gas tank was charged from the compressor until the maximum pressure was attained to ensure a constant air delivery.

The volumetric flow rate of the air jets was measured using two acrylic air flow meter series FR 4500, Key Instruments, with different ranges of measurements of 4:50 and 30:300 l/min and an accuracy of ±2% and ±3% full scale reading respectively. By knowing the air volumetric flow rate, we can calculate the air mass flow rate at the jet exit by using the air density, so we can obtain the air velocity at the injector exit by knowing the injector diameter.

To calculate the velocity of the air jet entering the water tank (initial jet velocity) we must known: the mass flow rate, the pressure at the measuring point and the pressure within the test section (place where the air is discharged from the air injector). To know this pressure, a pressure transducer was installed before the injector. Where the pressure at the injector exit was calculated by calculating the pressure loss during the injector length, also a pressure transducer was installed at the water tank wall at the same head of the air injector to measure the hydrodynamic pressure of the water head above the air jet.

The flow meter is calibrated at the standard pressure and temperature delivery (STP), so the flow rate must be corrected when used outside of its designer parameters. The air pressure at the inlet of the flow meter is more than the calibrated atmospheric pressure; therefore, the corrected flow rate will be higher than that monitored by the flow meter. To calculate the flow rate at the actual pressure, the following formula was used to calculate the measured flow rate at each measuring case:

$$Q_{Corrected} = Q_{reading} \times \sqrt{\frac{P_{in} + P_{atm}}{P_{atm}}} \tag{3.1}$$

where, $Q_{reading}$ is the volumetric flow rate measured by the flow meter, $Q_{corrected}$ is the corrected volumetric flow rate, P_{in} is the gauge pressure measured at the flow meter inlet and P_{atm} is the atmospheric pressure.

The air pressure (P_e) at the injector exit is calculated by measuring the air pressure before the injector (P_N) and then it correcting by the air pressure loss (ΔP) through the air injector length l_N=0.18 m, and it was found that ΔP has a small value for all injector tested. All the injectors used had the same length.

$$\Delta P = \frac{8 f l_N \rho_N Q_a^2}{\Pi^2 d_N^5} \tag{3.2}$$

$$P_e = P_N - \Delta P \tag{3.4}$$

$$Q_a = Q_{Corrected} \left(\frac{P_{atm} + P_f}{P_{atm} + P_e} \right) \tag{3.5}$$

where, Q_a, P_f, and P_e are the actual flow rate measured by the flow meter, the gauge pressure measured at the flow meter outlet and the calculated pressure at the injector exit respectively. By knowing the air pressure at the injector exit we can calculate the air density and air mass flow rate of the air jet at the injector exit as well as, the initial jet velocity at the injector outlet.

$$\rho_a = \frac{P_e}{RT_a} \tag{3.6}$$

$$\dot{m}_a = \rho_a \times Q_a \tag{3.7}$$

$$u_0 = \frac{\dot{m}_a}{\rho_a A_N} \tag{3.8}$$

The air mass flow rate was changed from 0.002 Kg/s to 0.042 Kg/s. The pipe from the flow meter to the air injector was a flexible PVC tube, 12 mm inner diameter.

3.3.2 Pressure Measurements

Pressure transducers were used for the different pressure measurements. In the present experiments the pressure measurements were taken with Drucker 1400-PTX transducers with an accuracy of ± 0.15% of the full-scale reading. Several pressure transducers with different ranges were used to measure the air pressure, in an effort to minimize errors. Table (3.1) shows the different pressure ranges of the pressure transducers used.

Nº	Pressure measurements	Pressure transducers range (MPa)	Accuracy (full scale reading)
1	Air pressure before flow meter	0 to 0.6	± 0.15%
2	Air pressure after flow meter	0 to 0.4	± 0.15%
3	Air pressure before air injector	0 to 0.4	± 0.15%
4	Hydrodynamic water pressure	0 to 0.0 25	± 0.15%

Table (3.1) Pressure transducers ranges

Pressure transducers are placed at different locations of the test facility as indicated in Figures (3.8) and (3.9).

3.3.3 Temperature Measurements

The experiments were conducted at the room temperature. The air temperature measurements carried out and recorded at three points during the experiments, at the outlet of the flow meter to calculate the air density for flow meter correction, and before the air injector to calculate the air densities to calculate the air pressure at the nozzle outlet, and finally, at the middle of the water tank. Figures (3.8) and (3.9) show the different locations of thermocouples in the facility indicated by (T) letter.

All temperature measurements were conducted by means of thermocouples installed at the different sections of the set-up as mentioned before. All thermocouples used were of type K thermocouples, and were calibrated by using

the comparison techniques against standard type K-thermocouple with 0.1^0C accuracy.

3.3.4 Photographic and Edge Detection Measurements

Visualization techniques are widely used in the study of different phenomena associated with two-phase flow. In particular, it is feasible to study the processes of rupture and coalescence of bubbles present in the fluid by visualizing them. Direct visualization technique has been used in this study by means of charge-coupled device (CCD) camera. The image acquisition system allows the dimensional measurement of the objects photographed. This requires a previous calibration; in addition, special care and attention must be paid to the illumination system. In a wide range of operations, the analysis is carried out by means of image processing software. This permits the detection and analysis of the jet interface and contours, as well as the measurements of the length and spread of the jet in the ambient fluid.

The images of the jet trajectory were acquired using a digital high speed video camera 10 bit (pco.1200 hs model) with 636 frame rate (fps) at the high resolution (1280×1024 pixel), and with an extremely fast image recording capacity 2 GB/s. The camera was used in conjunction with a Nikon AF Nikkor 50 mm f 1.8d (closest focusing: 045m/1.5ft, filter size: 52 mm) camera lens. The illumination system and the operation of the digital video camera and the computer are combined to form the basis for the flow visualization technique. Where, the camera was connected to the computer via a data-cable IEEE 1394a Firewire, camera link and was connected to a 3 MHZ function generator (TTI TG315 function generator model). Figure (3.10) shows the connection of different components of the visualization system.

Camware 32-bit windows application software was used to control every camera parameter and setting. The "camera control" window is the main interface for all camera settings. Where, camera delay and exposure times are adjusted, vertical and horizontal binning can be selected, also the camera can be set to various trigger modes, so a region of interest can be selected and information about the camera is displayed.
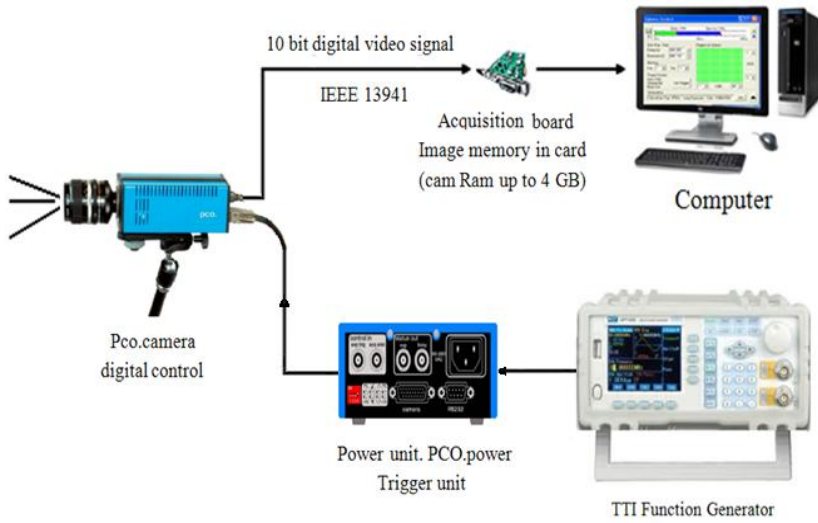
Figure (3.10): The connection of different components of the visualization system

Figure (3.11) shows the structural overview of the pco.camera system components.
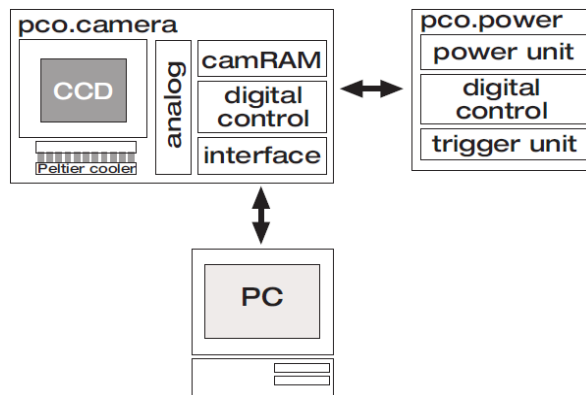
Figure (3.11): Structural overview of the PCO. Camera system components

The camera binning and exposure time are optimized to collect data at the fastest sampling rate possible. The exposure times are adjusted through the software that controls the camera's operation. The sampling rate, including both the exposure and delay time, is measured by connecting an oscilloscope to the camera's status output exposure port on the camera power supply box while operating the camera.

The camera was positioned in such a way that the lens of the camera was in the middle and perpendicular to the tank and focused on the area where the air jet was injected in the water tank, to reduce distortion effects caused by the curvature of the tank wall. The photographed gas jets were analyzed using the MatLab tools. A scale was also photographed in order to calibrate the photographic measurements. Although it is possible to carefully choose the position of the source for flows with two-dimensional trajectories so that they flow perpendicular to the camera axis. The camera was set at a distance that provided a view of the complete tank. It was positioned on the opposite side of the test section up to approximately 1.5 meters from the middle of the tank. During the experiments, the distances between the light source and the tank and between the tank and the camera were not altered.

3.4 Data Acquisition System

All pressure transducers and thermocouples used are connected to a 16-bit DAC 6259 (National Instruments), which works in conjunction with LAB VIEW software to monitoring and controlling the different values.

The measured signals obtained from the pressure (transducer) and temperature (thermocouples) sensors must be properly equipped and sampled in order to be interpreted by the Acquisition software. The acquisition system is divided into three blocks.

i. Treatment and signal conditioning
ii. Signal sampling
iii. Graphical representation and data storage

The first of them has the function to condition and filter the electrical signal of the transducers, in order to prevent the electrical noise produced by common sources such as computer monitors, power supplies, electrical network, etc.,

which may falsify the measurements. The equipment used is the SCXI-1000 of national instrument company.

The second block is responsible for sampling the analog signal from the SCXI-1000 module to turn it into a digital signal interpretable by the computer. It has been used for this object an acquisition card SCXI-1303 model installed in the computer, with 16 inputs and 2 analog outputs, one of them has been designed for the pressure signals and the other for the temperature signals.

Finally, the module for graphical representation and data storage is the graphical interface between the user and the machine for visualization, display and control the facility. This module works with a number of commercial programs as shown in Figure (3.12). It is seen as the signal sampled by the acquisition card, is processed by the Measurement and Automation software responsible for applying the calibration lines of transducers to convert the electrical signal into a valid physical signal. Subsequently, the obtained physical value was processed by LabView for representation and storage this value. Given that, LabView is not able to perform operations and calculations, Matlab is used to perform this task. Figure (3.13) illustrates the main screen of the data acquisition application by LabView software.
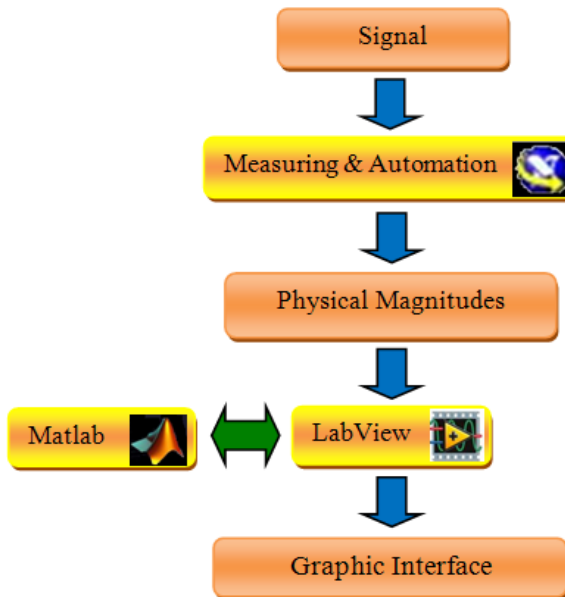
Figure (3.12): Software used and their relationship
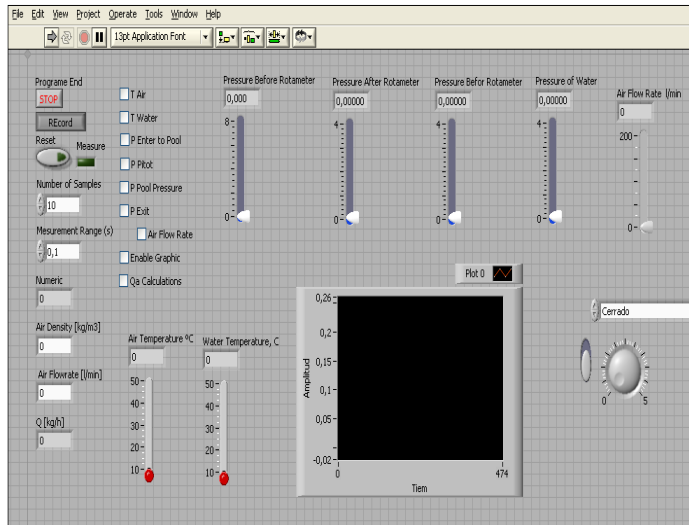
Figure (3.13): Main screen of the data acquisition

Chapter 4

Image Collection, Processing and Analysis Detailes

4.1 Introduction

The technological limitations imposed by traditional measurement techniques such as electroresistivity probes were unacceptable to study the jet interface motions. However, as indicated in Chapter (2), jet flows can be classified based on their trajectory. For those flows with two-dimensional trajectories, it is possible to observe the flow through a camera located such that it is perpendicular to the flow path. Thus, high-speed photography was used to record the position and motions of the entire gas jets in the horizontal buoyant gas jet system and the bubble penetration depth in the vertical plunging water jet system in time and the digital images were processing and analyzed to extract the interface position and penetration depth of the entrained bubbles.

This chapter details the photographic technique that used in the present work to study the two-phase flow. Measurements and steps taken to extract quantitative information from the digital images on the submerged gas jets are presented herein to explain the methodology. The same technique was applied on the vertical plunging water jets to measure the depth of the entrained bubbles in the water pool.

4.2 Photographic and Measurement Description

As mentioned before, direct visualization techniques are widely used in the study of different phenomena associated with two-phase flow. Their use usually involves the utilization of cameras (CCD) and illumination source. Recorded images are a projection of the density variations seen in the test section. Unlike Schlieren photography which is sensitive to the 1st derivative of the index of refraction of the medium (s) which occupy the test section, shadow photography is sensitive to the difference in the 2nd derivative of the index of refraction (Settles, 2006). Thus, the interface existing between air and water is very distinct. However, because the resulting shadowgraph image is a projection of the test section only two-dimensional information is recorded (Christopher, 2009).

Two different video sequences were recorded before start of each experiment of the jet recording process;

i) The first video recorded was the background (reference) video. The background video showed the tank filled with water only, without gas jet flowing in. This video was necessary to confirm that the halogen lights had properly warmed up and the light intensity was constant. In addition, it was used as a correction video for the jet recording video to eliminate the influence of the background. Figure (4.1) shows an example of a background image.
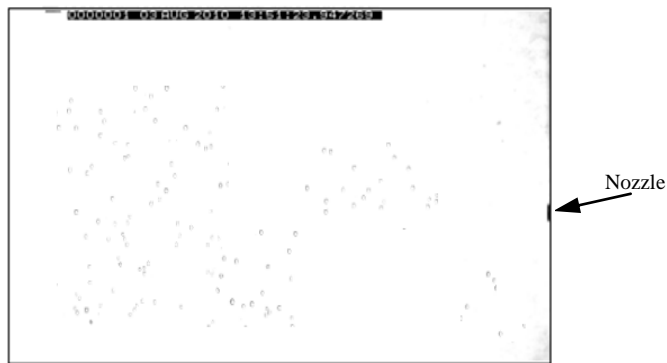
Figure (4.1): Background image, the tank filled with water without gas jet

ii) The second video recorded was the calibration video. Where a cross-shaped ruler inserted horizontally down into the tank at the position where the jet would be. During the analysis process, this image was used to calibrate and work out the length scales along the horizontal and the vertical axes in the images: by resorting to the divisions indicated on the ruler's edge and captured in the pictures, it is possible to determine the number of photograph pixels corresponding to one unit of length (pixels per centimeter). The last video sequence was that of the jet itself.

Due to the great injection momentum, the jet shape remains straight or is slightly diverging due to the high velocity of the jet but the jet diverging angle is not as significant as suggested by Ozawa and Mori (1983). After the jet penetrates into the liquid, buoyancy makes the jet bend vertically towards the free surface and the jet eventually becomes a plume. Therefore, the jet flow along the downstream distance can be divided into two main regions namely (i)

momentum jet region due to the jet momentum (near to the nozzle exit) and (ii) buoyant jet region due to the buoyancy effect (after the momentum region). In the present work, we have studied each region (momentum and buoyant region) individually by record each region alone at the same initial conditions as shown in Figure (4.2):
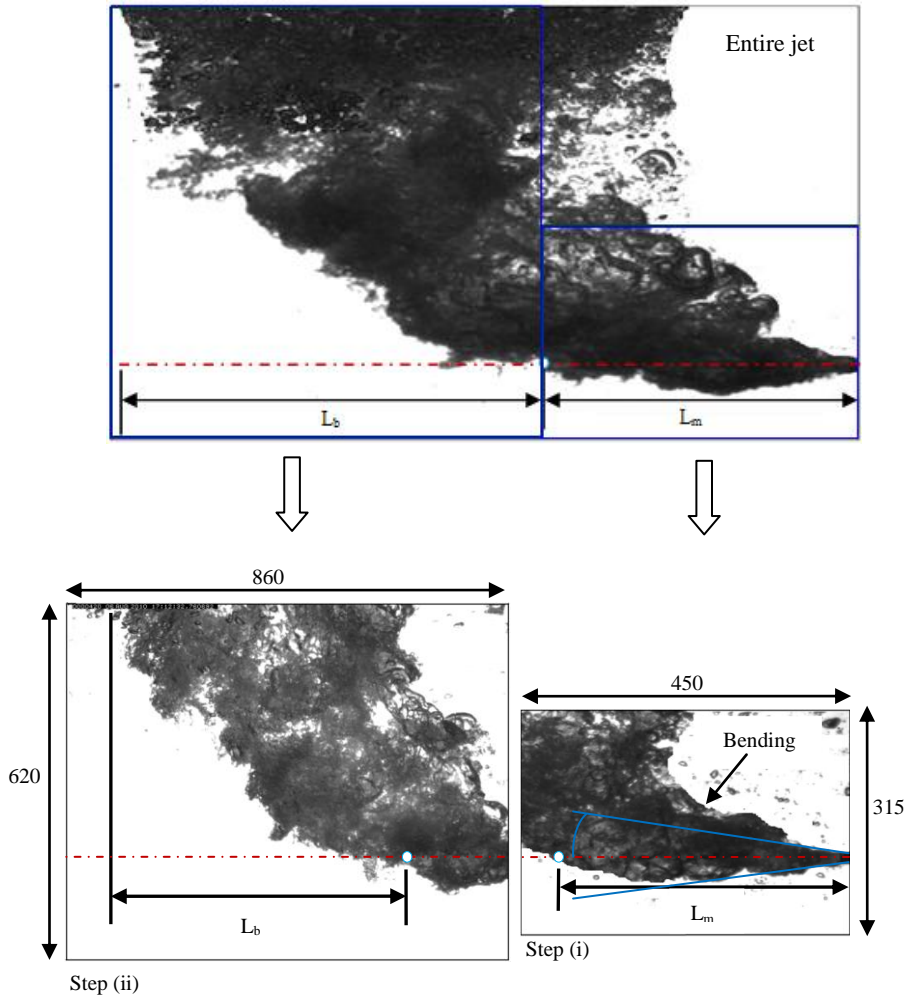
Figure (4.2): Two separated video were recorded for each jet, step (i) Momentum jet region and step (ii) Buoyant jet region at the same initial conditions

Step i) Momentum region (L_m), this region starts from the nozzle exit point to the point where the sharpest gradient occurred (jet starts to rise up) along the horizontal centerline as shown in step (i) of Figure (4.2). This video was

recorded at 1.2 kHz with CCD arrays and it had a resolution of 450x315 pixels, each centimeter was corresponds to 36.5 pixels. This region was used for calculating the momentum jet penetration length, jet-spreading angle and jet width.

Step ii) Buoyant region (L_b), this region starts from the first region which end (step i) to the maximum point in which the jet penetrates as shown in step (ii) of Figure (4.2). This video was recorded at 1 kHz with CCD arrays and it had a resolution of 860x620 pixels, each centimeter was corresponds to 38.5 pixels. This region was used for calculating the buoyant jet penetration length.

Division of the jet recording process on two separated steps acting to increase the number of frames captured per second by the digital camera. Since, when the recorded region of interest is smaller (less pixels overall), the number of frames captured per second will be higher and this lead to overcome the pressure pulsations cycle (frequency).

Measurements on the entire gas jet have been also attempted to study the jet pinch-off phenomenon, the jet interface unsteadiness, and to study the entire jet trajectory and to compare and validate the jet trajectories predicted by the mathematical model developed in Chapter (6) with the experimental results. This video was recorded at 1 kHz with CCD arrays had a resolution of 1090x872 pixels; each centimeter was corresponds to 40.5 pixels. An example of this video is shown Figure (4.3).
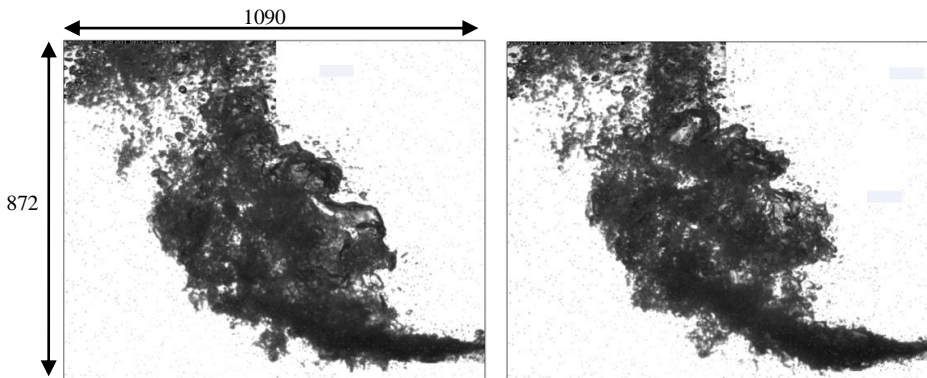
Figure (4.3): Recorded shadowgraph images of the entire gas jet

A series of experiments replicated under many different conditions on each test as shown in Table (5.1) in order to verify the different jet characteristics using the photographic technique. The large amount of data collected by the digital camera system was stored into a computer system and underwent further posterior processing by using MatLab software.

4.3 Resulting Image and Edge Detection Details

The results from the high-speed photography indicate that the gas-water interface tends to be very unsteady and the gas jet as a whole oscillating in the both size and position with the time. An example of the resulting recorded shadowgraph images of the "momentum region" is shown in Figure (4.4). The white section is water and the dark section is the gas jet. The perimeter of the first image (a) is overlaid with dashed red color to show the degree of perimeter instability with the other images (b to f). Note the clear distinction between the two phases that makes detection of the gas phase is relatively simple.
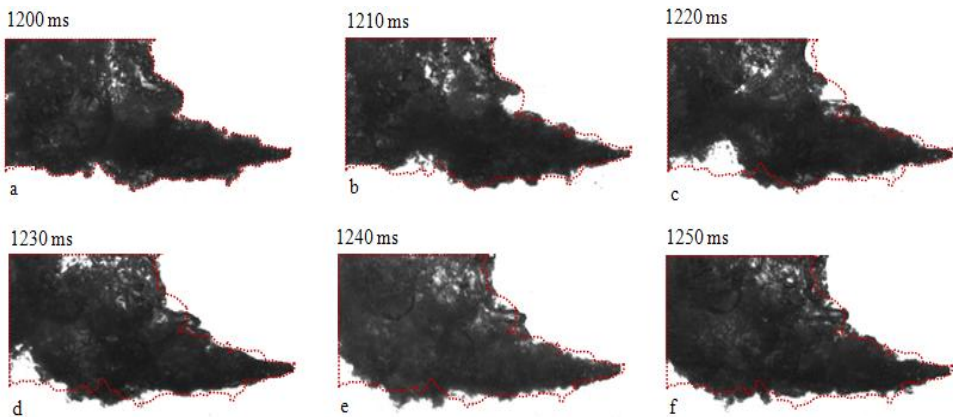
Figure (4.4): Recorded shadowgraph images for Fr_0=95 and d_N= 5mm at several instances in time. The first image is shown 1200 ms after the gas jet was begun and subsequent images are shown at 10 ms intervals

One difficulty in accuracy determining the jet interface position is the presence of bubbles which are ripped from the gas jet. They are clearly not part of the continuous jet, the jet which remains connected to the injector exit and a large bubble which can now rise independently of the jet or re-attaches to the jet. An additional difficulty is due to the pinch-off (breaking) phenomenon when the

continuous gas jet is ruptured into two independent entities: the gas jet that remains connected to the nozzle exit and a large bubble that can now rise independently of the jet. However, the algorithm developed for this work can handle both entities separately.

As the main objective of this work was to study the jet interface motion (unsteadiness and jet pinch-off phenomenon) over the time as well as the global jet properties (jet penetration length, jet spreading angle, jet curvature, etc.) from the acquired digital images an accurate determination of the interface (jet boundary) is required. To accomplish this task a routine was implemented in MatLab tools consisting of several steps to perform the task of the image processing. The jet boundary is computed using the following steps of the images processing method:

 i. Image binarization process,

 ii. Median filter,

 iii. Image fill,

 iv. Morphological functions,

 v. Edge detection. Each step is examined in detail below:

4.3.1 Image Binarization Process

The original images by the digital camera (as shown in Figure, 4.4) were a grayscale which simply means each pixel is assigned a value between 0 and 255. Image binarization converts a grayscale or color image into a binary image, based on threshold. The output binary image replaces all pixels in the input image (digitized) with luminance greater than level with the value 1 (white) and replaces all other pixels with the value 0 (black). Specify level in the range [0,1]. This range is relative to the signal levels possible for the image's class. Therefore, a level value of 0.5 is midway between black and white, regardless of class. However, binary images only have pixel values of 0 (black) and 1 (white). The primary difference between grayscale and binary images is the level of detail contained in the resulting image. This operation involves choosing a grayscale threshold such that the desired information is retained and noise is eliminated (Christopher, 2009).

The task of choosing a suitable grayscale threshold is somewhat qualitative and well obtained by trial and error method (see figure, 4.5). The appropriate threshold can change depending on the fluid mediums, the level of background lighting, and the clarity of the tank side-walls. It is quite apparent that either too low of a threshold value (30%) or too high of a threshold value (95%) are not optimal thresholds. The lower (30%) threshold does not retain enough information and sections of the interface are clearly lost. The higher (95%) threshold permits some noise to be retained which can be difficult to remove, such as the many small black dots bordering the jet region. The medium (60%) threshold was more appropriate and was used for image binarization.

Original image   30% Binarization

60% Binarization   95% Binarization
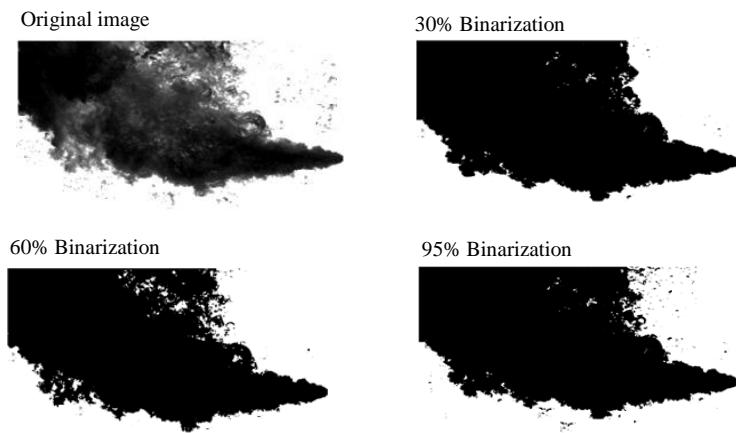
Figure (4.5): Various thresholds applied to the original image result in a varying level of information being filtered

4.3.2 Two-Dimension Median Filter

Median filtering is a nonlinear operation often used in image processing i) to remove image noise and ii) to remove small bubbles very near the jet interface. These bubbles are not part of the gas jet but rather were separated from the gas jet from unsteady processes. The median filter employs by [n x m] pixel median filter to the 2D image. To accomplish this task a [n x m] pixel rectangle is translated around the image where the center point value is updated based on the median value of the surrounding pixels.

Small median filter such as [3 x 3] size as shown in Figure (4.6) does not remove noise and appears that there is no difference between with the original

image. Large filters such as the [10 x 10] size are not advisable as although they are capable of removing large bubbles separated from the gas jet they significantly smooth the interface. This is clearly seen in Figure (4.6) and represents a loss of interfacial information. Thus it is better to choose smaller, rather than larger, median filter sizes. Through trial and error, the [6 x 6] size proved to be the most suitable filter size as it removed most bubbles separated from the gas jet while preserving the interfacial shape.
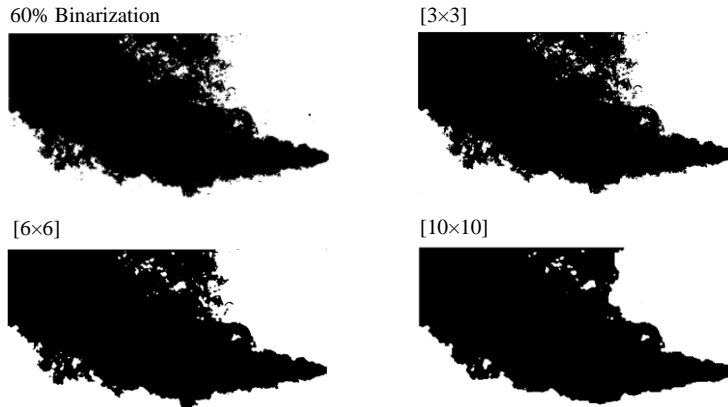
Figure (4.6): The median filter is used to smooth irregularities in the binary image. Only small median sizes are used to prevent filtering of actual interface data

4.3.3 Fill Image Regions and Holes

Due to the gas jets that is continuously expanding and contracting, there are regions of the jet composed of several shades. Although the image binarization step and other filtering operations can yield holes, or regions within the known gas jet identified as liquid phase, in some cases large holes exist in an otherwise continuous gas region. However, this work makes use of time-averaged jet penetration curves to make several points, and these curves require that all regions of the gas jet remain black (0) and all regions of the ambient water remain white (1).

An example of filling holes within the continuous gas jet is shown in Figure (4.7). Observation of the original and median filter image reveals regions of light inside the jet body. The background pixel value (white) is equal to the value of the holes within the bubble, yet there is no path from the holes to the ambient liquid one can take without first encountering the jet (dark pixels).

Original image   [6×6] Median filter   Holes filled
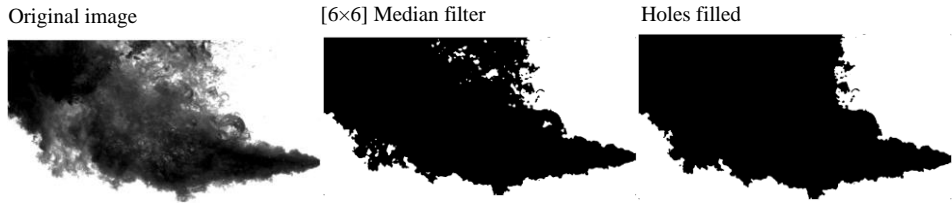
Figure (4.7): The region and holes in the gas jet are automatically identified and filled

4.3.4 Morphological Operations

The last step before determining the jet boundary is the morphological functions, which are used to determine which parts of the image should be removed and which should remain. Since the primary reason for the inclusion of this step is to remove small independent bubbles. The geometric shape can be anything, such as a rectangle, diamond, or circular object and of any size, in this work a circular shapes were used. Essentially this operation consists of a circular element which is traversed through the image and any structures which are smaller than the circular element are removed from the image.

The morphological operation consists of two tasks: image erosion and image dilation. These tasks have the effect of removing small objects from the image, such as small bubbles which have broken off from the gas jet. In the image erosion step the circular element is traversed through the image and the center of the element is set to the minimum value of all the pixels encountered within the element. This has the effect of removing information. The next step, image dilation, does the opposite and restores the prior boundary with the exception of those areas which were smaller than the geometric element.

Several structuring element sizes were used with all elements disks. The effect of increasing the disk size is quite clear: small bubbles or other noise unrelated to the gas jet is removed. However, a trade-off exists between the size of element used and the resulting image. As the disk size is increased the interface is greatly smoothed and information is again lost. Through trial and error it was determined that a disk size of 5 was the maximum that should be used in order to prevent the loss of crucial interface shape and information. Any sizes over 5 simply smeared the interface too much. The morphological operation is shown in Figure (4.8) for the same test image used in the other cases.

Original image

Holes filled

Disk size 2

Disk size 5

Disk size 10
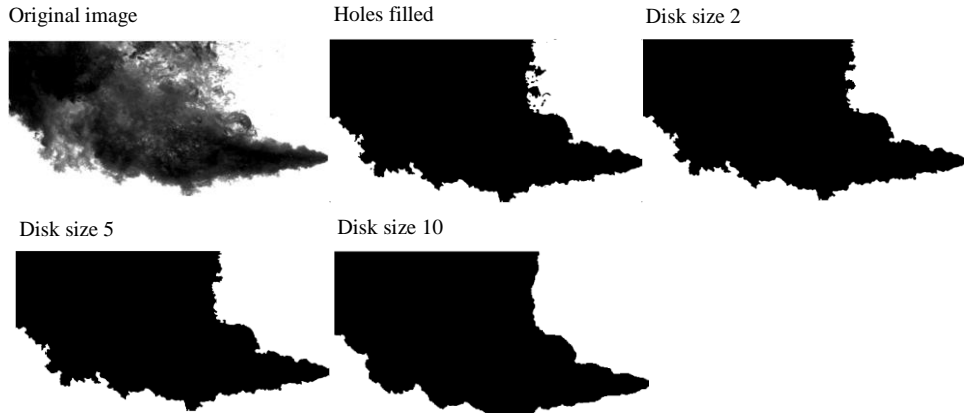
Figure (4.8): The morphological operation used to remove small detached bubbles

4.3.5 Jet Interface Detection

The last step consists of the jet edge (interface) detection to find the perimeter of the binary image, which is defined as any non-zero pixel which is adjacent to a zero value pixel. The algorithm thus searches adjacent pixels and forms the perimeter between dissimilar regions (air/water). Since this study is concerned with the jet interfacial motions, the jet perimeter is located and its coordinates are saved to a text file.

The result of this step is shown in Figure (4.9) as the "Detected Perimeter", for the same test image used in the other cases. The leftmost image is the original unfiltered photograph. The image to the right of this image is the one obtained after being digitized, median filtered, holes filled and adjusted. The original image was compared to the previous one at the different steps and the detected boundary agrees quite well with the original image.

Original image (a)

Binarization (b)

Median filter (c)

Image fill (d)

Adjusting process (e)

Detected perimeter (f)
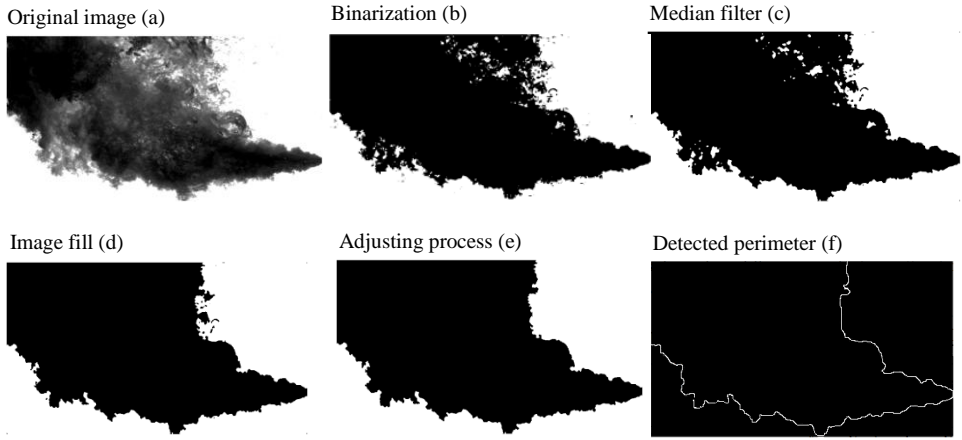
Figure (4.9): Edge detection steps to find the jet perimeter. The different steps is shown with the original image to show the degree of accuracy in determining the perimeter

The resultant processed images were stored in a 3D array (x, y, and z), where the two dimensional image (x and y pixels) is stored in the x and y directions and the third dimension (matrix depth, z) represents the frame number.

Figures (4.10) illustrate a summary of the main structure of the program (Flow Chart) that is used in this study to record, calibrate and process the images.
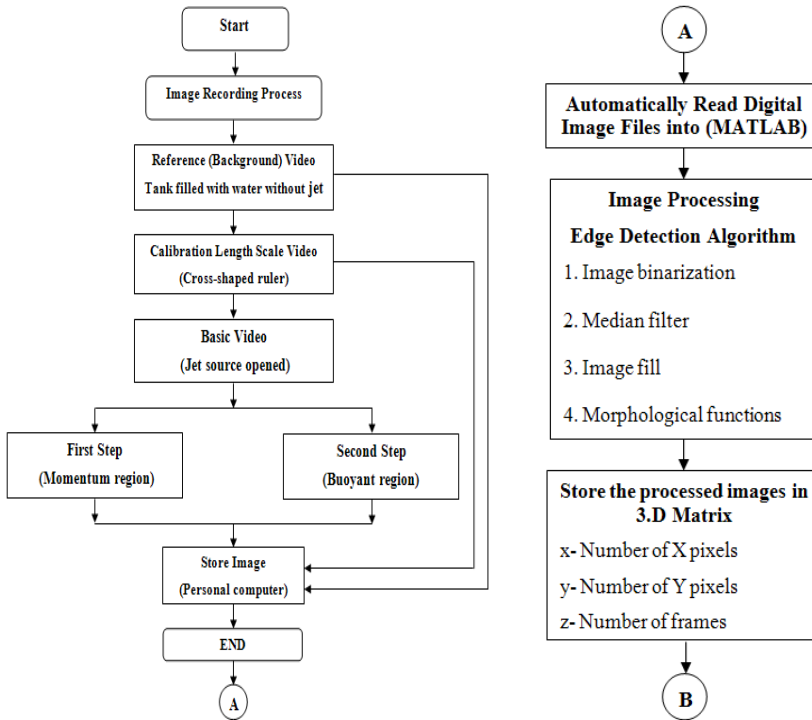
Figure (4.10): Flow chart of a) Image recording, calibration and storage steps and b) Image processing and store the data in 3.D matrtix

4.4 Image Analysis and Output System

After the morphological operations are applied to the original photographs of the gas jet as shown in section (4.3.4), the resulting image is ready for jet penetration computation. The resultant images are composed of only 0's and 1's, with a value of 0 and 1 indicating the presence of gas and water, respectively. For all tests and time steps, the jet perimeter coordinates were written to individual text files.

The image analysis was to take these perimeter coordinates and analyze them to extract the different jet parameters. To accomplish this task a routine was implemented in MatLab tools consisting of several steps were used to analyze and get the system of output. Two methods were used in the present study to analyze the data and get the output system, which was automated in digital files in MatLab named:

i) Summation method; where each processed image (of section 4.3.4) was added to the last one, which results in an image with a spatially varying intensity.

ii) Statistical method; where the jet perimeter (of section 4.3.5) for each image is located (determined) firstly and then summed. The resulting added image (matrix) then averaged statistically for the total number of frames. Figure (4.11) illustrates the flow chart program that used for loading the stored processed images and the two methods used to analyze the data system.

(i) Summation method   (ii) Statistical method
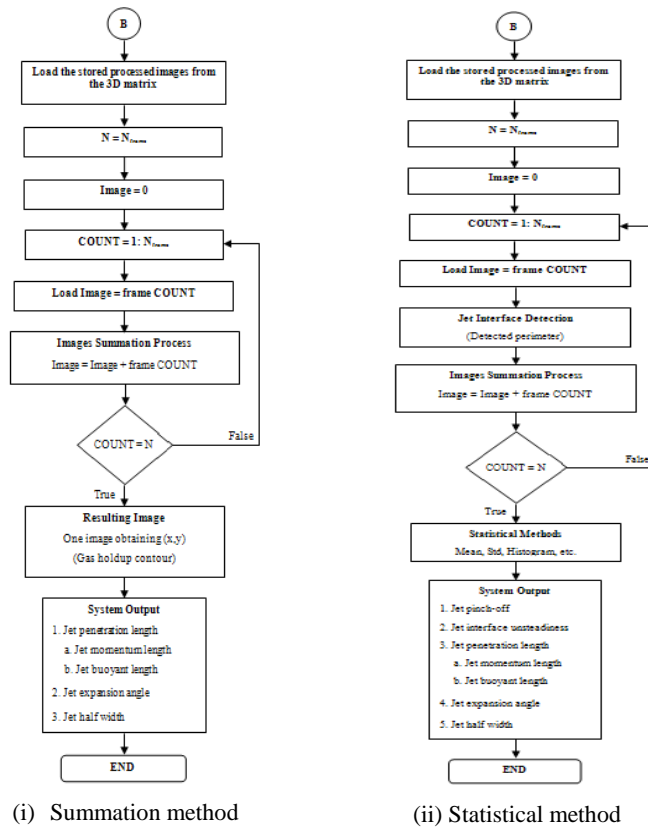
Figure (4.11): Flow Charts illustrate on the left and right the summation and statistical method respectively used to loading, storing, and linearization and output system

The results obtained by the two methods were compared and seem to be in good agreement with one another, yields almost identical results, the comparison results present in the next Chapter (5) section (5.3.3.1).

4.4.1 Determination of the Jet Pinch-Off Location

Jet pinch-off refers to the case when the continuous jet breaks into two or multiple independent entities as shown in Figure (4.12)-(a) and (b). To calculate the maximum axial distance (x_p) from the nozzle exit before the jet is pinch-off, the jet perimeter (interface) is linearized and separated into left and right sides as shown in Figure (4.12)-(c). Linearization means that for each x coordinate position only one radial interface position is permitted. However, in the linearized interface picture, for every axial position (x-coordinate) where the jet has multiple radial positions (y-coordinate) only the outer jet position is taken. An example of the resulting linearized interface positions and the original image is shown in Figure (4.12)-(a):(c) where the x and y coordinates are shown in units of pixels and the jet interface is separated a two into left and right sides by red and blue colors respectively.
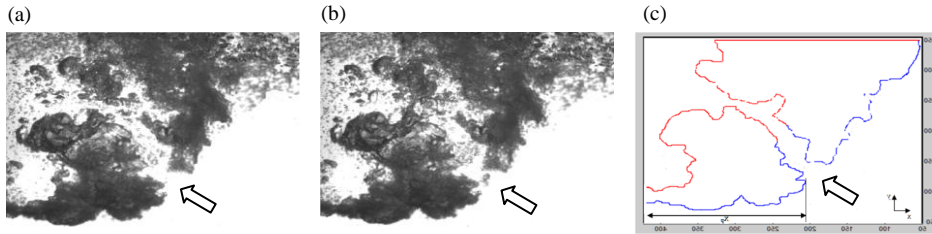
Figure (4.12): The Computed jet interface positions are linearized and separated into upper and lower jet edge, denoted by the symbol color

The jet interface and the maximum downstream distance (location) of pinch-off were recorded and their spatial distribution was automatically determined by summing across all times for each downstream position in MatLab. This procedure was realized for each image where the resulting (x_p) was summed and averaged statistically for the total number of frames over the time to find the average x_p for each test run.

From the previous procedure, it was easy to track all locations where the gas jet has pinched-off by simply recording the axial locations corresponding to an x_p coordinate value of zero. These values were recorded with the axial position of maximum jet continuity. In other words, if a gas jet were to pinch-off, the maximum axial position of the gas jet is recorded. Figure (4.13) shows an example of cumulative frames of the lower jet edge in 13 seconds for different Froude number and jet diameters that obtained. The zeros values indicate that the jet is pinched-off.

$Fr_0 = 43$, $d_N = 5$ mm

$Fr_0 = 99$, $d_N = 5$ mm

$Fr_0 = 92$, $d_N = 2$ mm

$Fr_0 = 143$, $d_N = 2$ mm
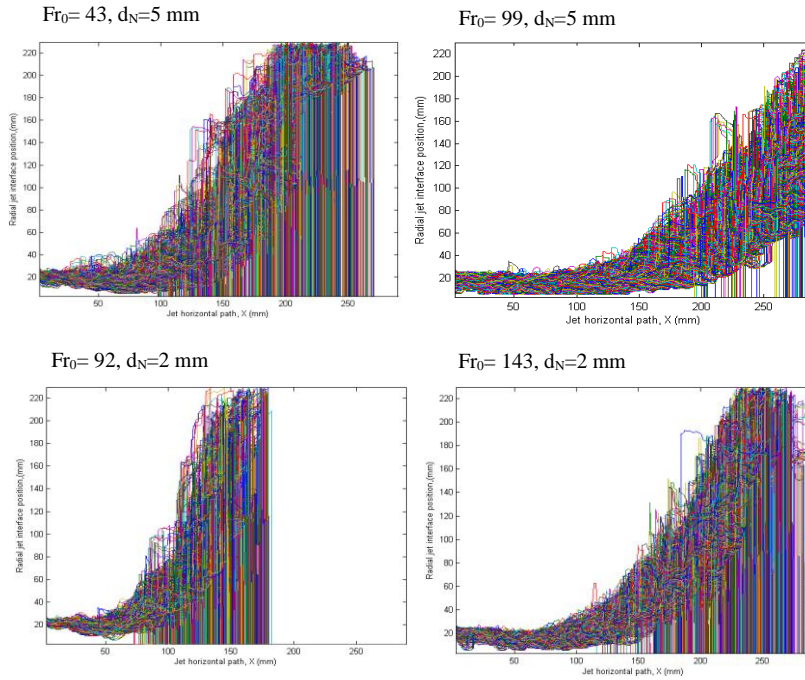
Figure (4.13): The images show the process of jet pinch-off detection

The interfacial data is padded both below and above with ten columns, all containing zeros (white), and thus both below and above of the interrogation region the data indicates on the jet. This is primarily for data processing to ensure that the entire interface is within the computation domain also to eliminate the injector part. The nozzle exit is located at $(x,y) = (425,100)$. The original interface picture shows the computed interface position.

4.4.2 Jet Penetration Length Computation

In this section, we discuss the methods to calculate the jet lengths in each jet region that mentioned in Figure (4.2) of section (4.2).

4.4.2.1 Momentum Gas Jet Length

The gas jet lengths in the first region (momentum region) were calculated as the follow:

Step i) A total of 15600 images of the momentum region were recorded at 1.2 kHz sampling rate for 13 second period as shown in section (4.2). The 13 seconds period was sufficient to overcome the pressure pulsation frequency at the nozzle exit. The added images will result in an image with a spatially varying intensity with different color scale (image intensity).

Step ii) The momentum gas jet length (L_m) was defined here as the horizontal axial distance along the nozzle centerline from the nozzle exit to the point where the sharpest gradient (largest image-intensity gradient) occurred in the intensity of the temporally averaged image.

Figure (4.14) shows an example of a comparison of 43 and 99 jet Froude number resulted by the summation method and statistical method (represented by black line).

A good agreement can be see with one another. However, from this figure we can observe an obvious difference between the two jets, especially in the penetration length of a gaseous core which occupies a volume for a large percentage of the test record. The contour colors indicate the percentage of time that a certain location in the field of view was occupied by the gas. Experiments were performed at least three times for each run and the values obtained for the gas jet lengths were averaged. The repeatability error was less than ± 2%.

Fr$_0$= 99, d$_N$=5 mm   Fr$_0$= 43, d$_N$=5 mm
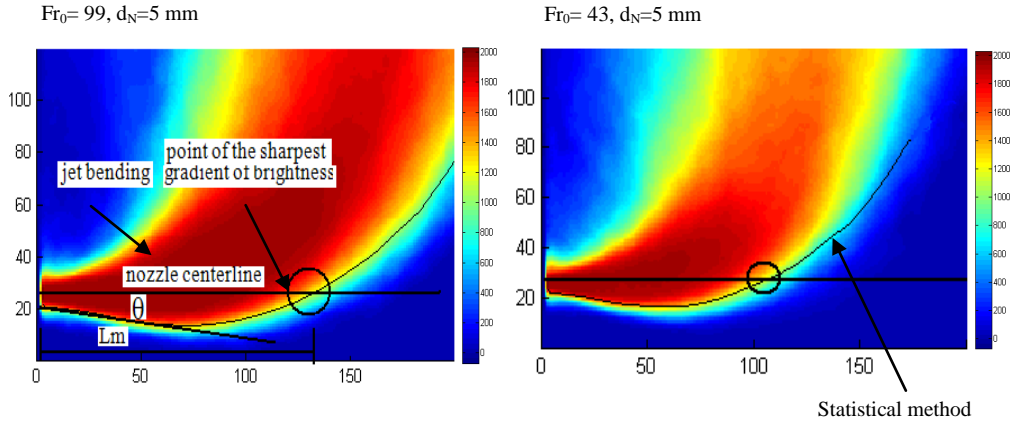
Figure (4.14): Momentum jet length (L$_m$) determination, which is computed by binary image addition, all pinched-off bubbles are neglected in the image addition

In the statistical method, the jet perimeters for each image are located firstly (as shown by section 4.3.5) and calculate the jet length and then accumulate all and averaged statistically by total number of frames. Figure (4.15) show an example of the statistical method where the black line presents the averaged value along the jet axis.
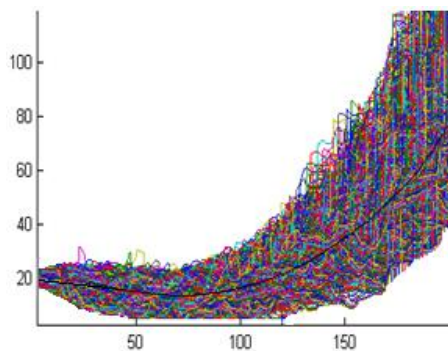
Figure (4.15): Momentum jet length (L$_m$) determination, which is computed by statistical method

4.4.2.2 Buoyant Gas Jet Length

At a downstream location, the flow is driven by buoyancy as opposed to momentum and the flow is controlled by the buoyancy force. In this region, the buoyant jet penetration length was calculated as follows:

Step i) A total of 9000 images of the buoyant region were recorded at 1 kHz sampling rate for 9 seconds period as shown in section (4.2). Each binary image is added to the last which results in an image with a spatially varying intensity in the same manner described in section (4.4.2.1) for the momentum gas jet length. This is graphically shown in Figure (4.16) which shows the image addition for the buoyant jet region for jets with Froude numbers of 99 and 74 (d_N=5 mm).

Step ii) The buoyant gas jet length was defined as the distance from the point where L_m ends to the point that is the intersection of the horizontal line from Lm, and the vertical line which is tangent to the plume when it becomes vertical (maximum point in which the jet penetrates) as shown in Figure (4.16). Experiments were performed at least three times and the results obtained for the gas jet length were averaged. The repeatability error was less than ±4%.
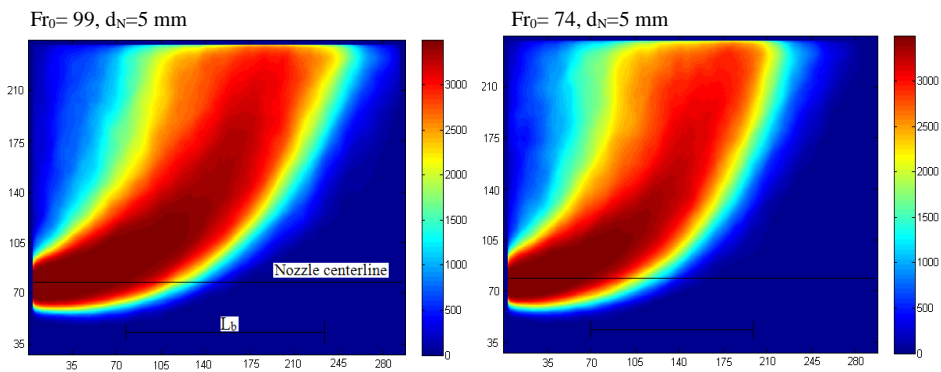
Figure (4.16): Buoyant jet length (L_b) in determination, which is computed by binary image addition. All pinched-off bubbles are neglected in the image addition

4.4.3 Computation of the Jet Expansion Angle and the Jet Half-Width

The jet spreading rate, which is indicative of mixing and entrainment at the interface, to determine the jet spreading angle and the jet half-width the recorded images focusing only on the region near the nozzle exit (momentum region) as the same explained of section (4.4.2.1). The image-intensity gradient in the region above the centerline was strongly affected not only by jet expansion and development but also by the rising bubbles. Therefore, the expansion angle and the jet half-width below the centerline was only considered in the present calculations. Although the jet could still be affected by the buoyancy even in that region, its velocity was quite large and the effect of the buoyancy on the expansion angle seemed small, at least in the upstream region.

The next steps were used to calculate the expansion angles and the jet half-width as follow:

Step i) After the averaging process of the images of section (4.4.2.1), the jet perimeter is linearized then, the jet interface is separated into above and below sides as discussed in section (4.4.1).

Step ii) The expansion angles and the jet half-width were determined by linear regression on the lower jet interface using the least squares method.

4.5 Entire Jet Interface Detection

To study the jet pinch-off phenomenon, the jet interface unsteadiness, and to compare and validate the jet trajectories predicted by the mathematical model developed in Chapter (6) with the experimental results, A total of 8000 images of the entire (whole) jet was recorded at 0.8 KHz, i.e., over a 10 second period. The initial conditions for all experimental is the same as that used to study the different jet parameters (jet penetration lengths, jet half width, etc.) of Table (5.1).

Another routine similar to the previous routine that was used to calculate the jet penetration length (section 4.4.2) was implemented in MatLab tools consisting of the similar steps that used to the image processing and the analysis task. The results of these steps are shown in Figure (4.17), where the original image was

compared to the different steps of the image processing and the detected boundary agrees quite well with the original image.

Original image (a)   Binarization (b)   Median filter (c)

Image fill (d)   Adjusting process (e)   Detected perimeter (f)
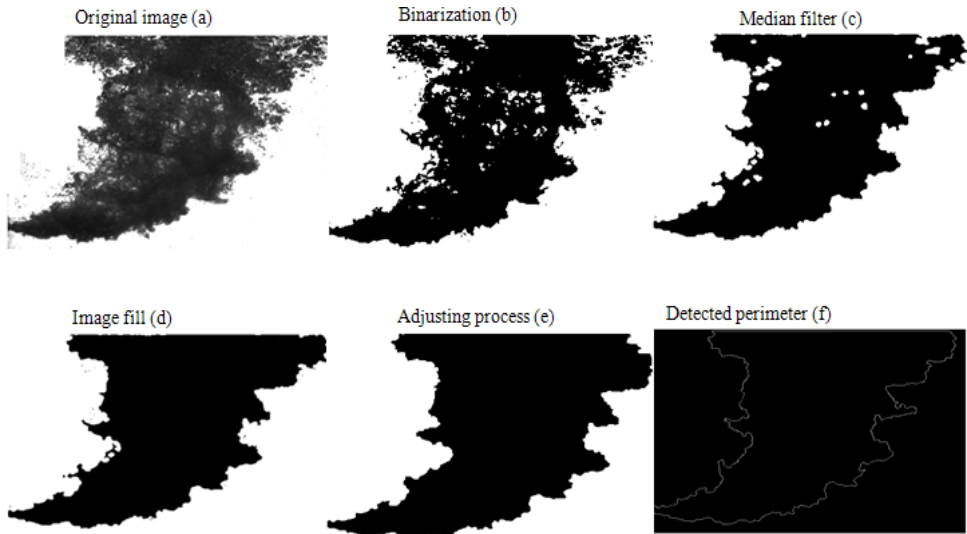
Figure (4.17): Steps used to detect the entire jet boundary, the resultant image was comparing with the original image

Chapter 5

Experimental Results and Discussion of the Submerged Gas Jets

5.1 Introduction

In this chapter, the experimental results obtained from the experiments on the submerged gas jets in water ambient are presented, discussed and analyzed. The jet mass flow rate and the injector diameter were the parameters whose values were varied in order to study the effects brought about.

5.2 Experimental Conditions (Experimental Matrix)

The jets were formed by a set of interchangeable straight tubes with different diameters 2, 3, 4 and 5 mm. The tubes were placed horizontally in such a way that there was a distance of 200 mm between the bottom of the tank and the injector center. The straight tubes used and its location in the water tank are shown and described in Chapter (3). All jets were shot at 0.40 m water depth. Thus, the vertical distance from the centerline of the injector to the free surface of the water was considered sufficient to avoid small effects caused by changes in the free surface (pressure).

Table (5.1) shows the initial conditions of the experimental runs, where all properties, such as Froude and Reynolds numbers are calculated based on the initial jet properties at the nozzle exit. The experiments were carried out for different nozzle diameters and different jet flow rates. The jet velocity at the nozzle exit was obtained directly from the jet mass flow rate and nozzle exit area.

	Run	Fr_0	Mach Num.	P_N Pa$\times 10^5$	P_e Pa$\times 10^5$	ρ_g Kg/m^3	T_0 (K)	$\dot{m}_a$ (kg/s)	u_0 (m/s)	R_e $\times 10^5$
d_2	1	143	0.98	3.21	2.95	3.46	296.8	0.0037	340	1.58
	2	120	0.88	2.44	2.31	3.01	297.2	0.0029	306	1.24
	3	92	0.76	2.14	2.05	2.41	296.8	0.0020	264	0.86
d_3	4	114	1.06	2.60	2.43	2.85	297.1	0.0074	367	2.11
	5	92	0.90	2.28	2.18	2.55	297.8	0.0056	312	1.61
	6	73	0.76	2.00	1.93	2.27	297.8	0.042	262	1.20
	7	62	0.67	1.84	1.79	2.09	297.8	0.0034	232	0.97
d_4	8	95	1.03	2.47	2.36	2.77	296.8	0.0124	357	2.66
	9	76	0.87	2.19	2.11	2.48	297.1	0.0094	302	2.01
	10	52	0.66	1.75	1.72	2.01	296.8	0.0058	229	1.24
	11	46	0.61	1.66	1.64	1.92	296.8	0.0051	209	1.08
d_5	12	99	1.05	3.24	3.12	3.66	296.9	0.0262	363	4.46
	13	74	0.86	2.67	2.60	3.05	296.7	0.0178	297	3.05
	14	54	0.70	2.18	2.14	2.51	296.8	0.0119	241	2.04
	15	43	0.59	1.88	1.86	2.18	296.2	0.0087	204	1.49

Table (5.1): Summary of experimental initial conditions: (d) straight tubes diameter, where, d_2, d_3, d_4 and d_5 represents d_N= 2, 3, 4 and 5 mm respectively and ($\dot{m}$) is the jet mass flow rate.

All the pressure values in this table are absolute, P_N is the jet pressure at a point located upstream of the nozzle (18 cm away from the nozzle exit) and P_e is the jet pressure at the nozzle exit. T_0 (K) is the jet temperature, ρ_g (kg/m^3) is the jet density at the nozzle exit, and u_0 (m/s) is the jet velocity at the nozzle exit. The schematic diagram shows the different locations of the pressure and temperature sensors in the test-rig is shown in Chapter (3) Figures (3.8) and (3.9).

5.3 Measurement Results and Discussion

Direct measurements of the interfacial behavior of submerged buoyant gas jets with speeds ranging from subsonic to sonic Mach numbers were performed

using visualization technique (CCD). The high-speed photography indicates that the gas-water interface tend to be very unsteady. The injection of gas into liquid introduces an additional level of complexity in the jet character, which is marked by the unsteadiness and pulsating behaviour of the phase interface, the gas jet as a whole oscillating in both size and position. An example of the resulting shadowgraph images is shown in Figure (4.4) which shows how the jet interface oscillate in both size and position in the time.

A further experimental observation indicates that a bulge phenomenon (gas-bag) enclosed by the surrounding water formed behind the nozzle exit. It should be pointed out; however, when the gas jets enter into the water initially, the pressure of the gas is not high enough to overcome the inertia effect of the water due to the large density ratio between the gas jet and the ambient water (Shi, 2010). The pressure inside the "gas bag" will accumulate and keep increasing, and once it is high enough to overcome the suppression of the water, the gas can expand freely to complete the expansion process. Bulging of the jet occurs many times before the more violent jet expansion feedback occurs. During the feedback process, the jet diameter can become several times that of the original one depending on the jet Mach number (Jia-Ning, 2011).

5.3.1 Jet Pinch-Off Phenomenon

At some downstream position from the nozzle exit, the gas jet can no longer support the local hydrostatic pressure and the jet will pinch-off (breaking). At this downstream location, the flow is driven by buoyancy as opposed to momentum. Here, the term pinch-off refers to the state in which the gas jet is no longer continuous from the nozzle to the free surface. Figure (5.1) shows an example of the jet pinch-off phenomenon with 1 ms intervals time for a 54 Froude jet (0.7 Mach). The pinch-off phenomenon may be seen at 1177 ms.

The jet goes through intermittent periods. Firstly, the jet maintains a continuous presence from the nozzle to the free surface, then pinch-off and the single and continuous gas jet has now ruptured into two independent entities: a gas jet which remains connected to the nozzle exit and a large bubble which can now rise independently of the jet or re-attaches to the jet. This behavior is indicative of jetting or bubbling, since by definition a continuous jet cannot pinch-off. The jet is considered continuous in the previous figure between 1172 ms to 1176 ms with pinch-off starting at 1177 ms and remains pinched-off in the remainder of the times shown.
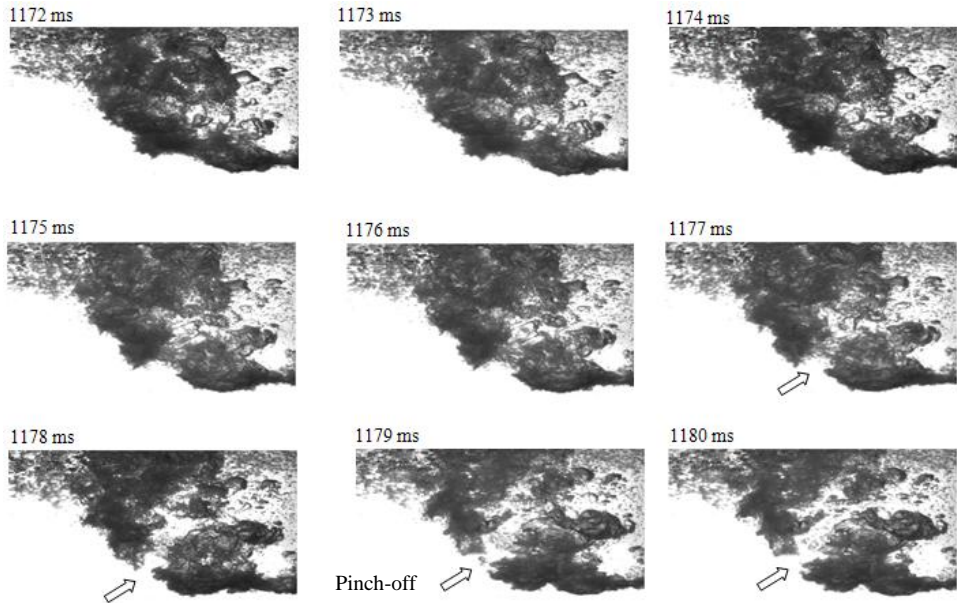
Figure (5.1): Shadowgraph images show the jet pinch-off phenomenon in a 54 Froude jet and d_N=5 mm. The first image is shown 1172 ms after the gas jet was begun and subsequent images are shown at 1 ms intervals

The phenomenon of jet pinch-off in the present study is largely due to the large density variation between the gas jet and the water ambient and due to sonic and subsonic Mach number jetting. Using the high speed photography and analysis methods presented in Chapter (4) section (4.4.1) the jet interface and the maximum downstream distance (location) of pinch-off were recorded and their spatial distribution was automatically determined by summing across all times for each downstream position in MatLab.

From the experiments, we have found a relationship between the jet pinch-off, the jet Froude number and the nozzle diameter at a constant hydrostatic pressure. The maximum axial distance (x_p) before the jet pinched-off increased with the jet Froude number at constant jet diameter. The higher Froude number jets have longer periods of jet stability (continuous presence) before pinch-off occurs since more time is spent in a longer time interval of continuous jetting behavior. The lower Froude number jets show a broader range of pinch-off locations.

Figure (5.2) shows the relation between the jet Froude numbers and the maximum axial distances before the jet is pinch-off (scaled by L_Q) for all nozzle jet diameters tested.
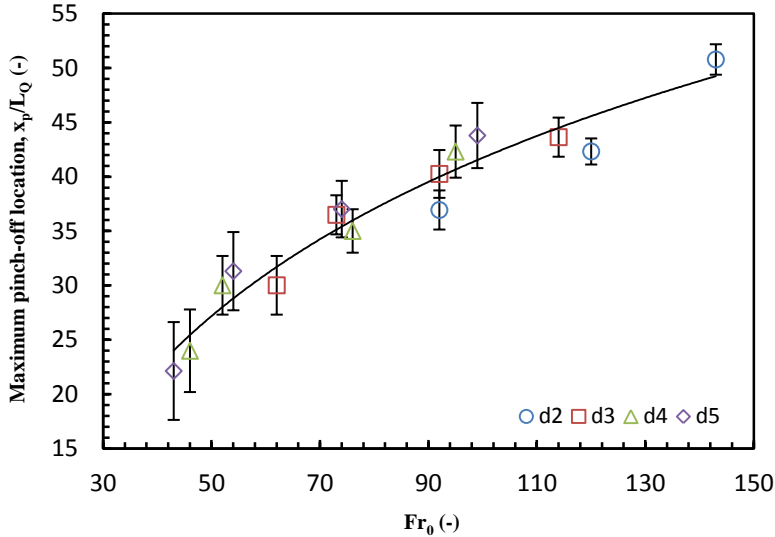
Figure (5.2): The maximum axial distance before the jet is pinch-off (breaking)

The figure shows that, the maximum axial distance of the jet pinch-off increases nearly in a logarithmic function with increasing Froude numbers and when appropriately scaled appears to be somewhat constant across all nozzle diameters. These results indicate that increasing jet Froude number decreases the likelihood of a pinch-off event as Froude number is increased. The same result is obtained by Christopher (2009) but for vertical rectangular gas jets.

Equation (5.1) expresses this relationship with a coefficient of correlation of 0.94:

$$x_p / L_Q = C_1 \ln(Fr_0) + C_2 \qquad (5.1)$$

where, x_p/L_Q is the axial distance ratio before the jet is pinch-off, Fr_0 is the initial jet Froude number at the nozzle exit and $C_1 = 21$ and $C_2 = -55$ are constants.

Also, the spatial distribution of pinch-off events was experimentally observed to be dependent on the nozzle diameter. The small nozzle diameter $d_N=2$ mm seems to pinched-off faster (before) than the other diameters, for the same Froude numbers.

The varians (as illustrated in the error bars) in the maximum pinch-off values with nozzle diameters suggests that the nozzle diameters also be a parameter that affect on the position of the pinch off values. It is possible that the stream wise turbulence levels act as a perturbing factor on the interface, being directly responsible for pinch-off.

5.3.2 Analysis of the Unsteady Jet Interface

When a gaseous jet is injected into liquid ambient through a nozzle, the flow structure and process are essentially unsteady and turbulent. Air jets submerged in water are complicated by these effects of unsteadiness especially at low flow rates, similar to the pulsatile behavior of highly buoyant single-phase flows. This involves oscillatory release of gas which can cause liquid to slug into the jet passage. The unsteadiness is accompanied by appreciable fluctuations of static pressure in the flow passage and beyond the jet boundaries, often resulting in excessive noise and vibration as well as blockage of the passage in cases where the gas reacts with the liquid (Kerney et al. 1972, Chan 1974, Avery and Faeth 1974, Loth and Faeth 1989).

The jet interface between the dissimilar regions (gas/water) was detected, positioned and recorded by the steps discussed in Chapter (4). The method presented herein builds upon the methods used by past researchers (Wraith and Chalkly 1977, Ozawa and Mori 1986, Christopher 2009) in their determination of jetting or bubbling behavior. An example of jet interface tracking in time (one second of time is shown for clarity) at fixed position 10 diameters downstream of the nozzle exit is shown in Figure (5.3) for 3 and 5 mm nozzle diameters scaled by the average values of the radial interface position. We focused here on the jet interfacial below the centerline of the nozzle.
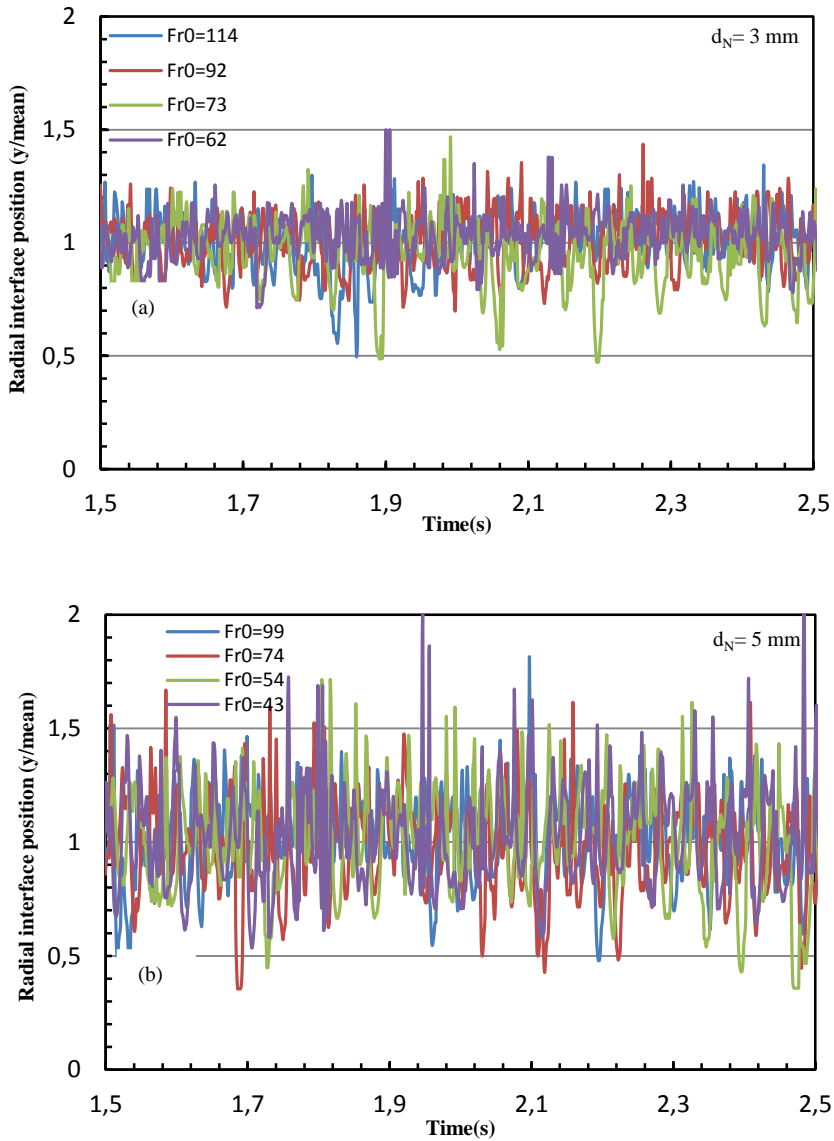
Figure (5.3): Variation of jet interface position with time for; a) d_N=3 mm and b) 5 mm diameter respectively. This information was computed for each test run at each downstream pixel location.

From the result curve, the magnitude of the jet interfacial oscillation seems to increase when increasing the nozzle diameter. The jet of 5 mm initial diameter clearly displays bigger oscillation amplitude than the one with 3 mm diameter as shown in the Figure (5.3). In addition, increasing the Froude number is seen to have a stabilizing effect on the interface having less interfacial motion than the jet with smaller Froude number. This finding can perhaps be explained from the internal characteristics of the turbulent gas jet, although, our experiments cannot quantify its internal characteristics. Christopher (2009) suggested that the turbulence acts as a perturbation on the interface to drive its unsteadiness hence leading to pinch-off.

One of the goals of this research was to quantify the effect of nozzle diameter and Froude number on the jet interface unsteadiness. The jet interfacial unsteadiness was directly computed here by taking the standard deviation (σ) of the jet interface radial position along the entire lower jet edge for all locations where the jet maintained a presence for 90% of the recorded time over a period of 13 second. The standard deviation is the square root of the variance as show in the following equation:

$$\sigma = \sqrt{\frac{1}{N-1} \sum_{i=1}^{N} \left(x_i - \overline{x} \right)^2}$$

(5.2)

where, N is the number of frames and $\overline{x}$ is the mean value.

The signal was mean-removed prior to calculating the σ values and thus only the unsteadiness of the jet interface was computed. Figure (5.4) shows the normalized σ of the jet interface location for different nozzle diameter and Froude number plotted against the downstream position x/L_Q.

The result shows that the unsteadiness is function of the jet Froude number and the nozzle diameter. All jets diameters have unsteadiness near the nozzle exit for all injector diameters. At approximately $x/L_Q \approx 8:10$ for all jet diameters and Froude numbers the jet interfacial unsteadiness undergo a switch in their trend (Christopher, 2009 obtained a similar result at $x/L_Q \approx 10:11$ for vertical gas jets). Prior to this location the higher Froude number jets (for example $Fr_0= 99$, $d_N=5$ mm) have a higher unsteadiness (less stable) but downstream of this point have a lower unsteadiness, and the opposite happens for the lower Froude number jets (for example $Fr_0= 43$, $d_N= 5mm$). The high unsteadiness near the nozzle exit for high gas jet with higher Froude numbers may be due to compressibility effects between the gas jet and water ambient.

Given the switch in the interfacial behavior for all the Froude numbers at $x/L_Q \approx 8:10$, this position appears to be the jet development length described for single phase jets (Crow and Champagne 1971, Fischer et al. 1979 and Christopher 2009). In the present experiment, we cannot confirm whether this development length is due to internal turbulence levels, compressibility effects, or some other phenomena. The correspondence of the switch in the interfacial behavior after $x/L_Q \approx 8:10$ with the interface unsteadiness suggests that the shear layers emanating from the diameter of the nozzle plays a large role in governing the jet development by directly contributing to the stability of the interface.
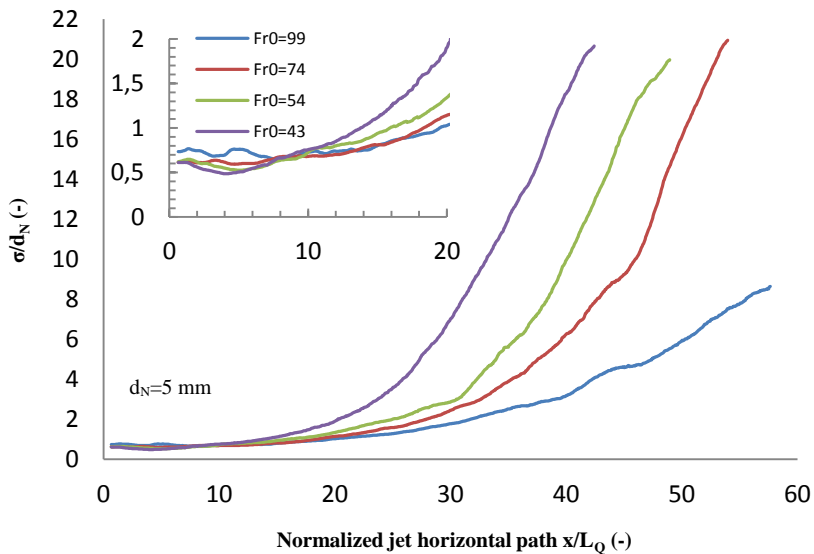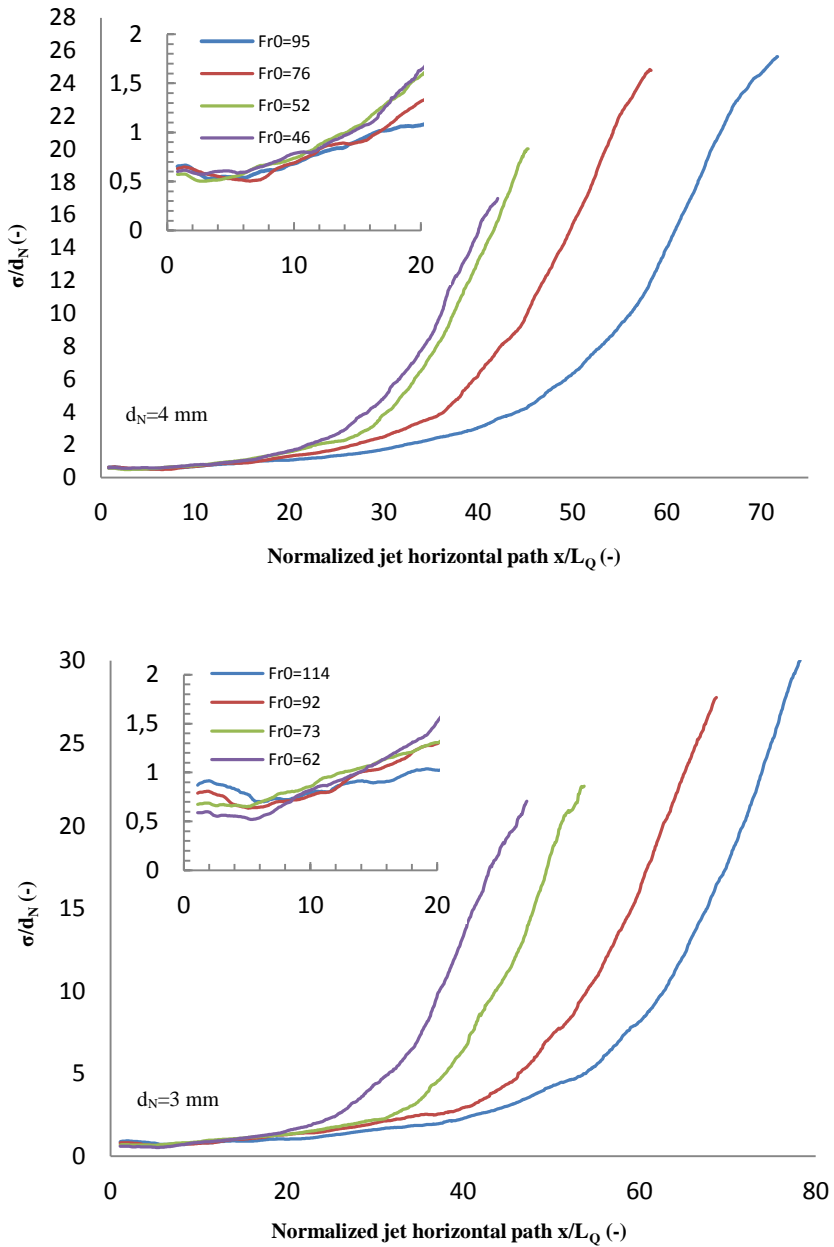
Figure (5.4): Standard deviation for nozzle 5, 4 and 3 mm respectively. In general, the interface unsteadiness increases downstream and decreases for higher Froude numbers.

Increase in the interfacial motion oscillations is experimentally correlated to a less stable jet exhibiting a greater number of pinch-off events. Thus it follows that as the σ of the interface values become smaller the jet approaches a perfectly stable interface. Additionally, if the interface unsteadiness can be linked to stability, then the slope of the σ versus downstream position is indicative of the spatial instability growth rate of the jet interface. Fitting the σ curve (the data shown in Figure, 5.4) after the inflection point at approximately $x/L_Q \approx 10$ (to ensure the jet is fully developed) with downstream position for all jet cases, it was found to have an exponential growth given by Equation (5.3) with high coefficient of determination approximately 0.99.

$$\frac{\sigma}{d_N} = C_3 e^{C_4 \left(\frac{x}{L_Q}\right)}$$

(5.3)

Table (5.2) shows the coefficient values of c_3 and c_4 for each jet diameter.

d_N	Fr_0	C_3	C_4
d_5	99	0.213	0.113
	74	0.216	0.084
	54	0.216	0.094
	43	0.336	0.057
d_4	95	0.214	0.105
	76	0.226	0.098
	52	0.261	0.079
	46	0.298	0.062
d_3	114	0.236	0.098
	92	0.27	0.08
	73	0.332	0.062
	62	0.314	0.055
d_2	143	0.241	0.101
	120	0.25	0.092
	92	0.254	0.09

We found that the exponential growth of the σ with the axial distance decreases with increasing Froude number, indicating increasing Froude number yields more stable jets with lower growth rates. This similarity in the growth rate as a function of jet diameter suggests a similar instability mechanism that governs submerged rectangular gas jets that studied by Chen and Richter (1997) and Christopher (2009).

Loth and Faeth (1989) observed a similar phenomenon in the study of underexpanded gas jet. They observed a large-scale of unsteadiness at comparatively low-pressure jets. They remarked that it might involve random fluctuations in gas release producing mushroom-like gas structures near the exit and the sudden appearance of gas below the nozzle exit. However, the mechanism of this phenomenon is currently unclear.

5.3.3 Jet Penetration Length

One of the goals of this work was to explore the relationship between the jet penetration length and the initial conditions that control the jet behaviour at a constant hydrostatic pressure. The length of gas jet penetration into the ambient water is thought to be governed by several parameters, such as the jet diameter, Froude number and the water depth. The buoyant gas jets in liquid ambient have two regions, momentum and buoyant that we have studied each region individually, as mentioned before in Chapter (4). A series of experiments that has been replicated under many different conditions as listed in Table (5.1) on each region to verify the effects of the different initial conditions on the a) gas jet length in the momentum and buoyant dominated regime. The buoyant jet penetration length is naturally pulsating as enter in the ambient fluid and its length varies in time, therefore the jet penetration length must be also described statistically.

5.3.3.1 Gas Jet Momentum Length

Two methods were used in the present study to analyze the processed images and get the jet penetration length as mentioned before in Chapter (4). Figure (5.5) shows a comparison between the results obtained from the summation and the statistical methods for the jet momentum length (L_m) calculations. The jet momentum length is non-dimensionalised by the injector diameter (d_N).

As mentioned before in Section (4.4) that, in the statistical method the jet perimeters (edge) for each photograph is firstly located then we calculate its jet length and finally we sum all and the resulting value are averaged statistically by the total number of frames:

$$\overline{L}_m = \frac{1}{n} . \sum_{i=1}^{n} L_{mi}$$ (5.4)

Figure (5.5) shows a comparison between the summation and statistical method for different Froude numbers and jet diameters.
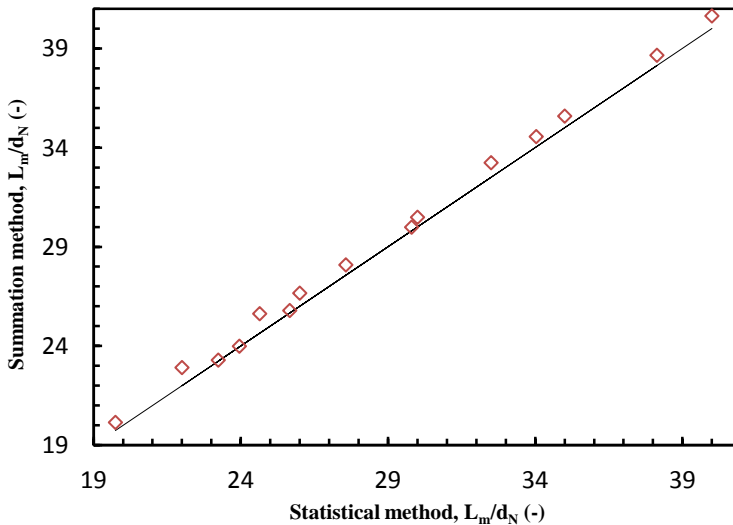
Figure (5.5): Comparison between the summation and statistical method

The results obtained by the two methods they seem to be in good agreement with almost identical results. However, the difference between the results obtained by these two methods was found not to exceed 5%, in fact between 2% and 5%.

Figure (5.6) shows an example of the histogram obtained for $Fr_0 = 95$, $d_N = 4$ mm and $Fr_0 = 99$, $d_N = 5$ mm. The horizontal axis of the graph represents the values of the jet penetration lengths, while the vertical axis represents the variation of the jet lengths. We found from the statistical calculations that the distribution of the axial jet penetration lengths with the time display nearly a Gaussian distribution.

Fr$_0$= 95, d$_N$=4 mm   Fr$_0$= 99, d$_N$=5 mm
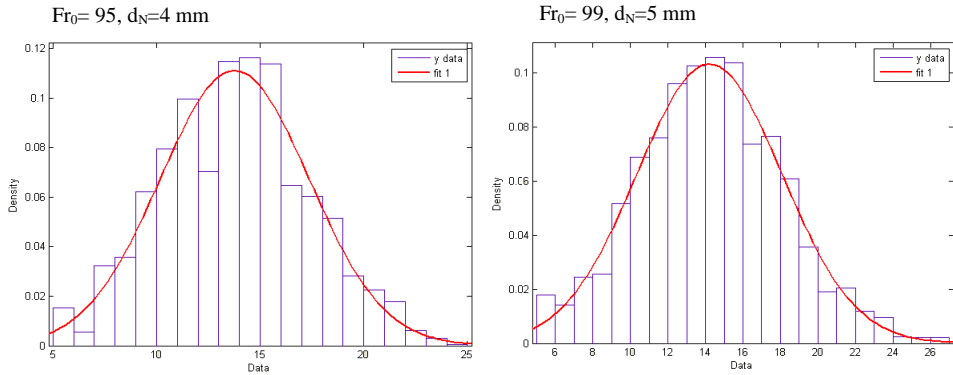
Figure (5.6): Variation (histogram) of the jet penetration length along the jet axis represented by a Gaussian distribution

Table (5.3) shows the statistical descriptors of the probability distribution for the values of the jet length along the jet axis.

Where, Kurtosis is describing the shape of the probability distribution and it is a measure of how outlier-prone the distribution is. The kurtosis of the distribution is defined as:

$$ku = \frac{E(x-\mu)^4}{\sigma^4}$$
(5.5)

Skewness measures the asymmetry of the data around the sample mean and can be positive or negative as illustrated in Table (5.3). If skewness is negative, the data are spread out more to the left of the mean than to the right. If skewness is positive, the data are spread out more to the right. The skewness of the normal distribution is zero. The skewness of the distribution is defined as:

$$Sk = \frac{E(x-\mu)^3}{\sigma^3}$$
(5.6)

where, μ is the first moment of x, σ is the standard deviation of x, and $E(t)$ represents the expected value of the quantity t.

d_N	Run	Fr_0	Mean, (cm)	Kurtosis (Ku)	Skewness (SK)
d_2	1	143	8.13	1.53	0.15
	2	120	7.12	2.1	-0.65
	3	92	6.1	2.31	0.16
d_3	4	114	11.6	2.44	0.1
	5	92	10.37	2.35	0.74
	6	73	8.43	2.53	0.12
	7	62	6.99	2.97	0.05
d_4	8	95	13.3	2.73	0.09
	9	76	10.67	2.58	0.15
	10	52	9.6	2.15	-0.2
	11	46	9.17	2.91	0.12
d_5	12	99	14.37	2.92	0.106
	13	74	12.9	3.12	-0.2
	14	54	12.82	3.51	0.25
	15	43	10.08	3.52	0.1

Figure (5.7) shows the results of the momentum penetration length in meter as a function of the jet mass flow rates and nozzle diameters as a parameter. It is found that the jet length for all jet diameters increases when increasing jet mass flow rates in a power relationship given by Equation (5.7), for which a coefficient of determination of $R^2 = 0.90$ was obtained.

$$L_m = C_5 \dot{m}^{C_6}$$

(5.7)

where, L_m (m) is the momentum jet length, $C_5 = 0.56$ m(s/kg)^{C_6} and $C_6 = 0.35$ are constants depending on the jet initial conditions and $\dot{m}$ (kg/s) is the jet mass flow rate at the nozzle exit. Christopher (2009) also obtained a power law relationship between the jet length and the jet mass flow rate when he studied rectangular gas jets with aspect ratio of 2, 10 and 20 with different coefficient of $C_5 = 1.95$ m and $C_6 = 0.74$.
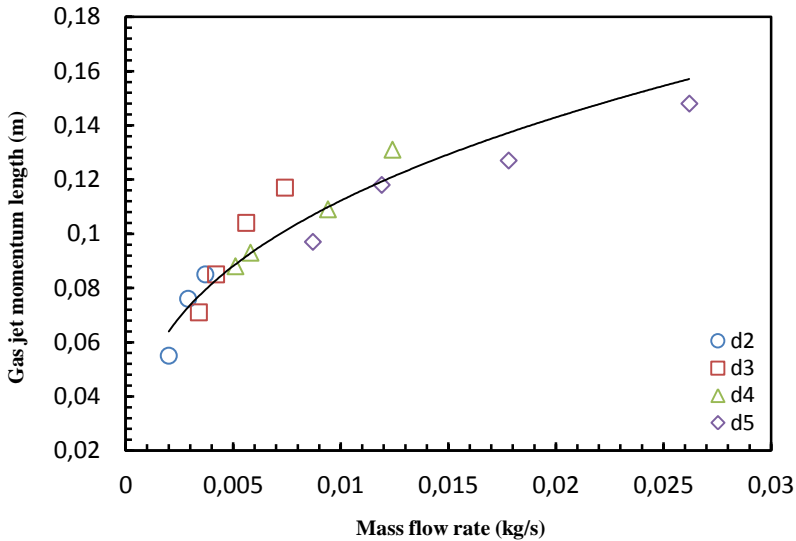
Figure (5.7): The jet momentum length increases with the mass flow rate

The jet is flow produced by a continuous source of momentum ($M_0 = u_0 \times \dot{m}_0$). Since velocity is momentum per unit mass, any means of producing velocity in a fluid is a momentum source. Figure (5.8) shows the relationship between the jet momentum flow rate (N) and the penetration length (m) and the nozzle diameters as parameter.

Increasing the jet momentum flow rate leads to an increase in the jet penetration length in a logarithmic relationship, for which a coefficient of determination of R^2=0.97 was obtained. Equation (5.8) expresses this relationship:

$$L_m = C_7 \ln(M_0) + C_8$$

(5.8)

where, M_0 (N) is the jet momentum flow rate at the injector exit and C_7 and C_8 are constants 0.031 (m) and 0.08 (m) respectively.
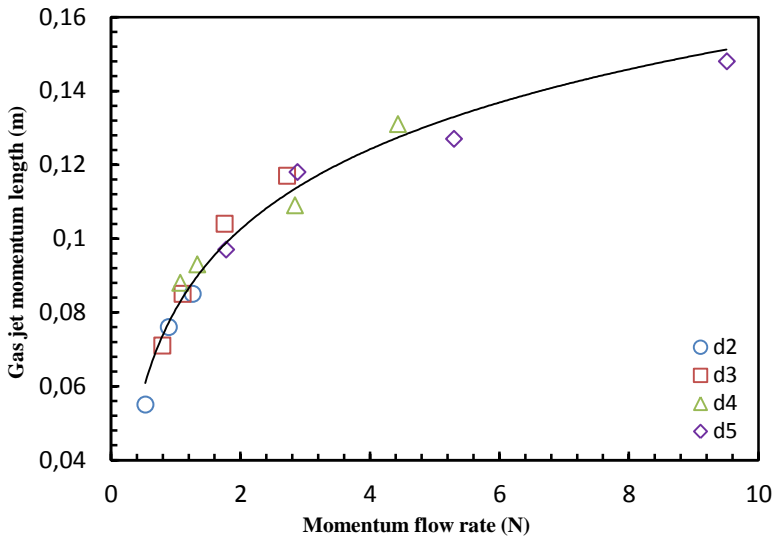
Figure (5.8): The gas jet momentum length increases with momentum flow rate

Densimetric Froude number is the ratio of inertial to buoyancy forces ($Fr_0 = u_0 / \sqrt{g_0' d_N}$) and can be use as a "measure" of how buoyant a jet is. The strength of the jet is directly related to the value of its Froude number. As the value of the Froude number becomes greater then, the flow is strongly determined by the jet initial momentum. The jet turns rapidly into a plume when Fr_0 is small. Figure (5.9) shows the normalized jet penetration length (L_m/L_Q) as a function of Fr_0 and the nozzle diameters as parameters. The curve collapses reasonably well with a nearly power relation.

A power fitting of the data yields the following relationship, for which a coefficient of determination of $R^2 = 0.91$ was obtained:

$$ L_m / L_Q = C_9 Fr_0^{C_{10}} $$

(5.9)

where, the coefficients C_9 and C_{10} takes the value of 2.29 and 0.61 respectively. This equation is valid for the experimental conditions that are listed in table (5.1). With the above equation, the non-dimensionalized horizontal penetration length of the turbulent gas jet can be calculated using its non-dimensionalized initial Froude number Fr_0.
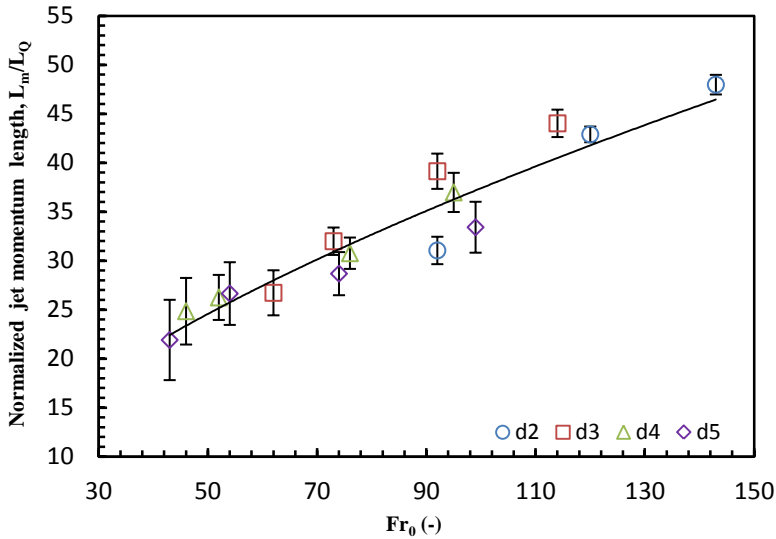
Figure (5.9): Normalized gas jet lengths increases with increasing Froude number

5.3.3.2 Gas Jet Buoyant Length

The buoyancy force, acting on a jet fluid element and directed upwards, is equal to the weight of the ambient fluid displaced by this element. It is the net force resulting from the difference between the upward pressure force and the downward pressure force due to the ambient fluid weighting over the element of the jet fluid that we have considered. The buoyancy force per unit volume of jet fluid is given by:

$$\beta = (\rho_a - \rho_g)g \qquad\qquad (5.10)$$

At some distance downstream from the injection source depending on the initial momentum, the gas jet can no longer support the local hydrostatic pressure and the gas jet will start to rise more dramatically depending on the relative densities of the two fluids according to Equation (5.10). At this downstream location, the flow is driven by buoyancy as opposed to momentum and the flow is controlled by the buoyancy force. In this region, we calculate the buoyant jet penetration

length as illustrated in Chapter (4). Figure (5.10) shows the measured buoyant jet length in physical units as a function of the jet mass flow rate.
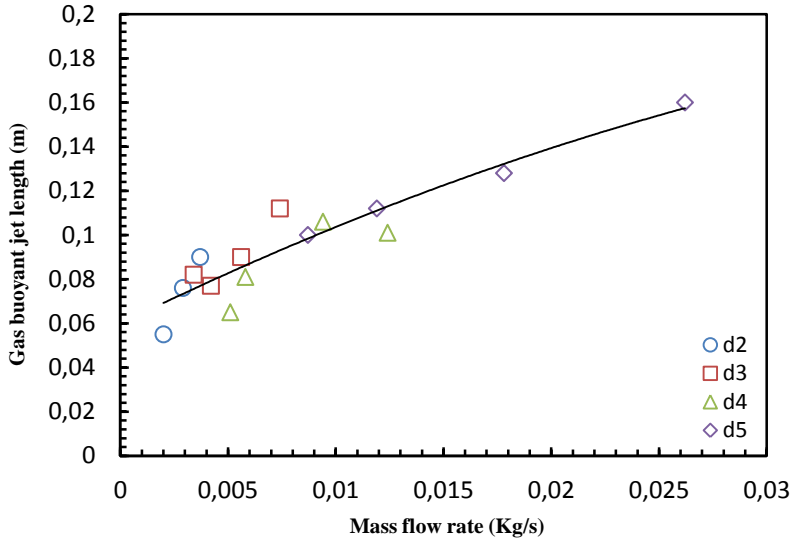
Figure (5.10): The jet buoyant length increases with jet mass flow rate

The jet penetration length for all jet diameters increases with the jet mass flow rate, and follow a nearly linear relationship with a coefficient of determination of 0.89 given by Equation (5.12).

$$L_b = C_{11}\dot{m}^2 + C_{12}\dot{m} + C_{13}$$

(5.11)

where, L_b (m) is the buoyant gas jet length and C_{11}=-40.52 (ms/kg)^2, C_{12}=4.79 (ms/kg) and C_{13}= 0.06 (m) are constants.

Figure (5.11) shows the relationship between the buoyant gas jet length (L_b) and the momentum flow rate and the nozzle diameter as parameter. A logarithmic relationship was obtained for which a coefficient of determination of 0.93 was obtained.
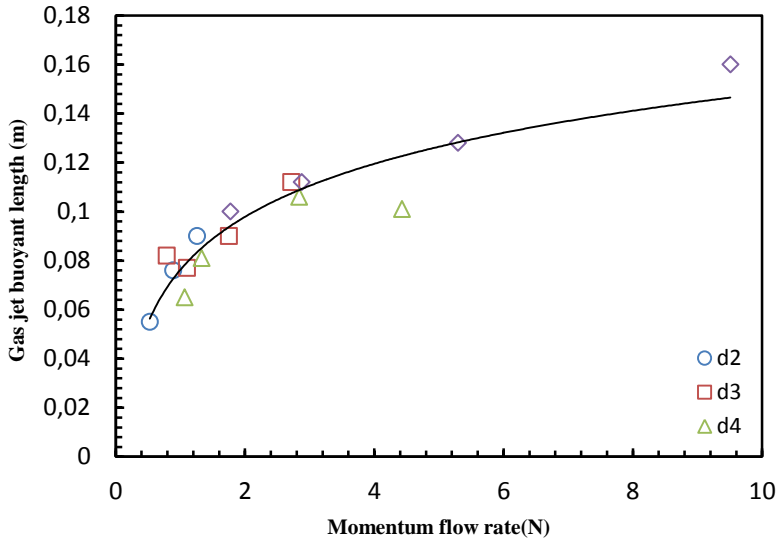
Figure (5.11): The jet buoyant length increases with the injector diameter and the momentum flow rate

$$L_b = C_{14} \ln(M) + C_{15} \qquad (5.12)$$

where, C_{14}= 0.031 (m) and C_{15}= 0.076 (m) are constants.

Figure (5.12) shows the buoyant penetration length scaled by the square root of the nozzle area (L_b/L_Q) as a function of Fr_0 and the jet diameters as parameter.

The results show that the normalized buoyant jet length increases in a nearly polynomial relationship given by Equation (5.13) with the Froude number with a coefficient of determination of 0.97 is obtained:

$$L_b / L_Q = C_{16} Fr_0^2 + C_{17} Fr_0 + C_{18} \qquad (5.13)$$

where, L_b/L_Q is the normalized buoyant jet length and C_{16}=0.0007 (m), C_{17}=0.14 (m), C_{18}=9.3 are constants.
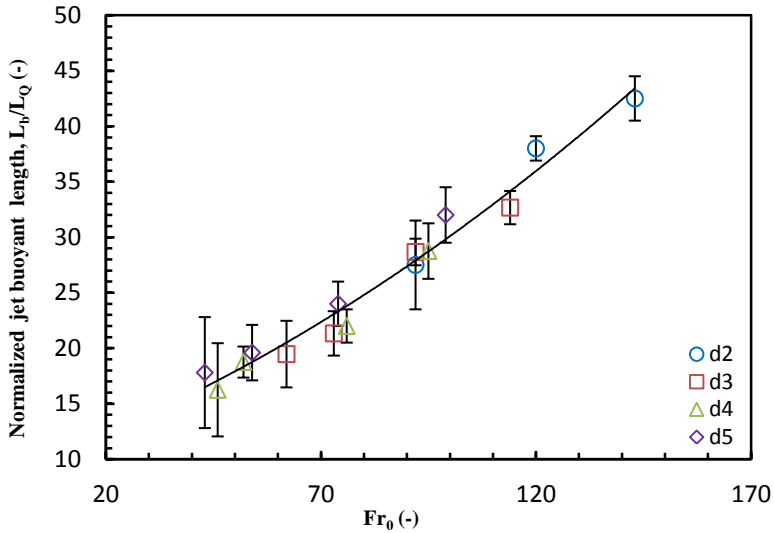
Figure (5.12): Non-dimensional buoyant jet length

5.3.4 Gas Jet Expansion Angle

In a general jet, there is a potential core where the velocity along the centerline of the jet is uniform at the jet exit. Downstream from this potential core, i.e., in the developed region, fully developed turbulent diffusion enhances mixing of the jet. The expansion angle of the jet becomes larger in the developed region than that in the potential core due to this mixing (Satoshi, 2011).

To study the effect of the different parameters on the jet expansion angle (θ), we used the recorded images focusing on the region near the nozzle exit (momentum region) and on the angle below the jet centerline axis as mentioned in Chapter (4). Wide expansion angles were observed in the first region of momentum, while downstream the jet expanded with a smaller angle. Figure (5.13) shows the relationship between the obtained expansion angle and the jet Froude number.
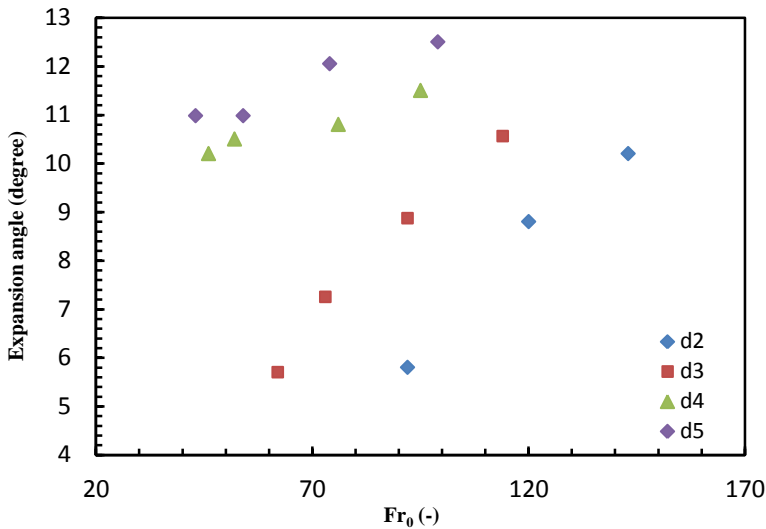
Figure (5.13): Expansion angle of the gas jet plotted as a function of the Froude number

The effect of the Froude number on the jet-spreading rate is less clear. It is interesting to note in Figure (5.13) the effect of Froude number on the expansion angles for the different nozzle diameters. The $d_N=4$ and $d_N=5$ mm nozzle expansion angles show a slowly increasing with the Froude number. This is in contrast to the $d_N= 2$ and $d_N= 3$ mm nozzles, which show a strongly increasing spreading rate as the Froude number is increased. Froude number plays a secondary role as seen in Figure (5.13) is apparently a triggering mechanism which can take a nominally stable jet, such as seen in $d_N=4$ mm nozzle with a jet spreading rate similar to the $d_N=5$ mm nozzle. In other words, may be that $d_N=4$ and $d_N=5$ jets have the same mechanism of entrainment, and on the other hand jets with $d_N=2$ and $d_N=3$ mm have the same mechanism that it is different from the previous one.

Based on these results, it is hypothesized that the interfaces generated by the round gas jets are primarily influenced by instabilities whose relative strength is dependent on the jet diameter as shown in section (5.3.2). Stability may be directly linked to entrainment, as interfacial wave production and subsequent collapse leads to entrainment of ambient fluid into the jet, and therefore exerts a strong influence on the jet-spreading rate (Christopher, 2009). This perturbation could come in the form of compressibility effects, such as shock-cell structures

(Loth and Faeth 1990) or screech feedback mechanisms (Zaman, 1999 and Zaman, et al. 2002).

An attempt was made to find the effect of the jet momentum flow rate on the jet expansion angle for different jet diameters. Figure (5.14) shows the jet expansion angle as a function of the jet momentum flow rate and the nozzle diameter as parameter.
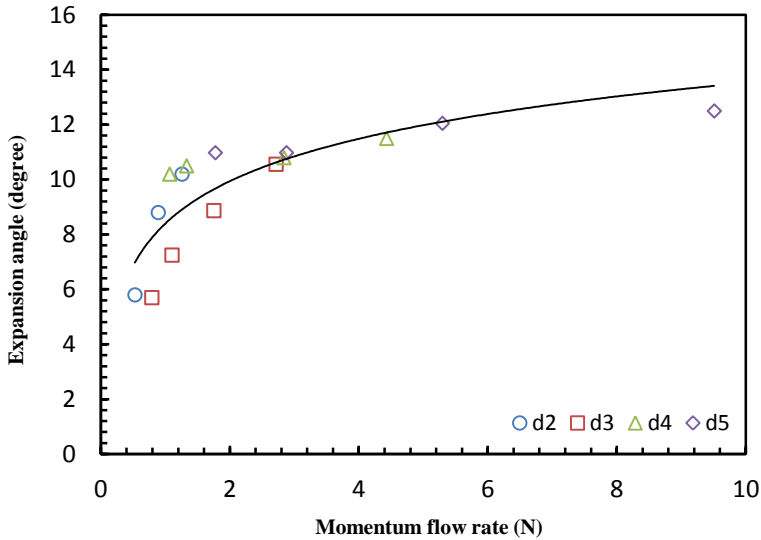
Figure (5.14): Expansion angle of gas jet plotted as a function of momentum flux

The experimental results showed that the expansion angle (θ) increases with the jet momentum flow rate in a nearly logarithmic relationship given by Equation (5.14), for which a coefficient of determination of 0.70 was obtained:

$$\theta = C_{19} \ln(M) + C_{20} \tag{5.14}$$

where, C_{19} and C_{20} are constants and has values of 2.227 (degree) and 8.3953 (degree) respectively and θ is the jet expansion angle in degrees.

5.3.5 Gas Jet Half Width

The jet spreading rate that is indicative of mixing and entrainment at the jet interface was found to be a function of the Froude number and the nozzle diameter. Due to its momentum, the jet entrains ambient fluid from outside the jet boundary into the main turbulent stream thus increasing the volume flux of the jet. The mixing results in a change of both the jet velocity and the jet width. In general, increasing the injector diameter increases the spreading rate. The jet spreads linearly as it entrains the ambient fluid Lee and Chu (2003). The radius of the jet (b) is expected to depend on the initial momentum flow rate of the jet (M_0), the jet density (ρ_g) and the distance from the source (x); i.e.,

$$b/x = f(M_0, \rho_g, x)$$

(5.15)

The only dimensionless parameter in this functional relation is b/x, which must be a constant. According to this dimensional consideration, the width of the jet increases linearly with distance from the source (Lee, 2003). The volume flux increases and the energy flux decreases with the distance (x) from the source. Figure (5.15) shows the normalized jet half width (b/d_N) of nozzle diameter $d_N=$ 3mm along the horizontal axis (x/d_N) which is reported for several Froude numbers.
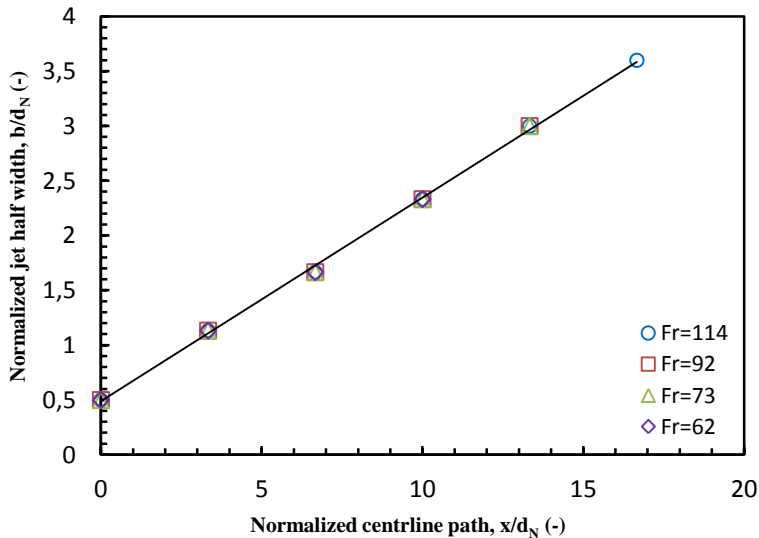
Figure (5.15): Normalized jet half width increases linearly with the horizontal direction. This holds for nozzle diameter 3 mm

The result indicates that the dimensionless jet half-width (b/d_N) increases linearly with the dimensionless axial distance (x/d_N) from the nozzle exit at different Froude numbers. The dimensionless half-width is mainly influenced by the axial distance and the Froude number. A linear relationship is obtained for which a coefficient of determination of 0.99 was obtained:

$$b/d_N = C_{21}(x/d_N) + C_{22}$$

(5.16)

where, $C_{21} = 0.19$ and $C_{22} = 0.49$ are constants.

Figure (5.16) shows the normalized jet half width (b/d_N) at nozzle diameter $d_N=4$ mm, that is reported for several Froude numbers. The width of the jet increases in the axial direction in a linear relationship for all Froude numbers and a coefficient of determination of 0.98 was obtained.
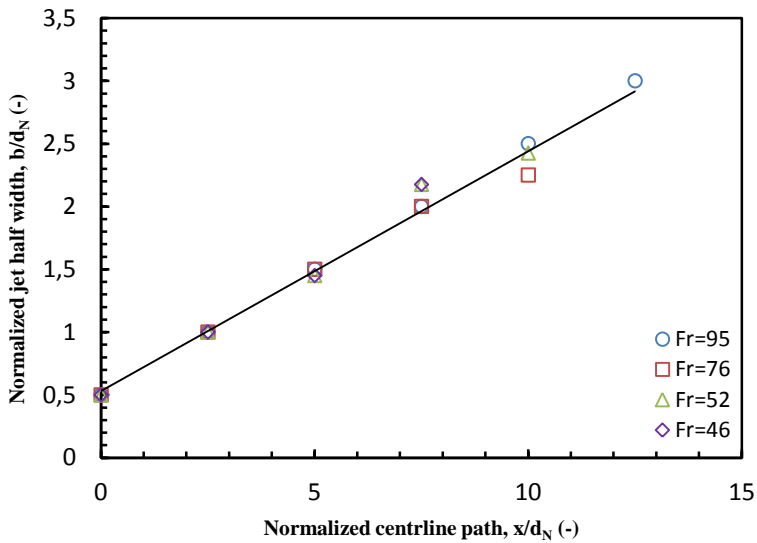
Figure (5.16): Normalized jet half width increases linearly with the horizontal direction. This holds for nozzle diameter 4 mm

The parameter fitting yields the following expression;

$$b/d_N = C_{23}(x/d_N) + C_{24}$$

(5.17)

where, C_{23}= 0.19 and C_{24}= 0.53 are constants.

Figure (5.17) illustrates the normalized jet half width (b/d_N) at nozzle diameter d_N=5 mm for each Froude number. The results showed that the jet half width increased linearly with the axial distance with a coefficient of determination of 0.996 was obtained.
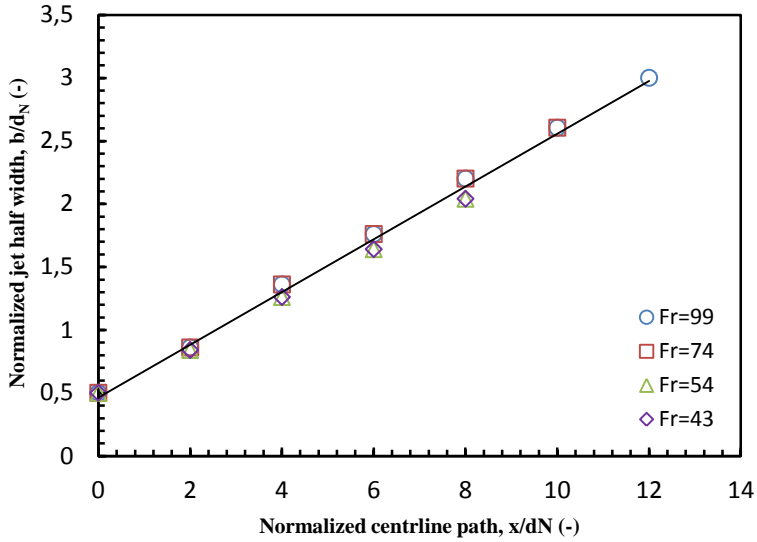
Figure (5.17): Normalized jet half width increases linearly with the horizontal direction. This holds for nozzle diameter 5 mm

The coefficients were obtained by linear regression, and yields;

$$b/d_N = C_{25}(x/d_N) + C_{26}$$

(5.18)

where, C_{25}=0.21 and C_{26}=0.47 are constants. Also, the same result was obtained for d_N=2 mm.

Chapter 6

Description of the Numerical Model

6.1 Introduction

The problem of low-density gas jet that injected into a higher density ambient is very important in the environment and industrial applications. In this chapter, a Mathematical Model and analysis of a gas jet injected horizontally into a quiescent liquid ambient is developed. The Numerical Model assist in the design and monitor the performance of the experimental work, also provided the opportunity to independently confirm parameters currently used to model buoyant discharges, as well as the ability to isolate issues that required more investigations. The present model is referred to as the Integral Model and is based on the integral approach, similar to (Xiao 2009, Houf and Schefer 2008, and Jirka 2004).

In the this section, the integral model is first derived based on the conservation equations for total mass and momentum fluxes and transformed to a set of ordinary differential equations using some similarity transformations. The newly introduced unknown variables in the model are highlighted. Finally, the set of equations for the integral model are summarized with the variables properly modeled based on the experimental results.

In the following section, the validation of this developed Integral Model is established with the available experimental results is carried out to confirm the accuracy of this model. The results of this validation and comparison can be found in Chapter (7).

6.2 Problem and Model Description

In this study, the horizontal buoyant air jet formed from a round orifice is discharged into stagnant uniform water ambient. Variables s and r are the natural (curvilinear) coordinates, which the axis of the jet is taken as a parametrical coordinate s, which measures the distance along the jet axis from the origin, and r is the coordinate perpendicular to the jet axis s, and θ is the angle of s-axis with the horizontal direction. The initial density, velocity, and diameter of the orifice are denoted by ρ_g, u_0, and d_N respectively. The density of the water ambient is ρ_a. In addition, u and ϑ denote the velocity components of the curvilinear natural coordinates and u_s is the centerline velocity along the s-axis. A coordinate system is defined so that the jet fluid flows initially in the same direction as the x-axis and then vertically due to the buoyancy force in the same direction as the y-axis as shown in Figure (6.1).
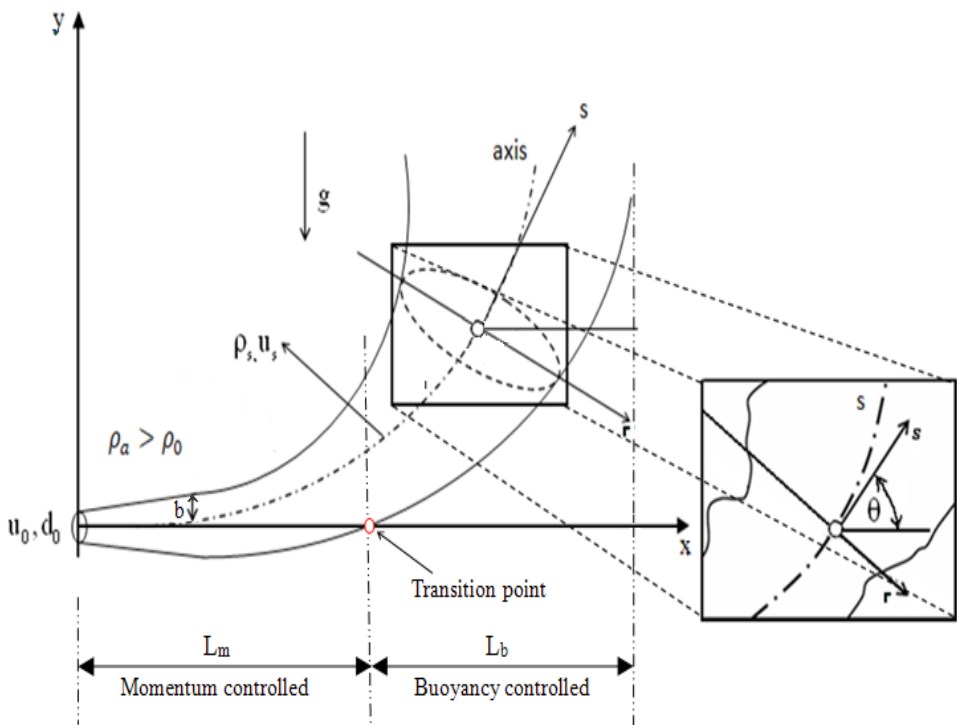
Figure (6.1): Definition sketch and details of the proposed mathematical model and coordinate system of a horizontal buoyant gas jet discharges from round orifice into the stagnant ambient

Within the path, the trajectory of the horizontal buoyant jet in stagnant ambient is no longer a straight line. The jet flow goes firstly through a region where its behaviour is jet-like and reaches a maximum horizontal penetration (L_m) where the flow dominated by the initial jet momentum flux that drives the flow in the horizontal direction (x). Then the flow starts to rise more dramatically and turns vertically rapidly depending on the relative density of the two fluids and the behaviour become plume-like (L_b) dominated by the buoyancy-generated momentum flux that drives the flow in the vertical direction. The two flow regions are connected by a relatively short transition region.

The variation of the spreading rate of the jet along the jet trajectory (s, axis) is a result of the internal structure of the jet in the limiting cases when the buoyancy is insignificant with the momentum domination and when the buoyancy becomes a major driving force. This variation in the spreading rate and therefore the entrainment rate is not a function of the jet trajectory or the local angle of inclination of the plume but is uniquely determined by local conditions.

Air injected in water ambient is an example of injecting a low-density gas jet into high-density ambient. This kind of buoyant jets 'plumes' is classed as non-Boussinesq flow; since the initial fractional density difference $\Delta\rho_0/\rho_a = (\rho_a - \rho_g) / \rho_g$) is high.

6.3 Underlying Model Assumptions

The general assumptions related to the analysis of the overall behavior of a buoyant jet-plume discharged through a submerged horizontally orifice into stagnant ambient fluid problems are listed as follows:

i. The profiles of velocity are similar at all cross sections normal to the jet trajectory.

ii. The pressure across the flow is assumed uniform and equal to the ambient pressure outside of the boundary.

iii. Longitudinal turbulent transport is small compared with latitudinal convective transport.

6.3.1 Velocity Profile

To simplify the problem the usual approach is to integrate the set of conservation equations of mass and momentum across the jet assuming a time averaged mean velocity profile normal to the jet axis. The most common profile used by investigators is Gaussian distribution, with no dependence on φ coordinate, which is suggested from various experiments (e g. Rouse et al. 1952, Chen and Rodi 1980, Rodi 1982, List 1982, Turner 1986, Bhat and Narasimha 1996, and Agrawal and Prasad 2003). The velocity profile is assumed to have the form:

$$u_g(s,r) = u_s(s) \exp(-(\frac{r}{b(s)})^2) \tag{6.1}$$

where, $u_g(s,r)$ is the initial jet mean velocity, $u_s(s)$ is the jet centerline velocity, and $b = b(s)$ is a characteristic jet half width (effective radius of the plume), that change along the jet trajectory.

6.3.2 Entrainment of Ambient Fluid (Local Rate of Entrainment)

One of the major difficulties in the turbulent two-phase jet plume analyses is in quantifying the rate of growth of the jet plume, which comes as a direct consequence of assumptions about the entrainment rate of ambient fluid into the jet. According to Turner (1986), the buoyant bubbles induce a turbulent flow, which in turn causes eddies from the plume to entrain ambient liquid which gets mixed into the plume. The entrainment hypothesis, introduced by Morton (1965) states that the mean entrainment velocity across a shear flow boundary, perpendicular to the direction of flow, is proportional to the characteristic velocity of the flow. The entrainment E is needed for closure the gas and liquid phases, and is not constant but varies as the relative buoyancy or local Froude number changes. Figure (6.2) shows a definition sketch for liquid entrainment to the gas jet.
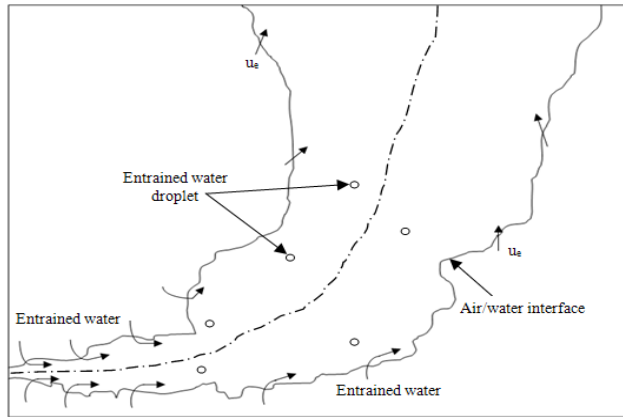
Figure (6.2): Definition sketch for liquid entrainment

According to the entrainment hypothesis, the rate of entrainment (E) around the circumference of the jet control volume is proportional to the velocity of the entrainment at the edge and the contact area $2\pi bds$. The amount of ambient fluid entrained per unit time can be given by:

$$dE = 2\Pi bu_e \rho_a ds \tag{6.2}$$

where, u_e denotes the entrainment liquid velocity at the jet-plume edge which is known as the inflow velocity from the liquid phase to the jet. The entrainment rate indicates that the surrounding water droplets are entrained by the gas jet. The form of entrainment dependent not only on the characteristic velocity, but also on the square root of the local density ratio of the jet and the ambient fluid. For example, Batchelor (1954) concluded that a vigorous entrainment of the ambient will be gotten as the density ratio tends to unity, $\rho_g/\rho_a \rightarrow 1$, while as the density ratio tends to zero, $\rho_g/\rho_a \rightarrow 0$, the entrainment falls to zero and as the density ratio varies between the two limits there will be a smooth transition. Ricou and Spalding (1961) based on their empirical measurements for an arbitrary density ratio, in order to determine the amount of water droplets entrained by the gas jet, suggested that the entrainment velocity can be calculated as follow:

$$u_e = \alpha \sqrt{\frac{\rho_g}{\rho_a}} u_s, \qquad (\rho_g / \rho_a \to 1) = \alpha u_s, \ \ (\rho_g / \rho_a \to 0) = 0 \qquad (6.3)$$

where, α is the local coefficient of entrainment.

Morton (1965) provides additional justification for this form of the entrainment on dimensional grounds assuming that the rate of entrainment into a strongly-buoyant plume is a function of ρ_g/ρ_a and the local Reynolds stresses which have local magnitude proportional to $\rho_g u_s^2$, it seems reasonable to assume a local entrainment velocity of $\alpha(\rho_g/\rho_a)^{1/2}u_s$. A similar assumption has been also made by different researchers (e g., Houf and Schefer 2008, El-Amin et. al 2010, El-Amin 2009, El-Amin and Kanayama 2009, and Steward 1970). Therefore, Equation (6.2) can be rewritten in the form:

$$dE = 2\Pi b \rho_a \alpha \left(\rho_g / \rho_a \right)^{1/2} u_s ds \qquad (6.4)$$

In contrast, for the Boussinesq case ((ρ_a - ρ_g) is sufficiently small to be neglected), the entrainment coefficient $\alpha = u_e/u_s$ is usually assumed constant for all heights (e.g. Turner, 1986). Although more complex so called 'modified' entrainment functions in which α varies according to the local fluxes in the plume have been proposed (e.g. Ricou and Spalding 1961, and Kotsovinos and List 1977). Hunt and Kaye (2005) showed that some reduced entrainment Boussinesq flows can be modeled using a constant α formulation. There is evidence to suggest that entrainment into a non-Boussinesq plume is not constant (Cetegenet al. 1982) and in the above model, $u_e/u_s = \alpha\sqrt{\rho_g/\rho_a}$ is dependent on the local density ratio between the jet and the ambient which, in turn, depends on the local fluxes $\dot{m}(s)$, $\beta(s)$, and $M(s)$ of mass, buoyancy and momentum respectively.

The expression for variation of the local entrainment coefficient (α) is studied and presented by many researchers before. In the buoyant jets, the initial flow is jet like and the final flow approximates a plume. They have reported from various experiments that the local rate of entrainment increases as the jet leaves the momentum-dominated region and enters a region where the effects of buoyancy become more pronounced. The local coefficient of entrainment is a function of the local Froude number (or local Richardson number) for the case when the jet ejected horizontally, according to Priestley and Ball (1955),

Kotsovinos (1975), List and Fischer (1979), Houf and Schefer (2008), Xiao et al. (2009), and Davidson et. al. (2002) and can be given as:

$$\alpha = \alpha_j + (\alpha_p - \alpha_j)\left(\frac{Fr_p \sin\theta}{Fr_s}\right)^2 \tag{6.5}$$

where, α_j is the pure jet entrainment coefficient, α_p is the pure plume entrainment coefficient and Fr_p is a constant of the plume and is between 3.4 and 3.7 and Fr_s is the local Froude number which is defined as:

$$Fr_s = \frac{u_s}{\sqrt{(\rho_a - \rho_g)/\rho_g gb}} \tag{6.6}$$

where, b is the jet half width along the jet axis, this formula allows the entrainment coefficient to be determined along the jet trajectory when there is either a jet or a plume. The entrainment coefficient varies from α_j to α_p during the transition from jet-like to plume-like. List (1979) and Rodi (1982) summarized much of the work on the entrainment hypothesis and proposed values of $\alpha_j = 0.052 \pm 0.003$ for the pure jets and $\alpha_p = 0.0833 \pm 0.0042$ for the pure plume. The entrainment rate of a plume is greater than that of a jet; the entrainment rate of a buoyant jet is in between the two, and can be expected to be as a function of the Froude number. It can be shown that a buoyant jet will approach the plume asymptotic Froude number as it rises and mixes with the ambient.

6.4 Ordinary Differential Equations

Five parameters are needed to describe the behavior of the buoyant-jet flow at any particular location. To solve the problem in this form, five equations are needed. These five equations are set up as ordinary differential equations with respect to the step-size, s, along the flow trajectory and rewritten in dimensionless form. The system of the ODE are solved by invoking the 4th order Runge-Kutta method, and using an appropriate boundary and initial conditions for the variables of jet width and velocity along the jet path to obtain the horizontal buoyant jet trajectory and the results are compared with experimental data.

6.5 Governing and Deriving Equations of the Model

The jet integral method proceeds by making use of the boundary-layer nature of the flow and by integrating all terms of the governing equations of motion across the cross-sectional plane $\int(\ )dA$ in which $dA = rdrd\varphi$. For the given axisymmetric profiles, the integration amounts to $2\pi \int_0^b (\ )dr$. The 'jet radius' b is understood in boundary-layer parlance as the 'edge of the jet' at which boundary conditions can be clearly specified or, alternatively, beyond which no further contributions to the integration should arise.

6.5.1 Continuity Equation

The fixed injection of gas flow rate $(\dot{m}_g)$ at a given submergence, can be expressed as conservation of mass flux and is given by the following:

$$\dot{m}_g = \int_0^{2\Pi} \int_0^b \rho_g u_g . rdrd\varphi = const \qquad (6.7)$$

The total jet mass flow rate $(\dot{m}_j)$ based upon a large variation of density between the gas jet and liquid ambient can be expressed as:

$$\dot{m}_j = \dot{m}_g + \dot{m}_L \qquad (6.8)$$

where, $\dot{m}_L = E$ is the liquid entrainment mass flow rate from the ambient to the jet flow as droplets. The rate of increase of the jet mass flow rate with stream wise distance given by:

$$\frac{d}{ds}(\dot{m}_j) = \frac{d}{ds}(\dot{m}_g + \dot{m}_L) = \frac{dE}{ds} \qquad (6.9)$$

In the entrainment hypothesis, one assumes that the viscous forces are negligible in comparison to pressure, inertia and interfacial tension forces. Equation (6.9) can be written as:

$$\frac{d}{ds}\int_0^{2\Pi}\int_0^b \rho_g u_g.rdrd\varphi + \frac{d}{ds}2\Pi b\rho_a u_e = \frac{dE}{ds} \qquad (6.10)$$

The left-hand side of equation (6.10) can be integrating after substituting values of u_g and u_e from equation (6.1) and (6.3) respectively:

$$\frac{d}{ds}\int_0^b 2\Pi\rho_g u_s e^{-(r^2/b^2)}rdr + \frac{d}{ds}\left(2\Pi b\rho_a u_s\alpha\sqrt{\frac{\rho_g}{\rho_a}}\right) = \frac{dE}{ds} \qquad (6.11)$$

$$\frac{d}{ds}\left[2\Pi\rho_g u_s\left(\frac{-b^2}{2}\int_0^b\frac{-2}{b^2}re^{-(r^2/b^2)}dr\right)\right] + \frac{d}{ds}\left(2\Pi b\rho_a u_s\alpha\sqrt{\frac{\rho_g}{\rho_a}}\right) = \frac{dE}{ds} \quad (6.12)$$

Let $I_3 = (1-e^{-1})$, the mass flux equation becomes,

$$\frac{d}{ds}\left(\Pi\rho_g u_s b^2 I_3\right) + \frac{d}{ds}\left(2\Pi b\rho_a u_s\alpha\sqrt{\frac{\rho_g}{\rho_a}}\right) = \frac{dE}{ds} \qquad (6.13)$$

The mass flux equation can be rewritten as:

$$\left(2\Pi b\rho_g u_s I_3 + 2\Pi\rho_a u_s\alpha\sqrt{\frac{\rho_g}{\rho_a}}\right)\frac{db}{ds} + \left(\Pi b^2\rho_g I_3 + 2\Pi b\rho_a\alpha\sqrt{\frac{\rho_g}{\rho_a}}\right)\frac{du_s}{ds} = \frac{dE}{ds}$$

$$(6.14)$$

6.5.2 Momentum Conservation Equations

6.5.2.1 The x-momentum flux (Horizontal)

Since the pressure is assumed to be hydrostatic and there is the shear force acting in the horizontal direction opposed to the main flow momentum. The x-momentum conservation equation can be given by:

$$M_x = \int_0^{2\Pi} \int_0^b \rho_g u_g (u_g \cos\theta) r dr d\varphi \tag{6.15}$$

After substituting in the value of u_g and make the integration, equation (6.15) become,

$$M_x = 2\Pi \left[\int_0^b \rho_g u_s e^{-(r^2/b^2)} (u_s e^{-(r^2/b^2)} \cos\theta) r dr \right] \tag{6.16}$$

$$M_x = 2\Pi \rho_g u_s^2 \cos\theta \int_0^b e^{-2(r^2/b^2)} r dr \tag{6.17}$$

$$M_x = 2\Pi \rho_g u_s^2 \cos\theta \frac{-b^2}{4} \left[e^{-2(r^2/b^2)} \right]_0^b \tag{6.18}$$

Let $A = \frac{1}{2}(1 - e^{-2})$, the momentum flux equation becomes,

$$M_x = \Pi A b^2 \rho_g u_s^2 \cos\theta \tag{6.19}$$

At sufficiently high jet velocities, a part of the liquid driven by the jet begins to move and flow in the jet direction whereas the rest of the liquid still stagnant. Therefore, a shear layer of thickness (δ) at the gas/liquid boundary appears. The interfacial shear stress (τ_i) acting at the interface between the jet flow and the liquid ambient is illustrated by the schematic diagram of Figure (6.3). The interfacial shear stress tends to increase with increasing the superficial gas velocity.
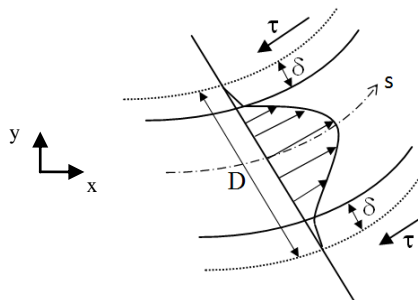
Figure (6.3): Schematic diagram shows that the interfacial shear stress acting at the interface between the gas jet and liquid ambient

The interfacial shear stress depends on the interfacial friction factor (f_i), jet density and the squared of the relative velocity at the interface between the jet and the ambient. The following correlations were proposed by Wallis (1970) to determine the interfacial shear stress:

$$\tau_i = f_i \frac{1}{2} \rho_g (\bar{u}_{gi} - \bar{u}_{li})^2 \tag{6.20}$$

$$\bar{u}_{gi} - \bar{u}_{li} \simeq \bar{u}_{gi} \tag{6.21}$$

where, $\bar{u}_{gi}$ and $\bar{u}_{li}$ are the mean gas and liquid velocity respectively at the jet interface, $\bar{u}_{li}$ is sufficiently small to be neglected as a comparison to $\bar{u}_{gi}$. The mean gas velocity at the jet interface can be calculated as:

$$\bar{u}_m = \frac{1}{\Pi b^2} \int_0^b u_g 2\Pi r dr = \frac{1}{\Pi b^2} \int_0^b u_s e^{-(r^2/b^2)} 2\Pi r dr = u_s I_3 \tag{6.22}$$

$$\bar{u}_{gi} = \bar{u}_m f_1 \tag{6.23}$$

where, $\bar{u}_m$ is the mean jet velocity at the jet cross section and f_1 is a coefficient between the jet mean velocity and jet velocity at the interface it is assumed as 0.8. The interfacial friction factor (f_i) is crucial in the determination of the interfacial shear stress, which strongly influences the loss of momentum of the jet. The interfacial friction factor can be given by:

$$f_i = c_1 R_{em}^{-c_2} (1 + 360 \frac{\delta}{D}) \tag{6.24}$$

where, $c_1 = 0.079$ and $c_2 = 0.25$ are constants, and R_{em} is the superficial jet Reynolds number at the jet interface, is defined as:

$$R_{em} = \frac{\rho_g \overline{u}_{gi} D}{\mu_g} = \frac{\rho_g \overline{u}_{gi} 2b}{\mu_g} = \frac{2 f_1 \rho_g \overline{u}_s I_3 b}{\mu_g}$$

(6.25)

where, μ_g is the gas dynamic viscosity ($\mu_g = 1.983 \times 10\text{-}5$ kg/m.s), D is the hydraulic diameter of the jet flow (D = 4A/p= 2b), and δ is the liquid perturbation thickness and it is assumed as:

$$\delta = f_2 D (1 - f_3 R_{em}^{f_4})$$

(6.26)

where, $f_3 = 2.5 \times 10^{-3}$ and $f_4 = 0.5$ are constants. And f_2 is variable has two values depending on the jet region, which has a value 1 in the momentum region (from the nozzle exit to the transition point) and 0.04 for the buoyant region (starting from the transition point to a maximum point in which the jet can be arrive) as shown in Figure (6.1).

Substituting Equations (6.24) into Equation (6.20) and multiplying by the jet contact area per unit length (2πb), the total interfacial shear force per unit length can given by:

$$\tau_{it} = c_1 \Pi b \rho_g (u_s I_3 f_1)^2 (1 + 360 * \frac{\delta}{D}) \left[R_{em} \right]^{-a}$$

(6.27)

The interfacial shear force per unit length in the x and y direction is given by:

$$\tau_{itx} = \tau_{it} \times \cos \theta$$

(6.28)

$$\tau_{ity} = \tau_{it} \times \sin \theta$$

(6.29)

Some flying water droplets entrain into the jet with a velocity less than the velocity of jet. The water droplets have a small value of momentum and in the opposite direction to the jet momentum flow. In the present study, the total momentum of the water droplets was calculated as the mass of water droplets entrained (m_d) in the velocity of entrained water droplets in the gas jet (u_d):

$$M_{dt} = \dot{m}_d \times u_d \tag{6.30}$$

M_{dt} is the total momentum of water droplets per unit length. The mass of water droplets $\dot{m}$d it was observed from the experiments was about 20% of the entrainment mass flow rate per unit length.

$$\dot{m}_d = f_e \dot{m}_e \tag{6.31}$$

and $\dot{m}_e = dE/ds$

Satoshi et. al. (2011) studied experimentally the gas jets injected in water ambient and he measured experimentally the velocity of the water droplets (ud). He concluded that, the water droplet velocity (u_d) was around 1/30~1/60 of the injected velocity of the gas at the nozzle exit (u_0), and increased with increasing the jet pressure and is hundred times as large as the entrainment velocity (u_e):

$$u_d = f_d u_0 \tag{6.32}$$

where, f_d is a constant. Momentum of the water droplets in x and y direction can given by:

$$M_{dx} = M_{dt} \cos\theta \tag{6.33}$$

$$M_{dy} = M_{dt} \sin\theta \tag{6.34}$$

M_{dx} is the entrainment momentum in the x-direction per unit length and M_{dy} is the entrainment momentum in the y-direction per unit length. The change of x- momentum gas flux per unit length can be calculated by:

$$\frac{dM_x}{ds} = -\tau_{itx} - M_{dx} \tag{6.35}$$

Substituting Equations (6.19) into the x-horizontal momentum conservation equation is given by:

$$\frac{d}{ds}\left[\Pi\rho_g u_s^2 b^2 A \cos\theta\right] = -\tau_{itx} - M_{dx}$$

(6.36)

That can be rewritten as:

$$2\Pi\rho_g u_s b^2 A \cos\theta \frac{du}{ds} + 2\Pi\rho_g u_s^2 bA\cos\theta \frac{db}{ds} - \Pi\rho_g u_s^2 b^2 A \sin\theta \frac{d\theta}{ds} = -\tau_{ix} - M_{dx}$$

(6.37)

6.5.2.2 The y- Momentum flux (Vertical Momentum Flux)

In horizontal buoyant jets, the jet axis is deflected upwards because of the increase of vertical momentum flux due to the action of buoyancy force. The buoyancy force acting on the jet vertically, which is equal to the rate of change of y-momentum flux, shear force and momentum of water entrained. The jet y-momentum flux can write as:

$$M_y = \int_0^{2\Pi}\int_0^b \rho_g u_g (u_g \sin\theta) r dr d\varphi$$

(6.38)

$$M_y = 2\Pi u_s^2 \rho_g \sin\theta\left[\int_0^b e^{-2(r^2/b^2)} r dr\right]$$

(6.39)

$$M_y = 2\Pi\rho_g u_s^2 \sin\theta \frac{-b^2}{4}\left[e^{-2(r^2/b^2)}\right]_0^b$$

(6.40)

$$M_y = \Pi\rho_g u_s^2 \sin\theta \frac{b^2}{2}\left(1 - e^{-2}\right)$$

(6.41)

$$M_y = \Pi\rho_g u_s^2 b^2 A \sin\theta$$

(6.42)

The buoyancy force per unit length (β) can be given by:

$$\beta = g\int_0^{2\Pi}\int_0^b (\rho_a - \rho_g) r dr d\varphi = 2\Pi g(\rho_a - \rho_g)\int_0^b r dr$$

(6.43)

$$= 2\Pi g(\rho_a - \rho_g)\frac{b^2}{2} = \Pi g b^2 (\rho_a - \rho_g) \qquad (6.44)$$

The change of y-momentum of the gas flux per unit length cane be calculated by:

$$\frac{dM_y}{ds} = \beta - \tau_{ity} - M_{dy} \qquad (6.45)$$

Substituting equations (6.42) and (6.44) into Equation (6.45), the change of the vertical momentum gas flux per unit length given by:

$$\frac{d}{ds}\left[\Pi\rho_g u_s^2 b^2 A \sin\theta\right] = \Pi g b^2 (\rho_a - \rho_g) - \tau_{ity} - M_{dy} \qquad (6.46)$$

and can be write as:

$$2\Pi\rho_g u_s b^2 A \sin\theta \frac{du}{ds} + 2\Pi\rho_g u_s^2 b A \sin\theta \frac{db}{ds} + \Pi\rho_g u_s^2 b^2 \cos\theta A \frac{d\theta}{ds} = \Pi g b^2 (\rho_a - \rho_g) - \tau_{ity} - M_{dy}$$

$$(6.47)$$

6.5.3 Solution Method

The set of Equations (6.14), (6.37) and (6.47) used to describe the jet-plume parameters along the jet trajectory from the source are solved here. The descriptive variables are; the jet width b(s), the local angle of inclination of the jet (Θ) and the jet centerline velocity (u_s). This system of equations are solved here using the same solution method as that used in the analysis of Hussain and Narang (1984) by the Cramer's rule, the system of equations is solved to give:

$$\frac{d\theta}{ds} = \frac{C_4 M_2 E_3 - C_4 M_3 E_2 - C_2 M_4 E_3 + C_2 M_3 E_4 + C_3 M_4 E_2 - C_3 M_2 E_4}{C_1 M_2 E_3 - C_1 M_3 E_2 - C_2 M_1 E_3 + C_2 M_3 E_1 + C_3 M_1 E_2 - C_3 M_2 E_1} =$$

$$f(u_s, b, \theta, s)$$

$$(6.48)$$

$$\frac{du_s}{ds} = \frac{C_1 M_4 E_3 - C_1 M_3 E_4 - C_4 M_1 E_3 + C_4 M_3 E_1 + C_3 M_1 E_4 - C_3 M_4 E_1}{C_1 M_2 E_3 - C_1 M_3 E_2 - C_2 M_1 E_3 + C_2 M_3 E_1 + C_3 M_1 E_2 - C_3 M_2 E_1} =$$

$$f(u_s, b, \theta, s)$$

$$(6.49)$$

$$\frac{db}{ds} = \frac{C_1 M_2 E_4 - C_1 M_4 E_2 - C_2 M_1 E_4 + C_2 M_4 E_1 + C_4 M_1 E_2 - C_4 M_2 E_1}{C_1 M_2 E_3 - C_1 M_3 E_2 - C_2 M_1 E_3 + C_2 M_3 E_1 + C_3 M_1 E_2 - C_3 M_2 E_1} =$$

$$f(u_s, b, \theta, s)$$

$$(6.50)$$

The system of equations to solve is as follows, where the coefficients are defined accordingly:

$$\begin{bmatrix} C_1 & C_2 & C_3 \\ M_1 & M_2 & M_3 \\ E_1 & E_2 & E_3 \end{bmatrix} \begin{bmatrix} \dfrac{d\theta}{ds} \\ \dfrac{du_s}{ds} \\ \dfrac{db}{ds} \end{bmatrix} = \begin{bmatrix} C_4 \\ M_4 \\ E_4 \end{bmatrix} \qquad (6.51)$$

Based on the derived conservation equations the expressions for the coefficients to solve the system of equations are:

$$C_1 = 0 \qquad (6.52)$$

$$C_2 = \Pi b^2 \rho_g I_3 + 2\Pi b \rho_a \alpha \sqrt{\frac{\rho_g}{\rho_a}} \qquad (6.53)$$

$$C_3 = 2\Pi b \rho_g u_s I_3 + 2\Pi \rho_a u_s \alpha \sqrt{\frac{\rho_g}{\rho_a}} \qquad (6.54)$$

$$C_4 = \frac{dE}{ds} \qquad (6.55)$$

$$M_1 = -\Pi \rho_g u_s^2 b^2 A \sin\theta \qquad (6.56)$$

$$M_2 = 2\Pi \rho_g u_s b^2 A \cos\theta \qquad (6.57)$$

$$M_3 = 2\Pi \rho_g u_s^2 b A \cos\theta \qquad (6.58)$$

$$M_4 = -\tau_{itx} - M_{dx} \qquad (6.59)$$

$$E_1 = \Pi \rho_g u_s^2 b^2 A \cos\theta \qquad (6.60)$$

$$E_2 = 2\Pi \rho_g u_s b^2 A \sin\theta \qquad (6.61)$$

$$E_3 = 2\Pi \rho_g u_s^2 b A \sin\theta \qquad (6.62)$$

$$E_4 = \Pi g b^2 (\rho_a - \rho_g) - \tau_{ity} - M_{dy} \qquad (6.63)$$

The entrainment rate of liquid to the gas jet is given by:

$$\frac{dE}{ds} = 2\Pi b \rho_a \alpha (\rho_g / \rho_a)^{1/2} u_s \qquad (6.64)$$

$$\alpha = \alpha_j + (\alpha_p - \alpha_j) \left(\frac{Fr_p \sin\theta}{Fr_s} \right)^2 \qquad (6.65)$$

$$Fr_s = \frac{u_s}{\sqrt{(\rho_a - \rho_g)/\rho_g g b}} \qquad (6.66)$$

6.5.4 Geometric Relations:

To determine the jet trajectory two additional equations (kinematic relations) are needed which are solved simultaneously with the previous set of equations:

$$\frac{dx}{ds} = \cos\theta \tag{6.67}$$

$$\frac{dy}{ds} = \sin\theta \tag{6.68}$$

In the above system of Ordinary Differential Equations there are five unknowns i.e. the jet centerline velocity $u_s(s)$, the jet half-width $b(s)$, the angle of inclination $\Theta(s)$ and the coordinates (x) and (y) of the jet axis. The numerical model starts the integration at $s=0$. The boundary conditions are the initial values for the unknown parameters;

$$x=0 \tag{6.69}$$

$$y=0 \tag{6.70}$$

$$\theta_{(s=0)} = 0 \tag{6.71}$$

$$u_{s(s=0)} = u_0 \tag{6.72}$$

$$b_{s(s=0)} = d_N/2 \tag{6.73}$$

6.6 Solving the Equations in MatLab

A MatLab subroutine has been developed to reproduce the five sets of governing ordinary differential equations formulated for the continuity, momentum and geometric equations (Equs. 6.48, 6.79, 6.50, 6.67, and 6.68). Also, with the interfacial shear stress integrated across the external surface of the jet, the entrainment coefficient depending on the Froude number and the modification to include momentum of the water droplets entrains to the jet. The equations are

rewritten in terms of the jet width (b), trajectory angle (θ) and jet velocity (u_s) which were variables along the jet-plume trajectory.

An ODE solver built into MatLab is used in the main program to call the subroutine (or function) to solve these five equations simultaneously at a particular location along the jet trajectory. This solver requires user input of appropriate boundary and initial conditions to solve the above mentioned jet variables along the jet trajectory. Simultaneously means integrate the system of differential equations and find answers for all five variables at a specific location and then checks the error involved in the integration.

The program only advances a step size if the error is smaller than a maximum tolerance that is specified beforehand. If the error is outside the tolerance level, MatLab shortens the step size and goes through the set of equations again. The order in which the derivatives are calculated is of importance. The differential equations for x, y, b, u_s and Θ are calculated first, as these do not depend on the results of any of the other equations. A MatLab m-file, JetModel2, is used to enter the initial conditions of a flow scenario, the source diameter, the initial velocity of the flow, the ambient density, the density difference used to calculate the initial buoyancy flux, and the initial angles of the discharge b_0, u_0, Θ_0, x_0, y_0. These initial conditions are used to calculate the scenario dependent constants, Fr_0, M_0, and B_0 as well as the first values for the five dependent variables. The scenario dependent constants and the initial values for the five dependent variables are then non-dimensionalised. A row-vector is created with the initial values of all the five non-dimensional ODE's. The JetModel2 m-file calls a second m-file, JetModel1, in which the five equations are defined in the above-mentioned order. The outputs of this model are the values for the five parameters at each step size.

Validation of this developed integral model is established with the actual experimental results to confirm the accuracy of the model, the validation results present in the next chapter. The equation system and solution procedure coded with input and graphical output routines into the MatLab program. The program can be run in a stand-alone mode to predict the different jet parameters, and it is imbedded into the image file subsystem for the prediction of the two dimensional jet trajectories.

Chapter 7

Two-Dimensional Trajectories and Model Validation

7.1 Introduction

The trajectory of the horizontal buoyant jet in a still ambient is no longer a straight line. The jet flow goes firstly through a region where its behaviour is jet-like and dominated by the initial momentum flux that drives the flow in the horizontal direction along the jet axis and then through a region where its behaviour is plume-like and dominated by the buoyancy-generated momentum flux that drives the flow in the vertical direction. The two flow regions are connected by a relatively short transition region.

This chapter undertakes to assess the different jet parameters by the Integral Model developed in Chapter (6) as well as the validation of this model with the two-dimensional trajectories of the experimental results obtained in the actual study. First the experimental procedures on the entire jet trajectory will be discussed in brief, and then the integral model validation will be established by comparison with the experimental results to confirm the accuracy of the model. Also the other jet parameters such as: jet lengths, jet half width, and jet centerline velocity will be predicted for different initial conditions. However, in the present work, the main objective of the model is to understand the jet trajectory and to predict accurately the transition behavior of the jet under different operating conditions.

7.2 Estimation of the Experimental Conditions for the Trajectory Prediction

In the buoyant jets, the momentum and buoyancy are discharged at a rate equal to M_0 and B_0 respectively, as defined in Chapter (2), and at an angle Θ_0 with the horizontal. Close to the jet source, jet momentum dominates. The jet spreads linearly as it entrains the ambient fluid. The buoyant force acts in the vertical direction of the gravity, it changes the vertical component of the momentum at a rate equal to the buoyant force.

A series of experiments on horizontal buoyant jets were performed using the photographic technique as described in Chapter (4) to record the position and motion of the entire gas jet trajectory (complete image includes the momentum and buoyancy region). The initial conditions for all the experiments that have been used to validate the model, and the initial conditions of model runs, are the same ones listed in Table (5.1). The digital images were analyzed to extract the interface position, in order to measure the two dimensional jet trajectories and to verify and validate the numerical model for different initial conditions.

7.3 Model Evaluation and Data Comparisons

The horizontal buoyant jets with large density variations, for instance air into water ambient, have not received sufficient research before, and almost no experimental data could be found in the open literature. In order to establish some level of confidence in the proposed analysis, it is imperative that the results obtained by means of the present model be comparable to other data. Unfortunately, the available experimental and numerical data in the literature are very limited. Therefore, validation and comparison of the present mathematical model was done with our experimental results for jets with different initial conditions. The air is injected horizontally into water ambient (297 K, 1 bar) with various initial jet velocities and nozzle diameters. Equation (7.1) gives the same relationship as presented before between the Froude number, the nozzle diameter, and the jet velocity,

$$Fr_0 = \frac{u_0}{\sqrt{(\rho_a - \rho_g)/\rho_g g d_N}} \tag{7.1}$$

The jet velocity from a buoyant jet can be related to the initial Froude number and jet diameter through Equation (7.1). For a given diameter, jets with higher Froude number have higher exit velocities and are dominated more by the initial momentum of the jet, while jets with lower Froude number have slower exit velocities and are dominated more by buoyancy. As stated earlier the Froude number represents the ratio of momentum to buoyant forces at the nozzle exit.

The system of O.D Equations that developed in the previous Chapter (6) from the mass and momentum equations is solved simultaneously here using an appropriate numerical scheme by marching along the path of the jet-plume (s-axis) as mentioned in Chapter (6) to get the jet trajectory coordinates, centerline jet velocity, jet half width, and trajectory angle. Also, this equation system and solution procedure has been coded with input and graphical output routines into the MatLab program. Therefore, this program can be run in a stand-alone mode to assess the different jet parameters, and it is embedded into the image file for the prediction and comparison of the jet two-dimensional trajectories. The solutions are obtained for continuous discharge of buoyant gas jet into liquid ambient, for different values of the initial conditions.

Figure (7.1) shows a comparison between the Numerical Model and the experimental results (summed images) for different Froude numbers and jet diameters 5, 4, and 3 mm respectively for the same initial conditions as illustrated in Table (5.1). The Figure shows the centerline and upper and lower jet trajectories expressed as y=y(x) plots. The experimental results for the location of the jet flow are noted with the red color symbol (gas), water ambient with blue color, and the predicted jet trajectories by black lines.

As shown in Figure (7.1) when increasing the initial jet velocity (Fr_0), the transition point to the buoyancy-controlled regime moves farther downstream from the nozzle exit. Along the downstream distance, the jet has three separated flow regimes. The one close to the jet nozzle, characterized as the 'horizontal' part of the trajectory, where the flow is essentially driven by the initial horizontal jet momentum (momentum-dominated regime). The second flow regime can be characterized as the bent regime of the flow (mainly for buoyant jets with low Fr_0), that is the result of the buoyancy force acting on the jet (buoyant-dominated regime). The regime between both previous cases is a transition flow (transition regime).

In all cases, the Numerical Model provides a satisfactory transition behavior from the momentum dominated to buoyant dominated region. The numerical model predicts reasonably well the two-dimensional jet trajectory determined from the experimental data (accumulated images) including; jet penetration lengths, jet spreading, as well as the local angle of inclination. The agreement with the numerical model with the experimental data for all the jet Froude numbers and nozzle diameters indicates that the present model solutions are providing adequate outer edge and spread predictions for these flows.

While the model appears to predict the path of the jet flow and its outer edge with reasonable accuracy, the outer edge of the 5 mm jet diameter for the Froude number $Fr_0= 99$ is not well predicted in the buoyant region. The prediction shows some deviations from the experiments particularly in the downstream region (buoyancy region). However, the differences are relatively small and it well predicted for the 3 and 4 mm jet diameters for Froude numbers $Fr_0= 95$ and $Fr_0= 92$ respectively.

From the experimental images, this discrepancy is seen to be caused by the transition to turbulent flow, which should be more pronounced for higher Reynolds number flows and in the downstream region.

Once the transition occurs, the bending angle begins to show a sudden decrease caused by rapidly losing the momentum, associated with the rapid turbulent mixing with the ambient (Kima et. al, 2009). In addition, it is due to the increase in the interfacial motion oscillations (instability) that is experimentally correlated to a less stable jet exhibiting a greater number of pinch-off events as studied in Chapter (5). However, the present model is capable to predict the trajectories of the gas dispersion jets from momentum to buoyancy dominant regions by considering the Froude number and jet diameter.

In the buoyant region, the jet edge is inherently unstable and buoyancy driven instabilities in this region generate a significant vertical flux of material out of the buoyant jet as it moves in a predominantly horizontal direction. This flux appears to destroy the typical entrained flows that one would expect to see near the edge of the jet, but in turn creates additional mixing in this region. The Numerical Model does not take into account the effect of the buoyancy-induced instabilities and therefore overestimate the rate of increase of the buoyancy-generated momentum flux. In addition, this small difference can be attributed to the increasing of time-scale of the turbulence. The relative importance of the initial momentum flux is thus smaller, decreasing the horizontal distance from the source to the point of maximum height.
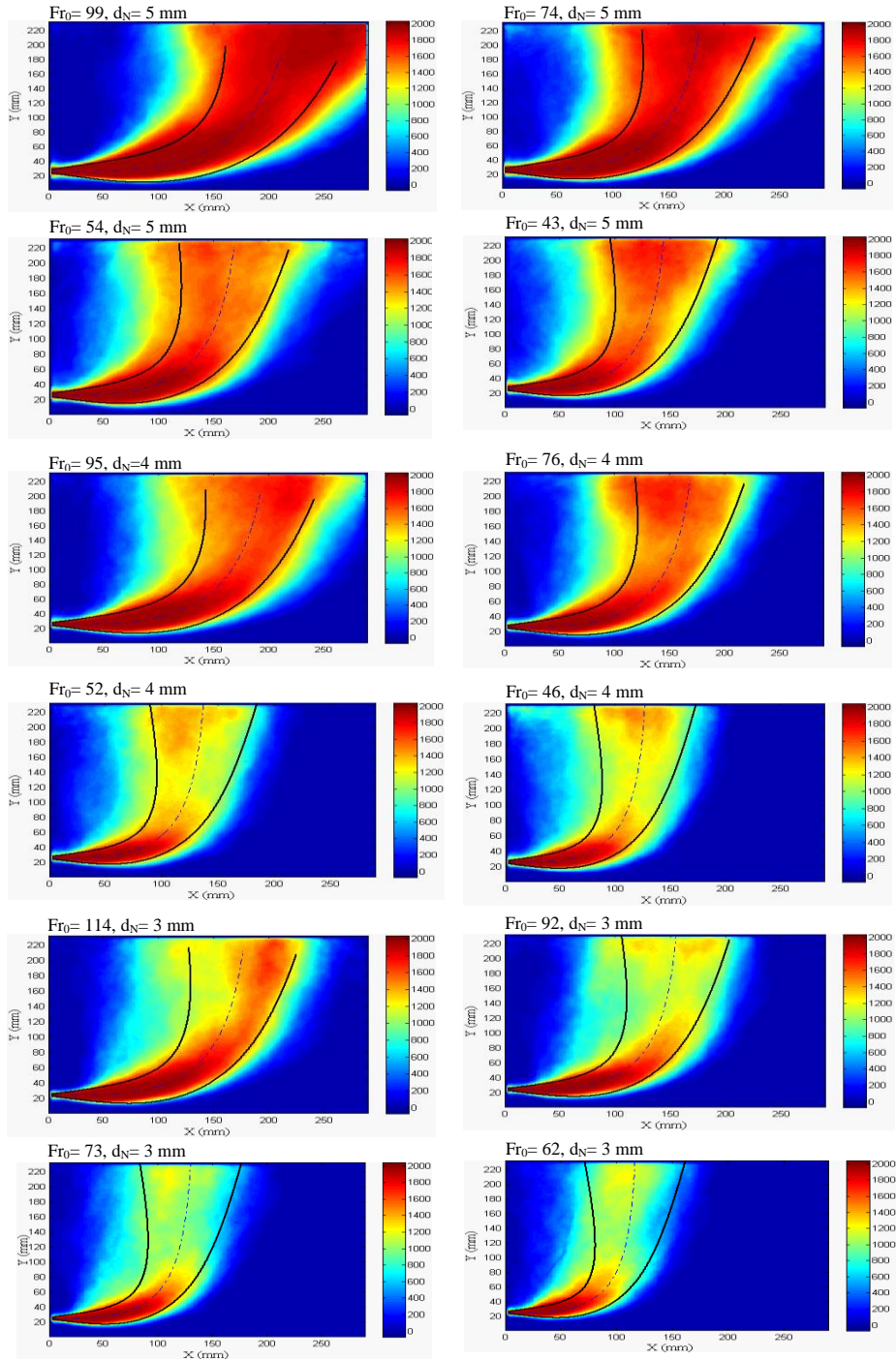
Figure (7.1): Comparison of the experimental data with model predictions trajectories for horizontal buoyant jets in still ambient.

7.3.1 Centrline Jet Trajectory Predictions

Comparison of the predicted jet centerline trajectories with the experimental results are shown in Figure (7.2) (a) to (d), when using Equations (6.52) to (6.54), for initial jet diameters 5, 4, 3 and 2 mm, respectively at different initial conditions. The corresponding centerline model jet trajectories are marked by solid lines.

In addition, it is noteworthy to see the differences between the jet trajectories in Figure (7.2). The jet trajectory has a strong dependence on Froude number, defined in Equation (7.1). For fixed Reynolds number, Froude number becomes proportional to $d_N^{-1/2}$, thus it means that if the nozzle diameter becomes smaller, the Froude number increases significantly, and consequently the jet momentum plays much more role than the buoyancy as shown in Equation (7.2).

$$Fr_0 = \frac{u_0}{\sqrt{(\rho_a - \rho_g)/\rho_g g d_N}} \propto c_1 R_{ed} d_N^{\frac{-1}{2}} \tag{7.2}$$

The comparison shows that, the theoretical analysis agrees relatively well with the experimental results for different jet Froude numbers and jet diameters in the momentum region, but in the buoyant region the model predicts the flow to rise more rapidly than the experimental data indicates.

Figure (7.3) shows the centerline trajectory data non-dimensionalised by the jet diameter and the Froude number, the vertical jet trajectory $y/d_N Fr_0$ as a function of the horizontal coordinate $x/d_N Fr_0$ at different initial conditions. The results show that depending on the value of the initial Froude number of the jet, the development of the momentum region can be significantly altered by the buoyancy forces.
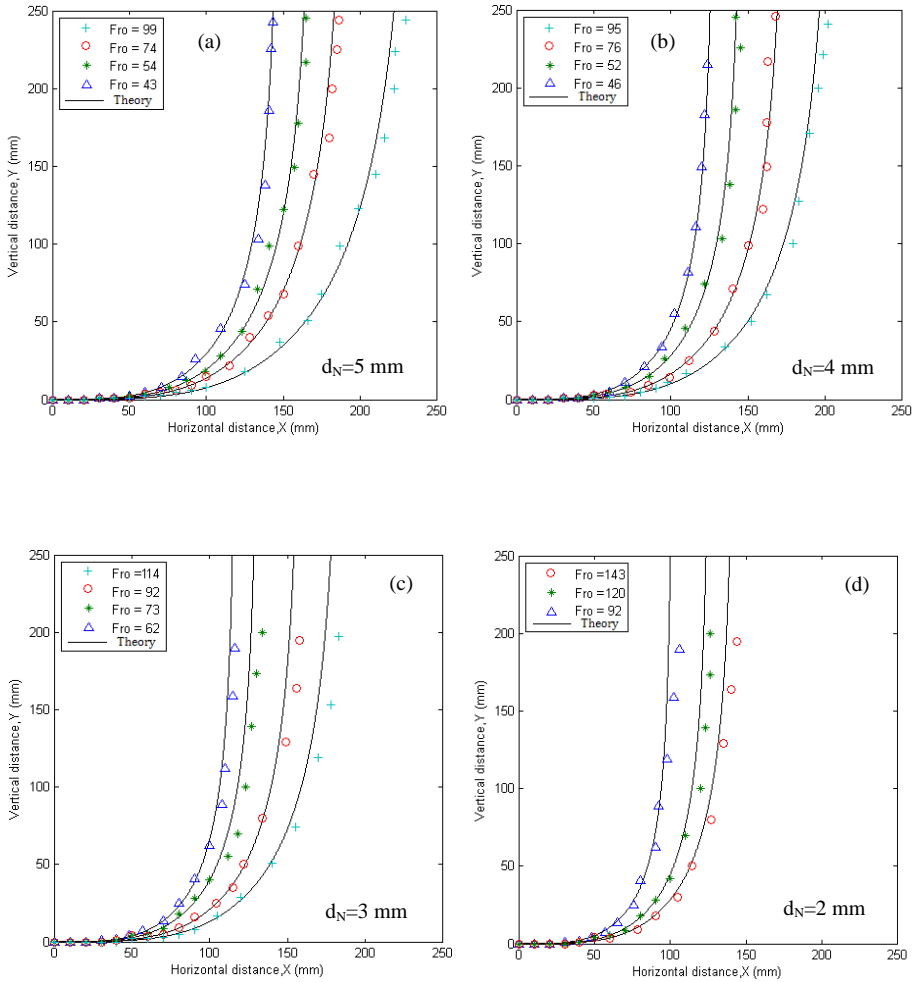
Figure (7.2): Experimental and predicted jet trajectories for different Froude numbers and jet diameters

Trajectories of jets with high initial Froude numbers persist traveling longer distances, before they bend over to follow vertical motion. Normalized trajectories of the buoyant jets seem to collapse in a narrow regime to the nozzle, which corresponds to the high values of Fr_0. If the Froude number is zero as in the case of plume produced by a fire; the core of the fire is contracting and highly unstable. A swirl is often observed in such strongly buoyant flows as the surrounding fluid is drawn into the low-pressure region of the core.
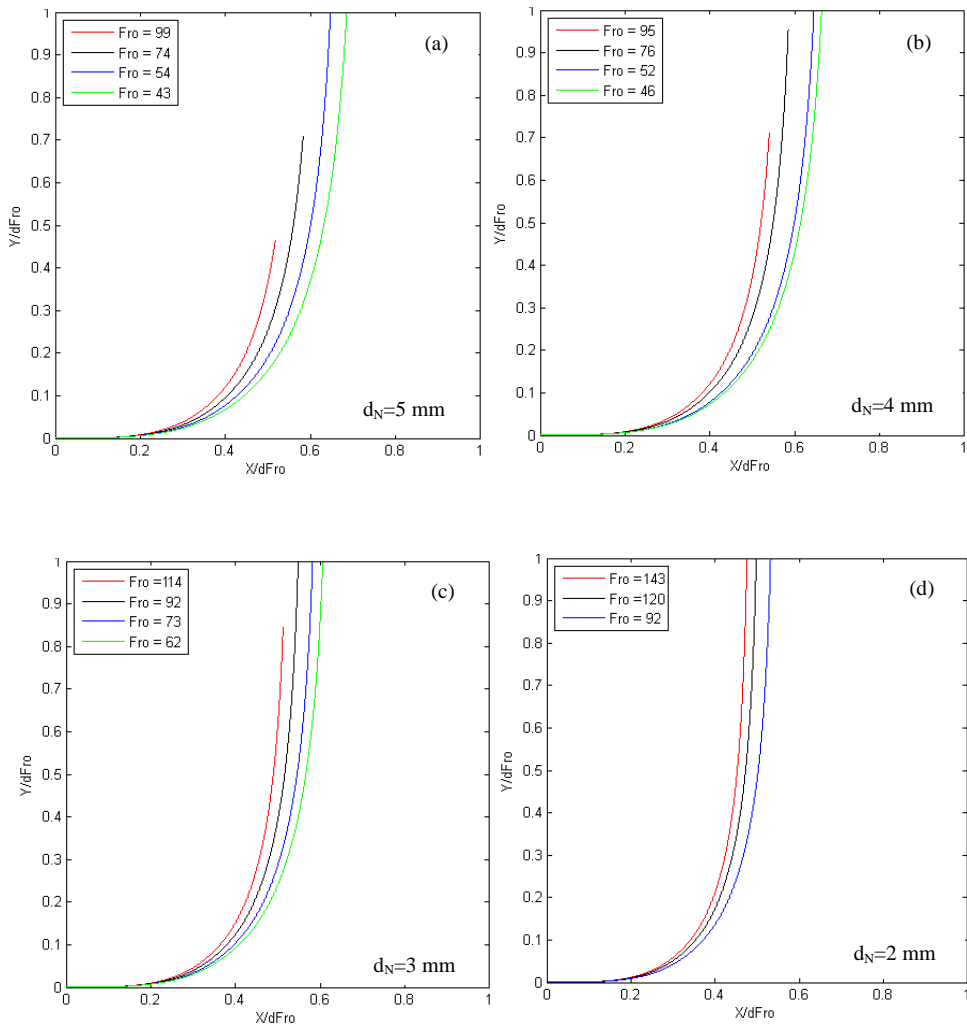
Figure (7.3): Predicted normalized trajectory at d_N=5, 4, 3, and 2 mm respectively

7.3.2 Jet Penetration Length

It should be noted here that the present mathematical model conserves the horizontal momentum flux and therefore, from a theoretical point of view, the jet will penetrate continuously in the horizontal direction. The distance L_m used in this work corresponds to the horizontal distance from the nozzle exit to the maximum point that the jet can arrive along the jet centerline as presented in Chapter (5). From a practical point of view at that point the jet starts to rise up to become vertical due to the buoyancy effect. Figure (7.4) shows a comparison between jet penetration lengths observed experimentally and those predicted from the mathematical model non-dimensionally by L_Q, for different jet diameter and Froude numbers.

However, the experimental values collapse well and are consistent with all the model predictions with $\pm 10\%$ error for both jet momentum and jet buoyant penetration length.
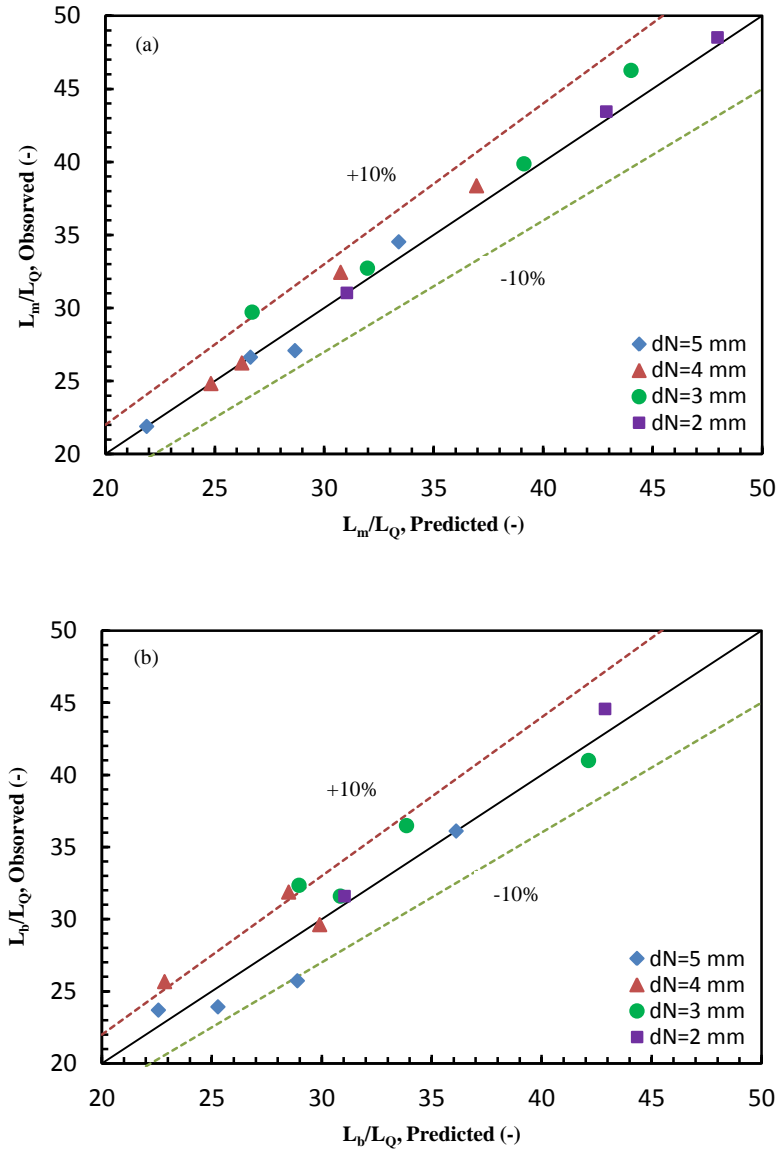
Figure (7.4): Comparison between jet penetration lengths observed experimentally and those predicted from the mathematical model

7.4 Centerline Velocity Decay

After the validation of the numerical model with the experimental results, the jet centerline velocity and the other jet parameters can be predicted. Due to the absence of measured velocity data in the present study, it was decided to perform a series of numerical calculations using the present Numerical Model. Figure (7.5) shows the decay of the normalized centerline velocity $u(r,s)/u_0$ along the non-dimensional jet trajectory (s/d_N) for different initial conditions.
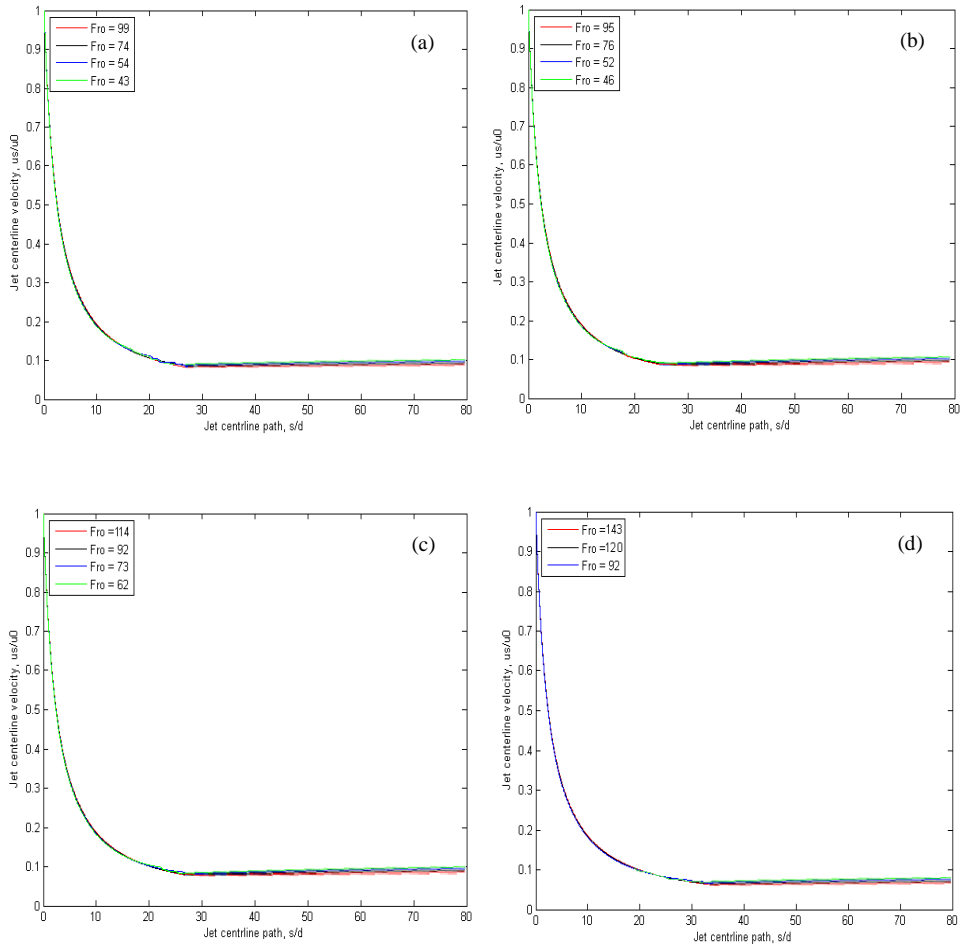
Figure (7.5): Centerline velocity decay of a horizontal buoyant jet. The initial conditions for this flow are $Fr_0 = 114, 92, 73,$ and $62,$ and jet diameter $d_N = 5, 4, 3$ and 2 mm respectively

It can be seen from this figure that, the normalized centerline velocity decreases in the downstream direction along the jet centerline path and there is little change in the normalized centerline velocities for all the cases. As the Froude number decrease the mean axial velocity decreases as well as it decreases in the downstream direction. However, the Froude number decreases along the jet centerline as the jet penetrates in the ambient.

Near the nozzle exit, the jet is in a forced convection regime with fully turbulent motion causing significant fluctuations near the jet edge. As the jet penetrates, it entrains liquid and thus increases its volume. This causes velocities to decrease in the stream wise direction, and buoyancy forces become more important in the downstream direction.

7.5 Summary

Five ordinary differential equations that describe the dependent parameters of the flow along its trajectory are the basis of the present Integral Model. The discharge at any particular location is determined by the relative magnitudes of distinct form of momentum flux and buoyant flux. The equations were solved simultaneously at a particular location along the trajectory. The jet-plume half-width, trajectory angle, and velocity along the axis defining the jets trajectory were solved as variables along the path. Functional relationships for entrainment, interfacial shear stress, and entrainment bubble momentum were obtained from relevant literature. Where needed, various underlying assumptions were made and justified in the context of a jet-plume.

Whenever was possible the results from the experiments were compared with the predicted results of the present Numerical Model. At the same time, the experimental results were used to verify the accuracy of the Model. The results from the current experimental investigation were consistent with the numerical model results, increasing the confidence in the flow visualization technique. The results for the buoyant jet experiments confirm that the model can also accurately predict the jet trajectory, spread and penetration length results for the intermediate angles, for the different boundary conditions included in the study.

Chapter 8

Experimental Apparatus and Instrumentation of the Vertical Plunging Water Jets
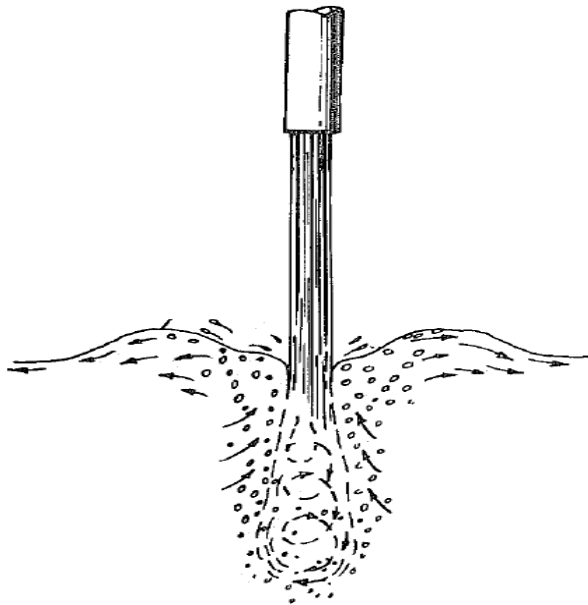
8.1 Introduction

The second part of this investigation thesis focuses on the air entrainment by vertical plunging water jets ejected by circular nozzles onto a water pool. In this sense it has been designed and built the second apparatus (test-rig) in the Thermal-Hydraulic and Nuclear Engineering Research Laboratory of the Institute for Energy Engineering at Polytechnic University of Valencia. Whose construction is to contribute to the understanding of the nature of two-phase flow, air entrainment, and more specifically the transport phenomena in liquid-gas flows similar to those occurring in many natural and industrial applications.

Similar facilities have been built in various parts of the world in order to study two-phase flows in industrial activities such as the use of nuclear energy for power generation, in the chemical industry applications, oil extraction, etc.. These facilities are distinguished by the geometry of the water tank (which may be circular or rectangular, with various sizes of hydraulic diameters and lengths), orientation and flow direction (vertical or inclined plunging jet), by the working fluids (water, air, oil-nitrogen mixtures alcohol air, viscous oils, hot air, etc.), and for the conditions under which the tests are performed (adiabatic or at atmospheric pressure). Another important difference in the various experimental facilities are the techniques used in measuring the characteristics of two-phase flow, for example there are research groups using visualization techniques and some electric invasive techniques, but especially the combination of two or more of these measurement techniques.

This chapter describes the experimental facility and instrumentation used in the experiments of vertical plunging water jets. The first part of this chapter describes the design and construction of the experimental facility and its main components. The second part shows the instrumentation that has been used for flow measurements as visualization technique, velocity, pressure, and far above the main phase flow parameters. The third part is devoted to describing the control software that enables the system of the installation can operate in both obtaining measurements as well as analysis.

8.2 Experimental Facility Description and Dimensioning

The entrainment of non-condensable gases by a plunging liquid jet impacting a liquid pool is related to some important practical problems. To study this process, a "closed loop" flow system with a complete re-circulation of the water and a constant water holdup was used here in this study to perform the experiments. The main components of the facility consisted of a water tank, test water nozzles supported vertically above the water tank, a water treatment, skimming and re-circulation system, and an illumination system for flow visualization technique. All these system components are described in detail in further sections. In all cases filtered treated tap water was used for the jet and ambient fluid. A schematic of the experimental set-up arrangement and photographs for the present study are shown in Figures (8.1) and (8.2) respectively.

8.2.1 Water Tank and Aluminum Support Frame

The liquid jet issued vertically downward from the nozzle impinges on the water contained within a rectangular transparent tank. The tank used has dimensions of (length x width x deep) 500mm x 700mm x 900mm respectively, and the upper side was opened to the ambient environment for air entrainment process. Five rectangular flat plates of 11 mm thick made from Perspex makes the bottom and sidewalls of the tank. 3 mm neoprene rubber was placed in between the aluminum structure and the Perspex plates to prevent stress concentrations at contact points, allowing the Perspex to safely rest on the aluminum profile. The tank has transparent viewing sides, through which the bubble plume was photographed.

A schematic diagram and a picture of the water tank illustrating its dimensions is showed in Figure (8.3).
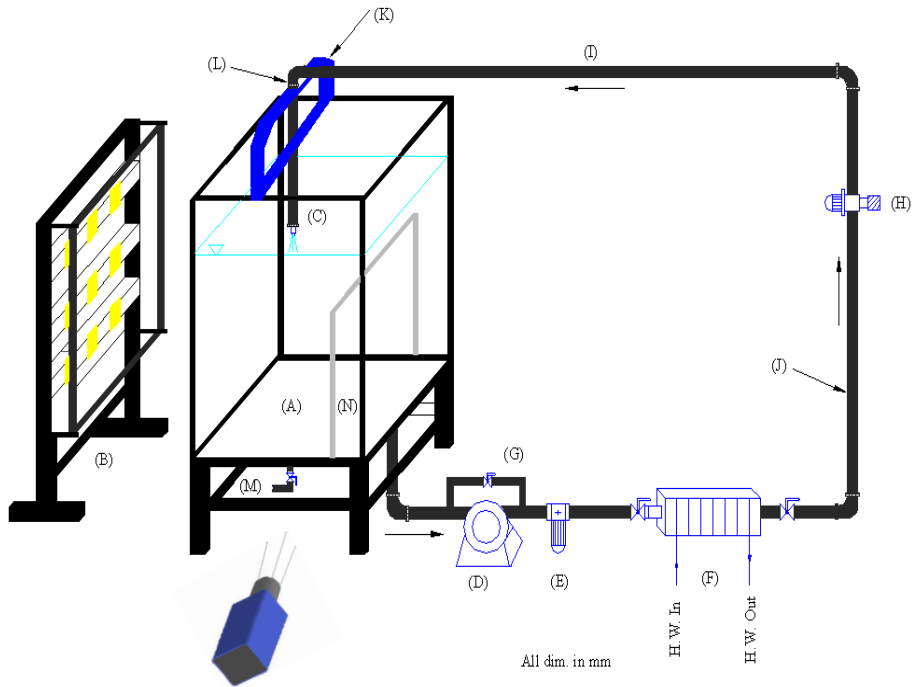
A.	Water tank	E. Water filter	I. Flexible tube
B.	Illumination system	F. Heat exchanger	J. Rigid tube
C.	Vertical nozzle	G. By-pass	K. Nozzle supporter
D.	Water pump	H. Regulator valve	L. Inflow pipe

Figure (8.1): Schematic diagram of experimental set-up for vertical plunging water jets

Figure (8.2): Pictures showing the experimental set-up of the plunging jet system
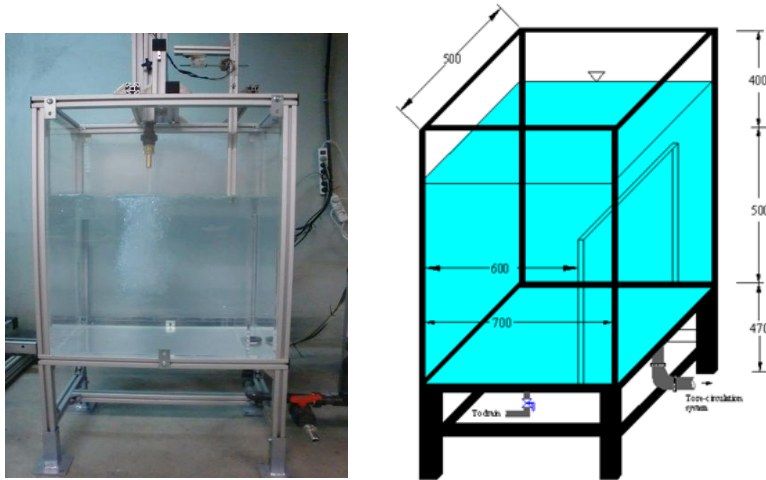
Figure (8.3): Schematic diagram and picture of the water tank

The transparent walls of the tank allowed optical access to the measuring points so that bubbles penetration depth and other measured parameters could be obtained. In addition, pictures of the jet can be taken at any angle through the tank walls. The lighting can also be set at different angles.

The Perspex bottom shows two holes at either end of the tank (see figure, 8.3) that accommodate bulkhead fittings to connect the suction of the tank and filtration system, as well as the pipe network required to drain and fill up the tank. The suction of the tank is necessary to keep constant the water depth. In order to minimize the influence of this flow on the two-phase jet's flow and to prevent air bubbles coming deep into the pump inlet, the suction tube is located as far from the liquid jet impact point as possible. Therefore, a small channel 500×500×100 mm contains this suction tube that located at the lower side of the tank as shown in Figure (8.3). During all experimental conditions, the penetration depth of the entrained air bubbles was always less than the water depth of the tank.

The main structure of the water tank had two separated aluminum profile structures, one to hold and provide support for the water tank walls, and situated 470 mm above the floor level. The second was to support the jet nozzle vertically above the water tank. The tank was designed to have a maximum water depth of water while keeping enough space between the Perspex bottom and the room floor for additional systems like laser optics (for future study), camera or

lighting. The aluminum profile structure also holds a piping network to fill and drain the tank, and also the set of water skimmers and system for water treatment.

8.2.2 Water Re-Circulation and Skimming System

The water for the jet is provided and circulated by a recirculating auto aspirant pump Jex-080, 0.6kW (0.8HP). The water pump was kept in a special housing made from aluminum frame and was mounted on dampers to eliminate and reduce the vibration on the test-rig caused by the pump vibrations as illustrated in pictures (8.4).

Figure (8.4): Water re-circulation and skimming system

The quality of the water was achieved by simple water filter and a reverse osmosis system to remove the hard water contaminants and reduce the hardness to avoid deposition on the test section and measurement instruments. Five stages osmosis (pur 75/5BP model) with capacity of 60:100 L/day and 95% of TDS were used. The decalcified water was stored in a large storage tank (500 L) to feed the experimental set-up through a submersible pump.

8.2.3 Jet Nozzle Design and Construction

A continuous circular water jet was directed vertically downwards from six interchangeable short cylindrical nozzles (lance) made of brass. The diameters of the nozzle entrance were all 25.4 mm, and the exit diameters of d_N= 4, 6, 8, 10, 12 and 14 mm, were used to vary the jet exit diameter onto the free water surface (see Figures, 8.5). Table (8.1) shows some of the important nozzles parameters where, l_N/d_N is the nozzle length-to-diameter ratio and θ is nozzle contraction angle. The range of nozzle length to diameter ratio (l_N/d_N) was varied between 3.33 and 5 (short circular nozzles ($l_N/d_N \leq$ 5)). The preferred nozzle inlet and outlet geometry was circular and it's attached with integral ball joint that allows to get parabolic or vertical jets, offering a wide range of water displays (in the present study only vertical jets were ejected).
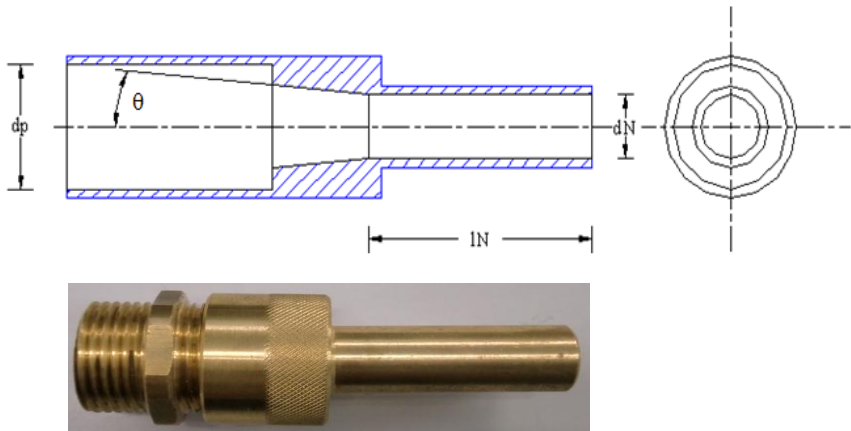
Figure (8.5) Schematic diagram and picture of circular nozzle design

d_N (mm)	4	6	8	10	12	14
θ, degree	12	7	9	5	7	5
l_N/d_N	5	3.33	4.63	3.7	4.42	3.79

Table (8.1): Characteristics dimensions of circular nozzles design

The nozzle was placed at the exit of a vertical inflow pipe (rigid PVC tube) with 27.2 mm internal diameter and 1.5 m long. The tube was long enough to supply a fully developed flow at the entrance to the nozzle. The tube and nozzle are adjusted such that the jet impinged vertically and centrally in the middle of the water tank to produces an axisymmetric liquid jet.

A mechanism made from aluminum profiles was attached by a special structure placed on the top of the water tank. This therefore was used to support the jet nozzle and permits the nozzle to move in the vertical direction above the water tank by changing the distance between the jet exit and the water surface (up to 0.3 m), also permits the nozzle to orientate with a certain angles for the future work. Figure (8.6) shows a picture of the aluminum mechanism used to support the jet nozzle vertically.

Figure (8.6): Mechanism to support the nozzle vertically

To quench the vibrations and eliminate the jet instabilities caused mainly by the pump, the vertical rigid PVC tube was connected with the tube from the pump by a flexible PVC tube. Moreover, the pump was installed above anti vibrators. The water tank, vertical tube and the nozzles were designed to achieve the lowest possible levels of jet turbulence.

8.2.4 Illumination System (Artificial Vision)

Observation of the entrained air bubbles by water jets were performed with a high speed digital camera (CCD). The camera was positioned on the opposite side of the water tank up to approximately 2 meters from the middle of the tank and we recorded images through the transparent tank sidewall. The flow was backlit with a continuous source of light contained in a separated aluminum frame.

During the experiments, several light sources were tested. The chosen light source was the one that give the most constant and uniform light intensity and was independent of time. The combination of the camera with the halogen lamplights at 50 Hz had the least variation and was the most uniform. The light source for the illumination system was a white-light bank consisting of nine 500 W halogen lamps, evenly distributed over the test section. Figure (8.7) shows a schematic diagram dimensioned and a picture of the used illumination system.
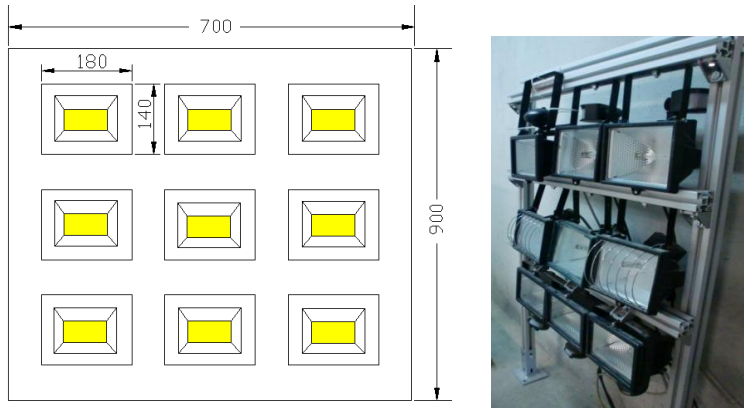
Figure (8.7): A schematic and picture of the illumination system

A light diffuser made from Perspex sheet covered with a sheet white paper had a thickness of approximately 10 mm (length and height were a 700 mm X 900 mm respectively) was attached to the sidewall of the tank closest to the light source. The Perspex sheet acted as a diffuser creating a uniform light sheet to reduce the intensity of light illuminating the jet before entering the camera. An aluminum frame was constructed to fit over and support the light system. The distance between the frame supporting the light bulbs and the frame supporting the diffusion sheet was approximately 300 mm. Also, the light bank was covered with black cloth to minimize the chance of light reaching the camera other than through the selected area.

Figure (8.8) illustrates a cross-sectional cut and a picture with the positions of the light source, Perspex sheet, and video camera relative to the tank. Light travels from the light source through the Perspex diffuser sheet and pass through the water tank and then is caught by the digital video camera located at the other side of the tank. The camera sends the recorded data to the computer to store it and then processing by the MatLab tools.

(A)   Illumination system (B) Diffusion sheet (C) Water tank (D) Camera (E) Computer
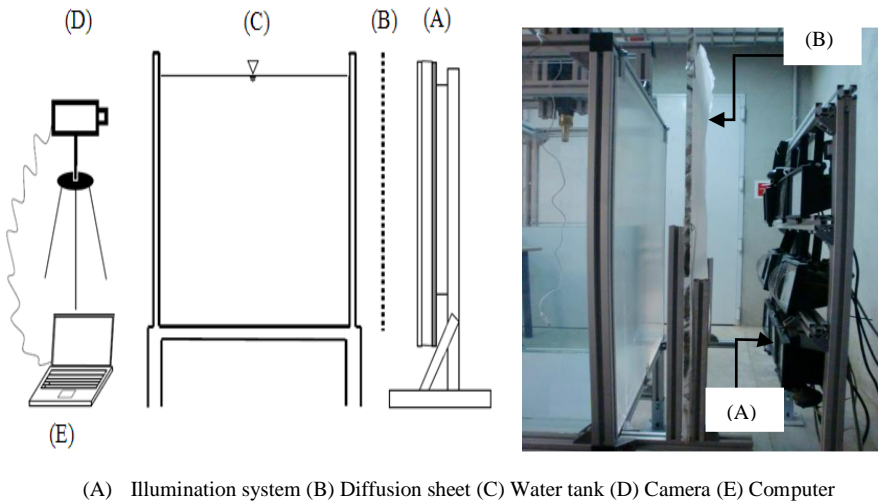
Figure (8.8): Schematic and picture showing the illumination system arrangement

8.3 Instrumentation and Measurement Description

A series of laboratory experiments and measurements as will be shown in chapter (9) were carried out to investigate the air entrainment by plunging jets ejected vertically by circular nozzles of 4 to 14 mm diameters and over a range of velocities (V_N) between 1.5 and 13 m/s with length of water jet (x_1) between 0.025 m and 0.3 m and plunge angle of water jet (θ) of 90°.

Figure (8.9) illustrates the schematic diagram of the instrumentation and control system.
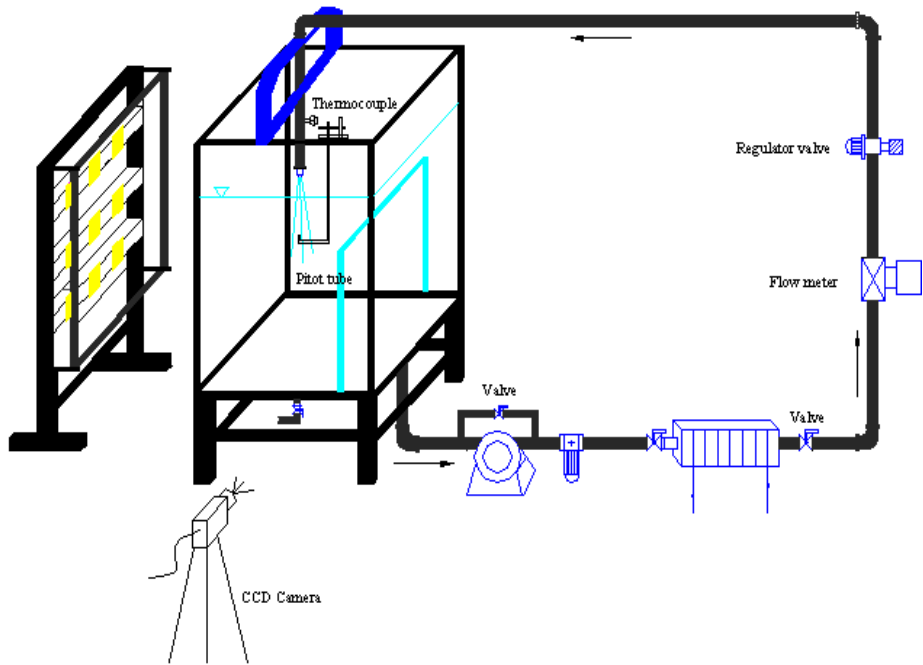
Figure (8.9): Schematic diagram of the instrumentation and control system

In this section, the description of the measuring instruments and the methods of operation are presented.

8.3.1 Volumetric Jet Flow Rate Measurements

The test-rig system was designed to deliver a constant flow rate to the nozzle jet over each run. In order to regulate the jet flow rate a regulator valve was used. By acting on the regulator valve, we were able to modify the jet liquid flow rate, therefore, jets with different velocities can be obtained at the nozzle exit. The opening of the regulating valve was set at the desired flow rate by using a flow meter in the supply line.

The volumetric flow rate of the water delivered to the jet was measured during the experiments by means of digital flow meter, which was installed at the line between the pump and the nozzle. Two different ranges of digital flow meter were used to measure the different ranges of the water flow rate in an effort to minimize errors and to obtain a wide range of measuring scales. The first digital flow meter was a model of PF2W540 with range of measurement between 3.5-40

l/min and the second was a model of PF2W511 with range of measurement between 10-100 l/min. Both flow meters have an accuracy ±1% of Full Scale reading, with operating pressure 0:1 Mpa and operating temperature of 0-50 °C.

Figure (8.10): Two different flow meters are used to measure the jet flow rate

The average jet velocity (V_N) at the nozzle exit was calculated from the water flow rate (Q_W) and the cross section area of the nozzle at the outlet.

8.3.2 Temperature Measurements

All experiments were performed at ambient conditions (298 K), where atmospheric air was the gas phase and the liquid solution was treated tap water. The temperature of the water jet was kept at 25±2 °C, was measured at each run. The temperature measurements were conducted by means of a thermocouple installed at the tank middle. The thermocouple used was of type K thermocouple calibrated by using the comparison techniques against standard type K-thermocouple with 0.1^0C accuracy. The physical properties of the water were calculated during the experiments at each run and were found to be almost constants.

8.3.3 Measurement of Water Jet Velocity Distribution

The water jet velocities of the submerged water jet (centerline jet velocity, V_c and axial velocity distribution, $V_x(x,r)$) in the flow developed region under the jet impingement point (in absence of entrained air bubbles) were measured by means of a Pitot tube.

In some situations when the direction of the velocity vector is known with a sufficient accuracy without taking any measurements. In this case, a Pitot-static tube may be properly aligned with this direction and accordingly the static and dynamic pressures could be determined. The Pitot tube used in the actual measurements was made from stainless steel, had an external diameter of $\emptyset=3.3$ mm and was connected to a digital differential pressure sensor (2082P digitron model) with operating range from 0 to 2 bar. During the velocity measurements, the pipe connecting the Pitot tube and the differential pressure sensor were always filled with water (without air bubbles) to prevent errors in reading.

The water jet was forced through the static and dynamic ports of the Pitot tube, allowing a fluid of constant density (water) to be maintained in the instrument. A differential pressure existed between the static and dynamic ports when placed in the jet stream. The differential was converted to a voltage via the differential pressure transducer, and an integrated data acquisition system recorded the voltage and converted it into a velocity head.

When the Pitot tube is placed into the jet flow, the difference between the total pressure of the fluid, P_t, and the static pressure, p_s, is sensed. This pressure difference (Δp) can be used to find an approximate corresponding velocity from Bernoulli's equation for incompressible flow. Solving Bernoulli's equation for V yields the following:

$$V = \sqrt{\frac{2(p_t - p_s)}{\rho_w}} = C_p \sqrt{\frac{2\Delta p}{\rho_w}}$$

(8.1)

where, C_p is the correction factor of the tube, was determined by a comparison technique with a standard flow meter and it was found about 0.85 and ρ_w is the water mass density.

The displacement of the Pitot tube probe in the flow direction and the direction normal to the jet flow was controlled by two adjustment travelling mechanisms made from aluminum frames and were moved by linear stepper motors controlled by data acquisition board system connected with the personal computer. Overall error in the probe position was less than 0.1 mm in each direction.

8.3.4 Air Bubbles Penetration Depth (Photographic Measurements)

The penetration depth of the entrained bubbles was measured by direct visualization technique, which involves the utilization of a CCD camera and illumination system as that used in the buoyant gas jet experiments in Chapter (4).

A high-speed video camera (CCD) was used to digitally record shadowgraph images of the air bubble entrained at a sampling rate of 500 Hz for 20 seconds. It was positioned 2 meters approximately from the middle of the tank to provide a complete view for the entire bubble penetration depth. The images were acquired using the same camera that mentioned in Chapter (4).

The camera was focused on the area below the water surface, which the water jet is plunging to reduce distortion effects caused by the curvature of the tank wall. During the experiments, the distances between the light source and the tank and between the tank and the camera were not altered.
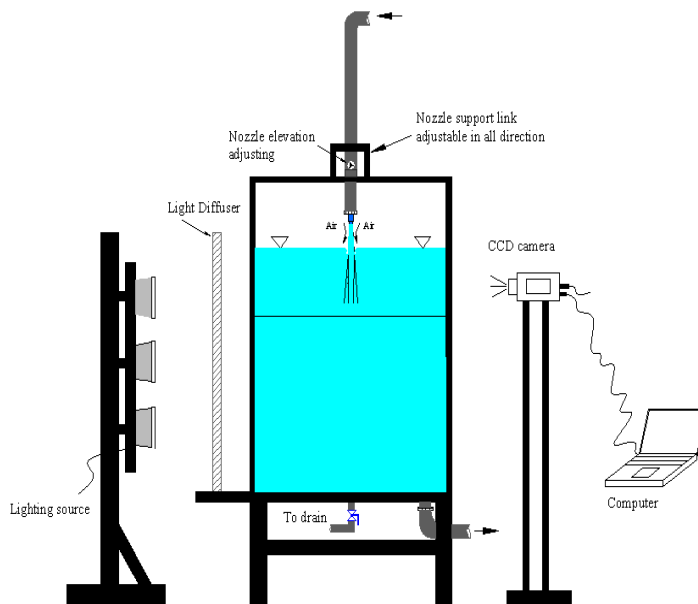
Figure (8.11): Schematic diagram shows the visualization technique used to measure the bubble penetration depth

The video camera was mounted on a 3-D traversing mechanism (Dantec Dynamics traverse), this system comprises of frame with X and Y traverse, Z traverse with mounting plate, 3 motor and traverse controller connected to the PC using a serial interface cable and to a personal computer with another cable. The traverse system controlled using Dantec Dynamic application software installed in the computer; this system provides maximum flexibility in moving the camera in the 3 directions (x, y and z positions) to adjust it in the correct position at the beginning. The traverse system shown in Figure (8.12) is used in the actual study for positioned the camera in such a way that the lens of the camera was in the middle of, and perpendicular to the tank.
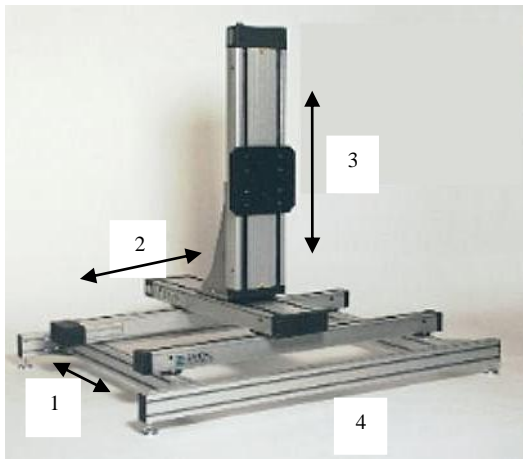
1. X- Axis. Axis No. 1
2. Y- axis. Axis No. 2
3. Z- axis. Axis No. 3
4. Frame with Adjustable Feet

Figure (8.12): 3D Traverse mechanism

8.3.5 Entrained Air Measurement

As mentioned before in Chapter (2) there are two known methods to measure the amount of air entrained (Q_a) by plunging jets, in this work we have used the first method that depends on catching the entrained gas bubbles after they have been entrained into the liquid pool. This method consisted of a bubble trap, plunging tube, connecting tube and flow meter apparatus as illustrated in Figure (8.13).
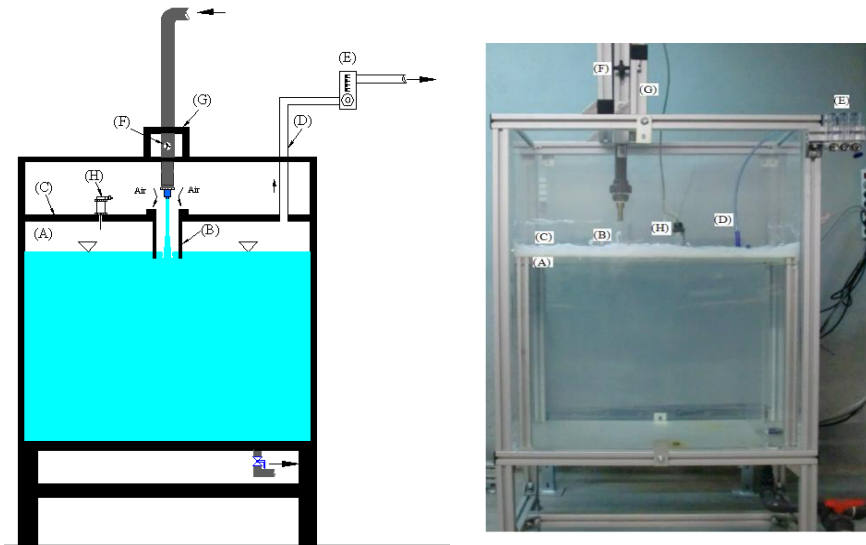
(A) Bubble trap, (B) Plunging tube, (C) Tank cover, (D) Connecting tube, (E) Air flow meter, (F) Adjusting vertical tube, (G) Nozzle support, (H) Pressure sensor

Figure (8.13): Air entrainment measurement arrangement

The water tank was contained a bubble trap (A) with dimensions 0.4 m length, 0.7 m width, and 2 cm depth above the water surface. The bubble trap was used to collect and accumulate the air bubbles that were entrained by the liquid jet and it is created by covering the water in the tank with a Polypropylene sheet (C) that had dimensions 0.4 m length, 0.7 m width, and 7 mm thickness as shown in Figure (8.12). Additionally, the Polypropylene sheet contained a large hole in the center to install the plunging tube (B) on the water surface. Also the sheet had two small apertures: one to install a pressure transducer (H) to measure the pressure fluctuations of the entrained air inside the bubble trap and the other one for the tube (D) that connect with the flow meter device (E) as shown in Figure (8.12).

The plunging tube was a cylindrical tube made from transparent Plexiglas (2 mm thickness) and had a constant length $L_C=15$ cm and we varied the diameter depending on the nozzle diameter being used. The plunging tube was used to ensure the jet plunging within the water tank and to give flexibility to the ambient air to contact with the water jet to perform the entrainment process. The plunging tube plunges only 1 cm under the free surface of the water tank. In such a way that the bubbles of the swarm rise up mostly at the outer limit of this

plunging tube and collapse at the free surface of the tank while the perturbation of the jet and the free surface due to the presence of the plunging tube is tuned as small as possible. Immersion of the plunging tube is small enough, so that no enhancement of the air entrainment can be attributed to a downcomer effect (Okhawa et al. 1986, 1987). To find the optimal plunging tube diameter, different tube diameters were tested, and D= 10, 15, and 20 mm were finally selected depending on the plunging jet diameter itself (d_N). The choice of the plunging tube diameter was subject to the following requirements:

i) To be able to measure as much as possible of the air entrapped by minimizing the air flow wasted via the few bubbles rising up within the plunging tube itself.

ii) To disturb as little as possible the entrapment hydrodynamics at the vicinity of the impinging point.

The first requirement leads naturally to a small tube diameter of the plunging tube, whereas the second leads to the opposite. To get an optimized system, the diameter of the plunging tubes (D) for a given diameter of the jet (d_N) was varied systematically. The conclusions of these trials are reported in Table (8.2).

d_N (mm)	6	8-10	12-14
D (mm)	10	15	20

Table (8.2): The optimal diameter (D) for the plunging tubes

The air bubbles entrained by the liquid jet penetrates into the water pool to some depth, and due to the buoyancy force these bubbles escape sidewall until they are free to rise to the water surface where they are accumulated and collected in the bubble trap. The collected air passes through the connecting tube (transparent PVC tube) (D) to an external flow meter (E) devoted to measuring the entrained air flow rate. The connecting tube was made up of a small convergent tube with 2 cm in diameter at the entrance facing the free surface of the liquid pool, 0.5 cm in diameter at the exit connected to the air flow meter apparatus. Since, the convergent connector mentioned above exhibited an important energy loss for any air flow and to allow the air flow to be guided to the bottom of the connecting tube as soon as a mass flow existed. No doubt, a part of the air entrained by the plunging jet should be emitted to the ambient atmosphere through the large aperture of the plunging tube (B).

Several air flow meters with different ranges were used to measure the entrained air, in an effort to minimize errors. Six acrylic air flow meter series FR 2000, Key Instruments with ranges of: 0.04-0.5, 0.1-1, 0.4-5, 1-10, 2-25, and 4-50 l/min and with an accuracy of ±5% of full scale reading, were used to measure the very low volumetric flow rate of the entrained air.

The flow meters are calibrated at the standard pressure and temperature delivery (STP) therefore; the measured flow rate must be corrected when used outside of its designer parameters. The air pressure at the inlet of the flow meter is more than the atmospheric pressure. Therefore, the corrected flow rate will be higher than that monitoring by the flow meter. The following formula was used to calculate the corrected flow rate at each measuring case:

$$Q_{Corrected} = Q_{reading} \times \sqrt{\frac{P_{in} + P_{atm}}{P_{atm}}} \qquad (8.2)$$

where, $Q_{reading}$ is the volumetric flow rate measured by the flow meter, $Q_{corrected}$ is the corrected volumetric flow rate at the actual conditions, P_{in} is the gauge pressure measured at the flow meter inlet (inside the bubble trap) and P_{atm} is the atmospheric pressure.

To get reliable data, it was found that a data set made up of about 10-20 measurements was necessary to perform a statistically relevant measurement of the air flow rate (Q_a).

8.3.5.1 Pressure Measurements inside the Air Trap

Before we perform the air entrainment measurements, the pressure of the entrained air at the air trap (above the water surface) was measured until an almost constant pressure was achieved inside the air trap and this means a nearly stable air flow rate to the flow meter.

Pressure measurements were performed with Druck 1400-PTX pressure transducers with a range of 0-250 mbar and an accuracy of 15% full scale. The measured mechanical pressure was converted into an electrical signal between 4 to 20 mA. This electrical signal was then digitized using a NI PCI-6280 card (National Instruments) at a sampling rate of 200 kHz and analysed using

LABVIEW software. The pressure transducer positioned in the tank cover of the bubble trap as shown in Figure (8.13).

Figure (8.14) shows an example of pressure versus time signals measured for 15 minutes with a 8 mm jet diameter, 10 cm jet length and 5.5 m/s jet velocity. The 15 minutes measuring period includes both the "jet start up" and the "quasi steady state" periods of the air entrainment.
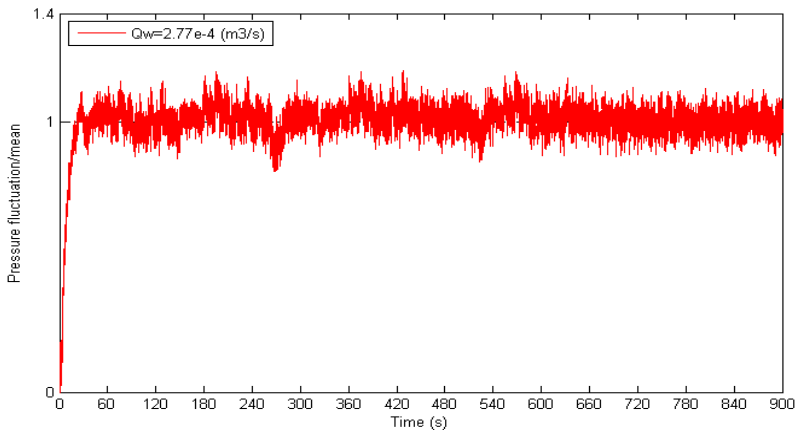
Figure (8.14): Pressure versus time at the air trap during the first 15 minutes from the jet was turned on for d_N= 8 mm, jet length 10 cm, and Q_w= 2.77×10^{-4} (m³/s). The pressure was nearly stable after approximately 10 minutes.

After the water jet is turned on, the air entrainment in the water tank started and the pressure inside the air trap increased rapidly. The constant pressure was achieved after approximately 10 minutes from the starting as shown in Figure (8.14). Therefore, the entrained air delivered to the air flow meter is more stable after 10 minutes at the jet conditions listed before. Also to get a reliable data, it was found that a data set made up of 5 to 10 measurements was necessary to perform a statistically relevant measurement of air flow rate (Q_a).

Figure (8.15) shows three examples of pressure-time signals (fluctuation of pressure) measured for increasing values of the water jet flow rate Q_w=2.77, 3.77, and 5.53×10^{-4} m³/s respectively and the measurement period for these flow rates are showed after approximately 10, 13 and 17 minutes respectively from the jet beginning. One minute of time is shown for clarity.
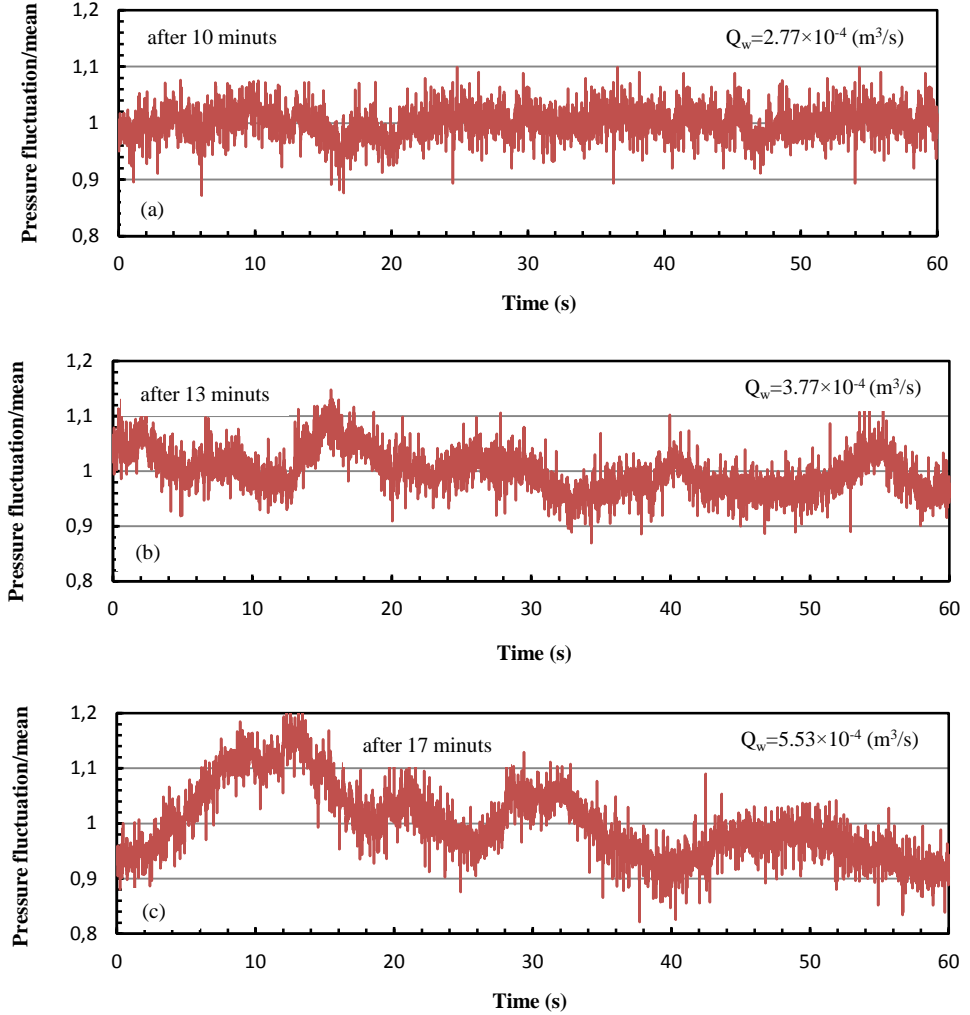
Figure (8.15): The effect of increasing the jet flow rate on the pressure fluctuation of the entrained air at d_N= 8 mm, jet length 10 cm

This example shows that, the pressure fluctuations increase with the jet flow rate and the pressure stability can be obtained at a certain time or can not be obtained.

From the figures, we can also observe that the relative amplitude of the pressure fluctuations in the time signals increases when increasing the jet velocity (at constant jet length and jet diameter). This increment may be due to an increase in the bubble formation events and is likely due to greater air entrainment and more break-up and coalescence events. It follows from the figure that maximum relative fluctuation amplitude of the pressure is obtained at the higher jet flow rate $Q_w=5.53\times10^{-4}$ m^3/s. The increase in the number of bubble pulses is due to an increase in the entrainment that consequently produces more bubble formation events.

However, the scattering of the air flow rate measurements was observed to be very small at low jet flow rates and consistently much larger when the jet increases the flow rate. Typically, the air flow rate ranges from 2.53×10^5 m^3/s to 77.3×10^5 m^3/s. Under these conditions, the relative error on Q_a varied from about $\pm$ 0,1% for $Q_a=2.5\times10^5$ m^3/s to $\pm2.2\%$ for $Q_a =77.3\times10^5$ m^3/s.

8.4 Data Acquisition System

The pressure transducer, motor to perform the displacement of the Pitot tube probe and the thermocouple are both connected to a 16-bit DAC 6259 (National Instruments), which works in conjunction with LABVIEW software, to monitoring and controlling the different values. The measured signals obtained from the pressure (transducer) and temperature (thermocouples) sensors must be properly equipped and sampled in order to be interpreted by the Acquisition software. The Acquisition System is divided into three blocks.

i). Treatment and signal conditioning
ii). Signal sampling
iii). Graphical representation and data storage

The first of them has the function to condition and filter the electrical signal of the transducers, in order to prevent the electrical noise produced by common sources such as computer monitors, power supplies, electrical network, etc., which may falsify the measurements. The equipment used is the SCXI-1000 of national instrument company.

The second block is responsible for sampling the analog signal from the SCXI-1000 module to turn it into a digital signal interpretable by the computer. It has been used for this object an acquisition card, SCXI-1303 model installed in the computer, with 16 inputs and 2 analog outputs, one of them has been designed for the pressure signals, and the other for the temperature signal.

Finally, the module for graphical representation and data storage is the graphical interface between user and machine for visualization, display and control of the facility. This module works with a number of commercial programs, and is displayed in Figure (8.16). It is seen as the signal sampled by the acquisition card, is processed by the Measurement and Automation software responsible for applying the calibration lines of transducers to convert the electrical signal into a valid physical signal. Subsequently, the physical value obtained was processed by LabView for representation and storage of this value. Given that, LabView is not able to perform operations and calculations, Matlab is used to perform this task.
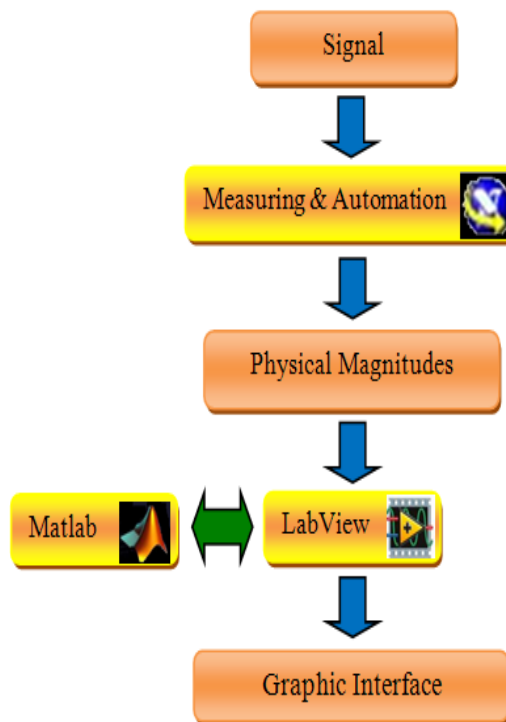
Figure (8.16): Software used and their relationship

Chapter 9

Experimental Results and Discussion of the Vertical Plunging Water Jets

9.1 Introduction

When a water jet impinges a pool of water at rest, air bubbles may be entrained and carried some way below the pool's free surface. This process is called air-entrainment or aeration by a plunging water jet. The main objective of this chapter consists in determining the plunging jet flow patterns, the influence of the jet parameters such as jet velocity, jet diameter, and jet falling length on the air-entrainment characteristics such as inception velocity of the entrained air, air-entrainment rate, and bubbles penetration depth in a plunging jet system using vertical circular nozzles. The instability of the jet influenced by the jet velocity and falling length as well as the jet velocity distributions is also probed.

Some parameters of interest in the plunging water jet system such as bubbles maximum penetration depth, the width of the two-phase mixture (gas and water), and the inception velocity of the entrainment air can be observed using a digital photographic technique as that mentioned in Chapter (4). An empirical correlation for vertical plunging jets is presented to predict the jet distribution velocities, jet penetration length, and air-entrainment rate as a function of jet parameters are predicted. Experimental findings can serve to validate and complement the available experimental and calculation results.

9.2 Jet Flow Characteristics

The jet length (x_1) is defined as the vertical distance that the jet travels from the issuance point to the impact with the water surface. Figure (9.1) shows the separation distance between the nozzle outlet and the air/water interface denoted by x_1. The origin of the cylindrical r and x coordinate system coincides with intersection point (plunging point) of the jet centerline and the free water surface. The axial coordinate, x, is pointing downward away from the free surface while the radial one, r, is measured along the horizontal free surface.
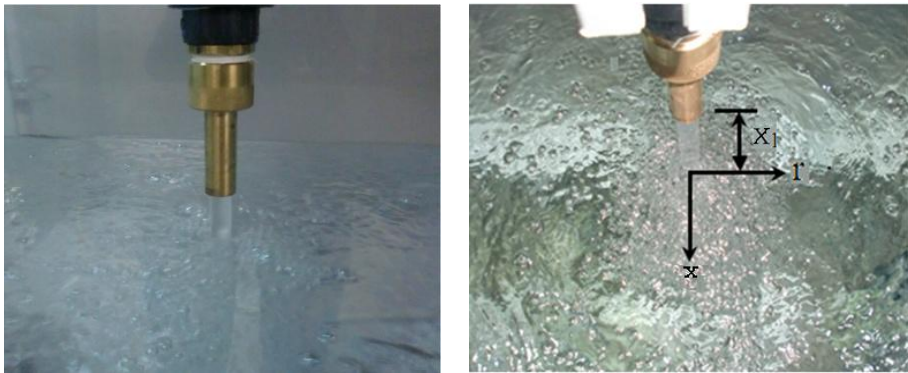
Figure (9.1): Photograph of above-water view of the jet impact site, free impinging jet and coordinate system

The turbulent water jet passing through the atmosphere and plunging into the water pool entrains into the pool an important amount of air and it forms a submerged two-phase region of considerable interfacial area. The submerged jet under the plunging point maintains its identity for a short depth along which it is surrounding by a sheath of entrained air bubbles. The collapse of the air sheath results in the formation of a multitude of very small, closely packed gas bubbles (primary bubbles) which move through the water pool downwards and also laterally, away from the jet axis, as they are entrained by the momentum of the jet.

Owing to the momentum transfer from the high velocity air-water (biphasic) jet, the amount of the entrained surrounding water increases and mixes with the two-phase region, in this way the velocity of the biphasic jet decreases steadily. As a consequence of the multiple coalescence of the primary bubbles, bigger bubbles are formed which are entrained further. When the diameter of these "secondary" bubbles increases above a certain value, so that their buoyancy exceeds the drag

exerted by the local downwards oriented velocity field, they will escape from the jet and rise to the water path surface. The submerged jet ceases thus to be biphasic and continues its motion until all its energy has dissipated. Typical values for the diameters of the bubbles escaping at the lower end of a water-air biphasic jet 2×10^{-3} - 3×10^{-3} m were observed by Suciu and Smigelschi (1976). Partially all the entrained gas escapes the biphasic jet at the bottom of the cone, as secondary bubbles. Only few of these escape laterally, before the base of the cone. The rising secondary bubbles delimit a roughly cylindrical volume which encloses the conical one. The penetration depth (H_p) and the diameter of the cone base define the volume occupied by the submerged biphasic region.

We must mention than at the cone base there is an spherical biphasic region due to the fact that the bubbles in the cone center penetrates more deeply than the bubbles located at the cone sides. The global form of the submerged biphasic system is an outlined conical volume, having the apex near the surface of the water pool, in the impact point of the impinging jet as shown in Figure (9.2). Within the conical volume, a strong downwards motion of the contained bubbles is visible. The height of the cone (H_p) is the maximum depth to which, in given conditions, the bubbles penetrate into the water layer.
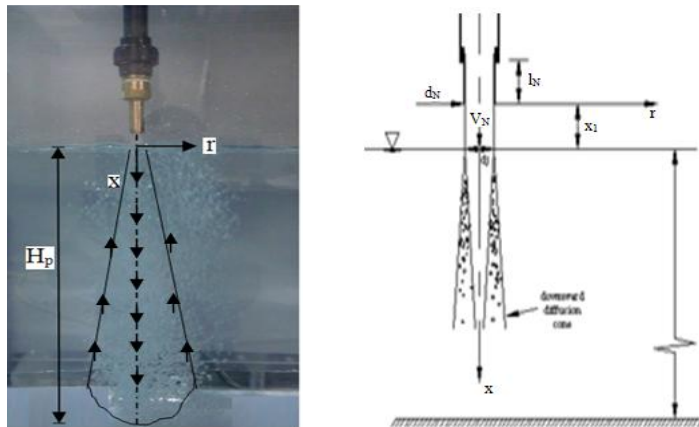
Figure (9.2): Vertical circular plunging jet (a) high-speed photograph (b) sketch of air entrainment

A series of experimental tests were conducted in the test facility. Each test was characterized by selecting a combination of jet length (x_1), jet diameter (d_N) and jet flow rate through the nozzle (Q_w). A summary of the testing matrix is presented in Table (9.1).

Parameter	Range
Nozzle diameter (d_N)	4 to 14 mm
Nozzle height (x_1)	0.025 to 0.3 m
Nozzle velocity (V_N)	2.5 to 13 m/s
Reynolds number ($Re_N = \rho_w V_N d_N / \mu$)	19,920 to 90,640

Table (9.1): A tabulation of experimental data for jet impingement into water pool

The range of employed flow parameters ensures a turbulent flow at the nozzle exit. The length-to-diameter ratio (l_N/d_N) of the nozzles were varied between 3.33 and 5 accordingly, the water flow at the nozzle exit was a turbulent and not fully developed jet. Fully developed jet flow leads to higher jet penetration length (H_p). This is an advantage in some industrial application that needs large entrained air.

The water jet impacted onto a water surface at an angle of $90°$, assuming free fall of the water after leaving the nozzle; the jet impact velocity (V_1) at the liquid surface ($x = x_1$), can calculated using Bernoulli equations as:

$$V_1 = \sqrt{V_N^2 + 2gx_1}$$

(9.1)

According to the jet velocities at the nozzle exit, jet lengths, and Equation (9.1), this yields impact velocities (V_1) between 2.596 m/s and 13.22 m/s in the present study.

9.2.1 Jet Instability and Free Surface Deformation

Air entrainment that occurs by water jets issued by circular nozzles is sensitive to the water jet velocity. A water jet with a relatively smooth surface issued from the nozzles produces air entrainment that takes place mainly at the surface of the water tank. As the water jet velocity increases, the surface of the water jet became roughened and entraining air occurs by the rough jet mechanism. This results in greater air flow into the water tank.

As the water jet penetrates into the ambient air, a gaseous film develops along its trajectory as an envelope surrounding its surface. The formation of a gas film adjacent to the surface of the jet is associated with the relative velocity between

gas and liquid phases, resulting in the generation of surface jet instabilities and deformations. According to previous studies, both axisymmetric and asymmetrical deformations can occur on the jet surface depending on its length, nozzle exit velocity and perhaps the nozzle diameter and surface tension (Qu, 2011).

An example of shadowgraph images obtained in the experiments is shown in Figure (9.3), which illustrates the jet surface instabilities, and the effect of jet surface instabilities on the gas entrainment.
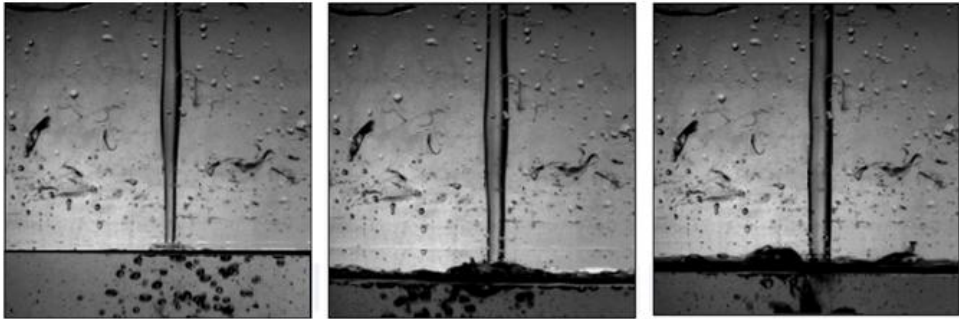
Figure (9.3): Jet instability and surface deformations at impact V_N=2.2 m/s, x_1=20 cm, and d_N=8 mm

The left picture shows the undisturbed jet, which does not entrain a lot of air. If the same jet is disturbed, bubbles are entrained immediately (right picture). The large surface waves caused by the jet are almost stationary here.

9.3 Inception Velocity of the Air Entrainment

It is observed from the experiments that air entrainment by the plunging jets takes place when the jet impact velocity (V_1) exceeds a critical value, V_e, called inception, threshold, or onset velocity, which is dependent among other things, on jet instability and its interaction with turbulence (Cummings and Chanson, 1997 a,b).

However, the inception of the air bubble entrainment is not a precise condition (Mckeogh 1978, Ervine et al. 1980, and Cummings and Chanson 1999). For example, entrainment of bubbles of less than 0.2 mm diameter is very difficult to detect visually. Further, a jet may entrain one or a few bubbles only every few minutes and the selection of the investigation period is critical.

To determine the minimum entrainment velocity for a given nozzle, a series of experimental tests were conducted by selecting a combination of jet lengths ranged from 0.015 to 0.3 m and jet diameter between 8 and 14 mm (see Table 9.1). Where, the water was first circulated with the nozzle submerged beneath the liquid level in the water tank. After all the air was purged from the line, the control valve was adjusted to set the jet flow rate slightly below the minimum required to entrain air. By maintaining the flow at this rate, the nozzle assembly was lifted slowly to set the nozzle at the desired height above the liquid surface (x_1). The jet flow rate was then gradually increased until bubbles were observed. From the flow rate and the jet diameter at the plunging point, the minimum entrainment velocity was calculated. Although this procedure was used to obtain the photographic data for the maximum bubble penetration depth with a slightly different procedure was required to obtain the data at velocities above the minimum entrainment velocity.

In the present experiments, the inception velocity (V_e) for the air entrainment was defined for d_N=14 mm as the flow conditions for which one or three bubbles, were entrained during one-minute period. But, in the smaller jet diameters d_N=8 and 10 mm a longer investigation period was selected because of occasional entrapment of fine bubbles: inception was defined when less than three bubbles were entrained during a 3 minutes period, in the absence of bubbles in the plunge water pool.

Depending on the initial jet conditions, an empirical correlation was found to correlate the inception velocity (V_e) with the ratio of the jet length to nozzle diameters (x_1/d_N) given by:

$$V_e = C_1 (\frac{x_1}{d_N})^{C_2} \tag{9.2}$$

where, C_1 and C_2 are empirical constants based on the experimental conditions. As a consequence of this study, the results obtained gave values for C_1 and C_2 of 0.9 and 0.2 respectively. An excellent agreement between the measured V_e and the V_e calculated values by using Equation (9.2) was found with R^2= 0.97 and within ±5% error. Figure (9.4) refers to experimental findings and illustrates a comparison between the calculated values of V_e and those observed experimentally.
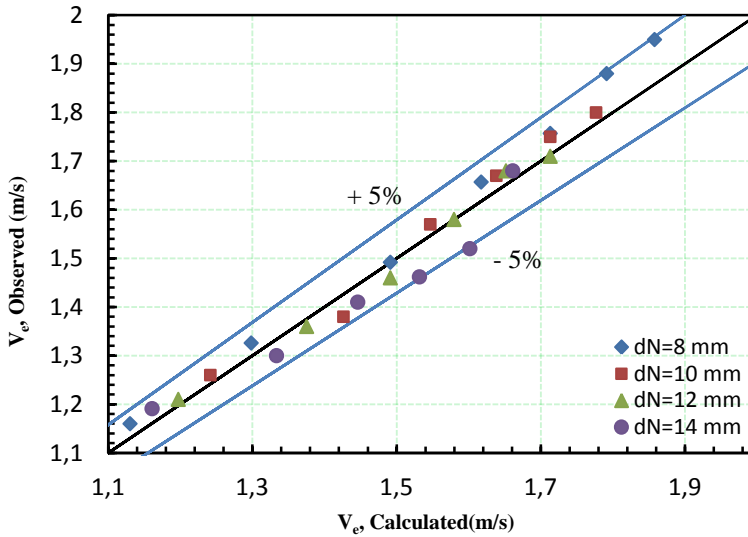
Figure (9.4): Inception velocity correlation

The results indicate that the inception velocity V_e increased with increasing the jet length x_1/d_N for a given experiment. During the present study, the jet length to jet diameter (x_1/d_N) was between 3.13 and 21.43. Visual observations showed a rapid jet contraction with increasing distance x_1 and increasing jet velocity V_N. It is hypothesised that the jet contraction led to a damping of jet turbulence and hence an increase in inception velocity consistent with the experimental trend.

Equation (9.2) is somewhat similar to the empirical correlation obtained by Bín (1993) with different values for the correlation coefficients;

$$V_e = 1.4 \left(\frac{x_1}{d_N} \right)^{0.164}$$

(9.3)

This correlation obtained for short cylindrical nozzles $(l_N/d_N \leq 3)$ with $d_N \geq 0.007$ m and within $x_1/d_N = 1\text{-}100$. The difference between the correlation coefficient may be due to the range of nozzle aspect ratio and the jet length (x_1/d_N).

However, the used V_N was always more than the required V_e in order to ensure air entrainment in the tank under every experimental condition throughout the experiments of this study.

9.4 Penetration Depth of the Air Bubbles

One of the important factors in the plunging jet systems is the penetration depth of the entrained bubbles, which affects the size of the submerged two-phase region where the transfer processes occur. The performance of the aeration process resulting from air entrainment due to plunging jets is highly affected by the residence time of the entrained bubbles. Therefore, the residence time is related to the bubble penetration depth (H_p) into the water tank. Five parameters affect the rate of air entrainment. These parameters were varied in the experiments as follows;

i). The jet velocity at the nozzle exit V_N, was varied from 2.5-13 m/s by increasing the acting on the regulator valve.

ii). The jet nozzle diameter d_N, was varied from 0.004 m to 0.014 m by placing in turn on the underside of the vertical rigid PVC tube.

iii). The water jet length x_1, which was the distance from the nozzle exit to the water surface, was varied from 0.025 m to 0.030 m.

iv). The nozzle length to diameter ratio l_N/d_N, we used in the present study short circular nozzles, $l_N/d_N \leq 5$.

v). The physical properties of the water that controlled by Ohnesorge number, ($O_h = \mu/\rho\sigma d_N$), it were constant at the ambient temperature T= ±22 ^{o}C.

The three major parameters mentioned above (V_N, d_N and x_1) were varied in turn to produce a comprehensive array of data in the present study. For each combination, a set of underwater high-speed movies of the two-phase region under the plunging point was taken. Several hundred results were obtained and it has not been possible to produce all the results in the interests of brevity.

Parameter		Range
Nozzle diameter	**(d_N)**	0.004 to 0.012 m
Nozzle height	**(x_1)**	0.025 to 0.030 m
Nozzle velocity	**(V_N)**	2.5 to 9.5 m/s
Nozzle aspect ratio	**(l_N/d_N)**	3.33 to5

Table (9.2): The experimental conditions of the air bubble penetration depth

During all of the experimental conditions of Table (9.2), the bubble penetration depth was always less than the water depth in the tank. The penetration depth H_p was measured by direct visualization technique using a CCD camera and illumination system as mentioned before in Chapter (4). A total of 4105 images at 1 KHz, i.e., over a 10 second period with CCD arrays had a resolution of 480x942 pixels were recorded at each test run to perform the penetration depth of the entrained bubbles.

An example of the typical shadowgraph images is shown in Figure (9.5) by four instantaneous images of the air bubble plume in the water tank, which illustrate the variability in the shape of the two-phase region, a phenomenon related to intermittency.

(a)   (b)   (c)   (d)
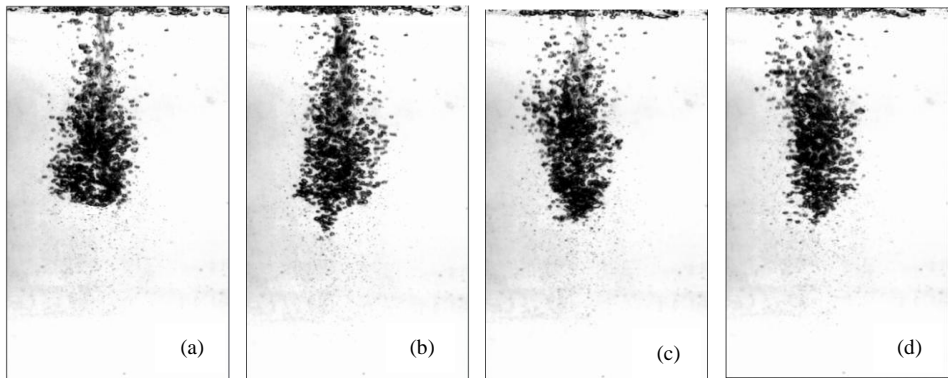
Figure (9.5): Four instantaneous realization of the cone-like plume of bubbles formed by a vertical plunging water jet. In all the four cases, the jet diameter was d_N=8 mm and the jet velocity was V_N= 2.2 ms^{-1} and the jet length was 10 cm

The maximum depth of the bubble penetration (H_p) is defined as the vertical distance between the free water surface to the lower end of submerged two-phase region (the point at which the gas arrives) in the water pool as illustrated in Figure (9.5).

Although accurate observations are difficult to carry out since the lower limit of the bubble swarm fluctuates continuously with time (the shape of the plume is not completely stable) also the gas sheath is not necessary always the same in shape and its variations are complicated, as displayed in Figure (9.5). A time average of the entrained bubbles was necessary in order to calculate the maximum bubble penetration length this can be estimated by the average

distance obtained from the accumulated image. Looking again at the shadowgraph images depicted in Figure (9.5), one can easily obtain a penetration depth by localizing the lowest large bubbles. For time-averaged gas plume pictures, this is more difficult, since the edges of the plumes are smeared out. A slight estimation error is thus expected and needs to be considered when comparing the experimental data with the other calculations.

Figure (9.6) shows six representative plume images for jets with an impact velocity of V_N= 1.5 m/s and V_N= 2.2 m/s and jet length of 2.5, 5 and 10 cm respectively. The jet with the higher flow rate (higher, V_N) entrains more bubbles than that the jet with low flow rate. However, due to the fluctuation of the plumes snapshots are not conclusive.

(a) V_N=1.5 m/s, x_1=2.5 cm	(c) V_N=1.5 m/s, x_1=5 cm	(b) V_N=1.5 m/s, x_1=10 cm

(d) V_N=2.2 m/s, x_1=2.5 cm	(e) V_N=2.2 m/s, x_1=5 cm	(f) V_N=2.2 m/s, x_1=10 cm
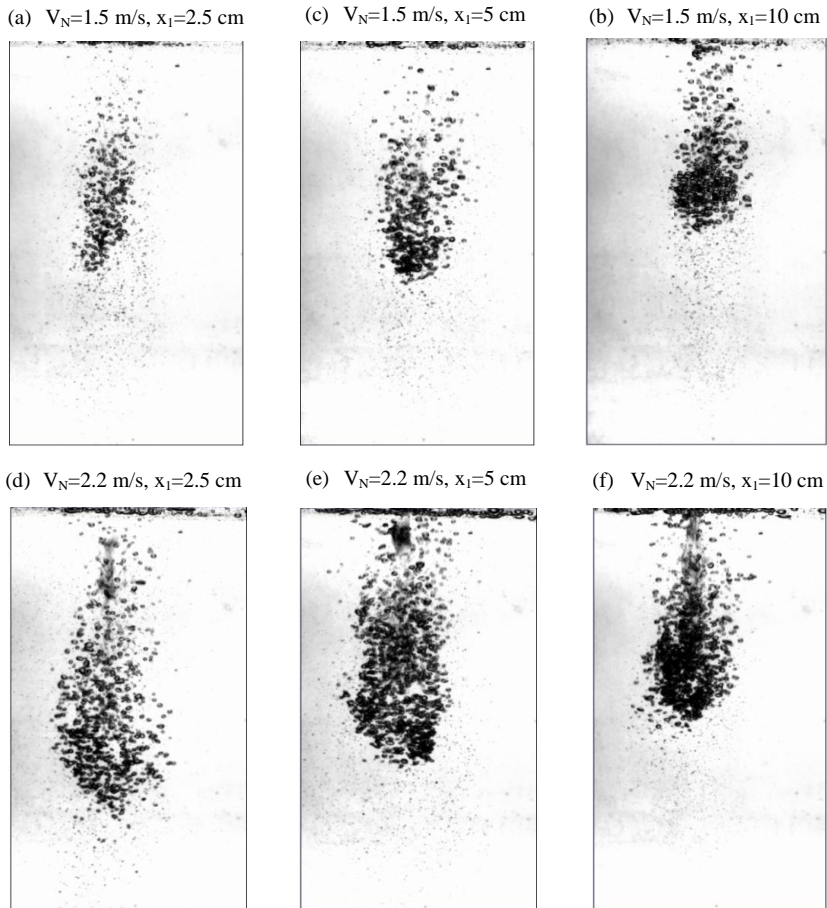
Figure (9.6): Six instantaneous realization of the cone-like plume of bubbles formed by a vertical plunging at d_N=8 mm and different jet velocity and jet length

For the calculation of the bubble penetration depth, we implemented an application using the Image Processing Toolbox of Matlab, which involves several processing steps for each image, e.g. background subtraction, thresholding, filtering, add the processed images (accumulation) as the same as those explained in Chapter (4) for horizontal buoyant gas jets.

Figure (9.7) shows an example and comparison between jets V_N=1.5 m/s and V_N=2.2 m/s of resultant added images for the cases mentioned previously of the figure (9.6). From this figure, we can observe an obvious difference between the different plums, especially in the penetration length of the air bubbles which occupies a volume for a large percentage of the test record.

Despite having the same impact velocity, it can be observed that the left plume is less populated with bubbles than the right one; however, it has a larger penetration depth (H_p). This reflects the general trend observed in this experiment; also, the higher velocities (or flow rates) produce higher entrainment rates (Q_a). The phenomenon could perhaps be physically explained as follows: increasing the jet velocity (V_N) with a fully developed turbulent jet flow hence with an appreciable turbulence content for a given diameter may trigger jet-interface instabilities, which when impacting on the water surface entrains more air bubbles beneath the surface. In turn, jet momentum is diffused by the presence of bubbles, causing a reduction of its penetration depth (H_p). The jet-interface instability phenomenon, is a function of the initial turbulence content, details of the nozzle design and length of free-falling jet, is therefore a key element affecting its lateral spreading and diffusion and penetration depth.

Alternatively, larger flow rates in combination with jet-interface instabilities could generate larger air bubbles which are more buoyant and predominantly localized just below the impact point, and hence escape rapidly the gravity effect leading thereafter to a shorter penetration (see Igushi et al. 1998).

The bulk of entrained bubbles did not penetrate deeply and never reached the bottom of the tank, fine bubbles with sizes less than 0.5 to 1 mm were consistently observed at the deeper depths. Visual observations showed that some tiny bubbles could be trapped in large vertical structures for a relatively long time before being ejected to another eddy or toward the free surface. Fine bubbles were consistently observed next to the bottom and, in some cases, bubbles trapped in turbulent eddies could remain next to the floor for over two or three minutes.
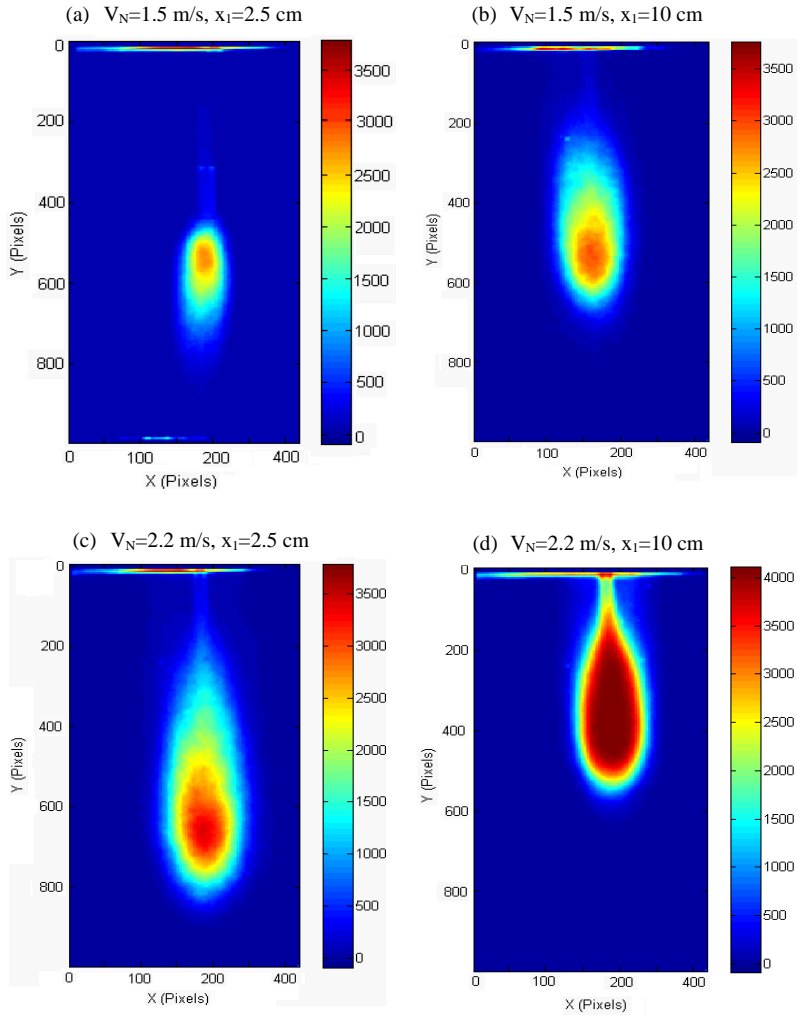
Figure (9.7): Time averaged images for a jet impact velocity 1.5 and 2.2 m/s and jet lengths of 2.5 and 10 cm respectively at d_N=8 mm.

The next section shows the effect of jet parameters such as x_1, V_N, and d_N on the bubble penetration depth, with the other variables held constant.

9.4.1 Effect of Jet Length (x_1)

The distance from the nozzle exit to the water surface was varied from 2.5 to 30 cm through the experiments. Figure (9.8) shows the relationship between H_p/d_N and x_1/d_N for various jet velocities and jet diameters. A comparison of H_p/d_N with other experiments is also shown.
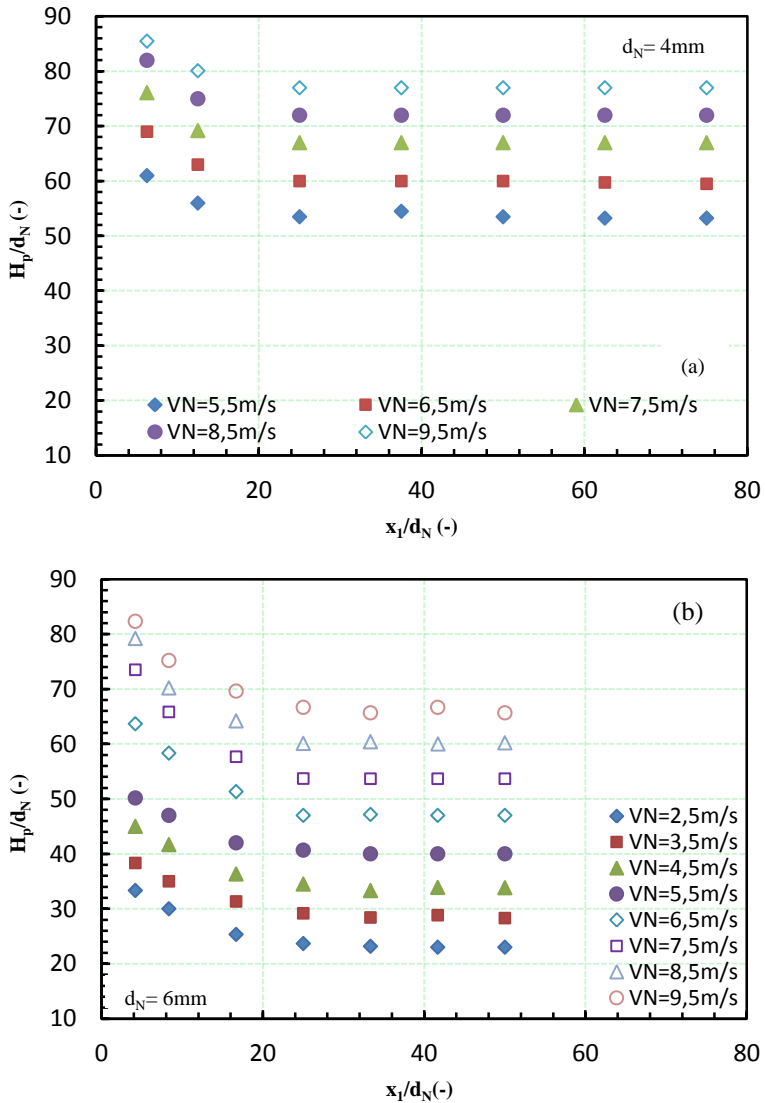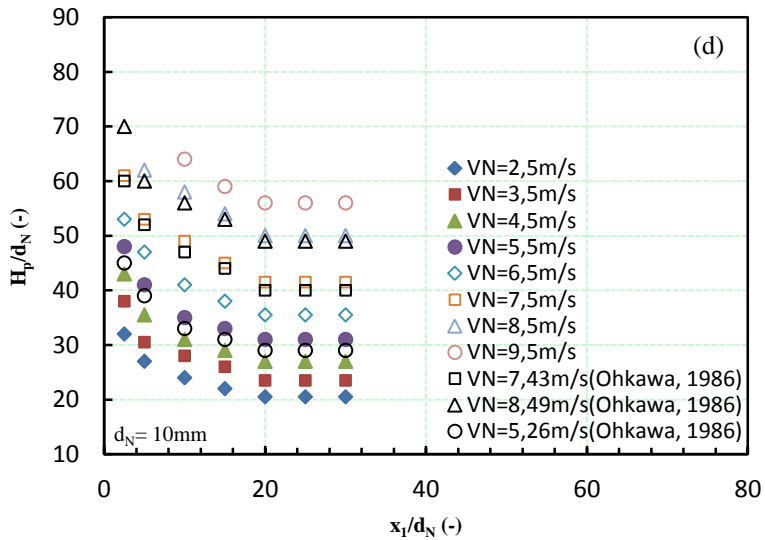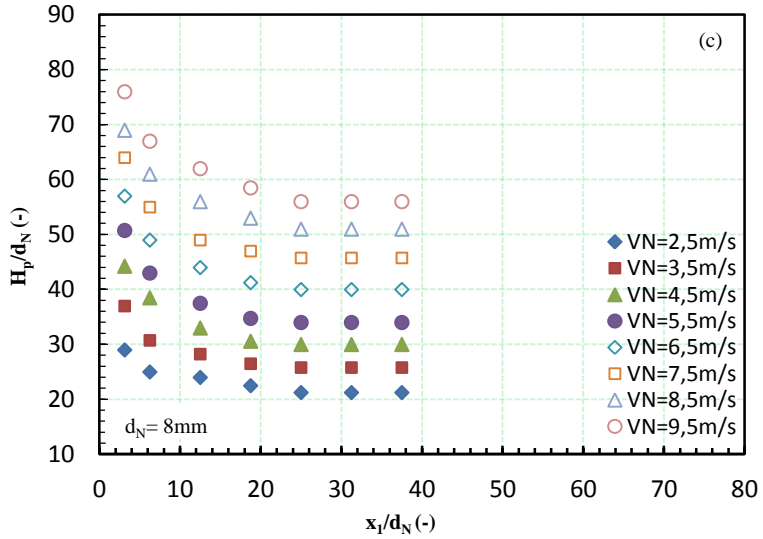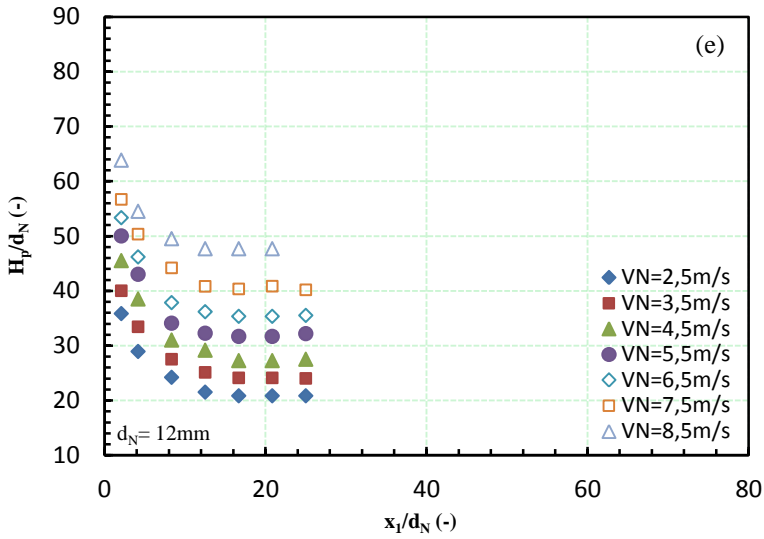
Figure (9.8): Dependence of the penetration depth ratio H_p/d_N on the jet length ratio x_1/d_N for various jet velocity V_N and nozzle diameters d_N

The results for each case of Figures (9.8)-(a) to (e) showed that the penetration depth ratio (H_p/d_N) decreased when the jet length ratio (x_1/d_N) increased, until a point at $x_1/d_N \simeq 25$ was reached where the ratio of the penetration level remained constant with the increasing of the jet length. Below this point, the values of H_p tend to decrease gradually with the x_1 satisfying approximately the following relation:

$$H_p / d_N \propto (x_1 / d_N)^{-0.2}$$

(9.4)

The decrease in H_p with x_1 can be considered due to the increase of the buoyancy force of the entrained bubbles as a result of the increase in the air entrainment rate, Q_a as will show in the next section of air entrainment rate. The air entrainment increase with the jet length as a result of the increase in the jet surface roughness, ε as shown in Figure (9.3) this fact has been also suggested by other researchers (e.g., Kusabirki et al. 1990, Ohkawa et al. (1986), and McKeogh and Ervine 1981). The air bubbles entrained into the water give a buoyancy effect to the diffusion of the jet and contribute to a velocity decrease in the diffusion region. These effects may result in bestowing a limit to the bubble diffusion depth. However, there is a limit to the depth to which bubbles penetrate

in this ordinary jet system. This is disadvantageous when the liquid in an apparatus of large depth has to be aerated.

However, the change of H_p/d_N with x_1/d_N for $d_N=10$ mm are found to be similar to those obtained by Ohkawa et. al (1986) as shown in Figure (9.8-d) at corresponding operation conditions, $l_N/d_N=5$, $d_N=10$ mm, $x_1=2.5\text{-}75$ cm and $V_N= 7.43\text{-}10.61$ m/s.

Suciu and Smigelschi (1976), and Ohkawa et al. (1987) have observed a similar tendency that H_p/d_N decrease with x_1/d_N ratio until $x_1/d_N =20$, being almost constant above this range. This difference in the range of x_1/d_N with our results is considered to be mainly attributed to the difference among the nozzle design.

9.4.2 Effect of Jet Velocity (V_N)

Figure (9.9) illustrates the variation in bubble penetration depths (H_p) as a function of the initial jet velocity (V_N) with the jet length, x_1 and nozzle diameter, d_N as parameters within almost the same ranges of operating conditions.

(b) d_N= 6mm

(c) d_N= 8mm
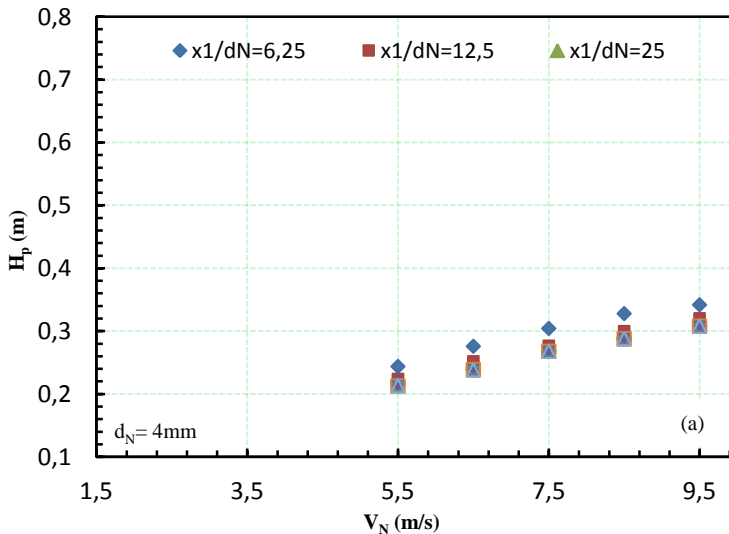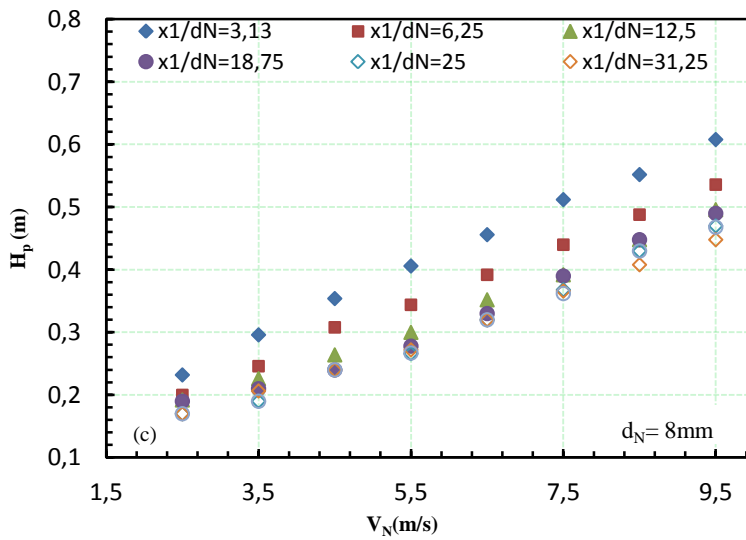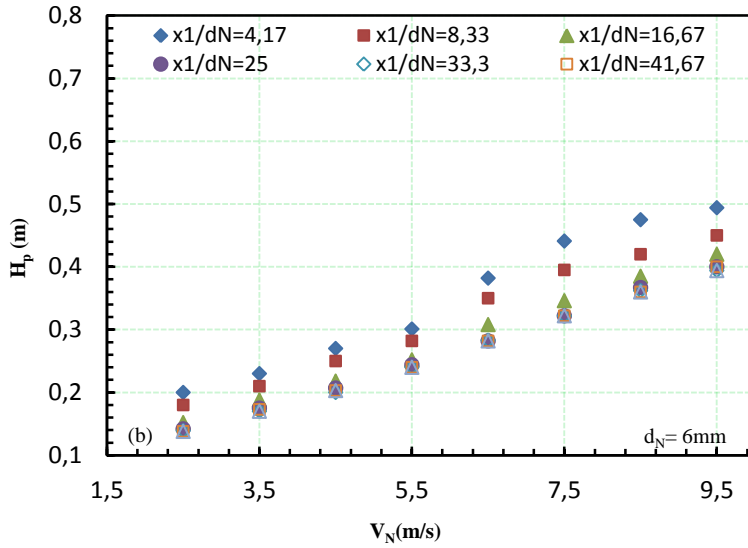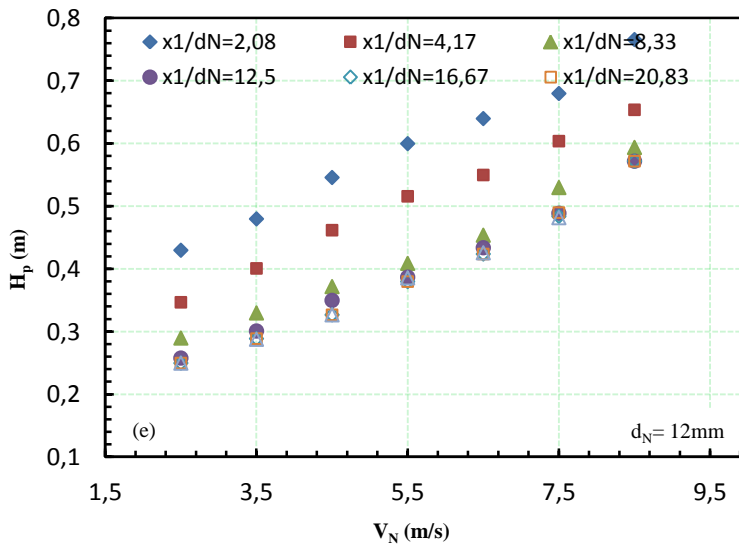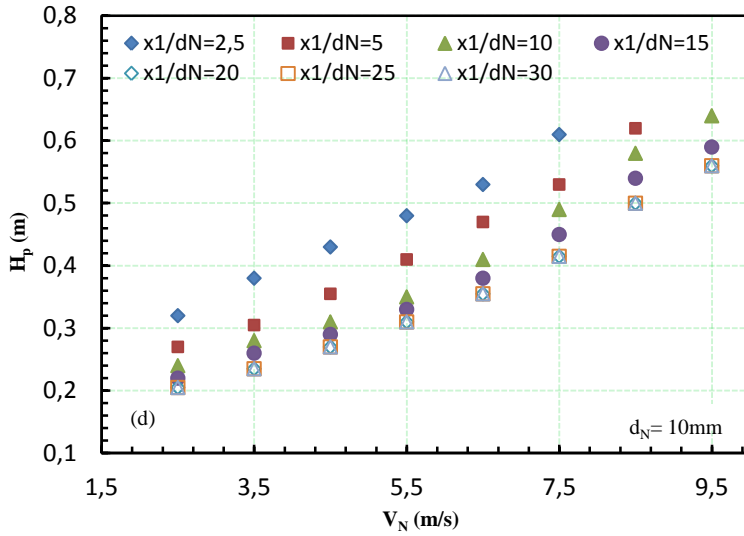
Figure (9.9): Variation of penetration depth with jet velocity

Figures (9.9)-(a) to (e) show that the penetration depth H_p tends to increase when increasing the initial jet velocity for all the jet diameters and decreases when increasing the ratio x_1/d_N. It means that, penetration depth is directly proportional to the jet velocity, irrespective of nozzle diameters also, the increase in H_p with increasing V_N and d_N may be due to the increase in the momentum of the water jet.

However, the penetration depth H_p depends largely on the downward velocity field in the two-phase region. To attain a deeper bubble penetration, it is required to provide enough downward water flow to overcome the buoyancy force of the bubble produced by the water jet.

9.4.3 Effect of Nozzle Diameter

Figure (9.10) shows the effect of the initial jet diameter (d_N) on the bubble penetration depth (H_p) for a constant jet velocity of 5.5 and 8.5 m/s and different jet lengths.

Under the same jet velocity (V_N), the bubble penetration depth increases with the jet diameter for all the jet lengths. Maximum bubble penetration depth has been achieved by the higher nozzle diameter than for the other nozzles tested. Also under the same jet diameter, the penetration depth at the lower jet lengths (x_1) is greater than for the larger lengths. However, the jet of 4 mm diameter was observed to have the lowest values of H_p among all nozzles tested.

The H_p at a low V_N tends to be smaller for the smaller nozzle diameters, but is larger compared to that in the large nozzle diameter at a given V_N. The cause probably seems to be due to the situation that the shape and surface roughness of the jet at the plunging point that may be dependent on the l_N/d_N ratio differs between a low and high V_N. As a result, the size of the bubbles formed and the buoyant effect on their bubbles also differ between the types of nozzles.
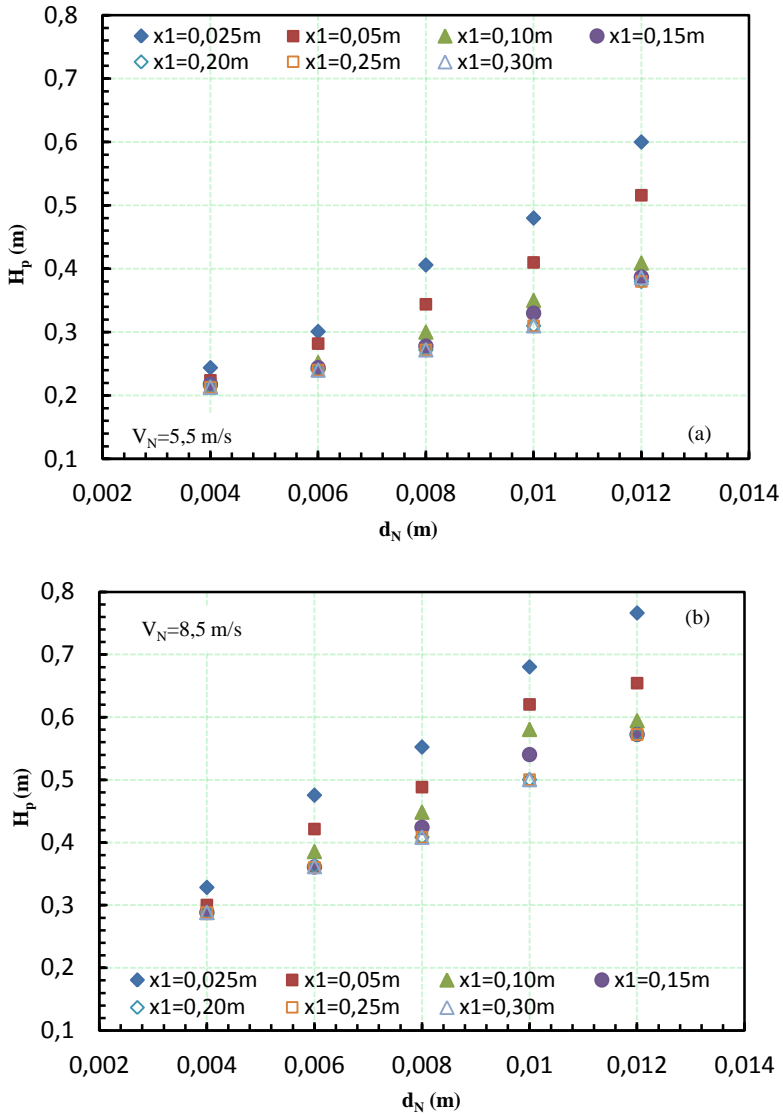
Figure (9.10): Variation of penetration depth with jet diameter

9.4.4 Effect of Jet Froude Number (Fr$_0$)

Figure (9.11) shows the effect of the jet Froude number (Fr$_0$) on the bubble penetration depth ratio (H$_p$/d$_N$) for jets 4 and 12 mm and the jet length ratio (x$_1$/d$_N$) is a parameter.
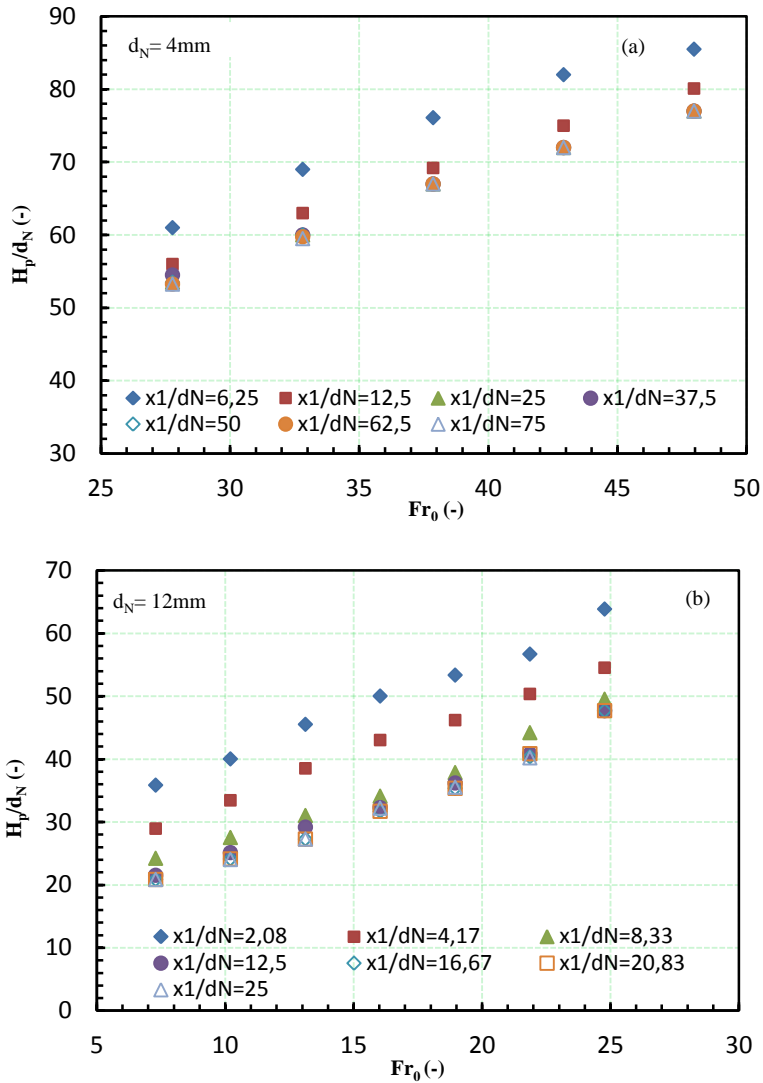
Figure (9.11): Jet penetration depth H_p against Froude number

The dependency of the Froude number (Fr_0) on the dimensionless penetration depth (H_p/d_N) was found to be similar for the different nozzle diameters. Increase the jet Froude number leads to increase the penetration depth. These results suggest that the change in the jet shape along the nominal jet length is similar for different nozzle aspect ratios below $l_N/d_N \leq 5$, although the initial level of turbulence generated in the nozzle is resulted to the nozzle configuration.

9.4.5 Correlations of Bubbles Penetration Depth

In this section, we will obtain and verify expressions for the penetration depth (H_p) against an extensive set of experiments. Since these expressions will be valid only for plunging water jet system with the same operation conditions that are listed in Table (9.2).

Variable $V_N d_N$, is a typical term was first studied by Suciu and Smigelschi (1976) from a semitheoretical consideration of H_p in the submerged biphasic diffusion region of vertical plunging water jet systems. This variable has been also used successfully by other researchers for the prediction of H_p in other vertical plunging water jet systems.

Figure (9.12) shows the values obtained for the bubble penetration depth H_p when plotted against the term $V_N d_N$ at a jet length $x_1 = 30$ cm also the figure includes a comparison with the results obtained from the empirical relationships of Suciu and Smegelshi (1976) and McKeogh and Ervine (1981), where the penetration depth is determined.
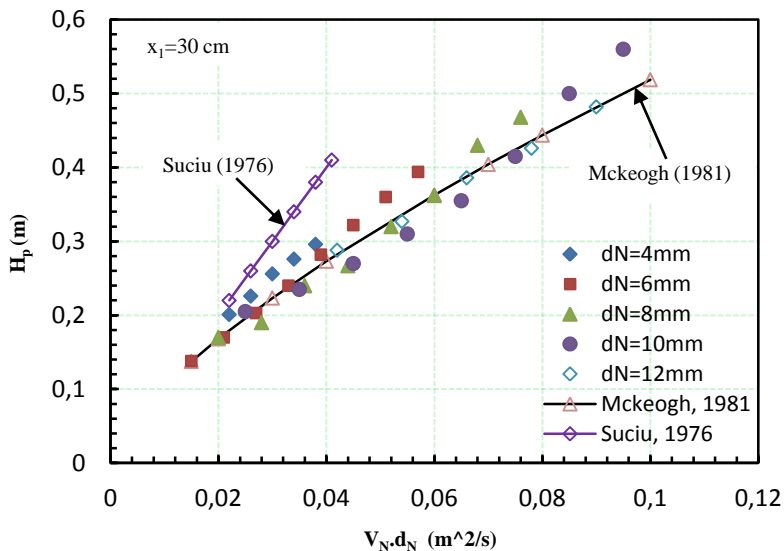
Figure (9.12): Relationship between penetration depth and jet parameters ($V_N d_N$)

From the results and the determination coefficient ($R^2 = 0.95$) it turns out that the term $V_N d_N$ has a great influence on the bubble penetration length and the relationship given by the following form is predicted well the experimental results:

$$H_p = C_3 (V_N d_N)^{C_4}$$

(9.5)

where, C_3 and C_4 are constants that have the values of 2.65 and 0.70 respectively. McKeogh and Ervine (1981) proposed a similar correlation but with different values for the constants C_3 and C_4 that has values of 2.6 and 0.7 respectively. Also, similar experiments were carried out by Suciu and Smegelshi (1976), they proposed a linear relationship given by:

$$H_p = 10(V_N d_N)$$

(9.6)

However, the results obtained from the present study which covered a more comprehensive range of $V_N d_N$ values and showed that the linear relationship does not adequately describe the correlation. It should be noted from figure (9.13) that the curve obtained by the present study correlates well the data obtained by McKeogh and Ervine (1981). Also, many different values of C_3 and C_4 have been reported by other researchers such as Ohkawa et. al., (1986).

The bubble penetration depth, H_p depends not only on $V_N d_N$ but also on the ratio of x_1/d_N and the nozzle aspect ratio l_N/d_N (e. g., Kumargi and Endoh, 1983). To correlate the H_p in terms of ($V_N d_N$), the jet length ratio (x_1/d_N) and for nozzle aspect ratio (l_N/d_N) the following correlation was investigated:

$$H_{p.Cal.} = C_5 (V_N d_N)^{C_6} (\frac{x_1}{d_N})^{C7} (\frac{l_N}{d_N})^{C_8}$$

(9.7)

where, C_5, C_6, C_7 and C_8 are empirical constants based on the experimental conditions. Figure (9.13) shows a comparison between the values of H_p calculated and those measured in the present study.
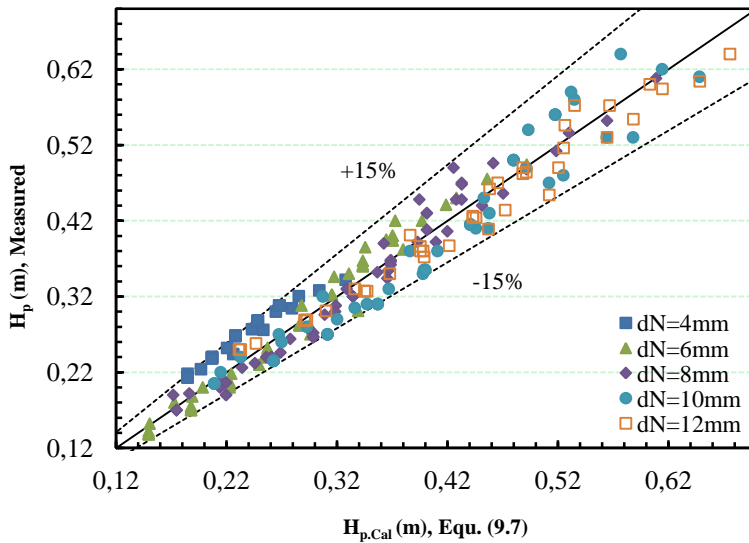
Figure (9.13): Comparison between H_p calculated from Equ. (9.7) and those measured

An excellent agreement between the measured H_p and the H_p calculated by Equation (9.7), can be observed in the last figure with $R^2 = 0.95$ and within $\pm15\%$ error. As a consequence of this study, the values for C_7 as illustrated in table (9.3) depended on the range value of (x_1/d_N) as below or above 25, as illustrated before in section (9.4.1).

x_1/d_N	C_5	C_6	C_7	C_8
< 25	5.3	0.68	-0.2	-0.12
> 25	3	0.68	0	-0.12

Table (9.3): The values of C_5 to C_8 calculated by Equ. (9.7)

To correlate the penetration depth, H_p on the basis of the non-dimensional analysis, other correlation was then carried out by plotting the results of the non-dimensional penetration depth obtained from the experiments against the dimensionless jet operating parameters as the Froude number (Fr_0), the jet length ratio (x_1/d_N) and the nozzle aspect ratio (l_N/d_N). The bubble penetration depth ratio H_p/d_N was shown to be given by the following correlation:

$$\frac{H_p}{d_N} = C_9 (Fr_0)^{C_{10}} (\frac{x_1}{d_N})^{C_{11}} (\frac{l_N}{d_N})^{C_{12}} \tag{9.8}$$

Figure (9.14) shows a comparison between the H_p/d_N values calculated by the relationship (9.8) and those measured experimentally. An excellent agreement between the measured and those calculated values can be observed $R^2 = 0.94$ and within ±15% error.
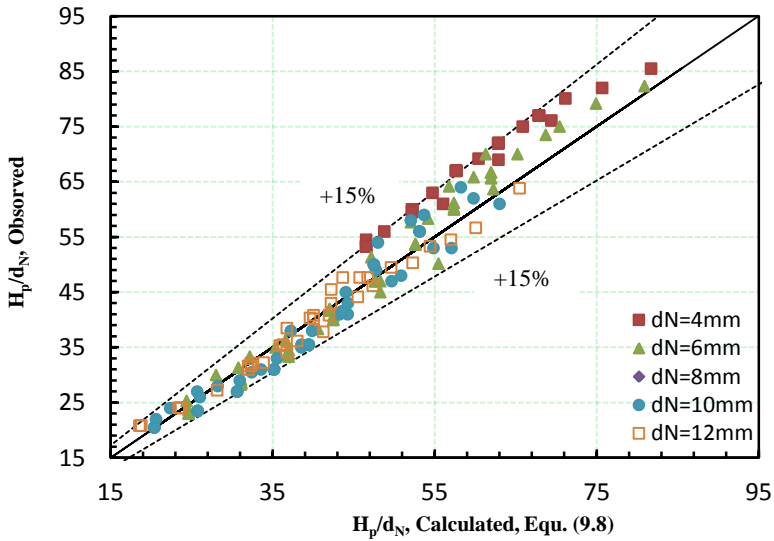
Figure (9.14): Comparison of H_p/d_N calculated from Eqs. (9.8) and with those measured

The result obtained by fitting to equation (9.8) gave values for C_9, C_{10}, C_{11} and C_{12} shown in Table (9.4). The value of C_{11} changes depending on the range of x_1/d_N, below or above 25, above 25 the values of H_p/d_N were constant with the increment in x_1/d_N. Equation (9.8) is applicable for the jet conditions as illustrated in Table (9.2).

x_1/d_N	C_9	C_{10}	C_{11}	C_{12}
< 25	9.5	0.69	-0.2	-0.12
> 25	5.7	0.69	0	-0.12

Table (9.4): The values of C_9 to C_{12} calculated for Equ. (9.8)

Equations (9.7) and (9.8) can be used for predicting the bubble penetration depth and hence the size of the submerged two-phase region in the vertical plunging water jet systems within the range of initial condition used.

9.5 Volumetric Flow Rate of the Entrained Air Bubbles (Q_a)

In this section, we will investigate the amount of air bubbles that it is entrained with the plunging water jet and describe expressions for the rate of the air bubbles entrained.

For a jet velocity slightly greater than the inception velocity, individual air bubble entrainment was observed. For larger jet velocities ($V_1 > V_e$), an unstable air cavity developed at one point along the impingement perimeter. The air cavity position changed with time in an apparently random manner. At larger speeds, the air cavity developed all around the perimeter and most air was entrained by elongation, stretching and breakup of the ventilated cavity. Visually most entrained bubbles tended to follow a somewhat helicoidal trajectory.

The three major parameters mentioned above (V_N, d_N, and x_1) were varied in turn to produce a comprehensive array of data. Also, several hundred results were obtained and it has not been possible to display all the results in the interests of brevity. Table (9.5) shows the experimental conditions of the rate of air entrainment Q_a.

Parameter		Range	
Nozzle diameter	(d_N)	0.006-0.014	m
Nozzle height	(x_1)	0.025-0.030	m
Nozzle velocity	(V_N)	2.5-13	m/s
Nozzle aspect ratio	(l_N/d_N)	3.33-5	

Table (9.5): Experimental conditions of the rate of air entrainment

9.5.1 Effect of Jet Velocity

Figure (9.15) shows the typical effects of the jet velocity V_N, on the volumetric air entrainment rate Q_a, with the nozzle diameter, d_N, and the jet length ratio x_1/d_N, as parameters, the relationship is shown in logarithmic scale.
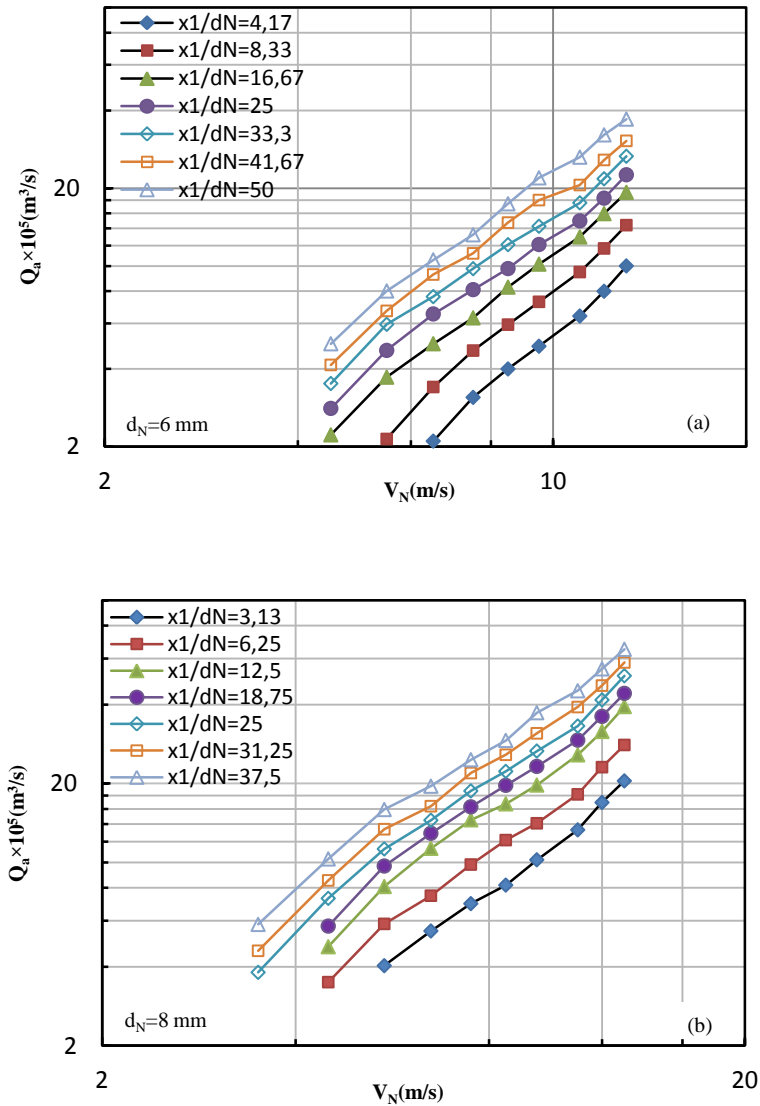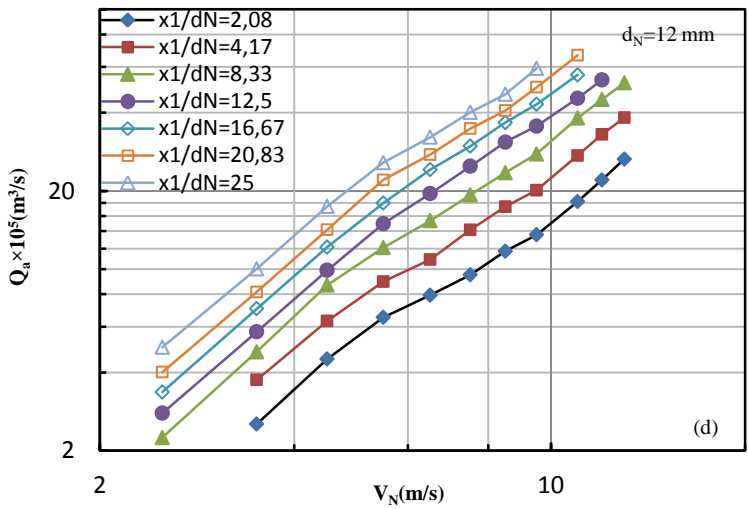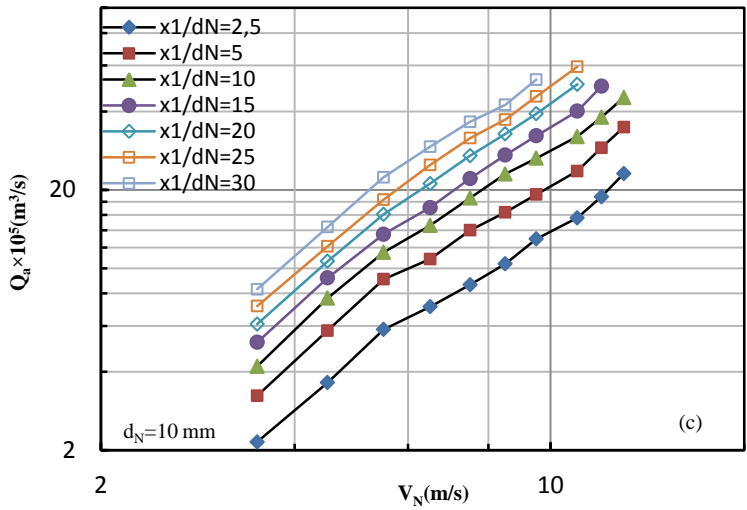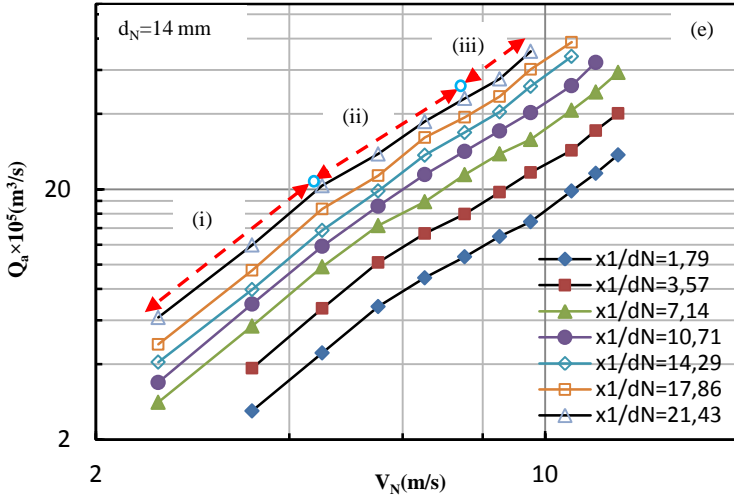
Figure (9.15): Relationship between air entrainment rate and jet velocity

As for the dependence of the gas entrainment rate (Q_a) on the jet velocity (V_N), it is found from Figure (9.15)-(a) to (e) that the curve of the air entrainment, Q_a (for given jet diameter between 6 to 14 mm) tends to increase with V_N and their curves can be divided into some regions depending on the range of V_N;

(i) A low jet velocity region, V_N below approximately 5.5 m/s, where Q_a increases proportionally to $V_N^{2.3}$;

(ii) A transition jet velocity region, V_N between approximately 5.5 and 11 m/s, where Q_a increases proportionally to $V_N^{1.5}$, and;

(iii) A high jet velocity region, V_N above approximately 11 m/s, where Q_a increases proportionally to V_N^2.

A similar tendency was observed by other researchers using different jet diameters (d_N). Ohkawa (1986) for example studied vertical liquid jets and showed that the Q_a against V_N can be divided into three regions, also Van de Sande and Smith (1973) and Kumagai and Imai (1982) showed four types of flow regions for inclined liquid jets systems, on the basis of the plot of Q_a against V_N.

It is interesting to note that a rough turbulent jet entrains more than a smooth jet at short distances from the nozzle end, but at longer distances from nozzle the smooth jet will entrain more air than the rough because it has a longer break-up length.

However, the turbulence structure of the issuing jet stream depends largely not only on the nozzle design but also the jet velocity and may also affect the shape and surface roughness of the plunging jet which affect the gas entrainment rate, Q_a. This way of changing their behaviour is assumed to be divided roughly into three forms depending on the range of V_N, considered this seems to provide a plausible explanation for the occurrence of a phenomenon such as dividing the jet entrainment curve depending on the range of V_N. In order to provide evidence for such changes, it may be necessary to carry out photographic observations to investigate the changes in the jets with V_N and at the same time to clarify the changes in the gas entrainment behaviour at the plunging point of the jet corresponding to these changes.

9.5.2 Effect of Jet Length

The entrainment rate was measured for various heights of fall x_1 from 0.025 to 0.30 m. Figure (9.16) shows the change in the rate of air entrainment Q_a as a function of the jet length for different jet diameters and jet velocities as parameters, also a comparison with the results of Ohkawa (1985) presented.

V_N(m/s)	3.5	4.5	5.5	6.5	7.5	8.5	9.5	11	12	13
key	■	▲	●	◇	□	△	○	◆	▲	■
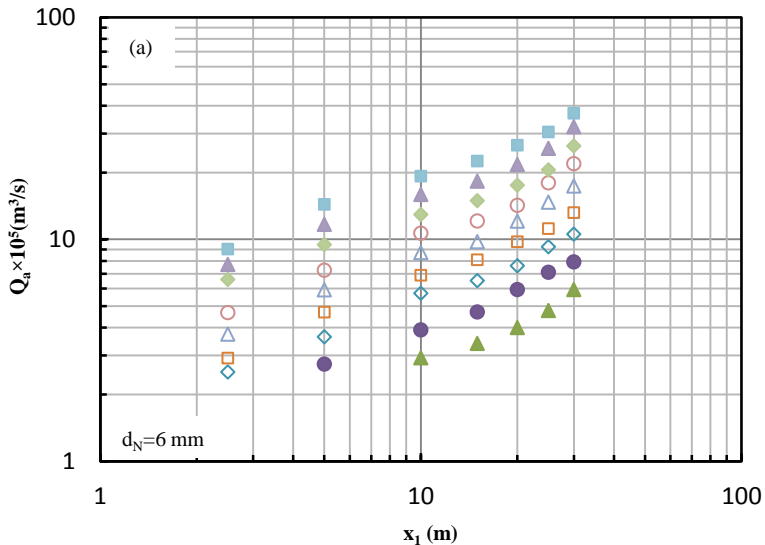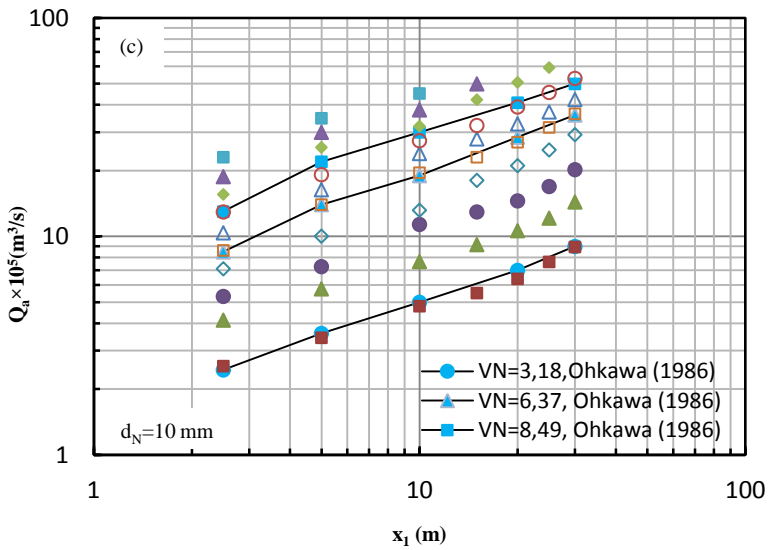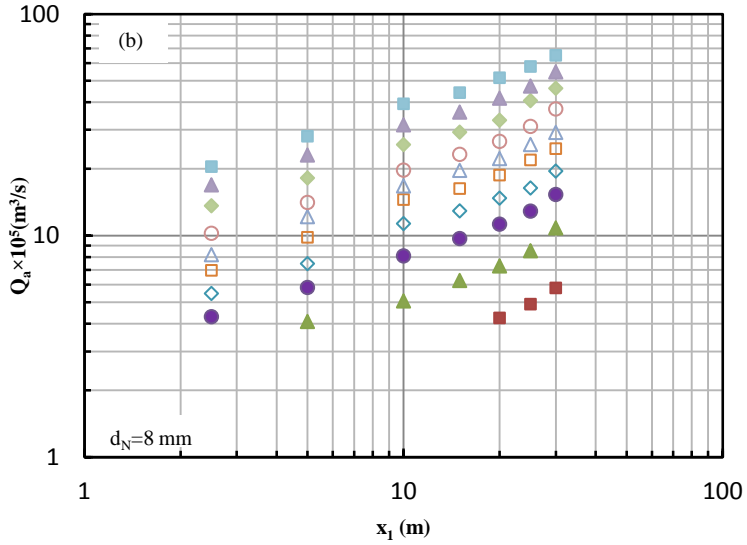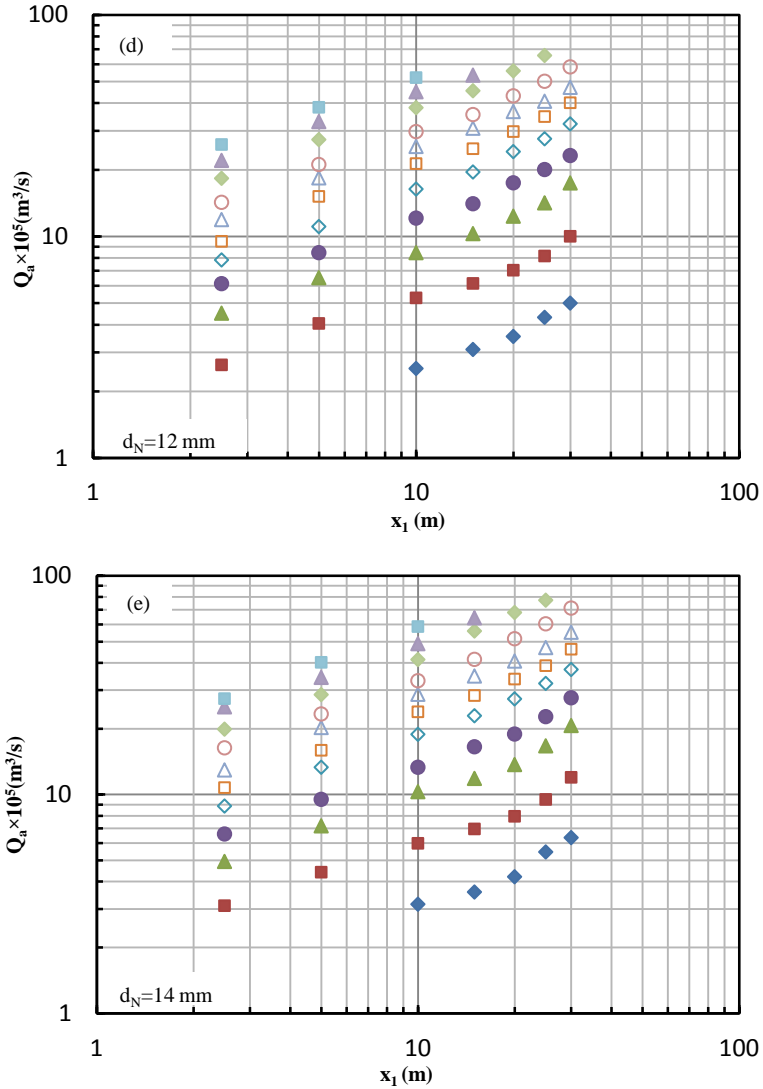
Figure (9.16): Relationship between air entrainment and jet length

It can be seen for each case of Figure (9.16)-(a) to (e) that the volumetric flow rate of entrained air bubble increases when increasing the height of the fall (x_1), also the Q_a changes as $Q_a \propto x_1^{0.5}$ regardless of V_N and d_N. Ohkawa et al., (1986) and McKrogh and Ervine (1980) studied the vertical plunging water jets by different jet diameters and their results showed a similar pattern. A comparison is

shown in figure (9.16-c) with the data of Ohkawa et al. (1985) and a good agreement was obtained for d_N=10 mm.

9.5.3 Effect of Jet Diameter

Figure (9.17) shows the effect of the jet diameters (d_N) on the rate of air entrainment (Q_a) for initial jet velocities of 7.5 and 11 m/s respectively at various jet lengths.
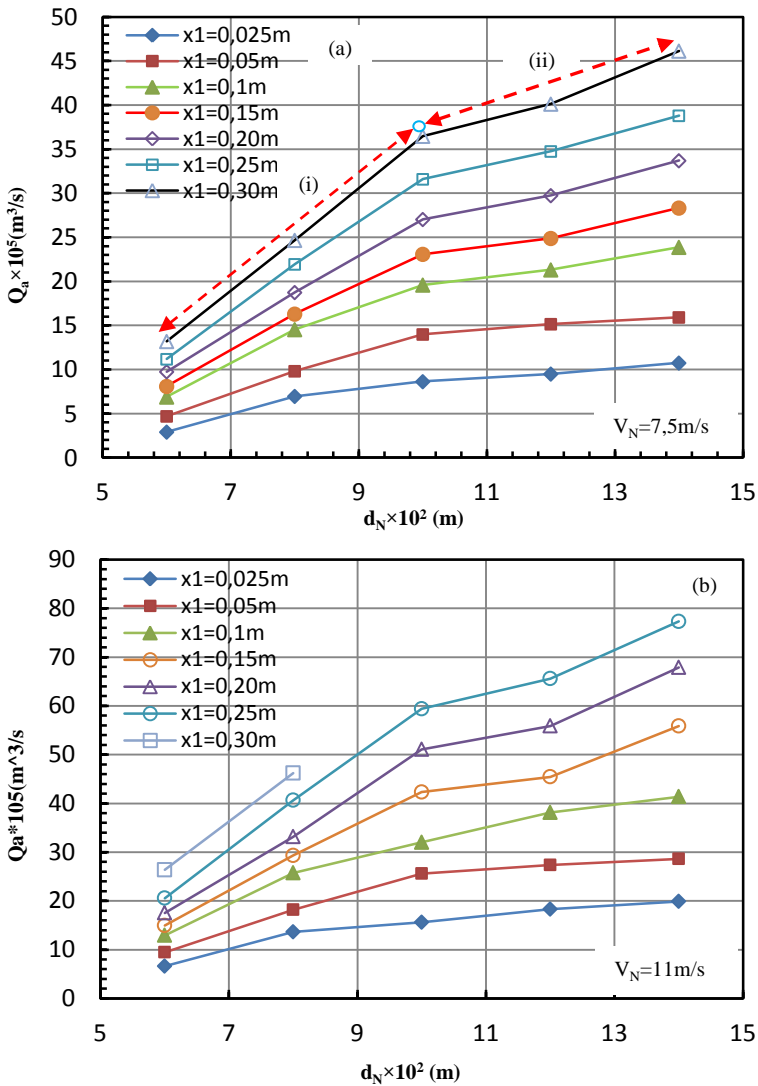
Figure (9.17): Relationship between air entrainment rate and jet diameter

The rate of air entrainment increases significantly by increasing the nozzle diameter for a given jet length. Since, the jet contact area with the atmospheric air increases when increasing the jet diameter. The results show that the effect of jet diameter on the entrainment rate can be divided into two regions, namely:

i)   The region of d_N between 6 and 10 mm, where Q_a is proportional to $Q_a \propto d_N^{1.9}$.

ii) The region of d_N between 10 and 14 mm, where Q_a is proportional to $Q_a \propto d_N^{1.5}$.

May be the jet nozzles between 6 and 10 mm have the same mechanism of buoyancy (or entrainment) and on the other hand jets between 10 and 14 mm have the same mechanism that it is different from the previous one.

A similar phenomena that the one mentioned above has also been observed by Ohakawa (1986) for vertical liquid jets, when $7 < d_N < 11$ mm, the Q_a is proportional to $Q_a \propto d_N^{1.9}$, and when $11 < d_N < 13$ mm the Q_a is in proportional to $Q_a \propto d_N^{1/3}$. Also Kumagi and Imai (1982) have also observed the same tendency but the Q_a has more dependence on d_N for cases using inclined liquid jets. However, in general the increase of gas entrainment rate, Q_a with increasing of V_1, d_N and x_1 may be ascribed respectively to the increased momentum of the jet flow, increased contacting perimeter between the jet flow and the liquid surface, and increased roughness of the jet surface.

9.5.4 Entrainment Rate Correlations

Air entrainment ratio (Q_a/Q_w) is defined as the ratio of the volumetric flow rates of air entrainment and water jet discharged (Q_w), and is a measure of performance of the plunging jets process (aeration).

According to the result obtained in section (9.5.1 to 9.5.3) and those by other researchers, the entrainment ratio will depend on the basic system parameters, such as jet velocity, jet length, nozzle diameter, angle of jet inclination, and the physical properties of the water.

In order to quantity the effect of the operational variables such as V_N, d_N and x_1 on the air entrainment rate, a correlation between these variables and the

measured air entrainment was expressed by the following Equation (9.9) with R^2 = 0.97.

$$Q_a = C_{13} V_N^{C_{14}} d_N^{C_{15}} x_1^{C_{16}}$$

(9.9)

where, C_{13}, C_{14}, C_{15} and C_{16} are empirical constants which depend on the ranges of the jet parameters. Table (9.6) summarized the values of these constants. Depending on the range of the jet diameter (d_N) and the velocity (V_N) the values of these constants will change.

d_N(m)	V_N(m/s)	C_{13}	C_{14}	C_{15}	C_{16}
0.006-0.008	2.5-4.5	5.2×10^{-3}	2.3	1.9	0.5
	5.5-9.5	18.8×10^{-3}	1.5	1.9	0.5
	11-13	6.2×10^{-3}	2	1.9	0.5
0.010-0.014	2.5-4.5	2×10^{-6}	2.3	0.15	0.5
	5.5-9.5	7.2×10^{-6}	1.5	0.15	0.5
	11-13	2.2×10^{-6}	2	0.15	0.5

Table (9.6): The values of C_{13}-C_{16} calculated in Equ. (9.9)

Figure (9.18) shows the relation between the predicted results by equation (9.9) and the experimental results, with an accuracy of $\pm 20\%$.

The variable $V_N^{C_{14}} d_N^{C_{15}}$ in Equation (9.9) is the term corresponding to the kinetic energy of the jet. A term like this has been employed to correlate the data of Q_a for vertical and inclined water jet systems by many researches. Ohakawa (1986) for example used a similar to expression for the vertical water jets.

In order to evaluate the impact of the jet parameters on the entrainment ratio (Q_a/Q_w), many researchers have developed different empirical expressions ranging from very simple ones neglecting the jet velocity to ones classifying different regions for air entrainment according to the velocity of the jet (e.g., Bin, 1993 and Ohkawa et al., 1986).
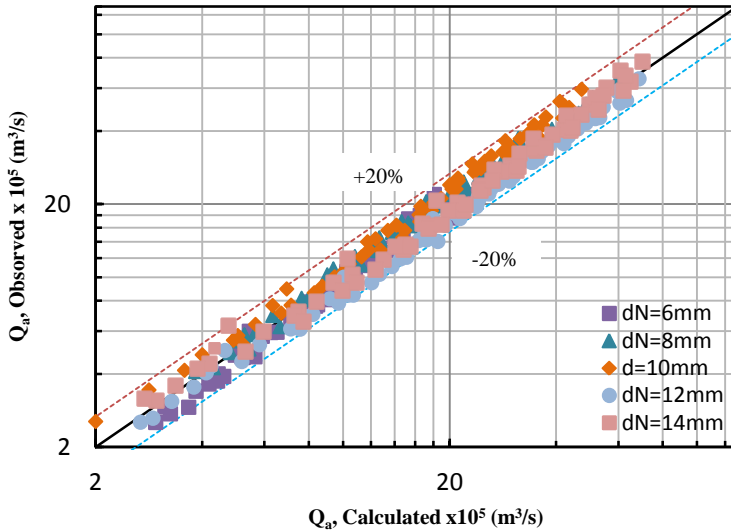
Figure (9.18): Comparison of the Q_a observed and those calculated by Equ. (9.9)

Bin (1993) suggested a general expression valid for the different regions of air entrainment resulting from the use of a vertical plunging jet as the following:

$$\frac{Q_a}{Q_w} = 0.04 Fr_0^{0.28} (\frac{x_1}{d_N})^{0.4}$$

$$(9.10)$$

This equation is valid for water jets with $x_1/d_N \leq 100$, $l_N/d_N \geq 10$ and $0.04 Fr_0^{0.28}(x_1/d_N) \geq 10$. Rearrangement of the gas entrainment rate, Q_a, based on the dimensionless analysis was difficult in the same manner as in the case of the bubble penetration depth. The correlation of Q_a has different values depending on the region of flow, low, transition or high velocity region, with the operation variables. By using dimensionless terms such as Fr_0, x_1/d_N and l_N/d_N a non-dimensional form can be obtained as:

$$Q_a / Q_w = C_{17} Fr_0^{C_{18}} (x_1 / d_N)^{C_{19}} (l_N / d_N)^{C_{20}}$$

$$(9.11)$$

where, Q_w is the volumetric rate of the water through the nozzle. The values of the empirical constants, C_{17}, C_{18}, C_{19} and C_{20} are determined for the three regions mentioned above of (i), (ii) and (iii) and jet diameters are summarized in Table (9.7).

d_N(m)	V_N(m/s)	C_{17}	C_{18}	C_{19}	C_{20}
0.006-0.008	2.5-4.5	0.41×10^{-2}	0.8	0.52	0.25
	5.5-9.5	4.8×10^{-3}	0.75	0.52	0.25
	11-13	5.8×10^{-3}	0.70	0.52	0.25
0.010-0.014	2.5-4.5	0.5×10^{-2}	0.8	0.52	0.25
	5.5-9.5	0.58×10^{-2}	0.75	0.52	0.25
	11-13	0.65×10^{-2}	0.70	0.52	0.25

Table (9.7): The values of C_{17}-C_{20} calculated in Equ. (9.11)

The values of (Q_a/Q_w) obtained from Equation (9.11) were plotted against the experimental results, as shown in Figure (9.19). A very good agreement can clearly be observed with a coefficient of multiple determination (R^2) value of 0.94 and an accuracy of $\pm 20\%$.
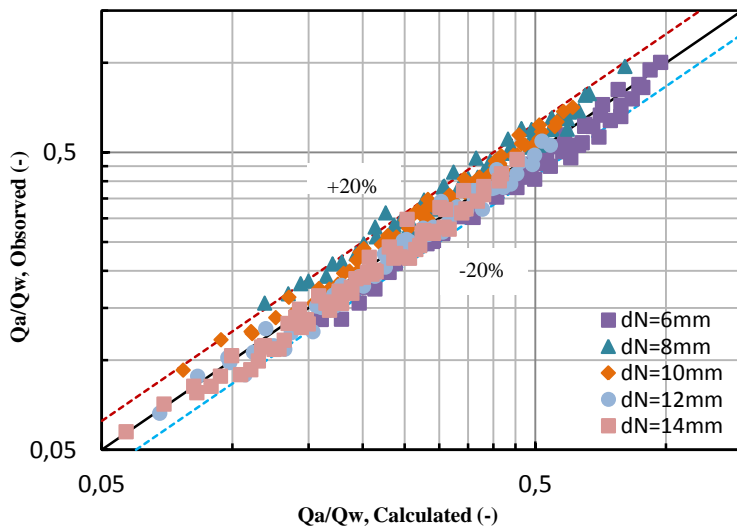
Figure (9.19): Comparison of the Q_a/Q_w measured and those calculated by Equ. (9.11)

The results showed that increasing the nozzle Froude number and (x_1/d_N) ratio (either by increasing, x_1 or decreasing, d_N) led to an increased of Q_a/Q_w ratio. Such an increase can be related to the increase in the turbulence (as V_N increased) and the surface roughness (as x_1/d_N increased) of the plunging jet. Variable x_1/d_N, is a term related to the jet surface roughness-to-radius, ϵ/r, which may affect the gas entrainment rate.

According to these results, it is concluded that Equation (9.11) would be useful for the prediction of Q_a/Q_w ratio, when a circular nozzle of the present type with jet diameter between 0.006 and 0.014 m is employed.

9.6 Water Jet Velocity distribution

Below the impingement point in the water tank, the flow structure basically comprises two distinct regions: (i) a diffusion cone with a downward flow motion induced by the plunging water jet, and (ii) a swarm of rising air bubbles which surrounds the former one as shown in Figure (9.20).
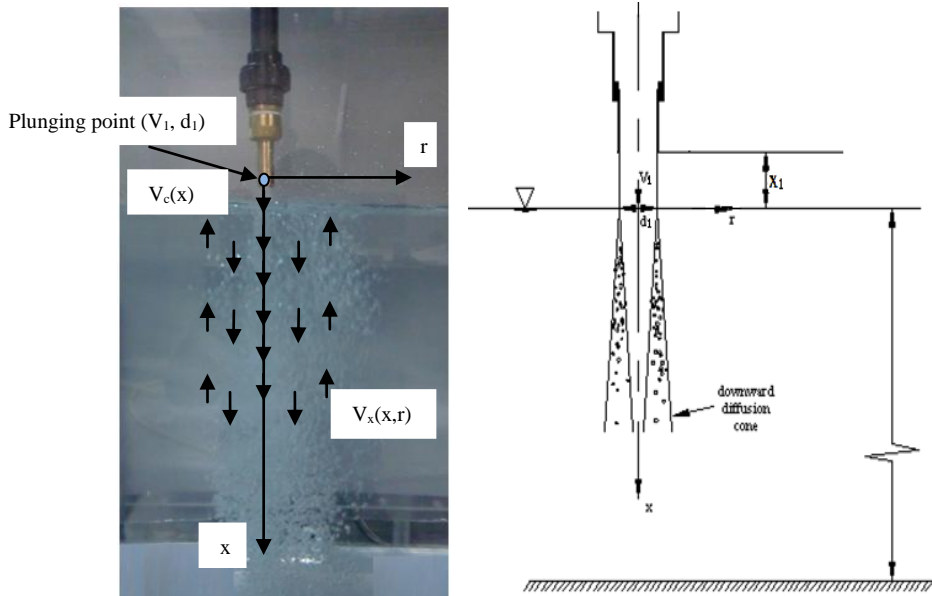
Figure (9.20): Sketch and picture of the impingement region

Theoretical predictions of the water jet velocity in a plunge water pool are difficult because of turbulence. Therefore, an empirical approach using dimensional analysis was considered by some researchers (e. g., Bohrer, 1998) that developed a procedure for predicting the velocity decay in the jet diffusion region. Many parameters affect the velocity decay of the free-falling circular jet as it disperses into a plunge water pool, as can be seen in the following general expression:

$$V_x(x,r) = f(V_1, d_1, x_1, x, r, \rho_a, \rho_w, g) \tag{9.12}$$

However, in the present study many experimental tests were performed and information was obtained for the developed jet condition, in which jet issuance velocity V_N, impact velocity V_1, jet length x_1, depth into the plunge pool x, , radial distance r, centerline velocity $V_c(x)$, and mean axial velocity distribution $V_x(x,r)$ were recorded.

The initial centerline velocity at nozzle exit (V_N), accelerating under the influence of gravity, yields the jet centerline velocity at the water surface (V_1) that can be estimated using Equation (9. 13):

$$V_1 = \sqrt{V_N^2 + 2gx_1} \tag{9.13}$$

Using this equation, the expected jet centerline velocity at the impact point is calculated and tabulated in Table (9.8) for the water velocity experiments. Also the ratio of the jet length to jet diameter and the percentage of increase in the centerline velocities at impact point compared to those obtained at the nozzle exit for different cases are listed. The calculations were applied for the jet diameters of d_N=0.008 m and d_N=0.014 m. The velocities of the water jet is measured for different heights of the nozzle to the undisturbed surface (x_1) at varying depths (x) from the undisturbed surface and radial distance (r) from the jet centerline.

	d_N= 0.008m				d_N= 0.014m		
Run	x_1/d_N (-)	V_N (m/s)	V_1 (m/s)	V_1/V_N (%)	**Run**	x_1/d_N (-)	V_N (m/s)	V_1 (m/s)	V_1/V_N (%)
1	0	3.5	3.5	100	16	0	3.5	3.5	100
2	0	4.5	4.5	100	17	0	4.5	4.5	100
3	0	6.5	6.5	100	18	0	6.5	6.5	100
4	0	8.5	8.5	100	19	0	8.5	8.5	100
5	0	13	13	100	20	--	--	--	--
6	18.75	3.5	3.90	111	21	10.71	3.5	3.90	3.90
7	18.75	4.5	4.82	107	22	10.71	4.5	4.82	4.82
8	18.75	6.5	6.72	103	23	10.71	6.5	6.72	6.72
9	18.75	8.5	8.67	102	24	10.71	8.5	8.67	8.67
10	18.75	13	13.11	101	25	--	--	--	--
11	37.5	3.5	4.59	131	26	21.43	3.5	4.593	131
12	37.5	4.5	5.11	114	27	21.43	4.5	5.112	114
13	37.5	6.5	6.94	107	28	21.43	6.5	6.938	107
14	37.5	8.5	8.84	104	29	21.43	8.5	8.84	104
15	37.5	13	13.22	102	30	--	--	--	--

Table (9.8): Jet centerline velocity at nozzle exit and at impact point for jet diameter of 8 and 14 mm

In this section, the measured distribution of the water jet velocity is discussed and compared with the empirical results found in the open literature. Velocity measurements were performed at least five times and the obtained values were averaged statistically. The repeatability error was less than ±4%.

9.6.1 Centerline Velocity Decay

9.6.1.1 Submerged Jet (Single-Phase Free Jet)

Single-phase free jet means a jet that was issued from a nozzle into an infinite space occupied by the same fluid as the jet in the absence of air bubbles (air entrainment). This happened when the nozzle exit was directly in contact with the water surface (at x_1= 0). No air bubbles observed in the water pool and the velocity measurements occurred in the absence of entrained air (single-phase jet diffusion).

Ishigaki (1982) and Iguchi et al. (1989) measured the change of V_c/V_N at values of x/d_N and they suggested the following empirical equation for the single-phase free jets:

$$V_c / V_1 = 6.2(d_1 / x)$$
(9.14)

where, x is the vertical axial distance measured from the water surface. This equation is known to be valid for $x/d_1 \geq 1 \, 0$.

Figure (9.21) shows the experimental result obtained for the centerline velocity ratio (V_c/V_1) at 8 and 14 mm nozzle diameters, and $x_1=0$ cm ($V_N=V_1$), together with the values predicted by Equation (9.14) that plotted against the axial distance ratio x/d_1.

It can be observed that the velocity at the jet centerline decreases gradually with the axial distance x along the jet axis, also the measured data can be approximated satisfactorily well by the equation (9.14) for single-phase free jets at $d_N=8$ mm and $d_N=14$ mm. However, no air entrainment was observed for all studied velocities when the nozzle was placed at the water surface, i.e. $x_1=0$ cm.

9.6.1.2 Diffusion Jet (Two-Phase Diffusion Jet)

When the distance between the nozzle exit and the water surface has a certain value, $x_1 > 0$, and the jet velocity is higher than the inception velocity, air from the ambient will be entrained and bubble diffusion region will appear in the water pool. The flow of the convected water exerts a drag on the entrained air bubbles which tends to force them to travel in the downward stream wise direction and this bubble motion is opposed by the natural buoyancy force of the bubbles. If the velocity of the convected water is large enough, it causes a sufficient drag on the bubbles to overcome the buoyancy forces and downward bubble motion results (see Figure, 9.22).
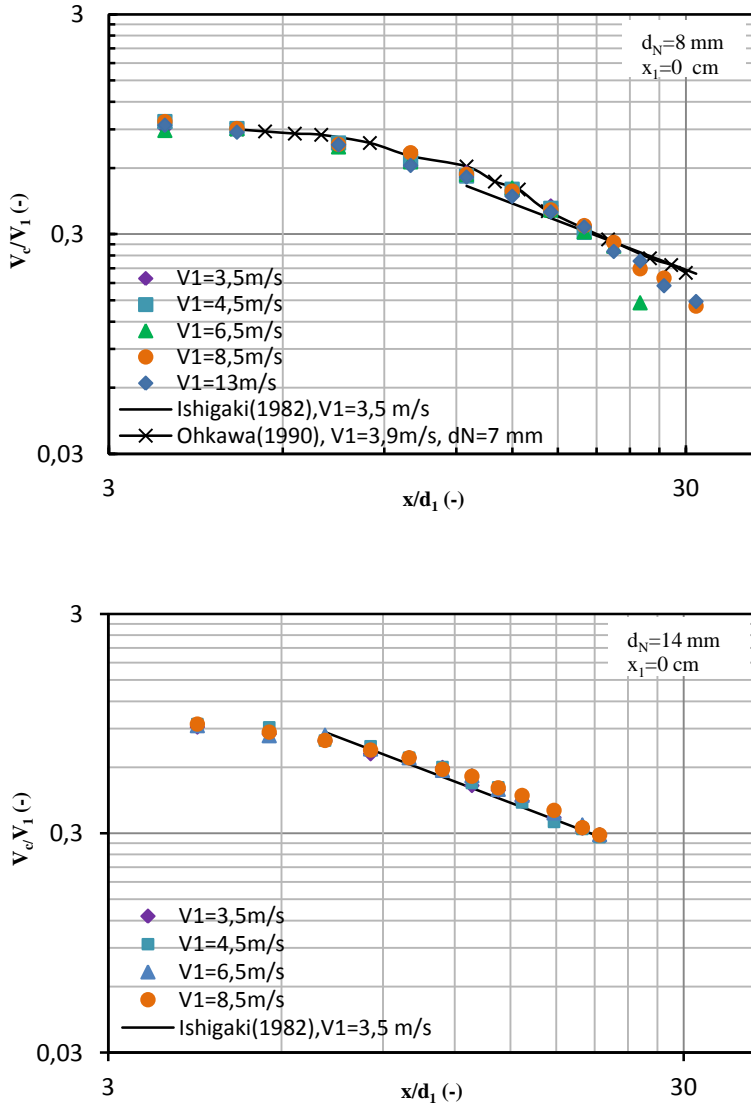
Figure (9.21): Centerline velocity decrease with distance in single-phase free jet
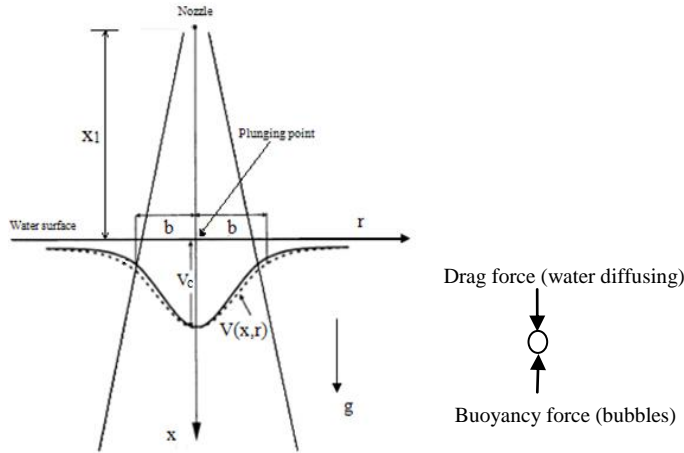
Figure (9.22): Sketch of the centerline and axial velocity distribution

McKeogh and Ervine (1981) measured the change of the centerline velocity ratio V_c/V_1 in the submerged jet region (within the biphasic cone) for smooth plunging liquid jets (d_N=9 mm and V_1=2.5-3.9 m/s) using a Pitot tube at values of x/d_1 ranging from about 3 to 20. They suggested that the centerline velocity decay V_c/V_1 decreased in a power relationship with the increase of x/d_1 and is given by the following expression:

$$V_c / V_1 = 3.3(d_1 / x)^{1.1} \qquad\qquad (9.15)$$

This equation reveals that the rate of decay of centerline velocity in the biphasic plume resulting from gas entrainment by a vertical plunging jet is greater than in the single-phase flow.

Kusabiraki (1990) also studied the vertical liquid plunging jet using different liquids and measured the velocity profiles in the submerged jet region at d_N=0.007 m, V_N =3.9 m/s, and jet length x_1 =30 cm. It was found that, the rate of decrease of V_c/V_1 was not constant throughout the whole range of x/d_1. Thus, the rate of decrease of V_c/V_1 for x/d_1 above 15 tended to larger that below 15, and depending on the liquids.

Figure (9.23) shows the experimental data obtained for the measured centerline velocity ratio (V_c/V_1) against the axial distance ratio (x/d_1) for jet diameters of 8 and 14 mm and jet length between 15 and 30 cm together with the results obtained by the empirical correlations of McKeogh and Ervine (1981) and the experimental results obtained by Kusabiraki (1990).

Figure (9.23-a) shows a similar plot to Figures (9.23-b) and (9.23-c) for different values of the jet length and jet diameter, the same trend of V_c/V_1 with x/d_1 was obtained. The results show that the rate of decrease of V_c/V_1 was not constant throughout the whole range of x/d_1, and this agree with Kusabiraki as shown in figure (9.23-a).
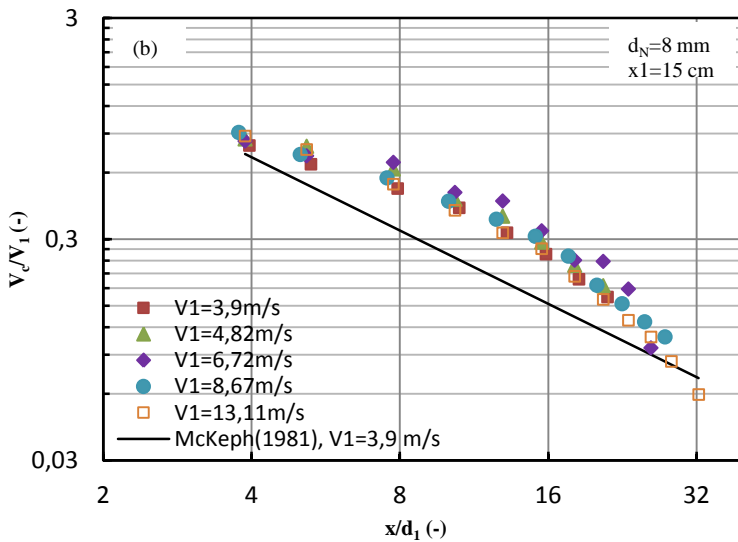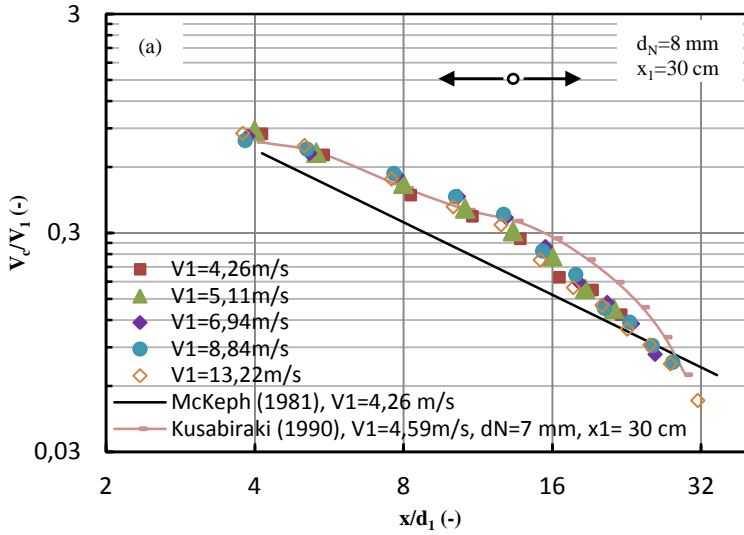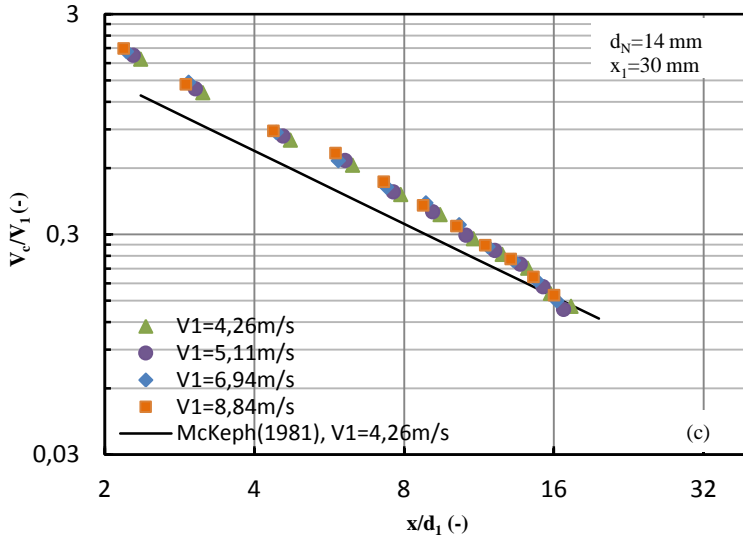
Figure (9.23): Relation between the centerline velocity ratio (V_c/V_1) and the distance ratio (x/d_1) under varied conditions of V_1 and d_N

Thus the rate of decrease of V_c/V_1 with x/d_1 above 16, tended to larger than below 16. Iwasaki and Senshu (1953) also observed that the rate of deceleration at x/d_1 above 15 was larger than below 15. The results obtained by Equation (9.15) does not agree well with the presently measured values but it makes almost a good agreement with the measured values at $25 \geq x/d_1 \leq 30$ for $d_N = 8$ mm for the jet lengths of 15 and 30 cm.

However, the profiles generated by the present experimental results are consistent in trend with the profile of Equation (9.15), although the experimental results predict higher velocities away from the centerline than Equation (9.15). A further observation indicates that experimental results predict marginally lower diffusion, by its radial spreading, in contrast to the Equation (9.15). More data on V_x should be accumulated to discuss the validity of Equation (9.15) and this may be cause the disagreement between the present measured values and McKeogh and Ervine (1981) values for $x/d_1 \leq 25$. Iguchi (1997) obtained the same conclusion and results. The present results show that some of our results show a good agreement with the results of Kusabiraki (1990).

Figure (9.24) shows a comparison between the cases with and without gas entrainment, at different jet lengths $x_1 =1$, 8, 15, and 30 cm and single phase flow at $x_1=0$ cm. Also, the results from correlation of Ishigaki (1982) and experiments of Kusabiraki (1990) for single phase-flow are presented.

The result shows that the decrease of the centerline velocity decay in the single-phase flow is found to be smaller than in the two-phase flow. Also, as the jet length (x_1) increase the decrease in the velocity decay will increase in the plunging jets, since increase in the jet length leads to increase in the rate of air entrainment.

The difference in the results between the jet diffusion with air entrainment and without air entrainment profiles is due to the velocity distributions of the impinging jet flow will be affected by the drag/buoyancy of the entraining gas. Since, the single phase jets has less turbulence generated in the diffusion process and there is no air bubbles that generate buoyancy force to oppose the drag force of the diffusion jet.

A good agreement between results of Ishigaki (1982) and Kusabiraki (1990) and the present study was found. McKeogh and Ervine (1981) and Iguchi et al. (1997) observed a similar phenomenon.
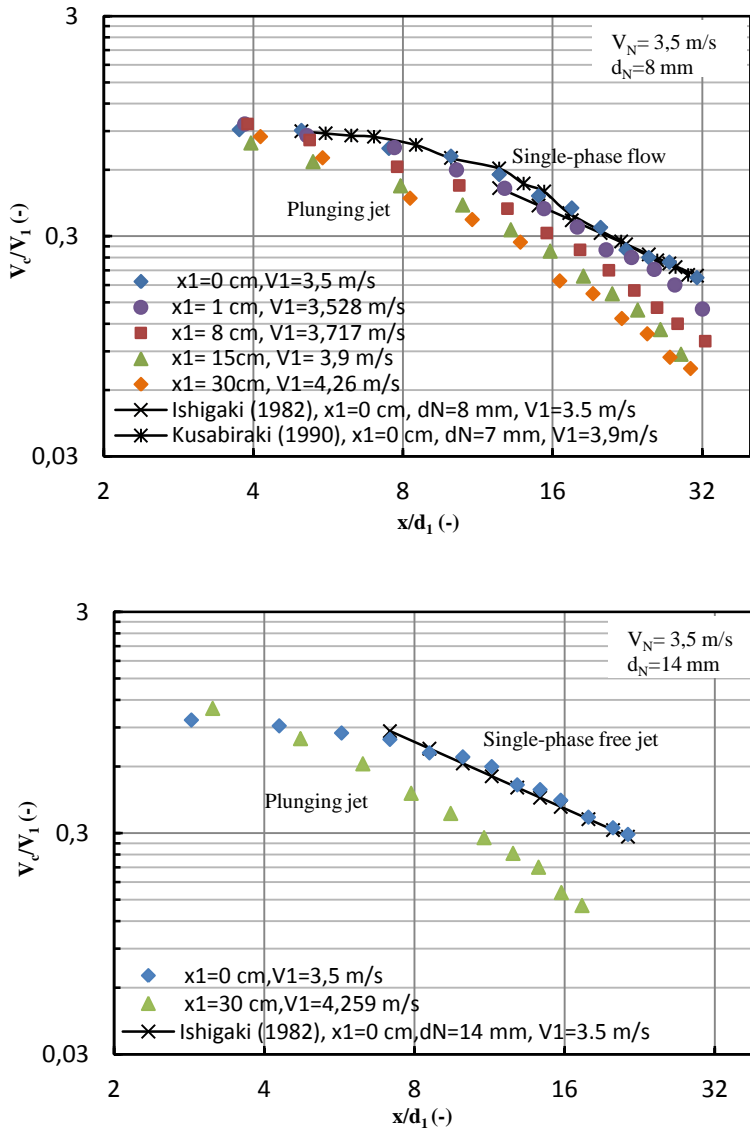
Figure (9.24): Velocity decay in the diffusion jet with and without gas entrainment

9.6.2 Axial Velocity Distributions in the Jet Diffusion Region

Due to the axis-symmetrical nature of the diffusion pattern produced by the vertical plunging jets, it was necessary only to take velocity measurements in one plane radiating from the jet axis. These velocity measurements were taken in the streamline direction only, i.e. parallel to the downward flow of the jet, since according to McKeogh and Ervine (1981) the transverse velocity components in such a jet diffusion pattern are negligible. Velocity measurements were taken at a series of radial positions extending from the jet centerline. These measurements were discontinued at a radius where negligible velocity was recorded. This procedure was repeated for a number of progressive depths (x) within the tank until a relatively low velocity reading was recorded at the jet centerline.

The velocity within the diffusion region decays with both downward movements from the impact point and lateral movement from the jet center line. There is a limit to both the lateral extent and depth to which the bubbles penetrate, i.e. at positions when the velocity is less than 0.26 m/s. According to McKeogh and Ervine (1981) a bubble of approximately 2 mm diameter will rise within a column of water at a velocity of 0.26 m/s. It seems reasonable to suggest that if the water is moved downward at this velocity a bubble will remain stationary relative to any arbitrary datum. The value of 0.26 m/s can be taken as a critical downward water velocity below which bubbles will rise to the surface.

Figure (9.25) shows an example of a typical set of axial velocity profiles measured for $d_N = 8$ mm against the radial position (r). The results are plotted in such a way that the vertical axis corresponds to the axial velocity (V_x) of the jet at different axial depth (x) within the pool and the horizontal axis represents the radial distance (r) from the jet axis. Measurements of the axial distributions of V_x were carried out at five representative axial positions x of 3, 6, 10, 16, and 20 cm from the water surface and for three jet length values (x_1) of 0, 15, and 30 cm and nozzle velocity of $V_N = 3.5$ and 6.5 m/s.
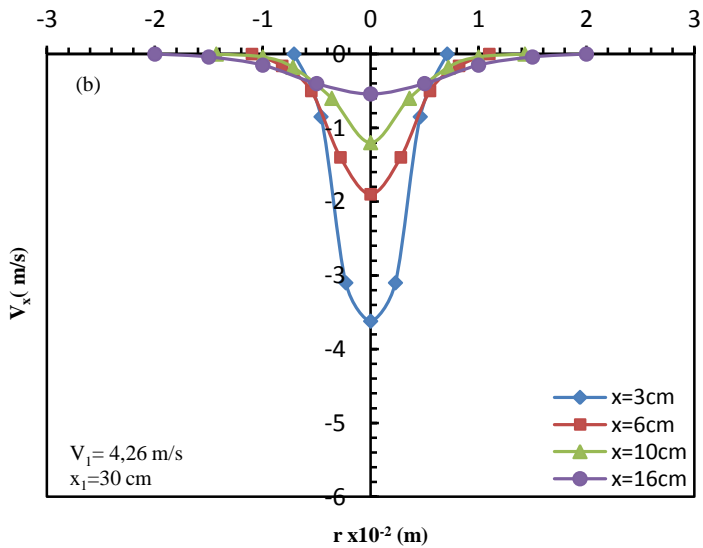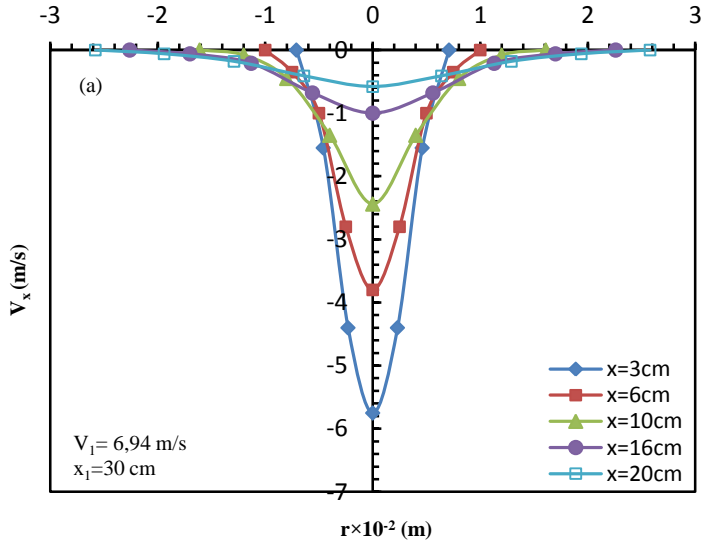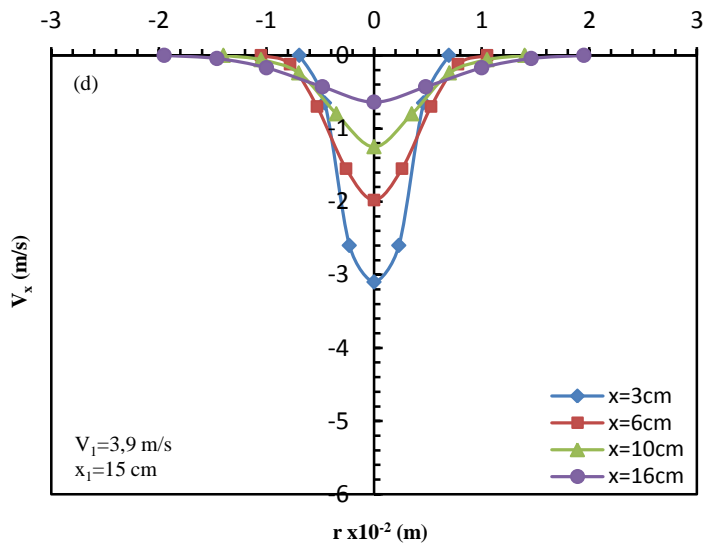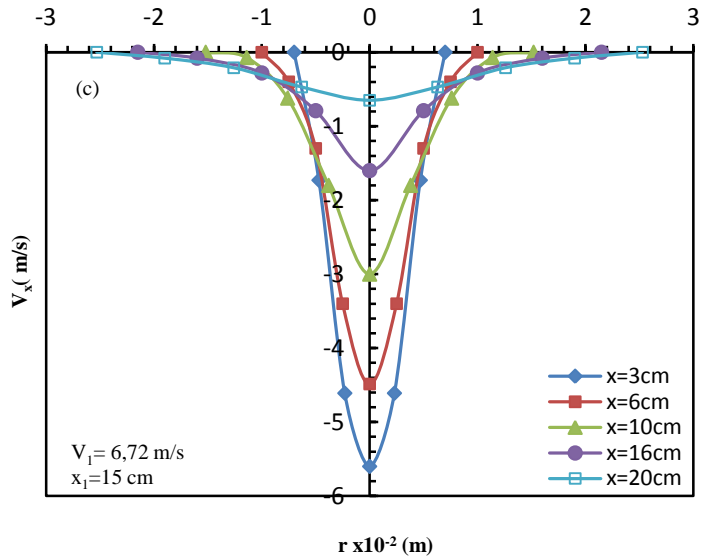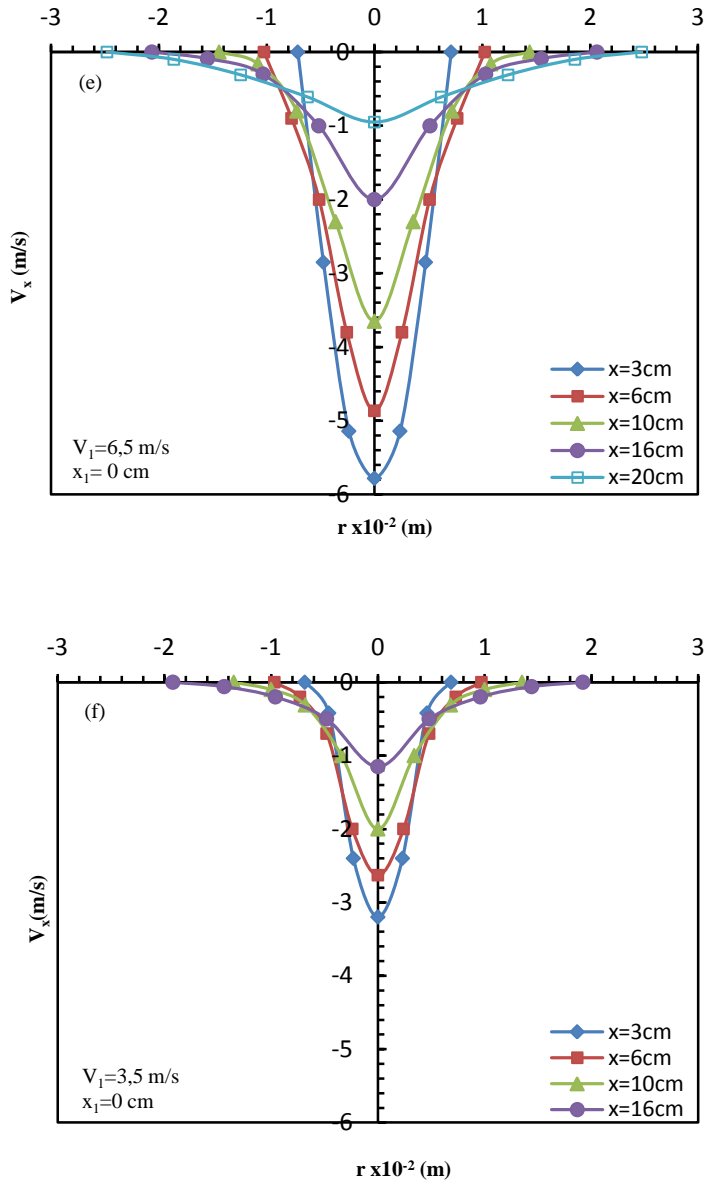
Figure (9.25): Axial velocity distribution for 8 mm jet diameter, $V_N = 3.5$ and 6.5 m/s and $x_1 = 0$, 15 and 30 cm

From the results, the tendency for the velocity to decrease gradually with the distance x from the water surface and with the radial distance r from the jet axis is common, but the velocity at each vertical and radial position is found to differ somewhat depending on the impact velocity and the jet length (x_1).

The direction of the inertia force of the plunging water jet and the buoyancy force of the bubbles are opposite. As x increase, the buoyancy force increase. The buoyancy force is so small as to be neglected near the nozzle but become significant away from the nozzle.

Figures (9.25)- (e) and (f) represent the mean velocity of the water phase in the flow-developing region, correspond to V_1=6.5 and 3.5 m/s respectively in the absence of entrained air bubbles (x_1=0 cm). Single phase impinging jet flow field, it shown that has a large velocity distribution than the two-phase jet $(x > 0)$ but it less diffusion (b_u).

9.6.2.1 Velocity Half-Width

A linear spread of velocity half-width (b_u) and linear decrease of the centerline velocity (V_c) with the distance downstream are predicted and a Gaussian velocity profile was observed for the axial velocity profile with the width (b_u).

The velocity half-width is a function of its momentum flux at the source M_0, the size of the source d_N, the fluid density ρ_w, the jet length x_1, the fluid properties, and the elevation from the plunging point x, as follows:

$$b_u = fn(V_1, d_N, x_1, x, \rho_a, \rho_w) \tag{9.16}$$

$$b_u = \beta x \tag{9.17}$$

where, β is a constant of the spreading rate of the plume. The width of the velocity distribution along the water plume increased linearly with the distance (x) from the plunging point. According to the experimental results by Iguchi et al., (1997) for an upward premixed water and air injection, the half-value radius, b_u, of the axial mean velocity component (V_x) can be expressed by the following equation in the presence of turbulence production in the wake of bubbles:

$$b_u = \sqrt{2.\ln 2}\, Cx \qquad\qquad (9.18)$$

where, C is the fitting parameter. This equation is valid for $x/d_N \geq 10$ and $0 \leq \acute{\varepsilon} \leq 1$. The coefficient C is 0.071 for water jets generated by bottom water injection and C= 0.117 for bubbling jets generated by bottom gas injection. Also, C is 0.071 for a single-phase free jet. Therefore, gas-liquid two-phase jets spread wider in the transverse direction than single-phase free jets. Equation (9.18) can be writing for single-phase free jets as:

$$b_u = 0.084x \qquad\qquad (9.19)$$

Figure (9.26) shows the experimental results of the jet half width along the jet centerline obtained for 8 mm jet diameter together with the prediction of Equation (9.19).
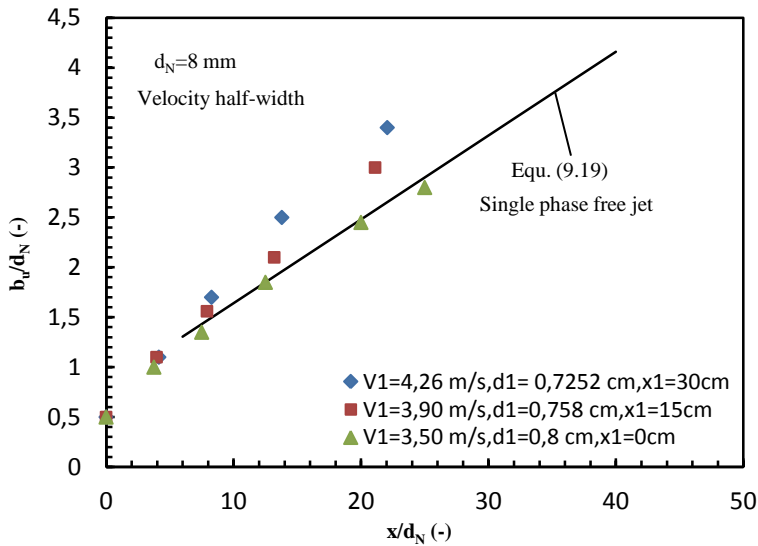
Figure (9.26): Relation between the half-value radius (b_u) and axial distance x

An acceptable agreement was obtained between the measured values at $V_N = 3.5$ m/s and $x_1 = 0$ cm (single phase jet) for x=10 and 20 cm and those obtained by Equation (9.19) for single phase free jet.

As x increases, the deviation of the measured values from Equation (9.19) increases. Since, the directions of the inertia force of the plunging water jet and

the buoyancy force of bubbles are opposite. This means that the buoyancy effect is so small as to be neglected near the nozzle but become significant away from the nozzle. The flow above x=30 cm is considered to be affected by a vortex motion induced by the bottom wall and the sidewall, and hence, Figure (9.26) overestimates the b_u value.

9.6.2.2 Dimensionless Analysis

In this section, the measurements of the axial distributions of the water jets velocity components (V_x) were normalized by its centerline value (V_c), and plotted against the non-dimensionalized radial distance (r/b_u).

The measurements were made for a jet diameters 8 and 14 mm and impingement velocity 3.5 and 6.5 m/s (corresponding to runs 1, 3, 6, 8, 11, and 13 respectively, of table 9.7) at axial positions x=3, 6, 10, 16, and 20 cm and jet lengths x_1= 0, 15, and 30cm. Figure (9.27) shows the non-dimensionalized mean velocity V_x/V_c plotted against the non-dimensionalized radial distance r/b_u. Where, b_u is the half-value radius of the radial distribution.
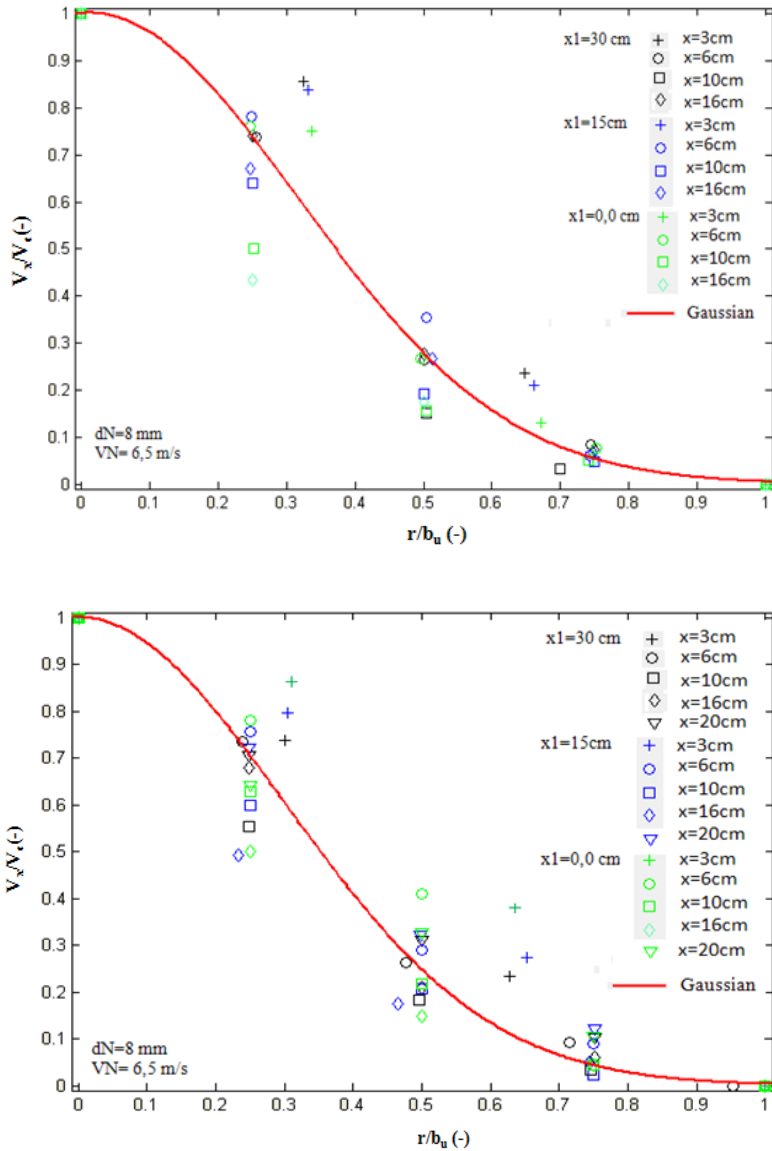
Figure (9.27): Universal nature of velocity profile in the jet diffusion pattern at different axial distance

The data shown in Figure (9.27)-(a) and (b) are the same data using the same value of jet diameter and values of x and r, but with varying in the nozzle velocity (V_N). It can be seen that the water diffusion velocity decays laterally from the nozzle centerline to reach zero away from the jet centerline and the V_x/V_c values became negative as r/b_u increased further due to upward moving motion of the water.

It is seen that the stream wise velocity profile is self-similar and all the measured values were able to be approximated by a Gaussian distribution. However, as x_1 decreased (i.e., as the water jet velocity increased), the deviation from the Gaussian distribution increased.

McKeogh and Ervine (1981), Bonetto and Lahey (1993), Khaled and Hammad (2010), and Ma et al. (2010) they also found that the general shape of the jet axial velocity profile is a Gaussian distribution. Such an agreement between the measured V_x/V_c values and a Gaussian distribution was also observed for vertical bubbling jets generated by injecting gas through a single-hole bottom nozzle or a single-hole bottom orifice into a water bath (Iguchi et al. 1995b). In addition, the same tendency was reported for vertical bubbling jets generated by injecting a premixed gas and water through a single-hole bottom nozzle into a water bath (Iguchi et al. 1997).

Chapter 10

Conclusion and Future Work

10.1 Introduction

The empirical correlations and the experimental results provide the insights necessary for a possible database for future analytical models of the air entrainment process. Moreover, they should also be useful for benchmarking phenomenological or mechanistic Computational Fluid Dynamic (CFD) analysis of the dispersion process in the induced two-phase jet. This chapter presents the main summary and conclusions obtained in this work and the suggested future work. Also a discussion on how the present study can help to understand the process of buoyant gas jets as well as the vertical plunging water jets. The major milestones of this thesis that have been accomplished are:

(i) Experimental study of the buoyant gas jets injected horizontally in stagnant ambient water and investigation of the different parameters that affect the jet characteristics.

(ii) Develop of an Integral Model to predict the jet trajectories and the other jet parameters of the buoyant gas jets.

(iii) Experimental study of the vertical plunging water jets on a free water surface and investigation of the different parameters that affects the water jet characteristics and the rate of air entrainment.

Based on the finding of this study, the following is a brief discussion of the major conclusions and milestones:

10.2 Buoyant Gas Jets

A theoretical and experimental investigation of the temporal development of round turbulent buoyant gas jets injected horizontally in stagnant water ambient is studied.

10.2.1 Experimental Study

Direct measurements of the jet interface were performed using a photographic technique (CCD camera) which allowed simultaneous measurements. This technique allows quantitative measurement of the entire gas jet and the

interfacial motion. Two different methods named summation and statistical were used to obtain and analyze the experimental results and it was found that both methods yield almost identical results as shown in Figure (5.5).

- Three regimes of buoyant jet flow have been observed at the injector exit; jetting, transition, and bubbling regimes. In the first regime, the gas leaves the injector as a continuous jet of gas, where the initial momentum flux dominates, in the third regime the jet is shown to expand and form seemingly discrete bubble, where the flow is driven by the buoyancy force, the buoyancy-generated momentum flux dominates and in this region the flow starts to rise more dramatically depending on the relative densities of the two fluids. In the transition stage, the effluent flow is governed by both momentum and buoyancy force and will cause the jet to move horizontally with radial velocities as soon as the jet reaches the water free surface. Therefore, the jet recording process by the CCD camera was divided into two separated stages namely (i) momentum jet region near to the nozzle exit and (ii) buoyant jet region after the momentum region. Each region was studied individually by recording each region separately with the same initial conditions.

- Buoyant jets were observed to consistently pinch-off at a spatial location. The maximum location before the jet pinch-off is shown to have a logarithmic relation with the Froude number for all the jet diameters tested and a relationship is found given by correlation (5.1).

- All injector diameters have unsteadiness near the nozzle exit which is a function of the Froude number and the diameter of the nozzle. At approximately $x/L_Q \approx$ 8:10 the interfacial unsteadiness undergo a switch in their trend. Prior to this point, the jets with higher Froude number have high unsteadiness, and after this point the smaller Froude numbers have higher interface unsteadiness. Increasing the Froude number is seen to have a stabilizing effect on the interface having less interfacial motion than for smaller Froude number jets. This finding can perhaps be explained from the internal characteristics of the gas jets. Interface unsteadiness suggests that the shear layers emanating from the width of the nozzle plays a large role in governing the jet development by directly contributing to the stability of the interface.

- The spatial instability growth rate was deduced from the downstream evolution of the interfacial unsteadiness, it was shown that follows an

exponential growth for all injector diameters and Froude numbers and is given by correlation (5.3).

- The jet penetration length was calculated from the gradient of the image intensity for both the momentum and buoyant region, and it was observed that is strongly influenced by the nozzle diameters and the Froude numbers as well as by the jet mass flow and jet momentum flow rate. Correlations were developed for the jet penetration length as a function of the initial jet conditions.

- The variation of the jet penetration length due to the momentum along the jet axis with the time was found to represent a Gaussian distribution as shown in Figure (5.6).

- The jet spreading rate, which is indicative of entrainment rate, shows dependence on both nozzle diameter and Froude number and has been found to increases linearly with the axial distance from the nozzle exit. Also, the expansion angle was calculated from the gradient of the image intensity and it was found that the Froude number play a large role in dictating the jet expansion angle and the jet half-width. Empirical correlations are developed to predict the jet expansion angles and jet-half width.

10.2.2 Theoretical Study

A numerical model has been developed to assist in the design and to monitor the performance of the experimental investigation. The model is an integral model, but unlike existing integral models, the trajectory of the buoyant-jet is divided into two separated regions named momentum-dominated and buoyant-dominated region. Each region was studied individually under certain assumptions and governing relations, which has some improvements over similar models presented by various other investigators. Also, the rate of entrainment is assumed to be a function of the jet centerline velocity and the ratio of the mean jet and ambient densities. The entrainment coefficient is considered as a variable because the local rate of entrainment is consisted of the entrainment due to jet momentum and the entrainment due to buoyancy. In addition, there is an interfacial shear stress acting at the interface between the jet flow and the ambient in the opposed direction to the main jet momentum flux. Also, an approximately assumption of the momentum of the entrained water droplets flying into the jet flow is considered.

However, the results is achieved in two steps; first, the integral model of the mass and momentum fluxes are obtained and transformed to a set of ordinary differential equations using particular non-dimensional transformations. Similarity forms are derived and solutions are obtained of the mean centerline quantities such as mean centerline velocity. Second, a complete set of results of interest including jet trajectory, jet penetration lengths, jet half-width, and jet velocity defining the jet trajectory were solved as variables along the jet path and compared with the experimental data.

- Predictions from the Integral Model are compared with the results of the experiments obtained by the image processing algorithms in the laboratory test installation as shown in Figure (7.1) and figure (7.2). The Predictions are shown to be consistent with the experimental data for a given nozzle diameters and Froude numbers and good agreement predictions were found.

- The predicted jet penetration lengths and those obtained experimentally have been plotted together as shown in figure (7.3). The experimental values collapse well and are consistent with all the model predictions with ±10% error for both jet momentum and jet buoyant penetration length.

- Due to the absence of measured velocity data in the present study, it was decided to perform a series of numerical calculations using the present Numerical Model. Figure (7.5) shows the normalized predicted centerline velocity. As the Froude number decrease the mean axial velocity decreases as well as it decreases in the downstream direction. As the jet penetrates, it entrains liquid and thus increases its volume. This causes velocities to decrease in the stream wise direction, and buoyancy forces become more important in the downstream direction.

- At the same time, the experimental results were used to verify the accuracy of the Numerical Model, the good agreement predictions lead to increasing the confidence in the flow visualization technique.

10.3 Vertical Plunging Water Jets

- We have performed a series of experimental work for short nozzles of small length-to-diameter ratios ($l_N/d_N \leq 5$), for which little studies have been carried out. The effects of different range of operating variables including initial jet diameters, initial jet velocity, and jet length on the flow characteristics and

their flow patterns such as the inception velocity of the gas entrainment, the bubble penetration depth, the gas entrainment rate, the jet axial velocity and lateral velocity distribution below the free water surface were investigated. Other parameters of interest, such as the height and width of the two-phase mixture due to the air entrainment, and the jet surface instability were also monitored. The following conclusions have been obtained:

- Air bubbles were observed in the water tank when the jet impact velocity at the plunging point becomes larger than a critical value of about 1.1 to 2.0 m/s. This velocity was found a function of the jet length and the diameter of the jet at the plunging point, a power relationship given by Equation (9.3) was obtained.

- The bubble penetration depths (H_p) and the average plume shape under each operating condition is determined by using images captured by CCD Video camera. The results obtained showed that the penetration depth ratio (H_p/d_N) decreases with the dimensionless jet length x_1/d_N satisfying the relation given by Equation (9.4) until a point at $x_1/d_N \simeq 25$ was reached where the ratio of the penetration level was almost constant with increasing the jet length. After this point the ratio of the penetration level was almost constant with increasing the jet length for all jet diameters. The decrease in H_p with x_1 can be considered due to the increase of the buoyancy force of the entrained bubbles as a result of the increase in the air entrainment rate, Q_a. The limit to the depth to which the bubbles penetrate in this ordinary jet system is considered a disadvantageous when the liquid in an apparatus of large depth has to be aerated.

- The effect of initial jet velocity was also evaluated and we found that H_p increased when increasing V_N for all the jet diameters. It means that, penetration depth is directly proportional to the jet velocity, irrespective of nozzle diameters. Also, we have found that the H_p increased with the initial jet diameter for all jet lengths and jet velocities.

- The maximum bubble penetration depth achieved by the higher nozzle diameter at a given jet velocity and x_1 was relatively small. The reason for these differences in H_p due to the jet diameter is that the water nozzles have different jet expansions and jet shapes that are different for each nozzle. The increase in H_p with increasing V_N and d_N may be also due to the increase in the momentum of the water jet. However, the penetration depth of the entrained bubble depends largely on the downward velocity field in the two-

phase region. To attain a deeper bubble penetration, it is required to provide enough downward water flow to overcome the buoyancy forces of the bubble produced by the water jet. The air bubbles entrained in the water give a buoyancy effect to the diffusion of the jet and contribute to a velocity decrease in the diffusion region.

- Empirical relationships have been proposed to estimate the penetration depth of the plunging jets; these equations can be very useful in determining and/or deciding the depth of the aeration tank within the range of tested initial condition. The maximum bubble penetration depth H_p is predicted by Equation (9.7) having empirical constants shown in Table (9.7), also a comparison with the results obtained from other previous empirical relationships was performed. An excellent agreement between the calculated H_p and the measured H_p as well as with the other previous correlation by other researchers was found.

- A non-dimensional correlation was found to predict the H_p/d_N ratio with the non-dimensional parameters such as Froude number, jet length ratio (x_1/d_N) and the nozzle aspect ratio (l_N/d_N) given by Equation (9.8) having empirical constants shown in Table (9.8). Good coincidence was found between the experimental results and the calculated formula within ±15%.

- The air entrainment measurements were performed when an almost constant pressure was achieved inside the air trap (see Figures, 8.14 and 8.15); this means a nearly stable air flow rate to the flow meter. The maximum relative fluctuation amplitude of the pressure is obtained at the higher jet flow rate $Q_w=5.53\times10^{-4}$ m^3/s. However, the scattering of the air flow rate measurements was observed to be very small at low jet flow rates and consistently much larger when the jet increases the flow rate. Typically, the air flow rate ranges from 2.53×10^5 m^3/s to 77.3×10^5 m^3/s. Under these conditions, the relative error on Q_a varied from about ±0,1% for $Q_a=2.5\times10^5$ m^3/s to ±2.2% for $Q_a=77.3\times10^5$ m^3/s.

- The rate of air entrainment increases significantly where increasing the nozzle diameter for a given jet length. Since, the jet contact area with the atmospheric air increases when increasing the jet diameter. However, the results showed that the effect of jet diameter on the entrainment rate can be divided into two regions depending on the values of the nozzle diameters. For d_N between 6 and 10 mm, $Q_a\propto d_N^{1.9}$ and for d_N between 10 and 14 mm,

Q_a is in proportion to $d_N^{0.15}$. Also the entrained rate was found to increases with the height of the fall (x_1) for all the operation conditions.

- The entrainment rate Q_a tended to increase when the jet velocity increased and their curves were divided into three regions depending on the jet velocity range. The values of the Q_a for water jets of the respective region i, ii and iii can be predicted by Equation (9.9) having empirical constants shown in Table (9.5).

- Based on the dimensionless analysis, and using dimensionless number a non-dimensional equation was obtained for predicting the Q_a/Q_w ratio given by Equation (9.11), and having empirical constants shown in Table (9.6). A good agreement with the experimental data with accuracy of ±20% was obtained.

- The jet centerline velocity decay (V_c) measured below the free water surface was found to be a function of the jet impact velocity (V_1), the jet diameter (d_1) and the plunge depth (x). The rate of decrease of V_c/V_1 was found to be not constant throughout the whole range of x/d_1, thus the rate of decrease for x/d_1 above 16, tended to be larger than below 16 and this result agree with previous results. When the jet length x_1=0 there is no bubble entrainment, the velocity distributions agreed well with the results for single-phase free jets correlations given by previous researchers. The axial velocity distribution (Vx/Vc) was found to be approximately represented by a Gaussian distribution when plotted against (r/b_u).

- Our experimental results and empirical correlations proposed to predict the jet parameters were found in a reasonable agreement with those obtained in some experimental and correlations available in the literature.

We hope that the results presented in this work could be used as a database (among others available in the literature) for future studies.

10.4 Recommendations for Future Work

There are several areas in which this work must continue, with the goal of further understanding the problem of the horizontal buoyant gas jets and the vertical plunging water jets. A brief list is provided below:

- The effect of nozzle diameters, jet mass flow rate and Froude number on the jet penetration length, gas jet half-width and jet expansion angle were presented. There is clearly a gap in the jet properties as the nozzle diameter is increased over the four diameters studied (2, 3, 4, and 5 mm). It is therefore recommended to repeat the experiments using many more nozzle diameters.

- Hydrostatic pressure is also thought to play an important role in the behaviour of the buoyant gas jet, having an especially important role in governing pinch off. It is recommended to study the effect of hydrostatic pressure on the gas jet characteristics.

- Injecting steam at different temperatures and steam mixed with air or hot water instead of injecting only air, and trying to predict the jet behavior and the moment at which it condenses, as well as the condensation rate. All of these data would be of interest in regarding the operation of many systems at work in commonplace nuclear power plants.

- For vertical plunging water jets, further study using a wide range of liquid-phase, other types of plunging jet system (rectangular nozzles for example), long nozzles, inclined jets and compare the results with the short nozzles of the present study.

- Develop an analytical model to predict the air entrainment rate and the different jet parameters and to validate the results with the correlations and experimental results that have been obtained.

- Use the particle image velocimetry (PIV) system to measure the two-phase jet velocities in both the lateral and axial positions and determine value of the bubble mean diameter. Other parameters of interest, such as gas holdup, distributions of bubble concentration, bubble chord length distributions, and turbulence.

- Further work is required to gain a better understanding for the bubble breakup process. Additional studies of plunging jet flows are also necessary to investigate the transition region between the near-flow field and fully developed flow regions.

References

Abraham, G., (1963), Jet diffusion in stagnant ambient fluid, Delft Hydraulics Laboratory Pub. **29**.

Agrawal, A., and Prasad, A. K., (2003), Integral solution for the mean flow profiles of turbulent jets, plumes, and wakes, ASME Journal of Fluids Engineering, **125** pp. 813-822.

Agrawal, A., Prasad, A. K., (2004), Evolution of a turbulent jet subjected to volumetric heating, Journal of Fluid Mechanics, **511** pp. 95-123.

Agrawal, A., Sreenivas, K. R., and Prasad, A. K., (2004), Velocity and temperature measurements in an axisymmetric turbulent jet with cloud-like off-source heating, International Journal of Heat and Mass Transfer, **47** (6) pp. 1433-1444.

Ahmed, A., (1974), Aeration by plunging liquid jet, Ph.D thesis, Loughborough University of Technology.

Albertson, M. L., Dai, Y. B., Jensen, R. A., and Rouse, H., (1949), Diffusion of submerged jets, American Society of Civil Engineers Proceedings, **75** (10) pp. 1541-1548.

Aoki, T., Masuda, S., and Hatano, A., (1982), Characteristics of submerged gas jets and a new type bottom blowing tuyere. In: Injection Phenomena in Extraction and Refining, Wraith A E, ed. Newcastle: Department of Metallurgy and Engineering Materials, University of Newcastle upon Tyne, pp. A1-36.

Avery, J. F., and Faeth, G. M., (1974), Combustion of a submerged gaseous oxidizer jet in a liquid metal, Symposium (International) on Combustion, **15** (1) pp. 501-512.

Batchelor, G. K., (1954), Heat convection and buoyancy effects in fluids, Quarterly Journal of the Royal Meteorological Society, **80** (345) pp. 339-358.

Batchelor, G. K., (1967), An introduction to fluid dynamics, Cambridge University Press.

Bhat, G. S., and Narasimha, R. A., (1996), A volumetrically heated jet: Large-eddy structure and entrainment characteristics, Journal of Fluid Mechanics, **325** pp. 303-330.

References

Bín, A. K., (1988), Minimum air entrainment velocity of vertical plunging liquid jets, Chemical Engineering Science, **43** pp. 379-389.

Bín, A., (1971), Investigation of the aeration effect of free liquid jet, Ph.D. thesis, Warsaw University of Technology.

Bin, A., K., (1993), Gas entrainment by plunging liquid jets, Chemical Engineering Science, **48** (21) pp. 3585-3630.

Bohrer, A., and Wittler, (1998), Predicting plunge pool velocity decay of free falling, rectangular jet, Journal of Hydraulic Engineering, **124** (10) pp. 1043-1048.

Bonetto, F., and Lahey, R. T., (1993), An Experimental Study on Air Carryunder due to a Plunging Liquid Jet, International Journal of Multiphase Flow, **20** (3) pp. 667-770.

Bonsignore, D., Volpicelli, G., Campanile, A., Santoro, L., and Valentino, R., (1985), Mass transfer in plunging jet absorbers, Chemical Engineering Process, **19** pp. 85-94.

Borisov, A. A., Gelfand, B. E., and Timofeev, E. I., (1983), Shock waves in liquids containing gas bubbles, International Journal of Multiphase Flow, **9** (5) pp. 531-543.

Brady, J. F., (1966), Underwater propulsion, AIAA and office of naval research, symposium on deep submergence propulsion and marine systems, forest park, ill. AIAA-1966-2408, pp. 204-225.

Brattberg, T., and Chanson, H., (1998), Air entrapment and air bubble dispersion at two-dimensional plunging water jets, Chemical Engineering Science, **53** (24) pp. 4113-4127.

Brodkey, R. S., (1967), The phenomena of Fluid Motions, Dover.

Burgess, J. M., Molloy, N. A., (1973) Gas absorption in plunging liquid jet reactor, Chemical Engineering Scince, **28** pp. 183-190.

Carlotti, P., and Hunt, G. R., (2005), Analytical solutions for turbulent non-Boussinesq plumes, Journal of Fluid Mechanics, **538** pp. 343-359.

References

Castillejos, A. H. and Brimacombe J. K., (1987), Measurement of physical characteristics of bubbles in gas-liquid plumes an improved electroresistivity Probe Technique, Chemistry and Materials Science, **18** (4) pp. 649-658.

Cetegen, B., Zukoski, E. E., and Kubota, T., (1982), Entrainmentand flame geometry of fire plumes, NBS-GCR-82-402, U.S, National Bureau of Standards, Gaithersburg, MD.

Chan, C. K., (1974), Dynamic pressure pulse in stream jet condensation, In Proceeding 5th International Heat Transfer Conference, ASME, New York, **3** pp. 226-230.

Chanson, H., (1992), Reduction of Cavitation on Spillways by induced Air Entrainment - Discussion, Canadian Journal of Civil Engineering, **20** pp. 926-928.

Chanson, H., and Brattberg, T., (1996), Air-Water Bubbly Flow in Free-Shear Layers, Proc. 1996 ASME Fluids Eng. Conf., San Diego, USA, ASME-FED **236** pp. 357-364.

Chanson, H., and Brattberg, T., (1997), Experimental Investigations of Air Bubble Entrainment in Developing Shear Layers, Report CH48/97, Dept. of Civil Engineering, University of Queensland, Australia, August.

Chanson, H., and Cummings, P. D., (1994), An Experimental Study on Air Carryunder due to Plunging Liquid Jet-Discussion, International Journal of Multiphase Flow, **20** (3) pp. 667-770.

Chanson, H., and P. Cummings (1992), Aeration of the Ocean due to Plunging Breaking Waves, Research Report No. CE142, Dept. of Civil Engineering, University of Queensland, Australia, Nov., 42 pages.

Chanson, H., Aoki, S., and Hoque, A., (2002), Similitude of Air Bubble Entrainment and Dispersion in Vertical Circular Plunging Jet Flows, An Experimental Study with Freshwater, Salty Freshwater and Seawater, Coastal/Ocean Engineering Report, No. COE02-1, Dept. of Architecture and Civil Eng., Toyohashi University of Technology, Japan, 94 pages.

References

Chawla, T., (1975), Rate of liquid entrainment at gas-liquid interface of a liquid submerged sonic gas jet, Nuclear Science and Engineering, **56** (1) pp. 1-6.

Chen, C. J., and Rodi, W., (1980), Vertical turbulent buoyant jets: A review of experimental data, HMT Science and Applications of Heat and Mass Transfer, Oxford, New York, **4** pp. 94.

Chen, K., and Richter, H. J., (1997), Instability analysis of the transition from bubbling to jetting in a gas injected into a liquid, International Journal of Multiphase Flow, **23** (4) pp. 699-712.

Cheung, S. K., Leung, D. Y., Wang, W., Lee, J. H., and Cheung, V., VISJET - A computer ocean outfall modelling system, CGI: The 18th Computer Graphics Internationa 'Humans and Nature', Jun 19-24 Jun 2000, Geneva, Switz, 75-80.

Christopher J. W., (2009), Characteristics of the high speed gas-liquid interface, Ph.D. thesis, Blacksburg, Virginia.

Chu, V. H., and Lee, J. H., (1996), General integral formulation of turbulent buoyant jets in cross-flow, American Society of Civil Engineers (ASCE), Journal of the Hydraulics Division **122** (1) pp. 27-34.

Ciborowski, J., and Bín, A., (1972), Investigation of the aeration effect of plunging liquid jets. Inz. Chem. (Polish) **2**, pp. 557-577.

Cieslinski, J. T., and Mosdorf, R., (2005), Gas bubble dynamics-experiment and fractal analysis, International Journal of Heat and Mass Transfer, **48** (9) pp. 1808-1818.

Crapper, P. F., and Baines W. D., (1977), Non-Boussinesq forced plumes, Atmospheric Environment, **11** (5) pp. 415-420.

Cumming, I., W., (1975), The impact of falling liquids with liquid surface, Ph.D. thesis, Loughborough University of Technology.

Cummings, P. D., and Chanson, H., (1997a), Air entrainment in the developing flow region of plunging jets, Part 1 Theoretical Development, Journal of Fluids Engineering - ASME, **119.**

References

Cummings, P. D., and Chanson, H., (1999), An experimental study of individual air bubble entrainment at a planar plunging jet, Chemical Engineering Research and Design, Trans. IChemE, Part A, **77** pp. 159-164.

Dai, Z. Q., Wang, B. Y., Qi, L. X., and Shi, H. H., (2006), Experimental study on hydrodynamic behaviors of high-speed gas jet in still water, Acta Mechanica Sinica, **22** pp. 443-448.

Davidson, M. J., and Pun, K. L., (1998), Hybrid model for prediction of initial dilutions from outfall discharges, Journal of Hydraulic Engineering, **124** (12), 1188-1197.

Davidson, M. J., Gaskin, S., and Wood, I. R., (2002), Astudy of a buoyant axisymmetric jet in a small co-flow, Journal of Hydraulic Research, **40** (4) pp. 477-489.

Dimotakis, P. E., Miakelye, R. C., and Papantoniou, D. A., (1983), Structure and Dynamics of Round Turbulent Jets, Physics of Fluids, **26** (11) pp. 3185-3192.

El-Amin, M. F., (2009), Non-Boussinesq turbulent buoyant jet resulting from hydrogen leakage in air, Science and Technology of Nuclear Installations, **34** pp. 7873-7882.

El-Amin, M. F., Kanayama, H., (2009), Similarity consideration of the buoyant jet resulting from hydrogen leakage, International journal of hydrogen energy, **3** (4) pp. 5803-5809.

El-Amin, M. F., Shuyu, S., and Kanayama, H., (2010), Non-Boussinesq turbulent buoyant jet of a low-density gas leaks into high-density ambient, Applied Mathematics and Computation, **217** pp. 3764-3778.

Engh, T. A., and Nilmani, M., (1988), Bubbling at high flow rates in inviscid and viscous liquids (slags), Metallurgical Transactions B, **19** (1) pp. 83-94.

Epstein, M., Fauske, H., Kubo, S., Nakamura, T., and Koyama, K., (2001), Liquid entrainment by an expanding core disruptive accident bubble-a Kelvin/Helmholtz phenomenon, Nuclear Engineering and Design, **210** pp 53-77.

Ervine, D. A., McKeogh, E. J., and Elsawy, E. M., (1980), Effect of turbulence intensity on the rate of air entrainment by plunging water jets, Proceedings of the Institution of Civil Engineers, London, **69** (2) pp. 425-445.

Evans, G. M., (1990), A study of a plunging jet bubble column, Ph.D. Thesis, university of Newcastle, Australia.

Fan, L. N., (1967), Turbulent buoyant jets into stratified or flowing ambient fluids, KH-R-15, W. M. Keck Laboratory of Hydraulic and Water Resources, California Institute of Technology, Pasadena, California.

Fan, L. N., and Brook, N. H., (1969), Numerical solutions of turbulent buoyant jet problems, KH-R-18, W. M. Keck Laboratory of Hydraulic and Water Resources, California Institute of Technology, Pasadena, California.

Ficher, H. L., List, E. J., Koh, R. C., and Brooks, N. H., (1979), Mixing in inland and coastal waters, Academic Press, New York, pp. 483.

Förthmann, E., (1934), Uber turbulente Strahlausbreitung, Archive of Applied Mechanics, **5** (1) pp. 42-54.

Funfschilling, Li, D., (2001), Flow of Non-Newtonian Fluids Around Bubbles: PIV Measurements and Birefringence Visualization, Chemical Engineering Science, **56** pp. 1137-1141.

Gongwer, C. A., (1960), Some aspects of underwater jet propulsion systems, Antioxidants and Redox Signaling Journal, **30** (12) pp. 1148-1151.

Görtler, H., (1942), Berechnung von Aufgaben der Freien Turbulenzaus Grundeinesneuen Näherungsansatzes, ZAMM, **22** pp. 244-254.

Gulawani, S. S., Deshpande, S. S., and Joshi, J. B., (2007), Submerged gas jet into a liquid bath: A review, Industrial and Engineering Chemistry Research, **46** pp. 3188-218.

Gustaaf, A. K., (2006), Buoyant jets with and three-dimensional trajectories, Ph.D thesis, University of Canterbury, Christchurch, New Zealand.

Helmholtz, H. V., (1868), On discontinuous movements of fluids, Philosophical Magazine, **36** (4) pp. 9.

Henderson, J. B., McCarthy, M. J. and Molloy, N. A., (1970), Entrainment by plunging jets, in Proceeding of Chemical 70, Melbourne, Section 2, pp. 86-100.

References

Hirst, E. A., (1971), Analysis of buoyant jets within the zone of flow establishment, Oak Ridge National Laboratory, Report ORNLTM-3470.

Hoefele, E. O., Brimacombe, J. K., (1979), Flow regime in submerged gas injection, Metallurgical and Materials Transactions B, **10** (4) pp. 631-648.

Hong, S., Guo, Q., Wang, C., Dong, R., Zhang, L., Jia, H., Wang, X., and Wang, B., (2010), Oscillation flow induced by underwater supersonic gas jets, **20** (4) pp. 347-352.

Houf, W. G., and Schefer, R. W., (2008), Analytical and experimental investigation of small-scale unintended releases of hydrogen, International Journal Hydrogen Energy, **33** (4), pp. 1435-1444.

Hunt, G. R., and Kaye, N. B., (2005), Lazy plumes, Journal of Fluid Mechanics, **533** pp. 329-338.

Hussain, N. A., and Narang, B. S., (1984), Simplified analysis of air-bubble plumes in moderately stratified environments, Journal of Heat Transfer, **106** pp. 543-551.

Iguchi, M., Okita, K., and Yamamoto, F., (1997), Structure of turbulent round bubbling jet generated by premixed gas and liquid injection, International Journal of Multiphase Flow, **23** pp 249-262.

Iguchi, M., Okita, K., and Yamamoto, F., (1998), Mean velocity and turbulent characteristics of water flow in the bubble dispersion region induced by plunging water jet, International Journal of Multiphase Flow, **24** (4) pp 523-537.

Iguchi, M., Tani, J., Uemura, T., Kawabata, H., Takeuchi, H., and Morita, Z., (1989), The characteristics of water and bubbling jets in a cylindrical vessel with bottom blowing, The iron and steel Institute of Japan **29** pp. 309-317.

Ishigaki, H., (1982), Turbulent round jets, Japan Society of Mechanical Engineering, **49** pp. 1692-1700.

Ito, K., Kobayashi, S., and Tokuda, M., (1991), Mixing characteristics of a submerged jet measured using an isokinetic sampling probe, Metallurgical Transactions B-Process Metallurgy, **22** (4) pp. 439-445.

Iwasaki, T., and Senshu, S., (1953), An experimental study on water fall, Doboku Gakkaishi, **38** pp. 337-341.

References

Jianing, T., Shipeng, L.,Ningfei, W., Yingjie W., and Wei S., (2010), Flow structures of gaseous jets injected into water for underwater propulsion, Acta Mechanica Sinica, **27** (4) pp. 461-472.

Jirka, G. H., (2004), Integral model for turbulent buoyant jetsin unbounded stratified flows-part I: single round jet, Environmental Fluid Mechanics, **4** (1), pp. 1-56.

Jirka, G. H., and Harleman, D. R., (1979), Stability and mixing of a vertical plane buoyant jet in confined depth, Journal of Fluid Mechanics, **94** Part 2 pp. 275-304.

Kawaguchi, T., Niwa, Y., Hishida, K., and Maeda, M., (2001), Spatial Distribution of Bubble Size and Velocity in Gas Absorbing Process Measured by Interferometric Laser Imaging, International Conference on Multiphase Flow, New Orleans, EEUU.

Kelvin, W., (1871), Hydrokinetic solutions and observations, Philosophical Magazine, **42** (4) pp. 15.

Kerney, P. J., Faeth, G. M., and Olson D. R., (1972), Penetration characteristics of submerged steam jet, AIChE Journal, **18** (3) pp. 548-553.

Khaled J. Hammad (2010), Liquid jet impingment on a free liquid surface: PIV study of the turbulent bubbly two-phase flow, Proceedings of the ASME 2010 3rd Joint US-European Fluids Engineering Summer Meeting and 8th International Conference on Nanochannels, Microchannels, and Minichannels, FEDSM-ICNMM2010 August 1-5, 2010, Montreal, Canada.

Kima, J. S., Yangb, W., Kimc, Y., Won, S. H., (2009), Behavior of buoyancy and momentum controlled hydrogen jets and flames emitted into the quiescent atmosphere, Journal of Loss Prevention in the Process Industries, **22** (6) pp. 943-949.

Kitscha, J., and Kocamusta, G., (1989), Breakup criteria for fluid particles, International Journal of Multiphase Flow, **15** (4) pp. 573-588.

Kotsovinos, N. E., (1975), A study of the entrainment and turbulence in a plane buoyant jet, Ph.D. Thesis, California Institute of Technology, Pasadena.

References

Kotsovinos, N. E., and List, E. J., (1977), Plane turbulent buoyant jets, Part 1, Journal of Fluid Mechanics, **81** pp. 25-44.

Kumagai, M., and Endoh, K., (1983), A note on the relationship between gas entrainment curve and its starting velocity, Journal of Chemical Engineering of Japan, **16** pp. 74-75.

Kumagi, M., and Imai, H., (1982), Gas entrainment characteristics of an impinging water jet, Kagaku Kogaku Ronbunshu, **8** pp. 1-6.

Kusabiraki, D., Murota, M., Ohno, S., Yamagiwa, K., Yasuda, M., and Ohkawa, A., (1990), Gas entrainment rate and flow pattern in a plunging liquid jet aeration system using inclined nozzles, Journal of Chemical Engineering, Japan, **23** pp. 704-710.

Kusabiraki, D., Niki, H.,, Yamagiwa, K., Ohkawa, A., (1990b), Gas entrainment rate and flow pattern of vertical plunging liquid jets, The Canadian Journal of Chemical Engineering, **68** (6) pp. 893-903.

Lin, T. J., (1963), Gas bubble entrainment by plunging laminar liquid jets, Ph.D thesis, wayne State University.

Lindken, R. W., (2002), A novel PIV Technique for Measurements in Multiphase Flows and its Application to Two-Phase Bubbly Flows, Experiments in Fluids, **33** (6) pp. 814-825.

List, E. J., (1982), Turbulent jets and plums, Annual Review of Fluid mechanics, **14** pp. 198-212.

List, E. J., and Imberger, J., (1973), Turbulent entrainment in buoyant jets and plumes, Journal of Hydraulic Division, **99** (9) pp. 1461-1474.

List, E. J., Fischer, H. B., Koh, R. C., Imberger, J., and Brooks, N. H., (1979), Mixing in inland and coastal waters, Academic Press.

Loth E., and Faeth, G. M., (1989), Structure of underexpanded round air jets submerged in water, International Journal Multiphase Flow, **15** (4) pp. 589-603.

Loth, E., and Faeth G. M., (1990), Structure of plane underexpanded air jets into water, AIChE Journal, **36** (6) pp. 818-826.

References

Ma, J., Oberai, A. A., Drew, D. A., Lahey, R. T., Moraga, F. J., (2010), A quantitative sub-grid air entrainment model for bubbly flows-plunging jets, Compute and Fluids, **39** pp. 77-86.

Mahad, S. B., Mohamed, G., Daniel, W. S., (2012), Characterizing two inclined circular water jets plunging into an aeration tank, International Journal of Multiphase Flow, **40** pp. 158-165.

Manase, R., Manase, S., Yoshida, M., Rudman., (1998), Bubble formation processes and bubble acoustic signals, Third International Conference on Multiphase Flow, (Lyon, France).

Martin, S., Dana, D., and Dirk, L., (2009), Air entrainment by impinging jets Experimental identification of the key phenomena and approaches for their simulation in CFD, Proceedings of the 17th international conference on nuclear engineering, Brussels, Belgium.

McKeogh, E. J., and Ervine, D. A., (1981), Air entrainment rate and diffusion pattern of plunging liquid jets, Chemical Engineering Science, **36** pp. 1161-1172.

McNallan, M. J., and King, T. B., (1982), Fluid-dynamics of vertical submerged gas jets in liquid-metal processing systems, Metallurgical Transactions B-Process Metallurgy, **13** (2) pp. 165-173.

Mersmann, A., (1980), Flooding point of liquid/liquid countercurrent columns, Chemical Engineering Technology, **52** pp. 933-942.

Miyahara, T., Haga, N., and Takahashi, T., (1983), Bubble formation from an orifice at high gas flow rates, International Chemical Engineering, **23**, pp. 524-531.

Mori, K., Ozawa, Y., and Sano, M., (1982), Characterization of Gas-Jet Behavior at a Submerged Orifice in Liquid-Metal, Transactions of the Iron and Steel Institute of Japan, **22** (5) pp. 377-384.

Morton, B. B., Taylor, G., and Turner, J. S., (1956), Turbulent gravitational convection from maintained and instantaneous sources, Proceedings of the Royal Society of London, Series A, Mathematical and Physical Sciences, **234** (1196) pp. 1-23.

Morton, B. R., (1965), Modelling fire plumes, In: 10th international symposium on combustion, pp. 973-82.

References

Morton, B. R., Taylor, G. I., and Turner, J. S., (1956), Turbulent gravitational convection from maintained and instantaneous sources, Proceedings of the Royal Society of London, **234** pp. 1-23.

Muellenhoff, W. P., Soldate, J., A., Baumgartner, D. J., Schuldt, M. D., Davis, L. R., and Frick, W. E., (1985), Initial mixing characteristics of municipal discharges, Vol. I and II, EPA-600/3-85-073a, United States Environmental Protection Agency, Newport, Oregon.

Ohkawa, A., Kusabiraki, D., and Sakai, N., (1987), Effect of nozzle length on gas entrainment characteristics of vertical liquid jet. Journal of Chemical Engineering Japan, **20** (3) pp. 295-300.

Ohkawa, A., Kusabiraki, D., Kawai, Y., and Sakai, N., (1986), Some flow characteristics of a vertical liquid jet system having downcomers, Chemical Engineering Science, **41** (9) pp. 2347-2361.

Otake. T., Otake, S., Tone, K., Nakao, Y., Mitsuhashi, (1977), Coalescence and breakup of bubbles in liquids, Chemical Engineering Science, **32** pp. 377-383.

Ozawa, Y., and Mori, K., (1986), Effect of physical-properties of gas and liquid on bubbling jetting phenomena in gas injection into liquid, Transactions of the Iron and Steel Institute of Japan, **26** (4) pp. 291-297.

Pantokratoras, A., (1998), Horizontal Penetration of Inclined Thermal Buoyant Water, International Communications in Heat and Mass Transfer, **25** (4) pp. 561-569.

Perry, R. T., (1967), Fluid mechanics of entrainment through liquid-liquid and solid-liquid junctures, Ph.D thesis, university of Minnesota.

Petipas, F., Massoni, J., Saurel, R., Lapebie, E. and Munier, L., (2009), Diffuse interface model for high speed cavitating underwater systems, International Journal of Multiphase Flow, **35** pp. 747-759.

Poynton, C. A., (1996), A Technical Introduction to Digital Video", John Wiley and Sons Inc, New York.

Priestley, C. H., and Ball, F. K., (1955), Continuous convection from isolated source of heat Quarterly Journal of the Royal Meteorological Society, **81** (348) pp. 144-157.

Qu, X., L., Khezzar, L., Danciu, D., Labois, M., and Lakehal, D., (2011), Characterization of plunging liquid jets: A combined experimental and numerical investigation, International Journal of Multiphase Flow, **37** PP. 722-731.

Rayleigh, J., (1879), On the instability of jets, Proceedings of the London Mathematical Society, **10** pp. 10.

Reichardt, H., (1943), On new theory of free turbulence, Royal Aeronautical Society Journal, **47** (390) pp. 167-176.

Ricou, F. P., and Spalding, D. B., (1961), Measurement of entrainment by axisymmetrical turbulent jets, Journal of Fluid Mechanics, **11**, pp. 21-31.

Rodi, W., (1982), Turbulent buoyant jets and plumes, The Science and Applications of Heat and Mass Transfer, reports, reviews and computer programs, **6**, Pergamon Press, New York, N.Y.

Rouse, H., Yih, C. S., and Humphreys, H. W., (1952), Gravitational convection from a boundary source, Tellus, **4** (3) pp. 201-210.

Ruzicka, M. C., Drahos, J., Zahradnik, J., and Thomas, N. H., (1997), Intermittent Transition from Bubbling to Jetting Regime in Gas-Liquid two Phase Flows, International Journal of Multiphase Flow, **23** (4) pp. 671-682.

Sahai, Y., and Guthrie, R. I., (1982), Hydrodynamics of Gas Stirred Melts: part 1. Gas-Liquid Coupling, Metallurgical Transactions B-Process Metallurgy, **13** (2) pp. 193-202.

Satoshi, S., Mitsunori, U., Yanrong, L., Hiroyuki, O., and Koji, O., (2011), An entrained droplet by an underexpanded gas jet into water, Journal of Visualization, **14** (3) pp. 225-236.

Schmidt, W., (1941), Turbulente Ausbreitung eines Stromes erhitzter Luft, ZAMM, **21** pp. 265-271.

Semanov, N. I., and Kosterin, S. I., (1964), Results of studying the speed of sound in moving gas-liquid systems, Thermal Engineering, **11** (46) pp.59.

Sene, K. J., (1988), Air entrainment by plunging jets, Chemical Engineering Science, **43** pp. 2615-2623.

Settles, G., (2006), Schlieren and shadowgraph techniques, Berlin, Springer.

Shakouchi, T., Akita, T., Uejima, T., Ota, H. and Sato, S. (1996), The flow characteristics of round plunging water jet, 15th Multiphase Flow Symposium '96, Fukui, 101-104 (in Japanese).

Shakouchi, T., Uejima, T., Ota, H., and Sato, S., (1995), Behavior of round plunging water jet, 14th Multiphase Flow Symposium '95, Ehime, 39-42 (in Japanese).

Shi, H. H., Wang, B. Y., and Dai, Z. Q., (2010), Research on the mechanics of underwater supersonic gas jets, Science China, **53** (3) pp. 527-535.

Shi, H. H., Wang, B. Y., and Qi, L. X., (2005), A submerged supersonic gas jet, In: Proc. 7th National Congress on Hydrodynamics and 19th National Symposium on Hydrodynamics. Beijing: Ocean Press, pp. 75-81.

Smigelschi, O., and Suciu, G. D., (1976), Size of the submerged biphasic region in plunging jet systems, Chemical Engineering Science **31**, pp. 1217-1220.

Snabre, P., Snabre, F., (1998), Formation and rise of a bubble stream in a viscous liquid. European Physics Journal, **4** pp. 369-377.

Spiegel, E., A., and Veronis, G., (1960), On the Boussinesq approximation for a compressible fluid, Astrophys Journal, **131** pp. 442-447.

Steward, F., R., (1970), Prediction of the height of turbulent diffusion buoyant flames, Combust Science Technology, **2** pp. 203-12.

Suciu, G. D., and Smigelschi, (1976), size of the submerged biphasic region in plunging jet system, Chemical engineering science, **31** (12) pp. 1217-1220.

Surin, V. A., Erchenko, V. N., and Robin, V. M., (1983), Propagation of a gas jet in a liquid, Journal of Engineering Physics, **45** pp. 1091-1101.

Tamer, B., and Nusret, S., (2003), Air-entrainment characteristics in a plunging water jet system using rectangular nozzles with rounded ends, Water S A, **29 (**1) pp. 35-38.

Taylor, G. I., (1958), Flow Induced by jets, Journal Aero Science, **25** pp. 464-465.

Tollmien, W., (1926), Calculation of turbulent unconfined flow Berechnung turbulenter Ausbreitungsvorgange, Zeitschrift fur Angewandte Mathematik und Mechanik, **6** (6) pp. 468-478.

Tross, S., (1974), Chracteristics of a turbulent two-phase submerged free jet, master thesis, mechanical engineering, university park, the pennsylvania state university.

Tsao, H. K., Tsao, D. L., (1997), Observations of high Reynolds number bubbles interacting with a rigid wall. Physics of Fluids, **9** (1) pp. 44-56.

Tse. K., Tse, T., Martin, C. M., McFarlane, A. W., (1998), Visualization of bubble coalescence in a coalescence cell, a stirred tank and a bubble column, Chemical Engineering Science, **53** pp. 4031-4036.

Turner, J. S., (1986), Turbulent entrainment: The development of the entrainment assumption, and its application to geophysical flows, Journal of Fluid Mechanics, **173** pp. 431-471.

Van de Donk, J. A. C., (1981), Water aeration with plunging jets. Ph.D. Thesis, Technische Hogeschool Delft, Netherlands.

Van de Sande, E., and Smith, J. M. (1974), Mass transfer in a pool with plunging liquid jets, in Proceeding of the International Chem. Engng Symposium Multiphase Flow System, Glasgow.

Van de Sande, E., and Smith, J. M. (1976), Jet break-up and air entrainment by low velocity turbulent water jets, Chemical Engineering Science, **31** pp. 219-224.

Van de Sande, E., and Smith, J. M., (1975), Mass transfer from plunging water jets, Chemical Engineering Science, **10** pp. 225-233.

References

Van de Sande, E., and Smith, J., M., (1973), Surface entrainment of air by high velocity water jets, Chemical Engineering Science, **28** pp. 1161-1168.

Wallis, G. B., (1969), One-dimensional two-phase flow, McGraw-Hill, New York, 265.

Wallis, G. B., (1970), Annular Two-Phase Flow, Part 1: A Simple Theory, Transactions of the ASME. Series D, Journal of Basic Engineering, **92** pp. 59-72.

Wang, B. Y., Dai, Z. Q., Qi, L. X., and Shi, H. H., (2006), Experimental study on back-attack phenomenon in underwater supersonic gas jets, Acta Mechanica Sinica, **39** (2) pp. 267-272.

Wang, H. W., and Law, A. W., (2002), Second-order integral model for a round turbulent buoyant jet, Journal of Fluid Mechanics, **459** pp. 397-428.

Weiland, C., Yagla, J., and Vlachos P. (2007), Experimental study of the stability of a high-speed gas jet under the influence of liquid crossflow, In: Proceedings of ASME Conference Proceedings, 5th Joint Fluids Engineering Conference July 30-August 2, 2007 , San Diego, California, USA.

Weimer, J. C., Faeth, G. M., and Olscn, D. R., (1972), Penetration of vapor jets submerged in subcooledliquids, AICHE Journal, **19** pp. 552-558.

Wislicenus, G. F., (1960), Hydrodynamics and propulsion of submerged bodies, Antioxidants and Redox Signaling Journal, **30** (12) pp. 1140-1148.

Wood, I. R., (1993), Asymptotic solutions and behavior of outfall plumes, American Society of Civil Engineers (ASCE), Journal of the Hydraulics Division **119** (5) pp. 555-580.

Woods, A. W., (1997), A note on non-Boussinesq plumes in an incompressible stratified environment, Journal of Fluid Mechanics, **345** pp. 347-356.

Wright, S. J., (1977), Mean behavior of buoyant jets in a cross flow, Journal of the hydraulics division, **103** (5) pp. 499-513.

Xiao, J., Travis, J., and Breitung, W., (2008), Non-boussinesq integral model for horizontal turbulent strongly buoyant plane jets, In Proceedings of the 16th International Conference on Nuclear Engineering, Orlando, Florida, USA.

Xiao, J., Travis, J., and Breitung, W., (2009), Non-boussinesq integral model for horizontal turbulent buoyant round jets, Science and Technology of Nuclear Installations, **2009** pp. 1-7.

Yang, Q. X. and Gustavsson, H., (1992), Effects of gas jet instability on refractory wear-a study by high-speed photography, Scandinavian Journal of Metallurgy, **221** (1) pp. 15-26.

Yang, Q. X., Gustavsson, H., and Burström, E., (1990), Erosion of refractory during gas injection-a cavitation based model, Scandinavian Journal of Metallurgy, **136** pp. 127-136.

Zaman, K. B., (1999), Spreading characteristics of compressible jets from nozzles of various geometry, journal of fluid mechanics, **383** pp.197-228.

Zaman, K. B., Dahl, T., Bencic and Loh, C. Y., (2002), Investigation of a transonic resonance with convergent divergent nozzles, journal of fluid mechanics, 463 pp. 313-343.

Zhao, Y. F., and Irons, G. A., (1990), The breakup of bubbles into jets during submerged gas injection, metallurgical transactions b-process metallurgy, **21** (6) pp. 997-1003.

Zimm, W., (1921), Flow phenomena in free air currents Ueber die Stromungsvorgange, Forschungsarbeiten auf dem Gebiete des Ingenieurwesens (234), 36.

Appendices

<div align="center">

Appendix A:

Coding and Reproducing Digital Images

</div>

The following is an introduction into the relevant operations of coding and reproducing digital images. A more thorough description can be found in Poynton (1996).

When the ray of light reaches the camera, the camera will perceive it as a Spectral Power Distribution (SPD). Visible light for the human eye has a wavelength between 400 nanometres and 700 nanometers and it depends on the SPD what colour the eye perceives. Wavelengths between 400 and 500 nanometres are perceived as blue by the human eye, wavelengths between 500 and 600 nanometres green and between 600 and 700 nanometers red. Figure (A.1) is an example of a SPD. This distribution shows what a standard person perceives as a bright yellow-green as determined by the CIE (Commission International de L'eclairage or International Commission on Illumination). The camera will receive a SPD for each pixel and transforms these into digital data. In order to do that the continuous SPD has to be broken up into different components so that a finite amount of data can define the SPD and thus be stored. A possible solution could have been to break a SPD up into 31 components all storing an average value over a range of 10 nanometers. But due to the trichromatic nature of vision, three components are enough if the appropriate spectral weighing functions are used (Settles, 2006). The three components together are called a tristimulus.
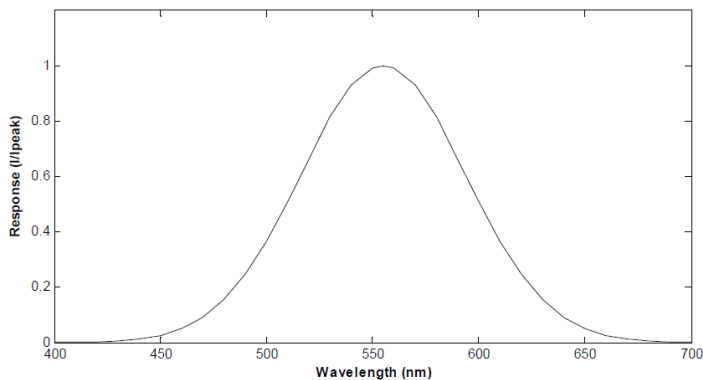

Figure (A.1): The CIE luminous efficiency function

Figure (A.2) Poynton (1996) shows that not just any three spectral weighing functions can be chosen. If a wideband filter with three peaks (one in the blue region, in the green and in the red) is chosen, as is shown in the top row of Figure (A.2), two monochromatic colours with wavelengths of 610 and 620 nanometers respectively will both be filtered out as red, while in actual fact the first one is orange. If a narrowband filter is chosen, as shown in the middle row in Figure (A.2), the problem of the wideband filter is solved but it creates a different problem. The monochromatic colour with a wavelength of 610 nanometers falls between the filters and thus will be reproduced as black.
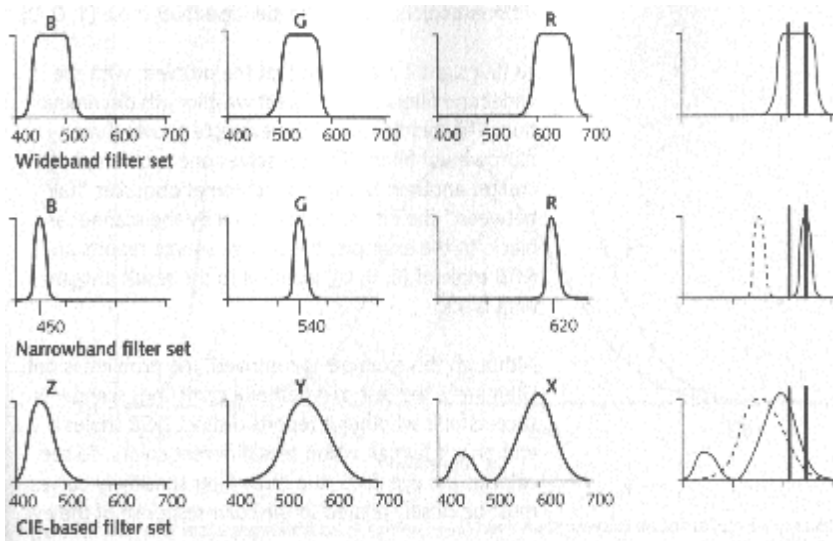

Figure (A.2): Examples of spectral weighing functions (Poynton, 1996)

Thus to always see a colour as the eye would, the response of the filters must be similar to the response of the human eye. The CIE has determined the spectral response curves that do just that for a standard observer, the CIE-based filter set. Together they form the Colour Matching Function enlarged in Figure (A.3) (Poynton, 1996). For a camera to capture all colours, the spectral response curves of the camera must be as shown in Figure (A.3) or a linear combination of them. However this is not viable in practice. In practice a different tristimulus XYZ is calculated from x-bar, y-bar, z-bar, where X is obtained by integrating its SPD weighted by the x-bar Matching Function etc. But the tristimulus XYZ turned out to be not perceptual uniform. A system is perceptually uniform if a small perturbation to a component value is approximately equally perceptible across the range of that value. To optimize this further transformations are done to create Tristimuli called L*u*v and L*a*b where L is the luminance or

brightness. But complexities make these Tristimuli not suitable for image coding. Instead R'G'B' is used as it is quite perceptually uniform and is fast enough for interactive applications. RGB is approximately the 0.45 power-law of RGB. RGB is related to XYZ with a 3x3 matrix.
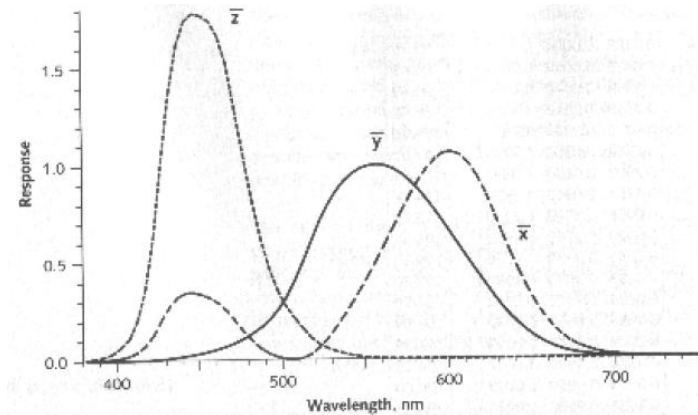

Figure (A.3): CIE colour matching function (Poynton, 1996)

The Tristimulus gives the three components that represent colour. Using these three components it is possible to reproduce the colours (and thus the picture) using the computer. Simplest way of doing that is by adding and mixing the beams of light of the three different colours. There is no need for the original SPD, just the Tristimulus. This is the case with a projector. Computer screens for example work differently. Still the three components are mixed together to form the colours, but the screen itself consists of small dots that produce red, green and blue light. From a distance the viewer will only see the new colours.

The actual transformation that goes on in both the coding of the colour, as well as the reproduction of it are a few steps more complicated than explained above but are based on the same theories (Gustaaf, 2006).

Appendix B:

Computer Vision System and Image Information

B.1 Computer Vision Systems

A basic computer vision system requires a camera, a camera interface and a computer. These days, some personal computers offer the capability for a basic vision system, by including a camera and its interface within the system. There are specialized systems for vision, offering high performance in more than one aspect.

B.1.1 Cameras

A camera is the basic sensing element. In simple terms, most cameras rely on the property of light to cause hole/electron pairs (the charge carriers in electronics) in a conducting material. When a potential is applied (to attract the charge carriers), this charge can be sensed as current. By Ohm's law, the voltage across a resistance is proportional to the current through it, so the current can be turned in to a voltage by passing it through a resistor. The number of hole/electron pairs is proportional to the amount of incident light. Accordingly, greater charge (and hence greater voltage and current) is caused by an increase in brightness. In this manner cameras can provide as output, a voltage that is proportional to the brightness of the points imaged by the camera. Cameras are usually arranged to supply video according to a specified standard.

There are three main types of camera: vidicons, charge coupled devices (CCDs) and, more recently, CMOS cameras (complementary metal oxide silicon, now the dominant technology for logic circuit implementation). Vidicons are the older (analogue) technology which, although cheap (mainly by virtue of longevity in production), are being replaced by the newer CCD and CMOS digital technologies. The digital technologies now dominate much of the camera market because they are lightweight and cheap (with other advantages) and are therefore used in the domestic video market.

Vidicons operate in a manner akin to a television in reverse. The image is formed on a screen, and then sensed by an electron beam that is scanned across the screen. This produces an output which is continuous; the output voltage is proportional to the brightness of points in the scanned line, and is a continuous signal, a voltage which varies continuously with time. In contrast, CCDs and CMOS cameras use an array of sensors; these are regions where charge is collected which are proportional to the light incident on that region. This is then available in discrete, or sampled, form as opposed to the continuous sensing of a vidicon. This is similar to human vision with its array of cones and rods, but digital cameras use a rectangular regularly spaced lattice, whereas human vision uses a hexagonal lattice with irregular spacing (Gustaaf, 2006).

Two main types of semiconductor pixel sensor are illustrated in Figure (B.1). In the passive sensor, the charge generated by incident light is presented to a bus through a pass transistor.
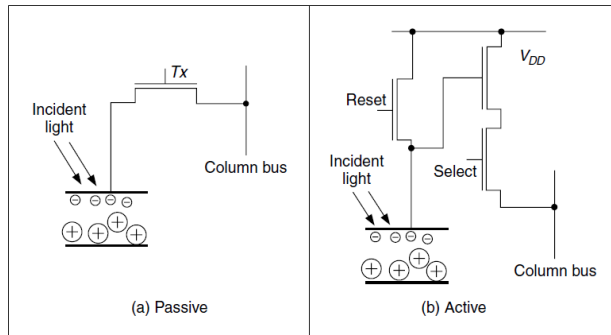

Figure (B.1): Pixel sensors

When the signal T_x is activated, the pass transistor is enabled and the sensor provides a capacitance to the bus, one that is proportional to the incident light. An active pixel includes an amplifier circuit that can compensate for limited fill factor of the photodiode. The select signal again controls presentation of the sensor's information to the bus. A further reset signal allows the charge site to be cleared when the image is rescanned.

The basis of a CCD sensor is illustrated in Figure (B.2). The number of charge sites gives the resolution of the CCD sensor; the contents of the charge sites (or

buckets) need to be converted to an output (voltage) signal. In simple terms, the contents of the buckets are emptied into vertical transport registers which are shift registers moving information towards the horizontal transport registers. This is the column bus supplied by the pixel sensors. The horizontal transport registers empty the information row by row (point by point) into a signal conditioning unit, which transforms the sensed charge into a voltage which is proportional to the charge in a bucket, and hence proportional to the brightness of the corresponding point in the scene imaged by the camera. The CMOS cameras are like a form of memory: the charge incident on a particular site in a two-dimensional lattice is proportional to the brightness at a point. The charge is then read like computer memory. (In fact, a computer RAM chip can act as a rudimentary form of camera when the circuit, the one buried in the chip, is exposed to light).
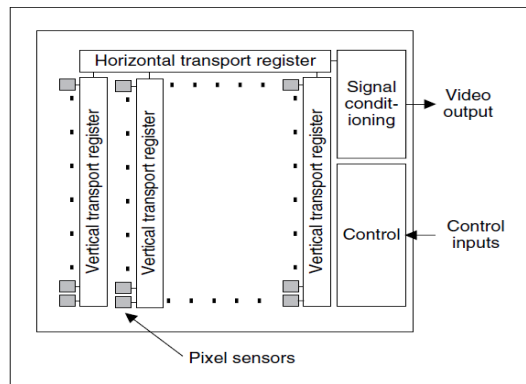

Figure (B.2): CCD sensing element

There are many more varieties of vidicon (Chalnicon, etc.) than there are of CCD technology (charge injection device, etc.), perhaps owing to the greater age of basic vidicon technology. Vidicons are cheap but have a number of intrinsic performance problems. The scanning process essentially relies on moving parts. As such, the camera performance will change with time, as parts wear; this is known as ageing. Also, it is possible to burn an image into the scanned screen by using high incident light levels; vidicons can also suffer lag, that is, a delay in response to moving objects in a scene.

B.1.2 Computer Interfaces

This technology is in a rapid state of change, owing to the emergence of digital cameras. Essentially, the image sensor converts light into a signal which is expressed either as a continuous signal or in sampled (digital) form. Some (older) systems expressed the camera signal as an analogue continuous signal, according to a standard, often the CCIR standard, and this was converted at the computer (and still is in some cases). Modern digital systems convert the sensor information into digital information with on-chip circuitry and then provide the digital information according to a specified standard. The older systems, such as surveillance systems, supplied (or supply) video, whereas the newer systems are digital. Video implies delivering the moving image as a sequence of frames and these can be in analogue (continuous) or discrete (sampled) form, of which one format is digital video (DV). An interface that converts an analogue signal into a set of digital numbers is called a frame grabber, since it grabs frames of data from a video sequence, and is illustrated in Figure (B.3). Note that cameras that provide digital information do not need this particular interface (it is inside the camera). However, an analogue camera signal is continuous and is transformed into digital (discrete) format using an analogue-to-digital (A/D) converter. Flash converters are usually used owing to the high speed required for conversion, say 11 MHz, which cannot be met by any other conversion technology. Usually, 8 bit A/D converters are used; at 6 dB/bit, this gives 48 dB, which just satisfies the CCIR stated bandwidth of approximately 45 dB. The output of the A/D converter is often fed to look-up tables (LUTs), which implement designated conversion of the input data, but in hardware rather than in software, and this is very fast. The outputs of the A/D converter are then stored. Note that there are aspects of the sampling process that are of considerable interest in computer vision (Gustaaf, 2006).
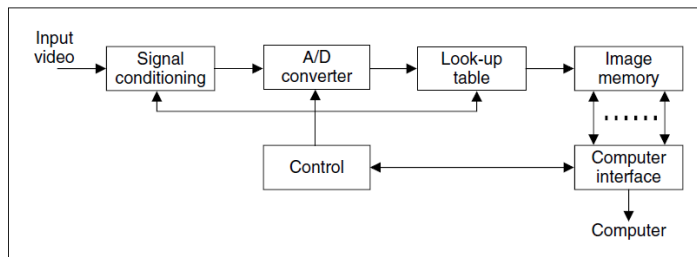

Figure (B.3): A computer interface: A frame grabber

In digital camera systems this processing is usually performed on the camera chip, and the camera eventually supplies digital information, often in coded form. IEEE 1394 (or firewire) is a way of connecting devices external to a computer and is often used for digital video cameras as it supports high-speed digital communication and can provide power; this is similar to universal serial bus (USB), which can be used for still cameras. Firewire needs a connection system and software to operate it, and these can be easily acquired. One important aspect of Firewire is its support of isochronous transfer operation which guarantees timely delivery of data, which is of importance in video-based systems.

B.1.3 Processing an Image

Most image processing and computer vision techniques are implemented in computer software. Often, only the simplest techniques migrate to hardware, although coding techniques to maximize efficiency in image transmission are of sufficient commercial interest that they have warranted extensive, and very sophisticated, hardware development. Chapter (4) has more information about image processing.

B.2 Image Formation

A computer image is a matrix (a two-dimensional array) of pixels. The value of each pixel is proportional to the brightness of the corresponding point in the scene; its value is usually derived from the output of an analogue-to-digital (A/D) converter. The matrix of pixels, the image, is usually square and an image may be described as N×N m-bit pixels, where N is the number of points and m controls the number of brightness values. Using m bits gives a range of 2^m values, ranging from 0 to 2^m-1. If m is 8 this gives brightness levels ranging between 0 and 255, which are usually displayed as black and white, respectively, with shades of grey in between. Smaller values of m give fewer available levels, reducing the available contrast in an image.

The ideal value of m is related to the signal-to-noise ratio (bandwidth) of the camera. This is stated as approximately 45 dB for an analogue camera, and since

there are 6 dB per bit, 8 bits will cover the available range. Choosing 8 bit pixels has further advantages in that it is very convenient to store pixel values as bytes, and 8 bit A/D converters are cheaper than those with a higher resolution. For these reasons images are nearly always stored as 8 bit bytes, although some applications use a different range. The least significant bit, bit 0, carries the least information (it changes most rapidly). As the order of the bits increases, they change less rapidly and carry more information. The most information is carried by the most significant bit, bit 7.

Color images follow a similar storage strategy to specify pixels' intensities. However, instead of using just one image plane, color images are represented by three intensity components. These components generally correspond to red, green and blue (the RGB model), although there are other color schemes. For example, the CMYK color model is defined by the components cyan, magenta, yellow and black. In any color mode, the pixel's color can be specified in two main ways. First, you can associate an integer value with each pixel, which can be used as an index to a table that stores the intensity of each color component. The index is used to recover the actual color from the table when the pixel is going to be displayed, or processed. In this scheme, the table is known as the image's palette and the display is said to be performed by color mapping. The main reason for using this color representation is to reduce memory requirements. That is, we only store a single image plane (i.e. the indices) and the palette. This is less than storing the red, green and blue components separately and so makes the hardware cheaper, and it can have other advantages, for example when the image is transmitted. The main disadvantage is that the quality of the image is reduced since only a reduced collection of colors is actually used. An alternative to represent color is to use several image planes to store the color components of each pixel. This scheme is known as true color and it represents an image more accurately, essentially by considering more colors. The most common format uses 8 bits for each of the three RGB components. These images are known as 24 bit true color and they can contain 16 777 216 different colors simultaneously. In spite of requiring significantly more memory, the image quality and the continuing reduction in cost of computer memory make this format a good alternative, even for storing the image frames from a video sequence. A good compression algorithm is always helpful in these cases, particularly if images need to be transmitted on a

network. Here we will consider the processing of grey-level images only, since they contain enough information to perform feature extraction and image analysis. Should the image be originally color, we will consider processing its luminance only, often computed in a standard way. In any case, the amount of memory used is always related to the image size.

Choosing an appropriate value for the image size, N, is far more complicated. We want N to be sufficiently large to resolve the required level of spatial detail in the image. If N is too small, the image will be coarsely quantized: lines will appear to be very 'blocky' and some of the detail will be lost. Larger values of N give more detail, but need more storage space and the images will take longer to process, since there are more pixels.

The choice of sampling frequency is dictated by the sampling criterion. Presenting the sampling criterion requires understanding of how we interpret signals in the frequency domain. The way in is to look at the Fourier transform. This is a highly theoretical topic, but do not let that put you off (it leads to image coding, like the JPEG format, so it is very useful indeed). The Fourier transform has found many uses in image processing and understanding; it might appear to be a complex topic (that's actually a horrible pun!), but it is a very rewarding one to study. The particular concern is the appropriate sampling frequency of (essentially, the value for N), or the rate at which pixel values are taken from, a camera's video signal (Gustaaf, 2006).
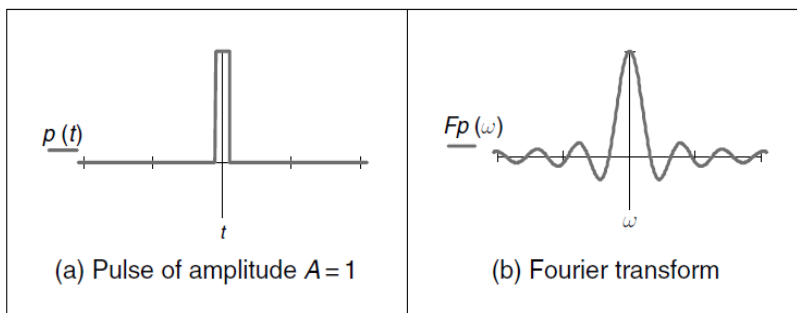

Figure (B.4): A pulse and its Fourier transform

VITA

Khaled Harby was born in Egypt. He received his elementary and secondary education there. In 2004, he earned a Bachelor of Science Degree with first class honors in Mechanical Power Engineering and Energy from El - Minia University, Faculty of Engineering. Upon completion of his degree requirements, he was honored by appointing him as a Teaching Assistant from 2004-2008 in Mechanical Power Engineering at the same department.

He then moved to Spain to study at the Polytechnic University of Madrid. He served there as a researcher from 2008-2009 in the Aeronautical Engineering majoring in Aerospace Structures at Higher School of Aeronautical Engineering. He then moved to Valencia to pursue graduate studies at the Polytechnic University of Valencia. There in 2009, he joined the official master program in Energy Technology for Sustainable Development at Institute for Energy Engineering and he obtained the master degree in 2010. After the M.Sc. degree, he started directly in a Ph.D program in Energy Technology majoring in Nuclear Thermal-Hydraulics and Reactor Safety at Department of Chemical and Nuclear Engineering, Institute for Energy Engineering where he has worked as a Research Assistant up until this point. When he will get the Ph.D, he will return to join the research group in his original university as a lecturer at the Mechanical Power Engineering and Energy Department. His research interests include fluid mechanics, experimental and numerical study of multiphase flows, and thermal engineering.

Permanent address: Department of Mechanical Power Engineering and Energy, Faculty of Engineering, Minia University, Minia, 61517, Egypt.

Email address: khaledharby8@yahoo.com.